EPR-INDUCED CHARGE TRANSPORT IN HIGHLY DOPED CRYSTALLINE N-TYPE SILICON CARBIDE

Vom Fachbereich Physik der

Universität-Gesamthochschule Paderborn

zur Erlangung des akademischen Grades

eines Doktors der Naturwissenschaften

(Dr. rer. nat.)

genehmigte Dissertation

von

María Isabel Grasa Molina

geboren in Huesca (Spanien)

1. Gutachter: Prof. Dr. J.-M. Spaeth

2. Gutachter: Prof. Dr. H. Overhof

Tag der Einreichung: 5. Juli 2000

Tag der mündlichen Prüfung: 10. August 2000

Contents

Chapter 1

Motivation

The electrical properties of semiconductors (conductivity, carrier lifetime and free carrier mobility) change dramatically with the introduction of defects and impurities in concentrations as low as 10^{11} cm^{-3}. Some defects are unwanted, such as impurities unintentionally introduced during crystal growth, others are intentionally prepared. Their presence may lead to dramatic performance improvements (or deteriorations as well) over the "ideal" material. Thus, the study of defects has great practical importance for material science. For this reason, defects in semiconductors have been thoroughly studied during the past 50 years and will continue to attract scientific and technical interest. The semiconductor revolution was made possible by the ability to grow highly pure and structurally perfect crystals and to add impurities as dopants to obtain the desired electronic properties.

There are many methods to characterize a semiconductor with respect to its defects, but only few of them can determine the defect structure on the atomic scale. Electron paramagnetic resonance (EPR) methods are the most powerful techniques for the determination of defect structures (see e.g. [Spaeth 92]). There are, however, some limitations to the application of the conventional EPR technique to the investigation of paramagnetic point defects in epitaxial layers and commercial semiconductor devices:

1. The samples are usually too small and the density of paramagnetic centres is too low. Thus, the number of paramagnetic centres present in the samples is smaller than the 10^{11} required for EPR detection.

2. The Q-factor of the cavity is strongly reduced by low resistivity samples.

3. Metallic contacts and other parts of devices may act as a good screen against the microwave field and illumination, preventing EPR measurements.

These limitations can be overcome by using electrically detected electron paramagnetic resonance (EDEPR). This technique offers several advantages over microwave-detected EPR:

1. It delivers information on the relevant microscopic transport processes in the sample, such as recombination, capture or tunnelling of charge carriers.
2. It offers enhanced detection sensitivity (just 10^8 electron spins are required, as has been demonstrated by Stich [Stich 96]).
3. The detection channel is not the microwave absorption, but the electrical conductivity. Thus, the reduction in the cavity Q-factor through contacts and low resistivity samples is less critical. Furthermore, the expensive microwave detection technique becomes superfluous.
4. *In situ* investigation under normal operating conditions is possible.

The mechanisms underlaying the EDEPR effect, i.e. the change of the sample conductivity at spin resonance conditions, have extensively been studied in the case of lowly doped crystalline semiconductors as well as amorphous material (for review see e.g. [Stich 96] and [Brandt 92], respectively). The aim of this work was to investigate the EDEPR effect for highly doped crystalline semiconductors and propose a model for the explanation of the microscopic processes involved. For this purpose we studied different n-type silicon carbide samples, the nitrogen concentrations of which were high, but still lower than the critical concentration corresponding to the transition to metallic behaviour. The conducted electrical characterization, EPR and EDEPR studies provided information on microscopic processes in the material and made the discussion of a model for the EDEPR effect possible.

Silicon carbide is receiving considerable attention because of its potential to provide improved performance in high temperature, high power and high frequency applications over silicon and gallium arsenide. Specific applications include high frequency technology (e.g. radar systems), high power electronics (e.g. MOSFETs), extremely high temperature applications (e.g. at turbines, engines), as well as optoelectronic devices (LEDs, UV sensors). Silicon, which becomes intrinsic at about 325 C,

cannot be used at high temperature and for high power requirements. Recently silicon carbide has also been used as a substrate for the growth of GaN epitaxial layers.

A thorough electrical and optical characterization of the starting material, as well as a microscopic understanding of defects are needed in order to improve device performance. Nevertheless, the knowlegde of defects in silicon carbide is not as complete as it is in silicon. This is partly due to the fact that the available SiC material was structurally imperfect and chemically rather impure. Not until a few years ago advances in growth technology have enabled the study of crystals with comparatively low concentrations of structural defects together with low concentrations of unwanted impurities.

The fact that highly doped silicon carbide samples still showing semiconducting behaviour show low resistivity at low temperatures [Kalabukhova 87], has been attributed to hopping conductivity. For such donor concentrations (or acceptor concentrations for p-type material), the separation between impurity centres is only a few times their Bohr radius. As a result, the donor electrons can move from one donor to another one by a thermally activated process, called hopping conduction [Miller 60]. Nevertheless, hopping can also be due to the absorption of energy from excited spins (EPR-induced hopping). EPR-induced hopping has often been identified as the EDEPR mechanism in amorphous semiconductors [Kishimoto 81, Dersch 84, Brandt 92]. This work deals with hopping conductivity and EDEPR in highly doped crystalline silicon carbide.

This work is structured as follows: following this brief introduction, the theoretical aspects of both EPR and hopping conductivity are presented in chapters 2 and 3, respectively. In chapter 4 the state-of-the art of the knowledge about EDEPR is summarized. Chapter 5 presents some relevant properties of silicon carbide. Chapter 6 shows some important information concerning the experimental equipment and the preparation of the samples used in this work. Chapter 7 deals with the electrical investigations conducted in this work aimed at the determination of the charge transport mechanism at low temperatures. Chapter 8 deals with experimental studies of the EDEPR signal. Chapter 9 is dedicated to the behaviour of both the EPR and the EDEPR signals for different defect concentrations. In chapter 10 different EDEPR mechanisms are discussed in terms of the experimental results

presented in this work. In chapter 11 the behaviour of the EDEPR signal of an epitaxial sample for certain current conditions is presented. Finally, in chapter 12 a summary is presented.

Chapter 2

Electron Paramagnetic Resonance

Electron paramagnetic resonance (EPR) is a successful method for the characterization of defects in solids. EPR investigations provide information on the symmetry of point defects and their electronic configuration. The first observation of electron paramagnetic resonance was made by Zavoisky [Zavoisky 45], who detected a radio frequency absorption line in a $CuCl_2 \cdot 2H_2O$ sample.

EPR spectroscopy deals with the interaction of electromagnetic radiation with electronic magnetic moments. The electron magnetic moment arises from the spin angular momentum with a (in most cases small) contribution from orbital motion. This technique is applicable to systems in a paramagnetic state (or which can be brought to such a state, for instance by irradiation), that is, a state having a net electron angular momentum. Let us take a state with electron spin S=1/2 and neglect interactions with nuclear spins. In a static magnetic field the energy degeneracy of the spin states $m_S = \pm 1/2$ disappears due to the electron Zeeman interaction. Transitions between the two Zeeman levels may now be induced by an electromagnetic field $\vec{\mathbf{B}}_1$ of the appropriate frequency ν, such that the energy $h\nu$ matches the energy level separation $\Delta\epsilon$:

$$h\nu = \Delta\epsilon = g\mu_B B \ , \tag{2.1}$$

where g designates the electronic g factor, μ_B the Bohr magneton and B the magnetic field that satisfies the resonance condition. Besides eq. (2.1), there is a second requirement that must be met for a transition to take place: the oscillating magnetic field must have a component perpendicular to the static magnetic field (see fig. 2.1).

In an EPR experiment the transitions between the two Zeeman levels are detected by recording the absorption of the electromagnetic field (in most cases, microwave field). Usually the microwave frequency is fixed and the magnetic field is varied until a resonant absorption is found.

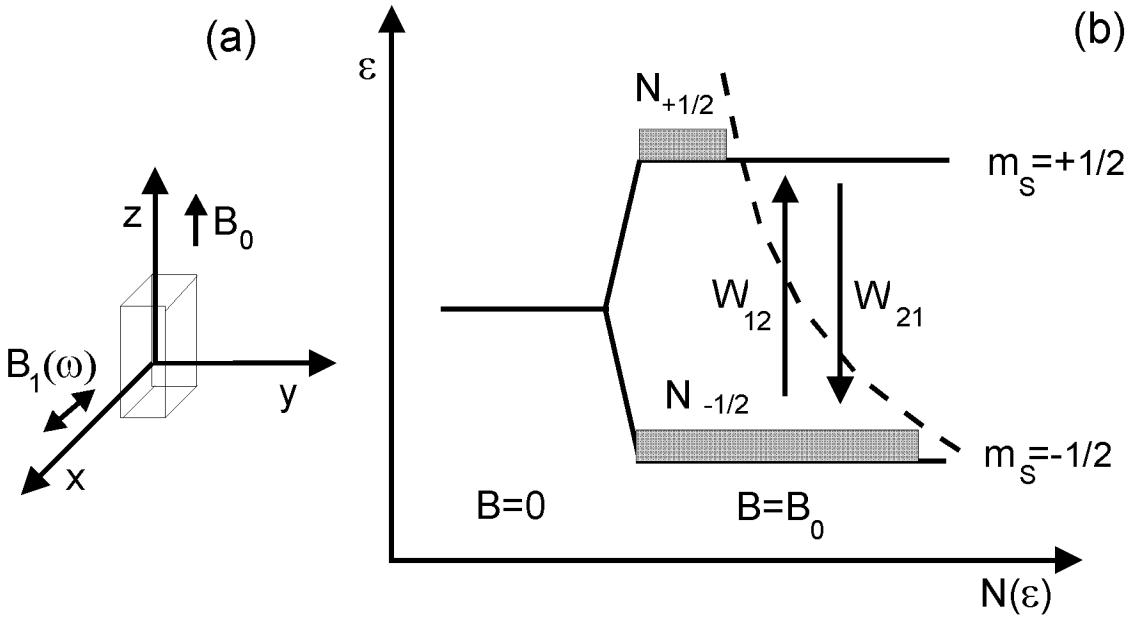

Figure 2.1: Basic EPR experiment (a) Experimental geometry: the oscillating microwave magnetic field $\vec{\mathbf{B}}_1(\omega)$ must be perpendicular to the static field $\vec{\mathbf{B}}$. (b) Schematic illustration of the Zeeman levels and their respective population densities for a system with spin S=1/2 in thermal equilibrium with the lattice. W_{12} and W_{21} denote the probabilities for the upward and downward magnetic dipole transitions.

2.1 Basic concepts of EPR

2.1.1 Magnetization

Let us consider an assembly of identical dipoles with a total angular momentum $\vec{\mathbf{J}} = \vec{\mathbf{L}} + \vec{\mathbf{S}}$ in thermal equilibrium. In a static magnetic field the energy degeneracy is raised and we obtain a set of $2J+1$ equally spaced *Zeeman* levels $\epsilon_j = g\mu_B B m_z$, $m_z = -J, -J+1, ..., J-1, J$. The probability that a dipole within the assembly at

temperature T has the energy ϵ_j is, according to Boltzmann statistics:

$$p_j = \frac{exp(-\epsilon_j/kT)}{\sum_i exp(-\epsilon_i/kT)} \ . \tag{2.2}$$

For the simple case of $J = S = 1/2$, one obtains $m_z = \pm 1/2$, $\epsilon_j = g\mu_B m_z B$, and eq. (2.2) can be written

$$p_{m_z} = \frac{exp(-g\mu_B m_z B/kT)}{exp(\frac{1}{2}g\mu_B B/kT) + exp(-\frac{1}{2}g\mu_B B/kT)} \ . \tag{2.3}$$

The magnetization M of a number N of dipoles per volume unit is then given by

$$M = N(p_{-1/2} - p_{1/2})g\mu_B \frac{1}{2} = \frac{1}{2}Ng\mu_B \ tanh\left(\frac{g\mu_B B}{2kT}\right) \ . \tag{2.4}$$

$p_{-1/2}, p_{1/2}$ being the probabilities for the lower and upper Zeeman states, respectively. This is the well-known *Langevin equation* for the magnetization. The Zeeman splitting is usually much smaller than the thermal energy: $g\mu_B B \ll kT$. In this case we can then make the approximation $tanhx \approx x$ and obtain

$$M = N\frac{g^2\mu_B^2 B}{4kT} \ . \tag{2.5}$$

This is the Curie law, describing the dependence of the magnetization on magnetic field and temperature: direct and inverse proportional, respectively. For the general case of a non-zero orbital contribution, $J > 1/2$, the magnetization is given by the Brillouin function

$$M = NJg\mu_B B_J(x) \tag{2.6}$$

$$B_J(x) = \frac{2J+1}{2J}coth\left(\frac{(2J+1)x}{2J}\right) - \frac{1}{2J}coth\left(\frac{x}{2J}\right) \ . \tag{2.7}$$

2.1.2 Spin-lattice relaxation

The probabilities for the transitions from the lower to the upper Zeeman level W_{12} (absorption) and from the upper to the lower W_{21} (induced emission) are equal. The probability for spontaneous emission is negligibly small. As a result, no microwave energy can be transferred from the microwave field to the spin system if both levels have the same occupation. The necessary condition for a net microwave absorption is an occupation difference $N_+ - N_- > 0$. Without further processes besides the magnetic dipole transitions the EPR transition is quickly saturated to zero as soon as

$N_+ - N_- = 0$ is reached. In a crystalline environment, however, an occupation difference between the Zeeman levels is maintained by the electron-phonon interaction. This occupation difference is determined by a Boltzmann distribution (see eq. (2.2)).

The electron-phonon interaction gives rise to the so-called *spin-lattice relaxation*. There are different mechanisms contributing to this relaxation, e.g. the oscillatory component of the local magnetic field at the site of the unpaired electron due to vibrations of magnetic neighbour atoms. The spin-lattice relaxation is usually discussed in terms of the spin-lattice relaxation time T_1. This is the characteristic time needed by a spin system to return to its equilibrium state after a perturbation, e.g. a microwave pulse. T_1 increases with decreasing temperature, and also depends on the magnetic field value. The precise temperature and magnetic field dependences differ for the various possible relaxation processes (direct, Raman and Orbach processes). In practice several processes can occur for one defect, depending on the temperature range. Therefore the prediction of the value of T_1 for given temperature and magnetic field conditions is not possible.

2.1.3 EPR parameters

The magnitude of the EPR signal is proportional to the net resultant polarization of the spin orientations of the ensemble, that is to the magnetization. Because of that, the signal varies with temperature and magnetic field as given by eq. (2.7).
The EPR signal increases with increasing microwave power up to a certain power level and then diminishes. This occurs when the rate of upward and downward transitions is equalized. In this case, no net energy is transferred between the microwave field and the spin system, and the system is said to be saturated. If the interaction between spin system and lattice is very weak, then the saturation occurs even at very low microwave power. In the opposite case, lifetime broadening may be so great that the line is broadened beyond detection.

2.2 The Bloch equations

The macroscopic properties of the EPR signal, i.e. the line intensity, linewidth, and lineshape are given by the dynamical properties of the spin system. These are the spin-spin interaction and the interaction of the spins with the thermal movements of the atoms (spin-lattice interaction). Such effects can be described with Bloch's phenomenological theory [Bloch 46]. The Bloch equations describe the time dependence of the total spin magnetization vector $\vec{\mathbf{M}}$ in the presence of static and oscillating magnetic fields externally applied.

Let us consider an ensemble of paramagnetic defects with the magnetization $\vec{\mathbf{M}} = \sum_i \vec{\mu}_i$ per volume unit. The equations of motion for the magnetization in a static magnetic field $\vec{\mathbf{B}}_0 \parallel z$ parallel to the z-direction can be written:

$$\frac{dM_x}{dt} = \gamma(\vec{\mathbf{M}} \times \vec{\mathbf{B}})_x - \frac{M_x}{T_2} \tag{2.8}$$

$$\frac{dM_y}{dt} = \gamma(\vec{\mathbf{M}} \times \vec{\mathbf{B}})_y - \frac{M_y}{T_2} \tag{2.9}$$

$$\underbrace{\frac{dM_z}{dt} = \gamma(\vec{\mathbf{M}} \times \vec{\mathbf{B}})_z}_{(1)} + \underbrace{\frac{M_0 - M_z}{T_1}}_{(2)} \tag{2.10}$$

Part (1) corresponds to the classical behaviour of a magnetic dipole $\vec{\mu}$ in an external magnetic field $\vec{\mathbf{B}}$. γ is the gyromagnetic ratio of the paramagnetic defect $\gamma = -g\mu_B/\hbar$ and M_0 the magnetization in thermal equilibrium. Part (2) takes into consideration relaxation effects. The time constant T_1 is called longitudinal relaxation time. It describes the spin-lattice relaxation, since the energy of the spin system is changed by (2.10). T_2 is called transverse relaxation time and describes the spin-spin relaxation.

In an EPR experiment the sample is irradiated with a microwave field, whose magnetic component $\vec{\mathbf{B}}_1(t)$ is perpendicular to the static magnetic field:

$$\vec{\mathbf{B}}_1(t) = 2B_1 cos(\omega t)\vec{\mathbf{x}} \; . \tag{2.11}$$

Then the magnetic field is given by:

$$\vec{\mathbf{B}} = \begin{pmatrix} 2B_1 cos(\omega t) \\ 0 \\ B_0 \end{pmatrix} . \tag{2.12}$$

We now define a complex microwave field B_C as:

$$B_C = 2B_1 exp(i\omega t) = 2B_1[cos(\omega t) + isin(\omega t)] \tag{2.13}$$

and a complex susceptibility χ_C with

$$\chi_C = \chi' - i\chi'' . \tag{2.14}$$

The complex magnetization is then defined as

$$M_C = \chi_C B_C . \tag{2.15}$$

The stationary solution of Bloch's equations is given by the real and imaginary part of the magnetic susceptibility (χ', χ'') and the component of the magnetization in the direction of the static magnetic field M_z [Spaeth 92]:

$$\chi' = \frac{1}{2}\frac{\gamma(\omega - \omega_0)T_2^2}{1 + (\omega - \omega_0)^2 T_2^2 + \gamma B_1^2 T_1 T_2} M_0 \tag{2.16}$$

$$\chi'' = \frac{1}{2}\frac{\gamma T_2}{1 + (\omega - \omega_0)^2 T_2^2 + \gamma B_1^2 T_1 T_2} M_0 \tag{2.17}$$

$$M_z = \frac{1}{2}\frac{1 + (\omega - \omega_0)T_2^2}{1 + (\omega - \omega_0)^2 T_2^2 + \gamma B_1^2 T_1 T_2} M_0 . \tag{2.18}$$

χ'' is proportional to the microwave power absorbed by the spin system at resonance. For this reason it is called absorption component of the magnetic susceptibility. χ', which has a phase shift of 90 degrees, is called dispersion.

2.3 Power absorbed at resonance

For a system with spin S=1/2 the microwave absorbed by the spins at resonance can be written [Pake 73]:

$$P = \frac{1}{4}\gamma^2 B_1^2 h\nu n_0 g(\nu) \frac{1}{1 + \frac{1}{4}\gamma^2 B_1^2 g(\nu)/\{\frac{1}{2}(W_{12} + W_{21})\}} , \tag{2.19}$$

where n_0 is the number of spins, B_1 the microwave magnetic field, ν the microwave frequency, and W_{12} and W_{21} the transition rates from the lower to the upper Zeeman level and viceversa. $g(\nu)$ is the lineshape function, which acknowlegdes the fact that the energy levels are not infinitesimally sharp, for a Lorentzian line it is given by [Pake 73]:

$$g(\nu) = \frac{2T_2}{1 + (\gamma B_0 - 2\pi\nu)^2 T_2^2} \tag{2.20}$$

for a Gaussian line:

$$g(\nu) = \frac{2\sqrt{\pi}}{\delta} \exp\left(-\frac{(\gamma B_0 - 2\pi\nu)^2}{\delta^2}\right) \tag{2.21}$$

Substituting eq. (2.20) in eq. (2.19) and using the relationship $W_{12} + W_{21} = 1/T_1$ we obtain

$$P = \frac{\frac{1}{2}\gamma^2 B_1^2 h\nu n_0 T_2}{1 + (\gamma B_0 - \omega)^2 T_2^2} \cdot \frac{1}{1 + \gamma^2 B_1^2 T_1 T_2 / [1 + (\gamma B_0 - \omega)^2 T_2^2]} \tag{2.22}$$

with B_0 the value of the static magnetic field and T_2 the spin- spin relaxation time. P grows first with the incident microwave power (B_1^2), reaches a maximum and then diminishes. The maximum absorbed microwave power is directly proportional to the microwave frequency and inversely proportional to the spin-lattice relaxation time:

$$P_{max} = \frac{n_0 (h\nu)^2}{2kT 2T_1} \tag{2.23}$$

For the case of a Gaussian line, we can write:

$$P_{EPR} = \frac{1}{4}\gamma^2 B_1^2 h\nu n_0 g(\nu) \cdot \frac{1}{1 + \frac{1}{2}\gamma^2 B_1^2 T_1 g(\nu)} \tag{2.24}$$

2.4 Analysis of EPR spectra

For the analysis of EPR spectra the eigenvalues of the spin Hamilton operator $\mathcal{H}$ have to be determined. This operator describes the energy levels involved in the EPR transition. It is composed of the energy terms connected with the spin of the electrons or nuclei involved in the resonance: electron Zeeman (EZ), fine structure (FS), hyperfine (HF), superhyperfine (SHF), nuclear Zeeman (NZ), and quadrupole (Q):

$$\mathcal{H} = \underbrace{\mu_B \ \vec{\mathbf{B}}_0 \cdot \underline{\underline{g}} \cdot \vec{\mathbf{S}}}_{EZ} + \underbrace{\vec{\mathbf{S}} \cdot \underline{\underline{D}} \cdot \vec{\mathbf{S}}}_{FS} + \sum_{i=1}^{N} (\underbrace{\vec{\mathbf{S}} \cdot \underline{\underline{A}}_i \cdot \vec{\mathbf{I}}_i}_{HF+SHF} - \underbrace{\mu_n \ g_{ni} \cdot \vec{\mathbf{B}}_0 \cdot \vec{\mathbf{I}}_i}_{NZ} + \underbrace{\vec{\mathbf{I}}_i \cdot \underline{\underline{Q}}_i \cdot \vec{\mathbf{I}}_i}_{Q}) \ , \quad (2.25)$$

where μ_B is the Bohr magneton, $\vec{\mathbf{B}}_0$ the static magnetic field, $\underline{\underline{g}}$ the electron g tensor, $\vec{\mathbf{S}}$ the electron spin operator, $\vec{\mathbf{I}}_i$ the nuclear spin operator of nucleus i, $\underline{\underline{A}}_i$ the SHF tensor of nucleus i, g_{ni} the g factor of nucleus i, μ_n the nuclear magneton, $\underline{\underline{Q}}_i$ the quadrupole tensor of nucleus i, and N the number of nuclei under consideration.

The electron and nuclear Zeeman terms describe the interaction of a static magnetic field with the magnetic moments of the electrons and nuclei, respectively. The electron $\underline{\underline{g}}$ tensor reflects the symmetry of the defect in the lattice and the orbital contributions to the magnetic moment of the defect. In its principle axes system the $\underline{\underline{g}}$ tensor can be divided into an isotropic and an anisotropic contribution. The anisotropic part is traceless and can hence be described with only two independent parameters:

$$\underline{\underline{g}} = g \ \underline{\underline{1}} + \begin{pmatrix} -h + h' & & \\ & -h - h' & \\ & & 2h \end{pmatrix} \ . \quad (2.26)$$

For a spin system with $S > 1/2$, the fine structure term has to be considered. It arises from the magnetic dipole-dipole interaction as well as from the crystal field felt by the spins through the spin-orbit interaction. The fine structure tensor $\underline{\underline{D}}$ is traceless. Thus, in its principal axes system it can be written as:

$$\underline{\underline{D}} = \begin{pmatrix} E & & \\ & -E & \\ & & D \end{pmatrix} - \frac{1}{3} D \begin{pmatrix} 1 & & \\ & 1 & \\ & & 1 \end{pmatrix} \ . \quad (2.27)$$

The hyperfine term gives the interaction of the electron spin with the nuclear spin of the central atom. Similarly, the superhyperfine term describes the interaction of the electron spin with the nuclear spins of the neighbouring nuclei. Both terms are usually divided into an isotropic and an anisotropic contribution:

$$\underline{\underline{A}} = (a\ \underline{\underline{1}} + \underline{\underline{B}})\ . \tag{2.28}$$

The scalar term a is called Fermi contact term and is proportional to the spin density at the nucleus. In the case of spin $S = 1/2$ it is given by:

$$a = \frac{2}{3}\mu_0 g \mu_B g_n \mu_n |\phi(0)|^2\ , \tag{2.29}$$

where $\phi(0)$ is the defect wavefunction at the nuclear site in a one particle approximation. The traceless anisotropic part can be written:

$$\underline{\underline{B}} = \begin{pmatrix} -b+b' & & \\ & -b-b' & \\ & & 2b \end{pmatrix}\ , \tag{2.30}$$

where b' describes the deviation from axial symmetry. The tensor elements of the anisotropic part of the hyperfine interaction are given by:

$$B_{ij} = \frac{\mu_0}{4\pi} g \mu_B g_n \mu_n \int \frac{3x_i x_j}{r^5} - \frac{\delta_{ij}}{r^3} |\phi(r)|^2 dV\ . \tag{2.31}$$

The quadrupole term arises for nuclear spins with $I > 1/2$. It originates from the electrostatic interaction between the nuclear quadrupole moment and the electrical field gradients at the nucleus. Analogous to the $\underline{\underline{B}}$ tensor, the quadrupole tensor $\underline{\underline{Q}}$ in its principal axes system can be written :

$$\underline{\underline{Q}} = \begin{pmatrix} -q+q' & & \\ & -q-q' & \\ & & 2q \end{pmatrix}\ . \tag{2.32}$$

The elements of the quadrupole tensor are given by:

$$Q_{ij} = \frac{eQ}{2I(2I-1)} \frac{\delta^2 V}{\delta x_i} \ . \tag{2.33}$$

In order to find the solution of the eigenvalue problem, the Hamilton operator is represented as a matrix with the states $|m_S, m_I\rangle$ as basis and diagonalized . A second way to solve the problem is to consider first the larger terms and to make an approximation. A solution obtained with an approximation of first or second order is sufficient in many cases. The electron Zeeman term is mostly much larger than the others, in this case we can make use of the perturbation theory and obtain the following solution in a first degree of approximation:

$$\begin{aligned} \varepsilon(m_S, m_I) = m_S g \mu_B B_0 + W_{FS}[3m_S^2 - S(S+1)] - m_I g_n \mu_n B_0 \\ + m_S m_I W_{SHF} + \frac{1}{2}(m_I^2 - \frac{1}{3} I(I+1)) W_Q \ , \end{aligned} \tag{2.34}$$

where m_S and m_I are the values of the electron and nuclear spin in the direction of the magnetic field. θ is the angle between the z-axis of the fine structure tensor and the magnetic field $\vec{\mathbf{B}}_0$. The parameters W_{FS}, W_{SHF}, and W_Q depend on the relative orientation of the principal axes of the tensors to the external magnetic field. Assuming a fine structure interaction with axial symmetry one can write:

$$W_{FS} = \frac{D}{6}(3cos^2(\Theta_D) - 1]) \tag{2.35}$$

$$W_{SHF} = a + b(3cos^2\Theta_A - 1) + b' sin^2(\Theta_A) cos(2\Phi_A) \tag{2.36}$$

$$W_Q = 3q(3cos^2\Theta_Q - 1) + q' sin^2(\Theta_Q) cos(2\Phi_Q) \ . \tag{2.37}$$

Here, $\Theta_{D,A,Q}$ is the angle between the magnetic field and the z-axis of the principal axes system of the respective tensor. $\Phi_{D,A,Q}$ is the angle between the rotation plane of the magnetic field and the x-axis of the principal axes system.

Chapter 3

Impurity conduction

At low temperatures the electronic properties of semiconductors are closely related to the structure of the electrically active defects, which introduce energy levels in the forbidden gap. The shallow level with largest concentration plays the role of the doping level, i.e. provides free carriers to the corresponding band. Levels deeper than the doping level capture free carriers and are called compensating levels. In n-type silicon carbide the nitrogen usually plays the role of the doping level. According to the effective mass (EMT) theory, used for the description of shallow defects in semiconductors, the energy ϵ_1 needed to remove an electron from the nitrogen into the conduction band is of the order

$$\epsilon_1 = me^4/2\hbar^2\kappa^2 \tag{3.1}$$

Here, κ is the dielectric susceptibility and m the effective mass. $m = (m_1 m_2 m_3)^{1/3}$, $m_{1,2,3}$ being the effective mass values for the three crystallografic directions [Persson 97]. The wave function of an electron attached to the nitrogen N^+ ion is like that of a hydrogen atom with the radius a_B given by

$$a_B = \hbar^2\kappa/me^2 \tag{3.2}$$

The energy ϵ_1 obtained for nitrogen in SiC with this approximation diverges considerably from the experimental value. According to Kohn's [Kohn 57] suggestion

the effective radius is corrected to the experimentally determined energy $a_B^{corr} = a_B(\epsilon_1^{emt}/\epsilon_1^{exp})^{1/2}$. The EMT theory delivers a sastifactory explanation of experimental data (hyperfine interactions, energy levels) in the case of the nitrogen donor in 3C-SiC and the nitrogen donor in the hexagonal position in 4H-SiC [März 99]. For the quasi-cubic position the validity of the EMT theory is restricted to long distances from the donor nucleus [März 99]. Meausurements of hyperfine interations in 6H-SiC are more difficult to interpret. For this reason the validity of the EMT theory in this polytype could not yet be checked.

For high donor concentrations $N > N_C$ the material behaves like a metal, in the sense that the conductivity tends to a non-zero value as the temperature tends to zero. One can estimate the critical donor concentration N_C for uncompensated materials by stating that the transition to metallic conduction occurs when the binding energy of the isolated donor is of the order of the average interaction energy: $\epsilon_1 \approx \frac{e^2}{\kappa R}$, R being the average distance between impurities ($R = \{\frac{4\pi}{3}N_D\}^{-1/3}$). With this assumption one obtains

$$N_C^{1/3} a_B \approx 0.3 \tag{3.3}$$

This agrees with the results of experimental investigations of doped semiconductors near the transition, which satisfy the relation $N_C^{1/3} a_B \approx 0.27$ [Edwards 78]. The transition moves to higher concentrations for compensated materials. In 4H-SiC there is a hexagonal site and a quasicubic site for nitrogen, with ionization energies ϵ_1 =52 and 92 meV, respectively. With $a_B^{corr} = 20\mathring{A}$ [März 99] for nitrogen at the hexagonal site in 4H-SiC, one obtains from eq. (3.3) $N_C(hex) = 3.4 \cdot 10^{18}\mathrm{cm}^{-3}$, i.e. a critical concentration for nitrogen in uncompensated 4H-SiC of $N_C \approx 6.8 \cdot 10^{18}\mathrm{cm}^{-3}$. The experimentally found critical concentration is of the order of 10^{19} cm^{-3} [Limpijumnong 99] in reasonable agreement.

For smaller concentrations the conductivity vanishes at zero temperature. Conduction at low temperatures for $N < N_C$ may then occur by the thermally activated movement from one localized state to another, a process called impurity conduction (for review see [Shklovskii 84]). The investigation of impurity conduction began with the discovery of phonon-assisted hopping conduction in doped and compensated

semiconductors such as germanium and silicon ([Fritzsche 60], [Mott 61]) and was very much stimulated by the theoretical analysis of Miller and Abrahams [Miller 60]. Centres between which hopping takes place can be any kind of defects besides the doping impurities, such as dangling bonds in amorphous semiconductors.

Hopping conduction is of great interest as it provides information on the concentrations of the doping and compensating defects (N_D, N_A) as well as on the spatial extension of the wavefunctions associated with the hopping centres.

3.1 Impurity bands

In a material with a finite impurity concentration the energies of the electron states are shifted by the potential of charged neighbouring impurities. The spatial distribution of defects is not perfectly uniform, and therefore the interactions between them present a certain variation. As a result an impurity band has a finite width $\Delta\epsilon$. This distribution is reflected in the temperature dependence of the hopping conductivity.

In an n-type compensated semiconductor at low temperatures all acceptors and N_A donors will be ionized, and $N_D - N_A$ donors occupied. Hence the Fermi level lies in the donor band. At low compensation most donors will be neutral, and the Fermi level will be located above the isolated impurity level. At high compensation all electrons will be able to find donors whose energy levels are substantially lowered by the potential of charged neighbouring impurities. The Fermi level will be therefore located below the isolated impurity level.

3.2 Hopping conduction

Hopping conduction can be observed when the following conditions are fulfilled:

1. $kT << \epsilon_1$: the temperature is sufficiently low to prevent the carriers from being excited into a band

2. the defect concentration is below the metallic regime, but large enough to allow a nonnegligible hopping probability

3. there are empty sites in which carriers can hop: the defects are partially compensated.

In a compensated n-type semiconductor at low temperature all acceptors will be negatively charged; some of the donors will be neutral and contain an electron while others are positively charged and thus empty. Conduction is possible then, since there are empty states above E_F to which the electrons in nearby occupied states below E_F can move by receiving energy from a phonon. The same is true for holes in compensated p-type semiconductors. This is called a hopping process and induces a net conductivity if an electric field is applied. Miller and Abrahams pointed out that the dc (direct current)-hopping conductivity problem may be reduced to the problem of calculating the current in a random-resistor network governed by the Kirchoff's laws. In this network the conductance between any two sites is proportional to the corresponding hopping probability. Miller and Abrahams suggested that the dc current is governed by certain one-dimensional paths connecting the electrodes. The probability for the hopping of an electron from site i to a nearby site j is a function of the distance r_{ij} between the sites and their (potential) energy difference ϵ_{ij} :

$$W_{ij} = \nu_{ph} exp(-2\alpha r_{ij} - \frac{\epsilon_{ij}}{kT}), \tag{3.4}$$

where $1/\alpha = a_B$ is the decay length of the localized wave function and ν_{ph} reflects the phonon distribution [Miller 60]. The first term of the exponential is known as the "tunnelling term", the second one as the "activation term". Thus there are two cases to be considered for the hopping probability:

1. $\frac{\epsilon_{ij}}{kT} \ll 2\alpha r_{ij}$. In this case W_{ij} is maximum when r_{ij} is minimum. A carrier hops from one site to the next-nearest one taking the necessary energy from a phonon. This process is the so-called "nearest neighbour hopping" or "thermally activated hopping".

2. $\frac{\epsilon_{ij}}{kT} > 2\alpha r_{ij}$ for nearby neighbour sites. This occurs at sufficiently low temperatures. The hopping probability is then maximum for couples of values (ϵ_{ij}, r_{ij}) for which the quantity $2\alpha r_{ij} + \frac{\epsilon_{ij}}{kT}$ is minimum. This mechanism is usually

called "variable range hopping", since the activation energy decreases while the hopping length grows with decreasing temperature. An electron just below the Fermi level jumps to a state just above it, requiring an energy ϵ_{ij}. The further it jumps, the greater the choice of states it has, and in general it will jump to a state for which ϵ_{ij} is as small as possible. This kind of conduction is only possible when there is sufficiently high density of localized states near the Fermi level. This was first proposed by Mott [Mott 68] .

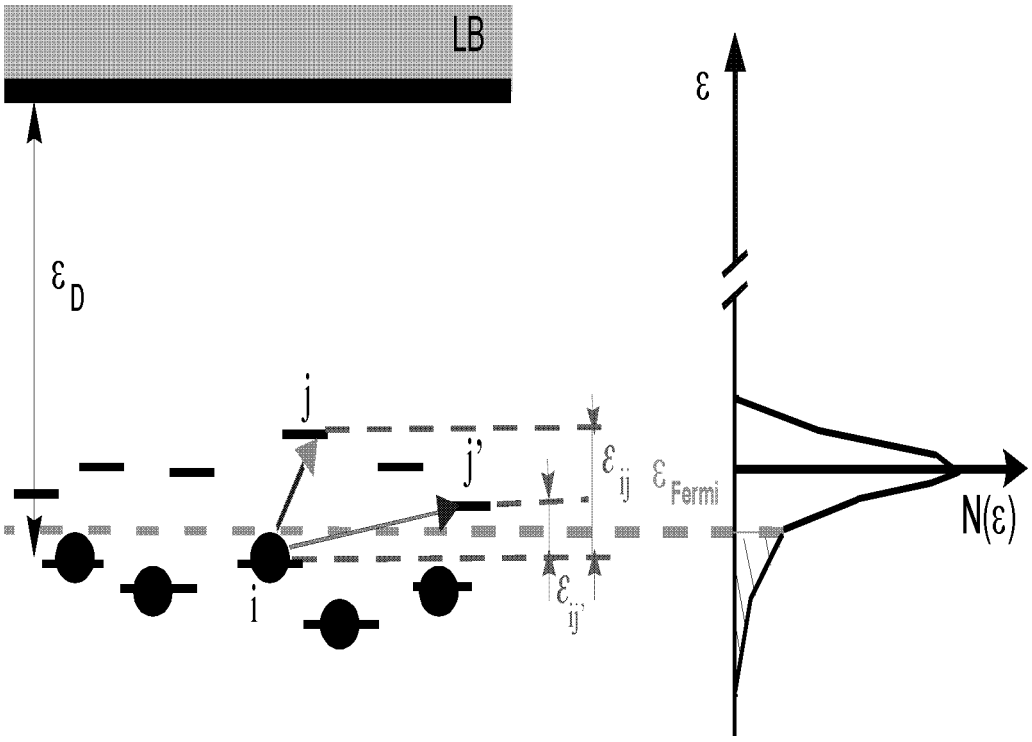

Figure 3.1: Schematic representation of the hopping processes in a compensated n-type semiconductor. An electron in a state (i) under the Fermi level can hop to a nearby empty state (j) above it, receiving the energy ϵ_{ij} from a phonon. At sufficiently low temperatures the electron will rather hop to a further lying state (j'), for which the energy difference $\epsilon_{ij'}$ is smaller.

When the distance between impurity states is small (but the electron states are still well localized), ϵ_{ij}/kT can be comparable to $2\alpha r_{ij}$ even at relatively high temperatures. This may occur for deep centres, since the electronic states are more localized and can therefore be present in large concentrations before inducing metallic conductivity. Variable range hopping has been observed, for instance below 200 K in

gallium arsenide heavily irradiated with fast neutrons [Coates 75]. For shallow impurity states the critical concentration for metallic conduction is smaller. Hence variable range hopping governes the conductivity only at very low temperatures. In an ion-implanted layer in silicon [Bourgoin 79], for instance, the conductivity was found to be hopping-like law below ≈ 0.3 K.

3.2.1 Nearest neighbour hopping

In the nearest neighbour hopping regime the conductivity shows a thermally activated behaviour:

$$\sigma = \sigma_3 \exp(-\epsilon_3/kT) \tag{3.5}$$

The activation energy ϵ_3 depends on concentration and compensation and was calculated by Miller and Abrahams [Miller 60] and later by Shklovskii et al. [Shklovskii 71]. It is expected to be of the form

$$\epsilon_3 \approx \frac{1}{N(\epsilon_F) a_B^3 4\pi/3} \tag{3.6}$$

The pre-exponential factor σ_3 varies as $\exp(-2R/a_B)$, where R is the average distance between centres and a_B the Bohr radius. For a detailed derivation of the hopping conductivity see e.g. [Overhof 76].

3.2.2 Variable range hopping

As stated above, at sufficiently low temperatures the electrical conductivity results from states whose energies are concentrated in a narrow band near the Fermi level. Near the Fermi energy, the density of states per unit energy range within a range R of a given site is

$$(4\pi/3)R^3N(\epsilon_F) \tag{3.7}$$

For the derivation of the expression for the conductivity in the variable range hopping regime, Mott assumed the average energy difference ϵ_{ij} to be roughly the reciprocal of the density of the interacting states, i.e.

$$\epsilon_{ij} = \Big((4\pi/3)R^3N(\epsilon_F)\Big)^{-1} \tag{3.8}$$

Thus the further the electron hops, the smaller will be ϵ_{ij}. On the other hand, hopping over a large distance involves tunnelling and the probability will contain the factor $\exp(-2\alpha R)$. This factor decreases with increasing R. The optimum hopping distance, for which the hopping probability W_{ij} (3.4) has its maximum, is given by

$$R = \{8\pi N(E)\alpha kT\}^{-1/4} \tag{3.9}$$

Substituting for R in equation (3.4) , we see that the hopping probability and thus the conductivity is of the form

$$\sigma \propto \exp\{(-T_0/T)^{1/4}\} \tag{3.10}$$

where [Mott 93]

$$T_0 = \frac{24}{\pi}\frac{\alpha^3}{kN(\epsilon_F)} \tag{3.11}$$

Mott and Davis [Mott 79] as well as Shklovskii and Efros [Shklovskii 84] used different methods for deriving this equation, giving somewhat different values of T_0 .

Near the transition to metallic behaviour the variable range hopping has been observed to follow a different temperature dependence:

$$\sigma \propto \exp\{(-T_1/T)^{1/2}\} \tag{3.12}$$

3.3 Magnetoresistance in the hopping regime

The magnetic properties of doped semiconductors in the hopping regime and for concentrations below that are of great interest and have been intensively investigated (for a review see the book by Kamimura and Aoki [Kamimura 89]). A giant positive magnetoresistance is a characteristic feature for the hopping mechanism of conduction [Sladek 58]. Several defects in semiconductors have sufficiently large values of the Bohr radius. Therefore, a relatively weak magnetic field may cause the electron orbits to shrink in directions perpendicular to the field. This leads to a sharp decrease in the overlap of the wave-function "tails" for an average pair of neighbouring impurities. As a result there is a high positive magnetoresistance in the hopping regime which depends exponentially on the strength of the magnetic field. The exponential dependence on the magnetic field strength is the same for the longitudinal and the transverse magnetoresistance (see fig. 3.2). Such magnetoresistance has been observed in n-InSb [Tokumoto 82], p-InSb [Gershenzon 74], n-Ge [Lee 67], p-Ge [Lee 67a], n-InP, [Biskupski 80] and n-GaAs [Halbo 68].

For cylindrical symmetry the effect of a magnetic field is reduced to an additional "magnetic" potential energy term, $\hbar^2\rho^2/8m\lambda^4$, where λ is the magnetic length [Shklovskii 79]

$$\lambda \equiv \left(\frac{c\hbar}{eH}\right)^{1/2} \tag{3.13}$$

The magnetic potential works like a spring pulling the electron to the z axis (the direction of the magnetic field). The physical meaning of the magnetic length is the narrowest length of electron localization due to the magnetic field. For weak magnetic fields the magnetic potential does not affect the wavefunction appreciably, because it is small compared to the Coulomb term at distances of the order of a_B or less from the donor. For high fields the magnetic field localizes the electron in a much narrower region in the transverse direction than the Coulomb potential.

We will restrict ourselves to the weak magnetic field regime. Shklovskii and Efros [Shklovskii 71] found the following expression for the magnetoresistance in a weak field in the activated hopping regime:

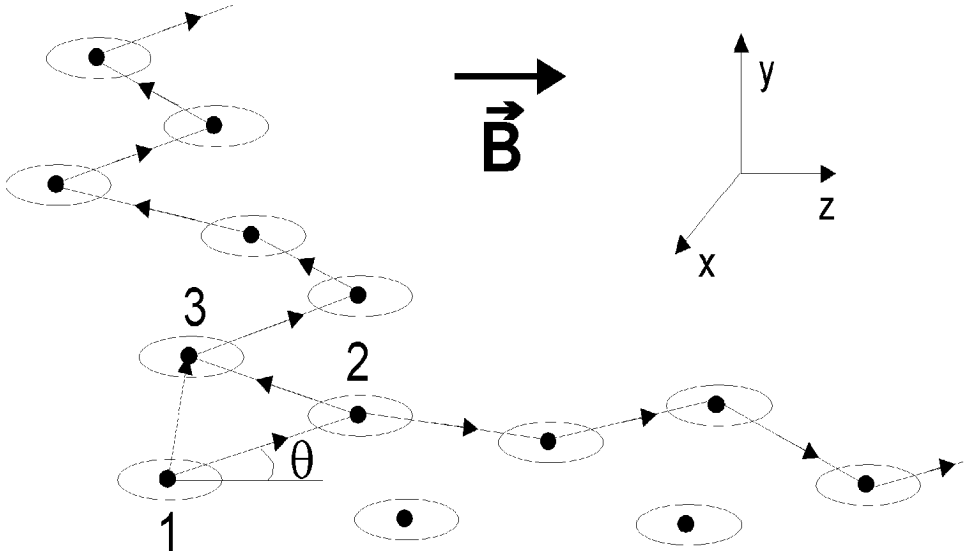

Figure 3.2: In high magnetic fields the electrons are localized in the direction perpendicular to the magnetic field. The exponential dependence of the magnetoresistance on the magnetic field strength is the same in all directions: An electron moving in the y direction will take path $1 \rightarrow 2 \rightarrow 3$ rather than path $1 \rightarrow 3$ (after [Shklovskii 79])

$$\frac{\rho(H)}{\rho(0)} = exp\left(t\frac{a_B}{N\lambda^4}\right) = exp\left(t\frac{a_B e^2}{Nc^2\hbar^2}H^2\right) \tag{3.14}$$

where $t = 0.06$. This equation is valid provided $\lambda \gg a_B$ and $(\lambda^2/a_B) \gg N^{-1/3}$. By using this, a critical magnetic field can be defined:

$$H_c = \frac{N^{1/3}c\hbar}{a_B e} \tag{3.15}$$

separating the weak- and strong-field limits. For example, with $a_B = 20\mathring{A}$ for the nitrogen donor at the hexagonal site we obtain a critical field H_c of 15T, 33T and 71T for a concentration N of 10^{17}cm^{-3}, 10^{18}cm^{-3} and 10^{19}cm^{-3}, respectively.
In the case of variable range hopping, the magnetoresistance in weak fields can be written [Shklovskii 79]:

$$\frac{\rho(H)}{\rho(0)} = exp\left[t\left(\frac{a_B}{\lambda}\right)^4\left(\frac{T_0}{T}\right)^{1/4}\right] = exp\left[t\left(\frac{a_B^2 e}{c\hbar}\right)^2\left(\frac{T_0}{T}\right)^{1/4}H^2\right] , \tag{3.16}$$

where t is a numerical coefficient ($t = 0.0025$). This behaviour is in agreement with experimental results, such investigations in silicon doped with phosphorus [Ionov 85], or in doped and compensated germanium [Ionov 83], [Schoepe 88].

We find that in both hopping regimes the magnetoresistance is positive and grows exponentially with H^2. In some cases, however, one observes a negative magnetoresistance. An anomalous magnetoresistance with positive and negative contributions has been measured in amorphous germanium and silicon in the hopping regime. Movaghar and Schweitzer [Movaghar 78] and Osaka [Osaka 79] developed a model to explain this anomalous magnetoresistance. The authors proposed a model in which the states at the Fermi level are essentially dangling bond-type states spread in energy due to disorder. These states can be empty, singly or doubly occupied. In the temperature range of interest, the hopping probability is much larger than the spin relaxation rate ($\nu_{hop} >> T_1^{-1}$). Thus the fast hopping electrons see an essentially frozen spin system. An electron hopping to a singly occupied state must have the correct spin orientation as the hop is forbidden otherwise. The authors suggested that spin-flip hopping processses would make observable contributions to the conductivity. In this picture, the anomalous magnetoresistance is the result of the modification of the spin-flip relaxation time by the external magnetic field. This phenomenon is closely related to the hopping induced spin-lattice relaxation [Mell 80].

3.4 Photon-induced hopping

Phonon-assisted hopping is not the only hopping mechanism. Hopping transport can also be due to absorption of photons ("photon-induced hopping") [Boettger 85] or absorption of energy from excited spins ("EPR-induced hopping") [Kamimura 76]. The typical activation energy for hopping conduction in semiconductors is of the order of some hundredth to a few meV. These energies lie in the microwave range, thus hopping conductivity is expected to increase in the presence of microwave radiation. An electron tunnels from site i to site j of higher energy by absorbing a microwave photon. This process is called "resonant microwave absorption". It can only happen if site j is empty and the interlevel spacing E_{ij} is close to the microwave photon energy $\hbar\omega$:

$$E_{ij} = (\epsilon_{ij}^2 + \Lambda_{ij}^2)^{1/2} \approx \hbar\omega \tag{3.17}$$

$$\Lambda_{ij} = \Lambda_0 exp(-r_{ij}/a_B) \tag{3.18}$$

Here, $\Lambda(r)$ denotes the tunnel integral, i.e., the off-diagonal matrix describing the tunnelling of an electron between the two sites. Λ_0 is of the order of the electron coupling energy.

For a fixed microwave energy $\hbar\omega$ there will be a number of "resonant" pairs with interspacing energy corresponding to $\hbar\omega$. The microwave absorption can be obtained after summation over all the resonant pairs. The real part of the hopping conductivity $\sigma(\omega)$ is directly related to the absorption coefficient J: $J \equiv 4\pi\sigma/c\kappa^{1/2}$ If the Coulomb repulsion is much larger than both the microwave and the thermal energy,

$$e^2/\kappa r \gg \hbar\omega, kT \tag{3.19}$$

then the linear (Ohmic) microwave conductivity is given by [Shklovskii 81]

$$\sigma_0^{abs}(\omega) = \frac{\pi^2}{3} a_B N(\epsilon)^2 \frac{e^4}{\kappa} \omega r_w^3 \tanh\left(\frac{\hbar\omega}{2kT}\right) \tag{3.20}$$

Here, κ is the dielectric susceptibility, $N(\epsilon)$ the one-electron density of states, while

$$r_\omega = a_B \log\left(\frac{\Lambda_0}{\hbar\omega}\right) \tag{3.21}$$

is the minimum "arm" of the pair with the interlevel spacing $\hbar\omega$. The factor $\tanh\left(\frac{\hbar\omega}{2kT}\right)$ is the equilibrium population difference between the lower and upper levels of a resonant pair. If the microwave amplitude is large enough, this difference decreases and the absorption becomes smaller. This is a typical hot electron phenomenon.

There is a second contribution to the microwave absorption: the relaxational absorption. It results from a modulation caused by the alternating field $\vec{E}(t)$ in the interlevel spacing ϵ_{ij}:

$$\epsilon_{ij}(\vec{E}(t)) = \epsilon_{ij}(0) + e\vec{E}(t) \cdot \vec{r}_{ij} \tag{3.22}$$

As a result, one can find [Shklovskii 81]

$$\sigma_0^{rel}(\omega) = \frac{e^4}{\kappa} g^2 a_B \omega r_c^3 \tag{3.23}$$

where r_c is the characteristic value of the pair in this case,

$$r_c = a_B \log\left(\frac{\Lambda_0}{kT\left[\omega\tau_{min}(T)\right]^{1/2}}\right) \tag{3.24}$$

τ_{min} is the minimum value of τ, the relaxation time given by the interaction with phonons.

In the presence of a magnetic field $\vec{H}$ the overlap integrals of the pairs, and hence the microwave absorption J become dependent on the direction and magnitude of $\vec{H}$. For low fields one obtains [Galperin 86]:

$$\frac{J^{\parallel}(H) - J(0)}{J(0)} = -\frac{1}{10}\left(\frac{a_B}{\lambda}\right)^4 L_c^2 \propto H^2 \tag{3.25}$$

$$\frac{J^{\perp}(H) - J(0)}{J(0)} = -\frac{1}{2}\left(\frac{a_B}{\lambda}\right)^4 L_c^2 \propto H^2 \tag{3.26}$$

where L_c depends on the absorption mechanism. We see that the change of the microwave absorption with the magnetic field, which is a small effect, should be proportional to H^2 and that the difference between the longitudinal and the transverse magnetoresistance is just a factor 5.

Chapter 4

Electrical Detection of Electron Paramagnetic Resonance

The electrically detected electron paramagnetic resonance (EDEPR) is a powerful method for the study of chemical and structural properties of defects in semiconductors. This method can be several orders of magnitude more sensitive than the conventionally detected electron paramagnetic resonance (EPR): 10^8 spins can be detected with EDEPR [Stich 96], 10^{11} with EPR e.g. [Spaeth 92]. The mechanisms on which EDEPR is based and also the sensitivity of the technique depend on the substance under investigation (single crystal, amorphous or polycristalline semiconductor, etc.), the defect concentration and the dominant charge transport process. Those mechanisms have been extensively investigated in the case of lowly doped semiconductors and different models have been proposed [Lépine 72, Kaplan 78, Rong 91, Xiong 93, Lanoo 94, Stich 96]. Most of them attributed the EDEPR effect to the spin dependent recombination of free charge carriers over paramagnetic defects (donor-acceptor recombination, see fig. 4.3). Nevertheless, some of the predictions of these models could not be proved by experiments or even conflicted with experimental results. Stich et al. [Stich 96] argued that previous models had focused on the spin dependent process and neglected the remaining processes in the charge conducting system. He took into account the relation between the concentration of charge carriers in the conduction and valence bands and the generation, dissociation and recombination of the donor-acceptor pairs. Considering all these processes, together with spin-independent recombination processes, Stich proposed a model aiming to describe the experimental findings of EDEPR. In the case of highly doped crystalline semiconductors

and amorphous semiconductors several models have been proposed, based on spin dependent scattering [Honig 66, Maxwell 66] or EPR-induced hopping processes [Kamimura 76, Kishimoto 81, Movaghar 80].

Schmidt et al. [Schmidt 66] were the first to use electrically detected magnetic resonance for the detection of phosphorus in crystalline silicon. This technique scarcely found consideration at that time, despite advantages such as its high detection sensitivity, which can be several orders of magnitude higher than for EPR. Not until the late 80's did EDEPR catch the general interest again, on account of the necessity of investigating thin semiconductor layers and high purity silicon material. The number of defects present in such samples is in most cases far below the detection limit of the conventional EPR.

Until the 90's, EDEPR investigations had mostly been carried out at room temperature, e.g. [Solomon 76], [Rong 90], and [Christmann 92]. This led to EDEPR spectra consisting of a single isotropic line with a g-factor of $g \approx 2$. Such spectra supply no structural information on the defect under study. Furthermore it was not clear under which conditions EDEPR works best, in contrast to the well understood optically detected EPR, ODEPR [Spaeth 92]. Stich [Stich 96] investigated the mechanism underlying the spin dependent conductivity change in lowly doped crystalline semiconductors. For this he carried out systematic EDEPR investigations on shallow and deep defects in silicon and silicon carbide at different temperatures and for different defect concentrations and compensations. He proposed the donor-acceptor pair recombination and the recombination over defects with triplet states as possible mechanisms of the EDEPR. In the case of highly doped crystalline semiconductors the EDEPR is not yet understood. This work is concerned with the mechanism determining the spin dependent conductivity in highly doped crystalline semiconductors.

4.1 Basic concepts of EDEPR

The electrically detected paramagnetic resonance detects magnetic dipole transitions of paramagnetic defects by a conductivity change of the sample. This technique

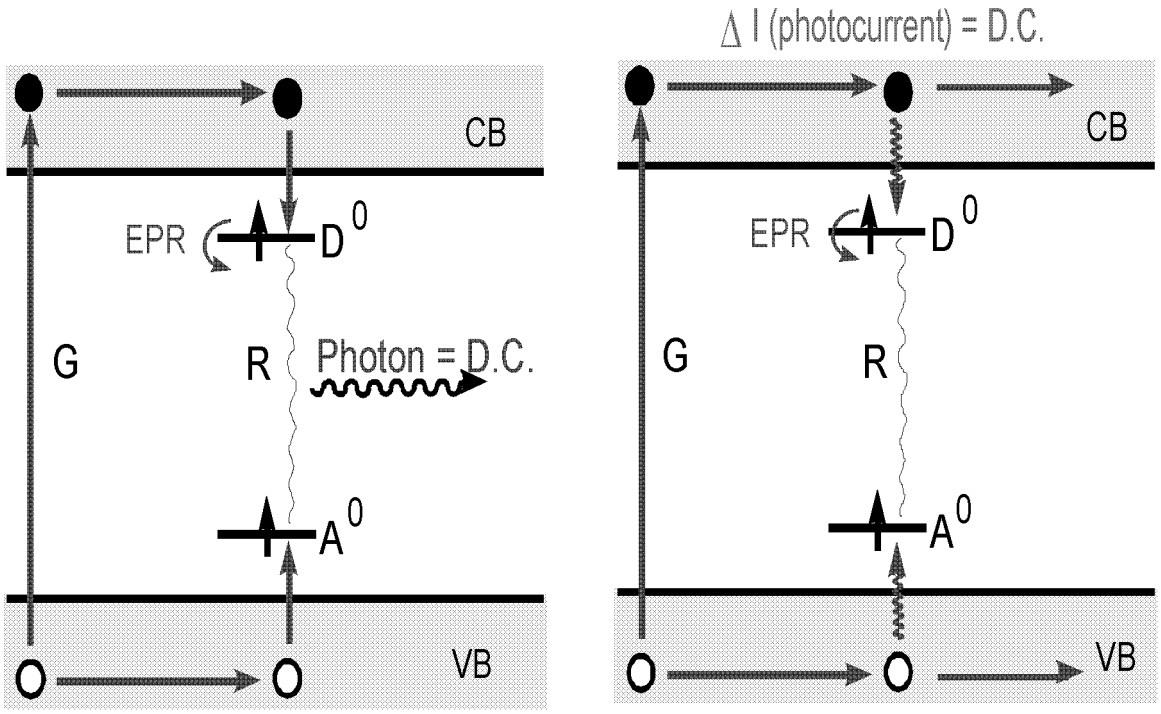

Figure 4.1: Schematic illustration of the optical and electrical detection of the spin dependent donor-acceptor recombination. The main difference between both techniques is the detection channel (D.C.). The recombination rate increases by inducing EPR transitions of the donor or acceptor (see fig. 4.3). This recombination enhancement can be detected as a luminescence increase (LDEPR) or a photoconductivity decrease (EDEPR). In the case of EDEPR the recombination does not need to be radiative.

is based on the spin-selection rules that govern certain transport processes. Such processes involve correlated spins, which can be either parallel or antiparallel to each other. Their relative orientation can be reversed by means of EPR, leading to an enhancement or a reduction of the conductivity. The conductivity of a semiconductor is given by

$$\sigma = |e|(\mu_n n + \mu_h h). \tag{4.1}$$

Here, e is the electronic charge, μ_n and μ_h are the mobilities of the electrons and holes, respectively, and n and h are the electron and hole concentrations. Thus a conductivity change can be due to a change in either the carrier mobility or the

carrier concentration. The former dominates for high defect concentrations and is based on spin dependent scattering processes, e.g. [Honig 66, Gueron 65]. The latter dominates for low defect concentrations and is based on the spin dependent recombination [Stich 96]. The spin dependent recombination is also the basis for the luminescence detected EPR (LDEPR), which has been succesfully applied for the study of defects on semiconductors [Spaeth 92]. The main difference between EDEPR and LDEPR is the detection channel: measurement of the conductivity in the first case, and of the luminescence in the second (see fig. 4.1).

4.2 Mechanisms for $\Delta\sigma_{EPR}$

Since the investigations of Gueron [Gueron 65], different authors have applied the EDEPR technique (though with different descriptions, such as spin dependent conductivity, relaxation detection of EPR, etc) for the study of crystalline, amorphous and porous semiconductors. Several mechanisms have been proposed which may lead to an EPR-induced change of the conductivity of a semiconductor (see fig. 4.2):

EPR-induced conductivity decrease: $\Delta\sigma_{EPR} < 0$

1. An EPR-induced conductivity decrease has been detected in doped but substantially uncompensated semiconductors and explained as a scattering of conduction electrons by neutral donor impurities at low temperatures. This phenomenon was studied in n-type Si:P by Honig and Maxwell [Honig 66, Honig 66a, Maxwell 66]. These authors proposed EDEPR as a new method for investigating neutral-impurity scattering in semiconductors. The method was based on the dependence of the scattering cross section on the electron-spin polarization. Since the electrical conductivity is inversely proportional to the scattering cross section, a polarization decrease leading to a larger scattering cross section induces a decrease of the conductivity. A polarization of the free carriers (created by irradiation with infrared light) and scattering centres can be achieved at low temperatures and sufficiently high magnetic fields. The polarization can then be reduced by inducing EPR transitions. This is detected as a change (decrease for hydrogenic centres) in the photocurrent. Besides an appreciable value of the carrier polarization, a substantial neutral-impurity

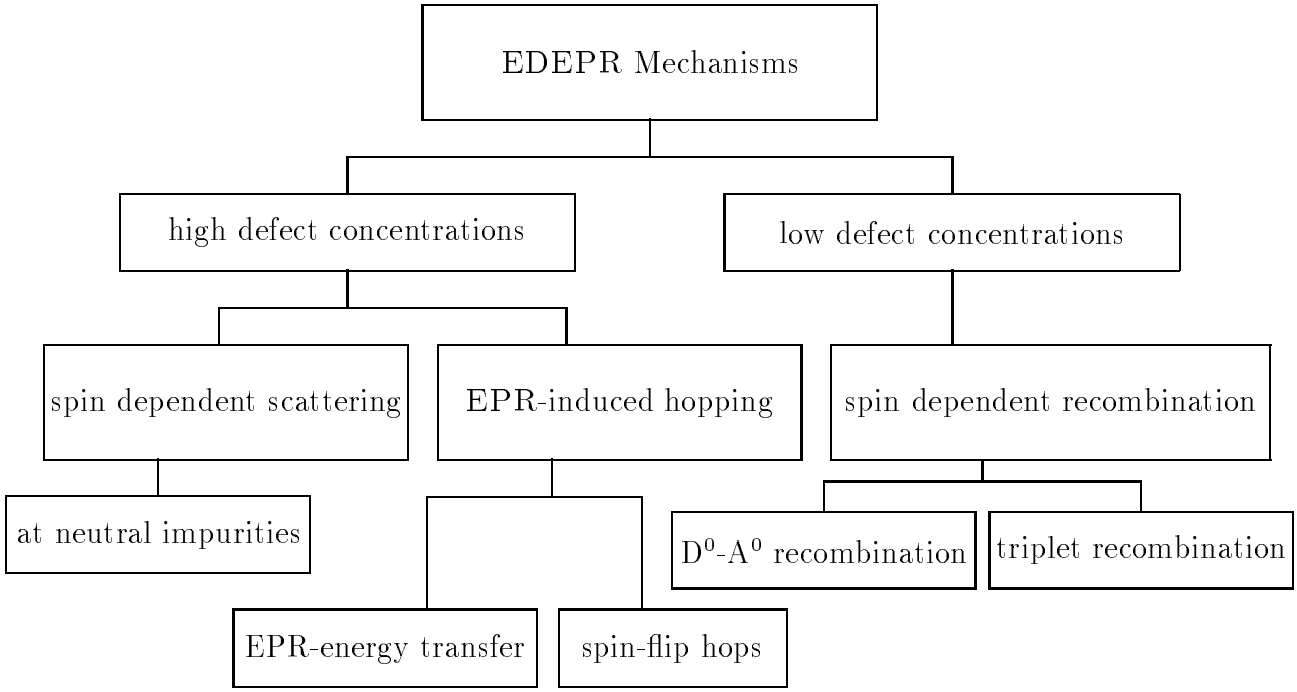

Figure 4.2: EDEPR mechanisms reported in the literature (see text).

scattering contribution to the conductivity is required for the applicability of this method. The reason is that none of the other scattering mechanisms, such as lattice or ionized-impurity scattering, should be spin dependent.

2. The spin dependent donor-acceptor recombination (see fig. 4.3) also results in a conductivity decrease at resonance conditions [Stich 96]. At low temperature and in thermal equilibrium the sample is irradiated with photons of energy $h\nu > \varepsilon_{GAP}$. As a result, charge carriers are generated in the valence and conduction bands with generation rate G. The generated electrons and holes can then be captured by the ionised donors (D^+) and acceptors (A^-), respectively. These are now in their neutral and paramagnetic state (D^0, A^0). A weak exchange interaction leads to the creation of donor–acceptor pairs, and the captured charge carriers can recombine consequently. This recombination depends on the relative spin orientation of the donors and acceptors. The recombination rate is higher for pairs with antiparallel spin orientation, since the final state $D^+ - A^-$ is diamagnetic with spin $S = 0$. The spin dependence of the $D^0 - A^0$ recombination causes a surplus of pairs with parallel spin orientation. By inducing EPR transitions of the donors or acceptors, pairs

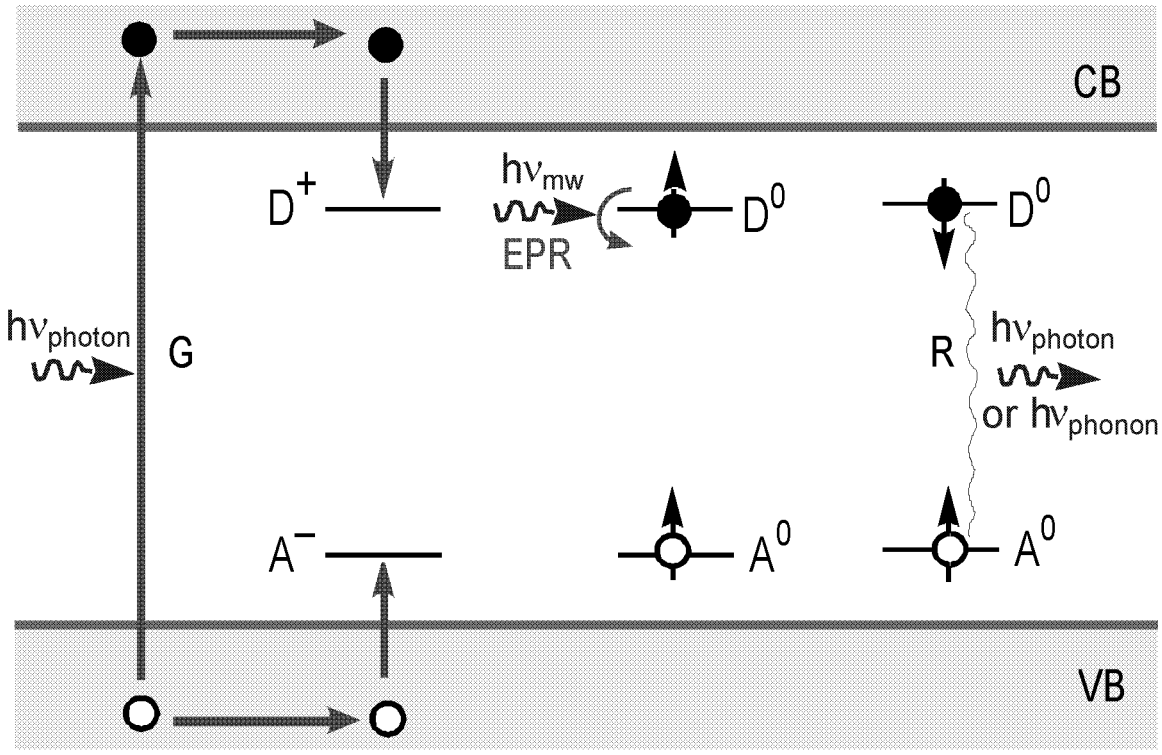

Figure 4.3: Schematic illustration of the spin dependent recombination. Electrons and holes are generated in the bands by illuminating the sample with photons of energy $h\nu_{photon} > \varepsilon_{GAP}$. The charge carriers can then be trapped by the ionized donors D^+ and acceptors A^-. D^0–A^0 pairs with parallel spin orientation recombine slowly. These pairs can be transferred into the antiparallel spin state by inducing EPR transitions of the donor (or the acceptor). Therefore the recombination is enhanced at spin resonance conditions.

with parallel spin orientation are transferred into the state with antiparallel spin. As a consequence, the recombination rate increases, as the number of fast recombining pairs has grown. A recombination enhancement involves a diminution of the stationary charge carrier concentration in the valence and conduction band. As a result, the electrical conductivity decreases, and this change of conductivity can be used to detect EPR transitions. The triplet recombination, which also gives rise to an EDEPR signal (e.g. [Stich 96], [Vlasenko 86]), can be considered as a special case of D^0–A^0 recombination with an extremely large exchange interaction [Spaeth 92].

EPR-induced conductivity increase: $\Delta\sigma_{EPR} > 0$

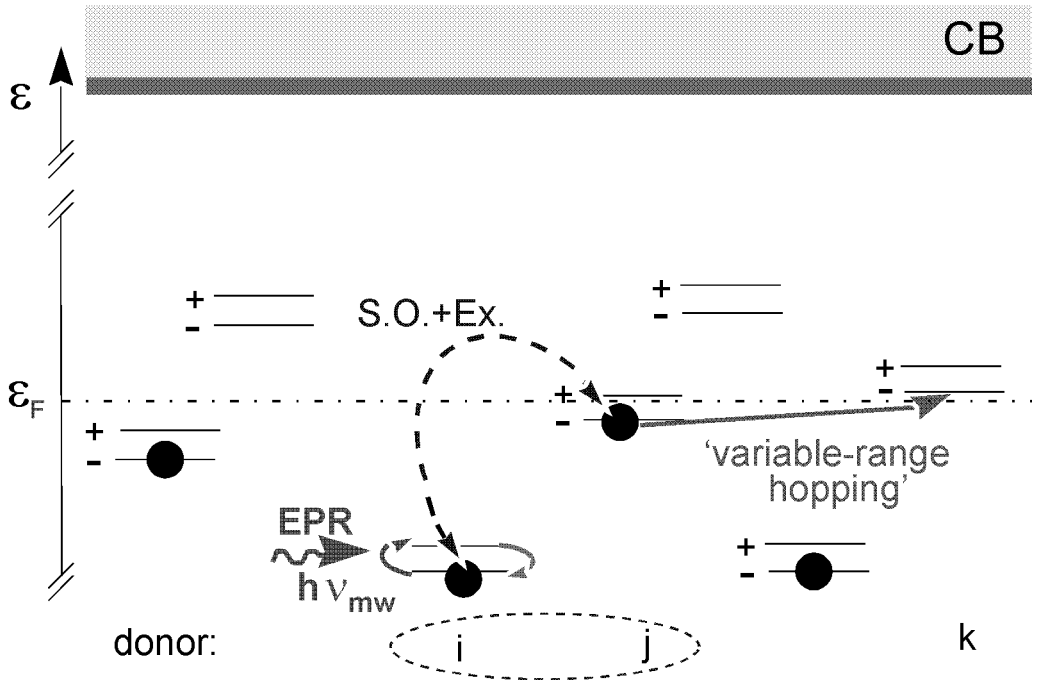

Figure 4.4: Scheme of the EPR-induced hopping (see text)

1. Gueron and Solomon [Gueron 65] observed the EDEPR of conduction electrons in n-type indium antimonide at liquid helium temperatures. They argued that the measured conductivity increase was due to the transfer of the microwave energy absorbed by the conduction electrons at resonance to the kinetic energy of the conduction electrons through spin-orbit interaction. For this reason they called this technique "relaxation detection of spin resonance". The power fed from the spins under resonance conditions raises the kinetic temperature of the electrons, and as a consequence, their mobility increases. This results in a conductivity enhancement, which is the measured quantity. This was the first clear evidence suggesting a contribution of spin-orbit coupling to relaxation in this system. For very small samples, the relaxation detection should be much more sensitive than the electromagnetic one.

2. Morigaki and Onda [Morigaki 72] measured a conductivity enhancement associated with donor spin resonance in arsenic- and phosphorus-doped germanium. The measurements were conducted at liquid helium temperature and the donor concentrations varied in the range around $10^{17}\mathrm{cm}^{-3}$. In order to explain their results they assumed the existence of two distinct electron systems: one responsible for the donor spin resonance, and the other for the

charge transport. They argued that the microwave energy absorbed by the donor spin system is transferred to the mobile electron system through their mutual exchange interaction. This leads to an increase of the kinetic energy of the mobile electrons and, consequently, to a mobility rise.

3. Kamimura and Mott [Kamimura 76] discussed the experimental results obtained by Morigaki and Onda and proposed a different model for their explanation. They explained Morigaki's results in terms of EPR-induced hopping. They attributed the EPR-induced conductivity increase to the transfer of the Zeeman energy from the excited spins to the localized electrons at the Fermi level. The Zeeman energy is transferred by the combined action of the exchange and the spin-orbit interaction and enables additional hopping. Figure 4.4 schematically shows Kamimura and Mott's model. First the localized electron at site (i) is excited to the upper Zeeman level by absorbing the microwave energy $h\nu_{mw}$. Then a localized electron at the Fermi level hops from site (j) to site (k) by exchange interaction with the electron at (i). The spin-orbit interaction must be taken into account, since the exchange interaction conserves the total spin of two electrons.

4. Kishimoto et al. [Kishimoto 81] studied the EPR-induced conductivity enhancement in amorphous $Si_{1-x}Au_x$ films at temperatures varying from 77K to 300K. They found that the conductivity increased when EPR transitions of the dangling bonds were induced. Electrical measurements showed that the conductivity was dominated by variable range hopping at the Au-impurity band. The authors argued that the EPR-induced conductivity increase was due to the transfer of EPR-energy from the dangling bond-spin system to the hopping electrons and finally into the lattice through spin-lattice relaxation. As hopping takes place between occupied states, the hopping process is spin dependent. An electron can only hop to sites occupied by an electron with antiparallel spin orientation. The probability of finding a site with antiparallel spin orientation increases by spin flips, and the hopping process is enhanced. For this reason the reversing of the hopping electron spin at the resonance of the localized spin leads to a conductivity enhancement. For the validity of this model the hopping time is required to be much shorter than the spin-lattice relaxation time.

5. Dersch and Schweitzer [Dersch 84] observed an enhancement of the dark conductivity at the spin resonance conditions of the valence band tail holes in

boron-doped a-Si:H. The hopping of these holes between localized states was found to contribute to the charge transport in this material. Their interpretation was that the EPR improves the mobility of the localized holes. The signal was found to decrease with increasing temperature (from 10^{-3} at 110K to $< 10^{-5}$ above 200K), pointing to a thermal excitation of the holes into the valence band. The authors gave no detailed explanation of the physical process underlying the conductivity enhancement.

6. Together with other authors, Movaghar and Schweitzer analyzed a variety of experimental findings in amorphous silicon and germanium: temperature dependence of the EPR linewidth [Movaghar 78a, Movaghar 77], anomalous magnetoresistance [Movaghar 78], EPR-induced changes in the photoconductivity [Movaghar 80] and in the luminescence [Movaghar 80] , as well as magnetophotoconductivity [Movaghar 80]. For the explanation of the cited effects, Movaghar et al. [Movaghar 80] studied the resonant and non-resonant photoconductivity changes due to a magnetic field and an additional microwave field. The measurements were conducted at room temperature. The authors suggested that a spin dependent, non-radiative recombination process was responsible for the resonant and non-resonant photoconductivity changes. They argued that these effects bear a close relationship to the anomalous magnetoresistance observed in amorphous semiconductors.

4.3 EDEPR parameters

In order to test the validity of a theoretical model, one has to compare its predictions with the following experimental results:

1. magnitude of the effect
2. microwave power dependence
3. dependence on the concentration of the paramagnetic centres
4. temperature dependence.

Models based on the spin polarization through the external magnetic field are not apt to explain the experimentally found *magnitude of the effect*. If the spin dependent change in the conductivity were due to a change in the polarization of the

paramagnetic centres, then it should be smaller than $(\frac{h\nu_{mw}}{k_B T})^2$. For room temperature and a microwave frequency of 9 GHz:

$$\frac{\Delta\sigma}{\sigma} \approx P_i P_j \leq (\frac{h\nu_{mw}}{k_B T})^2 \approx 10^{-6} \tag{4.2}$$

This contradicts experimental results on crystalline and amorphous semiconductors, where relative conductivity changes of $\frac{\Delta\sigma}{\sigma} = 10^{-3}$ have been found (e.g. [Brandt 92], this work).

The EDEPR in amorphous silicon [Brandt 92] has been reported to grow linearly with the *microwave magnetic field* B_1 and not to saturate, even for a microwave power of 1 watt. In crystalline silicon and silicon carbide ([Stich 96], this work) the EDEPR was found to grow first linearly with the *microwave power* and then tend to a constant value. Thus, in both cases the EDEPR exhibits a behaviour different from the conventionally detected EPR. The EPR signal grows with B_1 up to a certain value and then decreases: the EPR saturates [Poole 83].

In the case of the donor-acceptor recombination, a sufficient (but not too high) *concentration* of both donors and acceptors is needed (see chapter 4). The concentration for which the EDEPR line reaches its maximum is of the order of 10^{12} (for thermal donors in silicon [Stich 96])- 10^{14}cm^{-3} (for irradiated silicon [Stich 96]). For hopping-related effects a high *concentration* of donors or acceptors, or a sufficient *compensation* is necessary.
As regards the position of the *Fermi level*, this should play an important role in the case of the spin dependent change of the dark conductivity. In contrast it has no measurable influence on the EDEPR signal in case of the spin dependent recombination. The reason is that the sample is irradiated with photons of energy $h\nu_{photon} > \varepsilon_{GAP}$, and $D^0 - A^0$ pairs can be generated from already occupied as well as from unoccupied defects subsequent to the capture of a charge carrier. Nevertheless both donors and acceptors must be present in appropiate concentrations so that the spin dependent recombination may take place.

The EDEPR exhibits a strong *temperature* dependence and this, together with the temperature dependence of the conductivity, gives a hint to the spin dependent mechanism underlying the EDEPR effect.

We investigated the EDEPR signal in highly doped silicon carbide samples as a function of the parameters mentioned above, in order to find a model describing the EPR-induced enhancement of the dark conductivity. This will be developed in chapters 7 to 9.

4.4 Contact-free EDEPR

In an EPR experiment the transitions between magnetic sublevels of paramagnetic centres are detected as a change in the microwave absorption. In an EDEPR experiment these transitions are detected by measuring the conductivity by means of electrical contacts on the sample. Vlasenko et al [Vlasenko 86] proposed a contact-free technique in which the conductivity change is indirectly detected by measuring the variation of the cavity quality factor. This technique relies on the fact that the Q-factor is sensitive to the electrical conductivity of the sample. An ordinary EPR spectrometer can thus be used to detect spin dependent conductivity processes. It may be difficult, however, to distinguish between dielectric and magnetic losses. The former arise from the conductivity change of the sample at resonance producing the EDEPR signal. The latter are caused by the microwave absorption by the sample producing the EPR signal.

The quality factor of a microwave resonator with a sample inside results from adding the different energy losses of the microwave field [Poole 83]:

$$\frac{1}{Q} = \frac{1}{Q_R} + \frac{1}{Q_\varepsilon} + \frac{1}{Q_\chi} \tag{4.3}$$

- Q_R: cavity losses in absence of EPR transitions
- Q_ε: dielectric losses through a conductivity change of the sample. $Q_\varepsilon = f(\varepsilon'', \alpha)$
- Q_χ: magnetic losses through microwave absorption. $Q_\chi = f(\chi'', \eta)$

Here, ε'' and χ'' are the imaginary part of the dielectric constant and the magnetic susceptibility, respectively. α and η are the filling factors related to the electric and

magnetic field of the microwave. Assuming that the cavity losses Q_R are considerably larger than the magnetic losses Q_χ, then we can write [Poole 83] :

$$\Delta Q = -Q^2 \Delta(1/Q) = -Q^2 \chi'' \eta \tag{4.4}$$

Anologous to the change in the cavity quality factor induced by the magnetic losses, the change induced by the dielectric losses is given by :

$$\Delta Q = -Q^2 \Delta \varepsilon'' \alpha \tag{4.5}$$

At resonance conditions the conductivity σ of the sample is changed by an amount $\Delta\sigma$ resulting in a change in the quality factor given by [Greiner 91]:

$$\Delta Q = -Q^2 \frac{\Delta\sigma\alpha}{\varepsilon_0 2\pi\nu_{mw}} \quad with \quad \Delta\epsilon'' = \frac{\Delta\sigma}{\varepsilon_0 2\pi\nu_{mw}} \tag{4.6}$$

ε_0 is the dielectric constant of vacuum and ν_{mw} the microwave frequency.
In an EPR spectrometer the change in the cavity quality factor is detected by a microwave bridge. If the detector works in the linear range, the signal voltage will be given by:

$$\Delta V_{det} \propto \frac{\Delta Q \sqrt{P_{mw}}}{Q} \tag{4.7}$$

In consideration of the dielectric (4.6) and magnetic losses (4.4) caused by the EPR transitions, the signal amplitude at the detector can be written as:

$$\Delta V_{det} = -Q \left(\chi'' \eta + \frac{\Delta\sigma\alpha}{\varepsilon_0 2\pi\nu_{mw}} \right) \sqrt{P_{mw}} \tag{4.8}$$

As we see from eq. (4.8), the detector simultaneosly measures the resonant microwave absorption and the conductivity change at resonance. In principle, it is not possible to separate both contributions. Furthermore the signal depends on both the dielectric and the magnetic filling factor, making this technique inadequate for the investigation of small samples. We therefore prefer the detection of EDEPR by conductivity measurements to the quality factor-detected EDEPR. The latter technique is useful when good quality ohmic contacts are difficult to achieve.

Chapter 5

Properties of silicon carbide

The physics of SiC and the possibilities of its use in devices have found considerable interest due to its strong chemical bonding, physical stability, and other attractive electrical, optical and thermal properties. Silicon carbide is an attractive semiconductor material for high temperature electronic and electro-optic applications. A detailed knowledge of the electronic structure of the material, which itself depends on the atomic geometry, is required. The latter is rather complicated since SiC crystallizes in more than hundred modifications, i.e., polytypes. Although the arrangement of next neighbours is the same for each Si and C atom in all polytypes, the second and third neighbour shell result in slightly altered arrangements. These lead to crystallographically inequivalent lattice sites, with either cubic or hexagonal character.

The bandstructure of SiC and, in particular, the indirect fundamental gap varies remarkably with polytype hexagonality h, from 2.39 eV for 3C-SiC (h=0) to 3.33 eV for 2H-SiC (h=1) (see table 5.1). Among the SiC polytypes, 4H-SiC is the most promising one for high temperature and high power device applications due to its large band gap and a high and almost isotropic electron mobility [Schaffer 94].

The doping of silicon carbide can either occur during crystal growth or by subsequent ion implantation and annealing. Nominally undoped crystals are n-type caused by residual nitrogen. Impurity atoms in SiC substitute on either the silicon or carbon sublattice. The polytype does not affect the site preference of the impurities, but affects their ionization energy. Furthermore, in the more complex polytypes there is a manifold of inequivalent lattice sites divided into two types: (quasi)cubic

polytype	ABC sequence	sites		lattice constants		bandgap [eV]
		cubic*	hexagonal	a [$\AA$]	c [$\AA$]	indirect
2H	AB	-	1	3.0763	5.0480	3.33
3C	ABC	1	-	4.3596	-	2.39
4H	ABCB	1	1	3.073	10.053	3.26
6H	ABCACB	2	1	3.0806	15.1173	3.08

Table 5.1: Stacking sequences, number of inequivalent sites, lattice constants and bandgap of some of the most common SiC polytypes (after [Landolt-Börnstein 82]). *: the only true cubic site is in 3C-SiC, in the hexagonal polytypes the sites are quasicubic.

and hexagonal sites. The former correspond to a cubic-like atomic configuration of the first- and second-neighbour atoms, the latter to a hexagonal-like configuration. Impurities in SiC have differing energy levels associated with crystallographically inequivalent lattice sites [Patrick 72].

Nitrogen is the most common dopant in SiC and causes the n-type character of high purity material. It occupies the carbon sites. Nitrogen induces relatively shallow levels (see table 5.2) at 50-150 meV below the bottom of the conduction band. In this work we investigated highly doped n-type 4H- and 6H-SiC samples, with nitrogen concentrations of the order of 10^{18}cm^{-3}. They were found to be highly conducting, but not degenerate. With higher carrier concentrations of the order of $10^{19}cm^{-3}$, the shallow nitrogen defect levels broaden significantly into a band which overlaps with the bottom of the conduction band, forming a so-called band-tail [Limpijumnong 99].

5.1 EPR and ENDOR data for SiC:N

Until now 6H-SiC is the best studied polytype. Woodbury and Ludwig [Woodbury 61] conducted the first EPR investigations on nitrogen- and boron-doped SiC. The low abundance of isotopes with nonzero nuclear spin (^{29}Si with 4.7% abundance and nuclear spin I=1/2, ^{13}C with 1.1% abundance and nuclear spin I=1/2) results in EPR linewidths of about 0.1 mT.

polytype	site	nitrogen energy levels	reference
3C	cubic	$E_{CB} - 54.2$ meV	[Moore 95]
4H	quasicubic	$E_{CB} - 91.8$ meV	[Suttrop 92]
	hexagonal	$E_{CB} - 52.1$ meV	
6H	quasicubic 1	$E_{CB} - 137.6$ meV	[Götz 93]
	quasicubic 2	$E_{CB} - 142.4$ meV	
	hexagonal	$E_{CB} - 81.0$ meV	

Table 5.2: Energy levels of nitrogen (N^0/N^+) in different polytypes and for the different inequivalent sites quasicubic (1, 2) and hexagonal sites.

Centre	$g_{\|\|}$	$g_\perp$	a/h [MHz]	b/h [MHz]	q/h	reference
N_h (4H)	2.0055(2)	2.0010(2)	2.757(1)	0.081(1)	0.020	1, 2
N_c (4H)	2.0043(2)	2.0013(2)	51.019(1)	0.006(1)	0.010	1, 2
N_h (6H)	2.0048(2)	2.0028(2)	2.468(1)	0.137(1)	0.017	2, 3, 4
N_{c1} (6H)	2.0040(2)	2.0026(2)	33.221(1)	0.004(1)	0.007	2, 3, 4
N_{c2} (6H)	2.0037(2)	2.0030(2)	33.564(1)	0.009(1)	0.007	2, 3, 4

Table 5.3: EPR parameters for the different inequivalent sites of the nitrogen donor in the hexagonal polytypes 4H- and 6H-SiC. 1: [Kalabukhova 90], 2: [März 99], 3: [Kalabukhova 87], 4: [Greulich-Weber 95]

Table 5.3 shows the EPR parameters of nitrogen in the most common hexagonal polytypes, 4H- and 6H-SiC. In 4H-SiC there are two inequivalent lattice sites, one hexagonal and one quasicubic; in 6H-SiC there are one hexagonal and two quasicubic sites. The g-tensors for the inequivalent lattice sites are very similar, therefore it is almost impossible to separate the corresponding EPR signals in X-band (10 GHz). The g-tensor values of 6H-SiC were determined with accuracy by means of high frequency (142 GHz) EPR investigations [Kalabukhova 87]. For a precise determination of the hyperfine interaction it is necessary to make use of the ENDOR technique. By means of this technique the parameters for the hyperfine interaction with the ^{14}N central nucleus (I=1, 100% abundance) were determined [Greulich-Weber 95].

The energetic position of the shallow donor states depends on the lattice symmetry

and the structure of the conduction band, as well as the wavefunction character. The latter is given by the orbital momentum, this so-called valley-orbit interaction produces a splitting of states with different symmetry. Valley-orbit splitting stands for the energy difference between the A_1 and E states, arising from the valley-orbit interaction.

Luminescence and infrared-absorption measurements [Dean 77, Suttrop 92, Götz 93] show series of transitions from the nitrogen states 1s(A_1) and 1s(E) into higher (n=2,3,...) p states. These optical measurements deliver the value of the valley-orbit splitting ΔVO, but no information about which state (A_1 or E) lies energetically lowest. The E state is antisymmetrical, the A_1 symmetrical, therefore a large Fermi-contact interaction points to the symmetrical A_1 state as ground state. This is the case for the quasicubic sites in 4H- and 6H-SiC (51 and 33 MHz, respectively) and the separation between the ground state and the E state is clear (ΔVO= 45 and 62 meV, respectively). For the cubic site in 3C-SiC and the hexagonal sites in 4H- and 6H-SiC, on the contrary, the Fermi-contact interaction is quite small (2.45 to 3.5 MHz) and the valley-orbit splitting is also small. Therefore it is more difficult to decide which state is the ground state in these cases. The temperature behaviour of the EPR signals, however, points to A_1 as ground state. With increasing temperature the hyperfine interaction of ^{14}N is found to decrease. This can be attributed, in the case of the hexagonal sites, to a mixture of the antisymmetrical state E into the ground state, resulting in a reduction of the isotropic part of the hyperfine interaction and a measurable anisotropy. The hyperfine interaction in 3C-SiC is isotropic, therefore there can be no mixture of the E state.

5.2 Thermal conductivity of SiC

From the device application point of view silicon carbide shows better thermal properties than copper, AlN, Al_2O_3 and BeO. The actual value of the thermal conductivity varies with polytype and doping [Morelli 93, Parafenova 90]. Burgemeister et al. [Burgemeister 79] stablished that the thermal conductivity of silicon carbide is lowered by the presence of defects, and in particular, nitrogen.

The thermal conductivity at low temperatures has been studied for different polytypes and impurity concentrations [Koshchenko 79, Morelli 93] Best fits of experimental data show a T^n temperature dependence, with $n = 3$ for very pure or highly compensated material and $n = 2$ in other case. The T^2 dependence is attributed to the scattering of phonons by electrons in an impurity band [Slack 64].

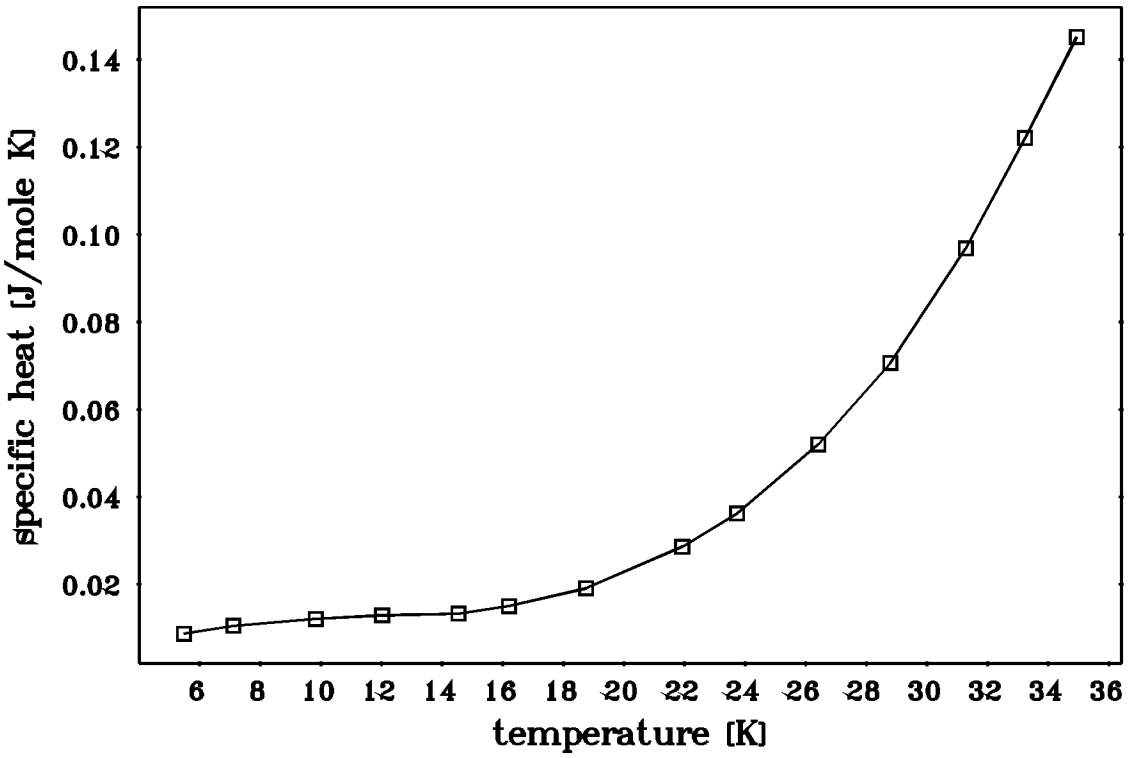

Figure 5.1: Experimental values of the specific heat of 6H-SiC as a function of temperature [Koshchenko 79]

Chapter 6

Experimental details

This chapter briefly illustrates the experimental components of the EPR spectrometer and the additional elements for the electrical detection of magnetic resonance. In addition to it the preparation of the investigated samples is described.

6.1 EPR/ EDEPR spectrometer design

The spectrometer used in this work is a custom built, X-band (10 GHz) EPR spectrometer equipped with additional elements for detection of current-voltage characteristics. The supplementary components enable the conduction of EDEPR and resistivity measurements.

6.1.1 EPR elements

The magnetic field could be varied from 0 to 1100 mT. At the beginning of this work a klystron with an output power of P_{mw} = 400mW was used for the generation of microwaves. Later a YIG oscillator with an output power of 1200 mW was used. The microwave frequency was stabilized at the resonance frequency of the TE_{011} mode of the cylindrical cavity by an automatic frequency controller (AFC) integrated in the microwave bridge. Two resonators with slightly different dimensions were used during this work, with a resonance frequency of about 9.4 GHz and 10 GHz, respectively. Both resonators are equipped with slits enabling illumination of the sample during the measurements. The temperature could be varied between 5 and

300K by means of a helium-flow cryostat.

In most cases it was made use of lock-in technique for sensitivity enhancement. For this purpose, either the static magnetic field or the microwave amplitude was modulated. The applied modulation frequencies were in the range of f=1-10 kHz for EDEPR detection, and of about 50 kHz for the conventional detection of EPR.

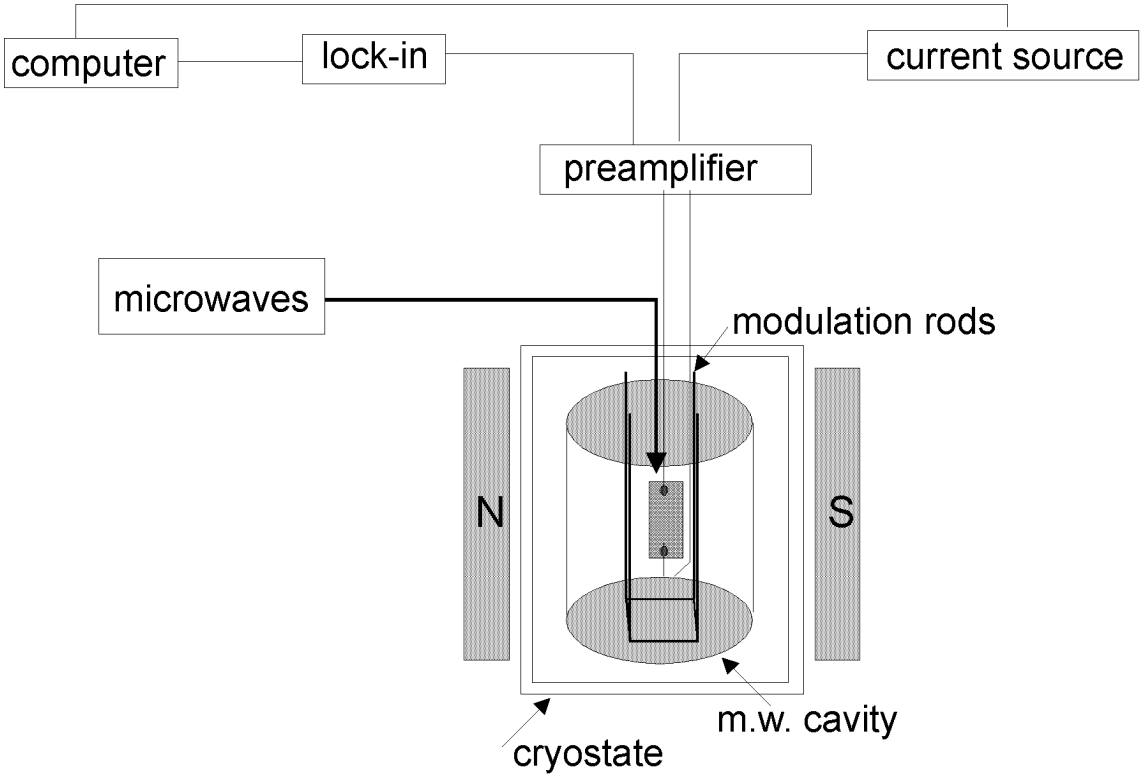

Figure 6.1: Schematic illustration of the EDEPR spectrometer.

6.1.2 Electrical elements

For the electrical detection of EPR, and for resistivity measurements as well, the conventional EPR spectrometer must be complemented with additional devices, such as sample holder, d.c. current-voltage source and signal amplifier. These can be described as follows:

1. *sample holder.* In order to conduct current-voltage measurements at low temperatures the sample holder must fulfill two conditions. It must be equipped

with electrical connections from the voltage source to the sample and be vacuum tight. A further requirement is the rapid exchange of samples. All three requirements are met by the sample holder used, which was described in Bernd Stich's doctoral thesis [Stich 96].

2. *d.c. current and voltage source.* A current and voltage source *Keithley 237* was used in this work. With this source it is possible to set a current value and detect the voltage at the sample, as well as to set a voltage value and measure the current through the sample. This enables the recording of current-voltage characteristics *in situ*. For EDEPR experiments we set the current and detected the voltage while scanning the magnetic field, but in principle it could be done the opposite way. The *Keithley 237* makes currents in a range I = 10pA-100mA, and voltages in a range U = 10nV-1100V available. This enables the investigation of both very high and very low resistivity samples. A further advantage of this source is its low noise level, approximately 20 ppm according to the manufacturer. As a consequence we can assume that noise in the EDEPR signal generated from the current-voltage source is negligible.

3. *signal amplifier* The sample holder described above is connected to a voltage amplifier with three possible amplification factors: $U_{output} = a \cdot U_{input}, a = 1, 3, 30$. The different amplification factors make possible to choose the most appropiate I-U conditions for EDEPR measurements in a wider range.

6.2 Samples

6.2.1 List of the investigated samples

A number of n-type silicon carbide samples with different nitrogen concentrations were investigated in this work. Two of them were epitaxial layers, the others bulk material. Sample E1 was a 7μm n-typ (N_D-N_A= $6{\cdot}10^{15}$cm^{-3}) 4H-SiC epilayer on an n-typ (N_D-N_A= $8 \cdot 10^{18}$cm^{-3}) 4H-SiC substrate from *Cree*. The sample was sixfold implanted with helium (depth=1.6 μm), resulting in a vacancy concentration of $9{\cdot}10^{15}$cm^{-3}. It was subsequently annealed at 1000°C for 10 minutes and at 1700°C for 15 minutes. After this treatment, the resulting Z-center concentration was $8 \times 10^{13} cm^{-3}$. These centers have an energy of ionization of 620-670 meV measured from the conduction band (DLTS measurements by Pensl et al). The sample

sample	growth	polytype	N-concentration	source
E1	epitaxial layer	layer: 4H substrate: 4H	$6 \cdot 10^{15}\mathrm{cm}^{-3}$ $\approx 10^{18}\mathrm{cm}^{-3}$	Cree
B1	bulk	6H	$2 \cdot 10^{18}\mathrm{cm}^{-3}$	Siemens
B2	bulk	4H	$1 \cdot 10^{18}\mathrm{cm}^{-3}$	Siemens
B3	bulk	6H	$2 \cdot 10^{19}\mathrm{cm}^{-3}$	Cree
B4	bulk	6H	$6 \cdot 10^{19}\mathrm{cm}^{-3}$	Cree

Table 6.1: List of the investigated samples

was provided with ohmical Ni-contacts.

Sample B1 was a 6H-SiC bulk sample from *Siemens*, with an estimated nitrogen concentration of $2{\cdot}10^{18}\mathrm{cm}^{-3}$ (from EPR investigations, [März 99]). Sample B2 was a 4H-SiC bulk sample cut from a *Cree* wafer, with an estimated nitrogen concentration of $10^{18}\mathrm{cm}^{-3}$ (from EPR investigations, [März 99]). Samples B3 and B4 were cut as well from Cree wafers, in this case 6H material, their nitrogen concentration was very high (estimated $2 \cdot 10^{19}\mathrm{cm}^{-3}$ and $6 \cdot 10^{19}\mathrm{cm}^{-3}$, respectively).

6.2.2 Electrical contacts

For the performance of electrical and EDEPR measurements it is necessary to provide the samples with good electrical contacts, which do not influence appreciably the conductivity properties of the sample. An ideal electrical contact would have a zero resistivity: $R = 0$. In practice a good electrical contact is one with a vanishing ohmic resistivity. It consists of a metal-semiconductor transition and is called: "ohmic contact".

Contact resistance (R_C) is a term that describes the total electrical resistance present at the interface between the metal and the semiconductor in an ohmic contact. It depends on the area or geometry of the contact. The interface itself, however, has certain properties which influence the contact resistance. This interfacial property is known as the specific contact resistance, r_C, and should in principal be independent of the area of the metal- semiconductor interface. Assuming that the entire contact area takes part in the conduction process, which is not always true, the contact

resistance and the specific contact resistance are related by $R_C = r_C/A$, where A is the cross- sectional area of the metal-semiconductor interface. The units of contact resistance are Ω while specific contact resistance has units of Ω times length squared. Generally the unit of length used is cm, thus specific contact resistance is given in $\Omega{\cdot}\mathrm{cm}^2$.

There is a wide spectrum of contacting techniques, suitable for different materials and applications. The contact technology for silicon carbide must, in contrast to silicon, still catch up. There are several problems to solve: the used annealing temperatures are too high, the contacts penetrate too deep, they deteriorate when devices operate at elevated temperature, and the contact resistance is too high. The area of ohmic contacts is one of the key technology issues that still must be adressed before SiC can realize its great potential for uses in high power and high temperature applications.

The most commonly used metals for contacting SiC are nickel, aluminium, titanium and chromium (for review see e.g. [Crofton 97] [Harris 95]). The metal is evaporated and rapidly thermally annealed at high temperatures varying from 700 to 1200°C.

Samples B1, B2, B3 and B4 lacked electrical contacts. Contacts were fabricated on the four corners of each sample by rubbing titanium onto the surface. Gold wires were subsequently soldered with titanium to the contacts. In the case of the epitaxial layers, copper wires were glued to the samples with a silver solution.

Chapter 7

Electrical Investigations

This chapter deals with the electrical investigations conducted on the samples subsequently used for EDEPR studies. The aim of this work, as stated in chapter 1, was to find a model for the explanation of the mechanism underlying the electrical detection of EPR on highly doped semiconductors, i.e. the processes interrelating charge transport and magnetic resonance. First of all we have to find the electrical characteristics of the samples: concentration of donors and compensating centres and the dominating charge transport mechanism at the low temperatures used for EDEPR investigations. By means of Hall measurements and subsequent analysis using the neutrality equation the donor concentration and the compensation of the samples (and thus the Fermi level position) could be determined. All samples but B3 and B4 were found to be non-degenerate. Studies of the temperature and magnetic field dependence of the resistivity of the non-degenerated samples pointed to hopping conductivity as the dominating conduction process. Furthermore, the influence of microwave irradiation was studied.

7.1 Hall Measurements

We have initially started to determine the concentration of donors and acceptors in the material under study. This can be achieved by means of Hall effect investigations. In this experiment an electrical field is generated through the deflection of the charge carriers by a magnetic field (Lorentz force). The resulting electrical

field is perpendicular to both the applied current and magnetic field. The potential difference arising from the electrical field, the so-called Hall voltage U_H, can be measured, its sign delivers the conduction type (n or p) of the sample. The Hall voltage is proportional to the current I and the magnetic field B, as well as inversely proportional to the sample thickness d: $U_H = R_H \frac{IB}{d}$. The proportionality constant R_H is called Hall constant, it depends on the concentration and compensation of electrons and holes. For an n-type semiconductor it is given by:

$$R_H = -\frac{r_H}{en} \quad , \tag{7.1}$$

where r_H is the Hall scattering factor, e the electronic charge and n the charge carrier concentration. From the temperature dependence of the Hall constant (and therefore of the carrier concentration) the concentration of donors and compensating centres can be found out.

The samples studied in this work had high nitrogen concentrations and were partially compensated. ODEPR investigations of sample E1 showed that the compensating impurity was the boron acceptor. Boron is besides aluminium the most common acceptor in SiC. Figure 7.1 shows the energy levels position of nitrogen and boron in 4H-SiC and 6H-SiC. As noticed in chapter 5, the energetic position of the impurity states depends on the lattice symmetry, the nitrogen donor state at the hexagonal lattice site is in both polytypes shallower than the nitrogen donor state at a quasicubic site. At low temperatures the Fermi level will lie near the energy level of the nitrogen donor at the hexagonal or quasicubic site for a low or high degree of compensation, respectively. The concentrations of nitrogen substituting on the hexagonal and quasicubic lattice sites $(N(h), N(c))$, the corresponding ionization energies $(\Delta\epsilon(h), \Delta\epsilon(c))$, as well as the concentration of compensating acceptors N_A can be determined by a least-squares fit of the neutrality equation to the measured values of the free electron concentration n. The latter is given by $n = r_H/(e|R_H|)$ (eq. (7.1)), where we assume r_H to be unity [Schadt 94]. The neutrality equation (total number of negative charges = total number of positive charges) can be written as [Schadt 94]:

$$n + N_A = \frac{N(h)}{1 + (gn/N_C)exp\{\Delta\epsilon(h)/kT\}} + \frac{N(c)}{1 + (gn/N_C)exp\{\Delta\epsilon(c)/kT\}} \; , \tag{7.2}$$

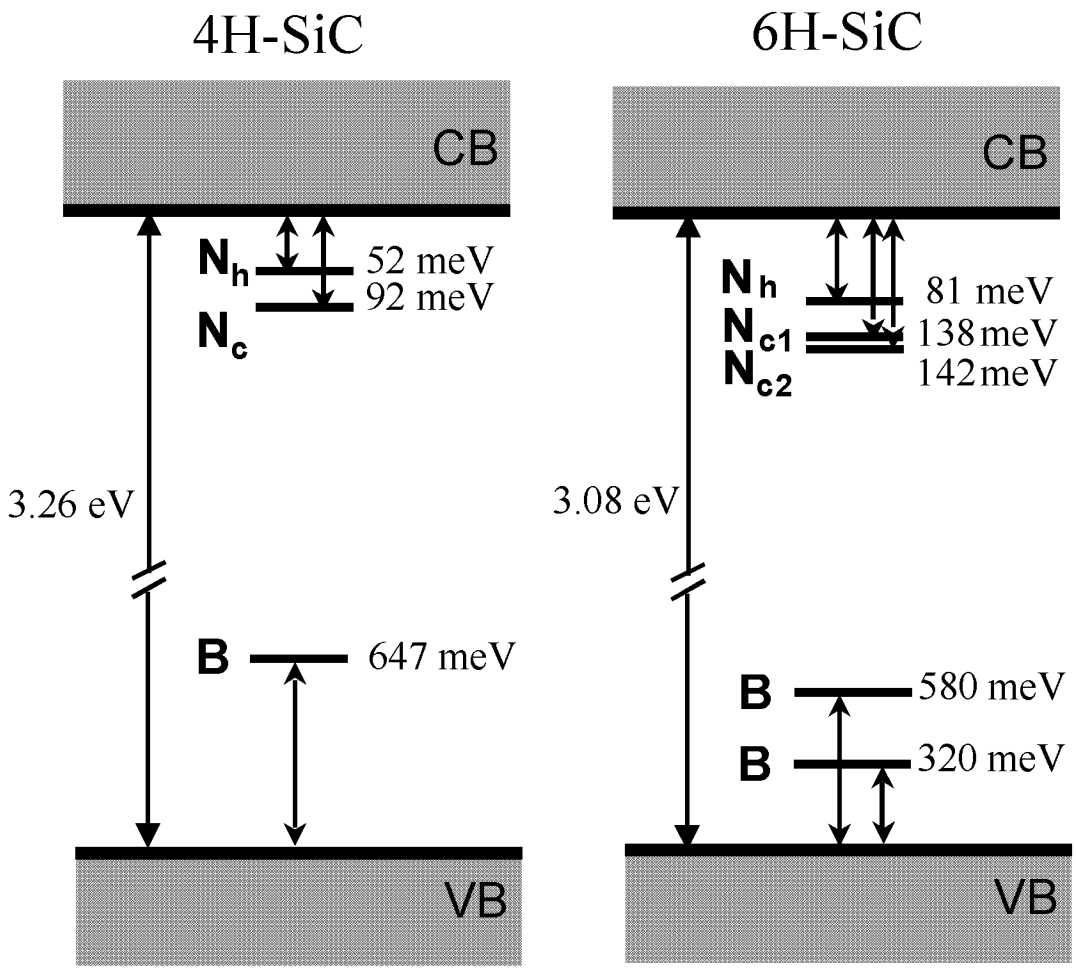

Figure 7.1: Energy levels of the nitrogen donor in hexagonal SiC. The values for the energy bandgap, the energy levels of the nitrogen donor in 4H-SiC and 6H-SiC and the energy levels of the boron acceptor in 4H-SiC were taken from [Landolt-Börnstein 82], [Suttrop 92] and [Suttrop 90], respectively.

where N_C is the effective density of states:

$$N_C = 2M_C \left(\frac{2\pi m_{eff} kT}{h^2} \right)^{3/2} , \tag{7.3}$$

m_{eff} the effective mass for the conduction band, $g = 2$ the spin degeneracy factor, M_C the number of equivalent conduction band minima (M_C= 12 for 4H-SiC, 6 for 6H-SiC [Patrick 72]) and k the Boltzmann constant. The concentration ratios $N(h) : N(c)$ for 4H and 6H are 1:1 and 1:2, respectively, since there are an hexagonal

and a quasicubic lattice sites in 4H-SiC and an hexagonal and two quasicubic lattice sites in 6H-SiC. We neglect the difference in the energy levels of the two quasicubic lattice sites in 6H-SiC, since it is only 4 meV.

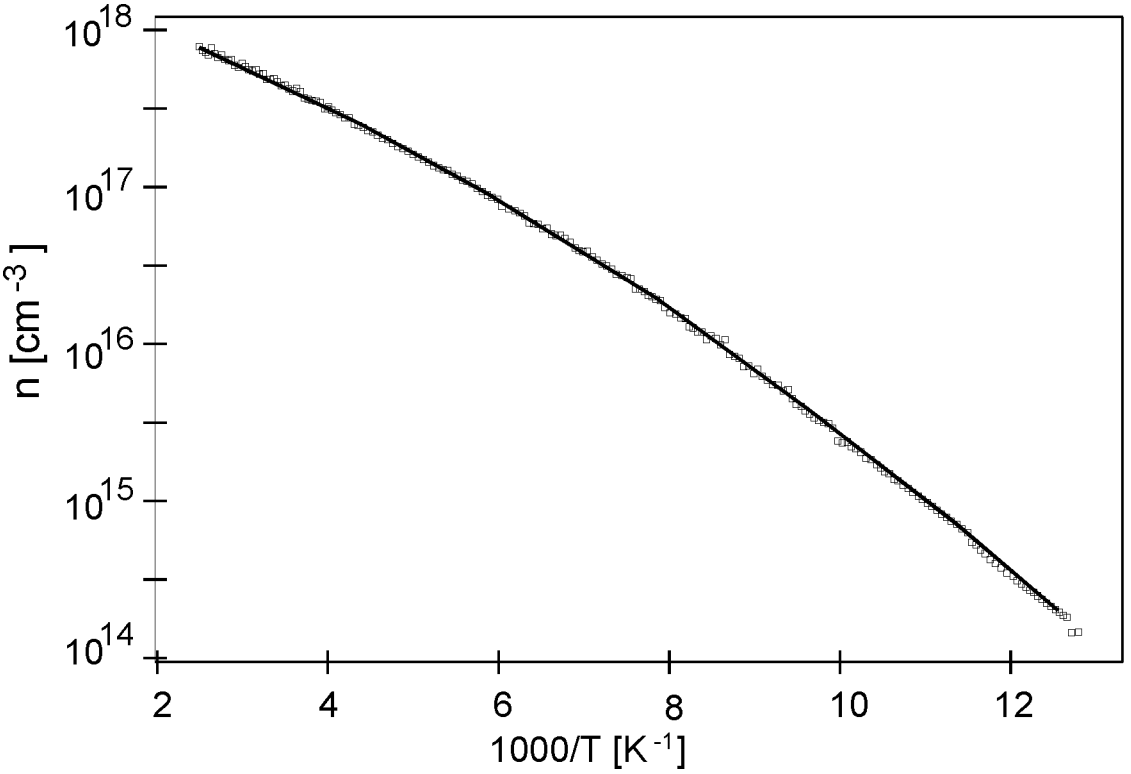

Figure 7.2: Free carrier concentration of sample B1 as a function of the inverse of the temperature in a semilogarithmic scale. The squares show the experimental data, the full curve is a fit using the neutrality equation (eq. (7.2)). The concentration of nitrogen donors, as determined from the experiment, is $N(h) = 0.83 \cdot 10^{18} cm^{-3}$, $N(c) = 1.66 \cdot 10^{18} cm^{-3}$ and the compensation is $N_A = 9.0 \cdot 10^{17} cm^{-3}$.

The free electron concentration in the conduction band n of sample B1 (6H polytype) was investigated. Figure 7.2 shows the experimental values of n as a function of the inverse temperature in a semilogarithmic scala. At room temperature, it was found to be $n \approx 5 \cdot 10^{17} cm^{-3}$. By means of the neutrality equation (7.2), with $N(c) = 2 \cdot N(h)$ and with the literature values for the ionization energies $\Delta\epsilon$ and the effective mass ($\Delta\epsilon(h)$ =81 meV, $\Delta\epsilon(c_{1/2})$ =142/138 meV, $m_{eff}/m_0 = 0.27$), we obtain from a fitting of the experimental data: $N(h) = 8.3 \cdot 10^{17} cm^{-3}$ and $N_A = 9.0 \cdot 10^{17} cm^{-3}$. From $N(c) = 2 \cdot N(h)$ (for 6H-SiC) we obtain $N(c) = 1.66 \cdot 10^{18} cm^{-3}$ and as a result the total nitrogen concentration amounts to $2.49 \cdot 10^{18} cm^{-3}$, in good

agreement with the data from the supplier $\approx 2 \cdot 10^{18} cm^{-3}$ [Siemens AG Erlangen]. From the comparison of the obtained values for N_A, $N(h)$ and $N(c)$, we can say that at low temperatures the Fermi level will lie near the energy level of nitrogen in the shallower quasicubic position. At such low temperatures, all acceptors will be ionized as well as N_A donors (all nitrogens at hexagonal sites and some nitrogens at quasicubic sites), whereas the remaining nitrogen donors (at quasicubic sites) will be neutral. The donor concentration is high, but still below the critical concentration for metal behaviour $N_C \approx 10^{19}\mathrm{cm}^{-3}$ (see equation (3.3)).

The remaining samples were also investigated with electrical methods, all of them exhibited n-type behaviour, as expected. Sample B2 was found to be non-degenerate, resistivity measurements as a function of temperature were however not possible, due to the bad quality of the contacts. Hall measurements on samples B3 and B4 showed that their nitrogen concentration exceeded the critical concentration N= $10^{19} cm^{-3}$. The electrical characterization showed that the donor states had broadened into a band overlapping with the conduction band.

As regards the epitaxial sample E1, by electrical investigations we measure the substrate, which has a nitrogen concentration of $N = 6 \cdot 10^{18} cm^{-3}$. By means of Hall measurements we found that the degree of compensation k=N/N_A was some percent. We can thus conclude that for this sample the Fermi level lies near the energy level of the nitrogen donor in the hexagonal position N_h. From luminescence and luminesce-detected EPR (LDEPR) investigations we found that the compensating impurity was the boron acceptor.

7.2 Resistivity Measurements

A further step towards the determination of the dominating conduction mechanism at low temperatures is the investigation of the temperature behaviour of the resistivity. We studied sample E1 with dc resistivity measurements in a temperature range from 4.9 to 17K. The resistivity was found to increase by two orders of magnitude when the temperature decreased from 17K to 5K: $\rho(5.2K) = 349k\Omega$, $\rho(17K) = 1.7k\Omega$. Fig. 7.3 shows the experimental data in logarithmic representation. The temperature dependence of the resistivity shows two regions with different

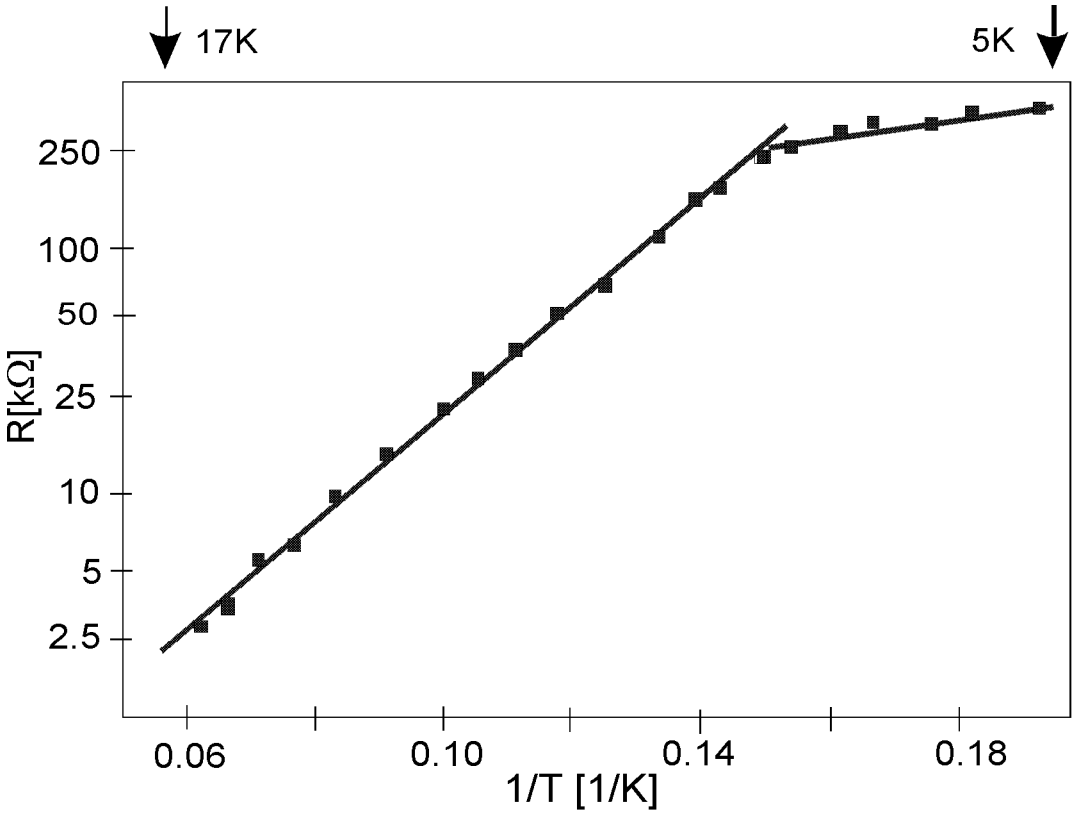

Figure 7.3: Resistivity (in kΩ) of sample E1 as a function of the inverse of the temperature in semilogarithmic scale. The squares show the experimental data, measured at I=40μA and with the electrical field perpendicular to the crystallographic c-axis. The full curve is a fit yielding a temperature dependence as $\rho = \rho_3 e^{\epsilon_3/kT} + \rho_0 e^{(T_0/T)^{1/4}}$, with $\epsilon_3 = 3.9 \pm 0.2$ meV, $\rho_3 = 135\Omega$, $T_0 = (5.4)^4$ K and $\rho_0 = 40.5k\Omega$.

slopes. In the first region, it exhibits an exponential dependence on the inverse of the temperature, $\rho \propto e^{1/T}$, whereas in the second region it fits best to a $\rho \propto e^{1/T^{1/4}}$ dependence. Furthermore, the resistivity was quite low and did not change in several orders of magnitude under illumination of the sample with UV light. All these facts, together with the values found for donor concentration and compensation, point to hopping as the conduction mechanism at low temperatures. As seen in chapter 3 (sections 3.2.1, 3.2.2), the resistivity in a hopping system is given by:

$$\rho = \rho_3 \exp(\epsilon_3/kT) + \rho_0 \exp\{(T_0/T)^{1/4}\} \ , \tag{7.4}$$

where the first term describes the temperature behaviour at not too low temperatures (nearest neighbour hopping) and the second one predominates at very low temperatures (variable range hopping). When comparing the experimental curve with equation (7.4) we see that the two temperature regions would correspond to the two hopping regimes. A fit of the experimental data for T$\geq$ 7K yields $\epsilon_3 = 3.9$ meV and $\rho_3 = 135\Omega$. The activation energy of approx. 4 meV is similar to the one found by other authors in n-type silicon carbide samples with similar nitrogen concentrations. Fig. 7.4 shows the resistivity in the low temperature range as a function of $T^{-1/4}$ in semilogarithmic scala. The line is a simulation with $\rho_0 \exp\{(T_0/T)^{1/4}\}$, $\rho_0 = 40.5k\Omega$ and $T_0 = (5.4)^4$K. The fact that we observe hopping conductivity indicates that we measure the resistivity of the substrate, which has a nitrogen concentration typical for hopping: N= $6\cdot10^{18}$cm^{-3}, and therefore N(h)=N(c)=$3\cdot10^{18}$cm^{-3}.

From these results we can estimate the density of states at the Fermi level $N(\epsilon_F)$ by making use of equations (3.6)

$$\epsilon_3 \approx \frac{1}{N(\epsilon_F)a^3}$$

and 3.11

$$T_0 \approx \frac{24}{\pi}\frac{\alpha^3}{kN(\epsilon_F)}) \ ,$$

with $\alpha = 1/a_B = 5\cdot10^6$cm^{-1} [März 99] for the nitrogen donor at the hexagonal lattice site in 4H-SiC and an average distance between donors of $< R >= 50\mathring{A}$ (N(h)=$3\cdot10^{18}$cm^{-3}) we obtain from $\epsilon_3 = 3.9$meV a density of states at the Fermi level $N(\epsilon_F) \approx 7\cdot10^{21}$cm^{-3}eV^{-1} and from $T_0 = (5.4)^4$K $N(\epsilon_F) \approx 1.5\cdot10^{21}$cm^{-3}eV^{-1}, in reasonable agreement.

Hopping conductivity in silicon carbide has been reported before. Busch and Labhart [Busch 46] were the first to observe impurity conduction in p-type silicon carbide. The activation energy, however, was not determined. Evwaraye et al. [Evwaraye 96, Smith 97] measured the activation energies for hopping conduction in n-type 4H-SiC samples with N_D-$N_A > 10^{18}$cm^{-3} by both temperature dependent resistivity measurements and thermal admittance spectroscopy (TAS). The experimental values for ϵ_3 ($\rho \propto \exp(\epsilon_3/kT)$) were 4-5 meV and 2.3-3.0 meV, respectively. The difference between the obtained activation energies was attributed to the fact that resistivity and TAS measurements were taken on perpendicular

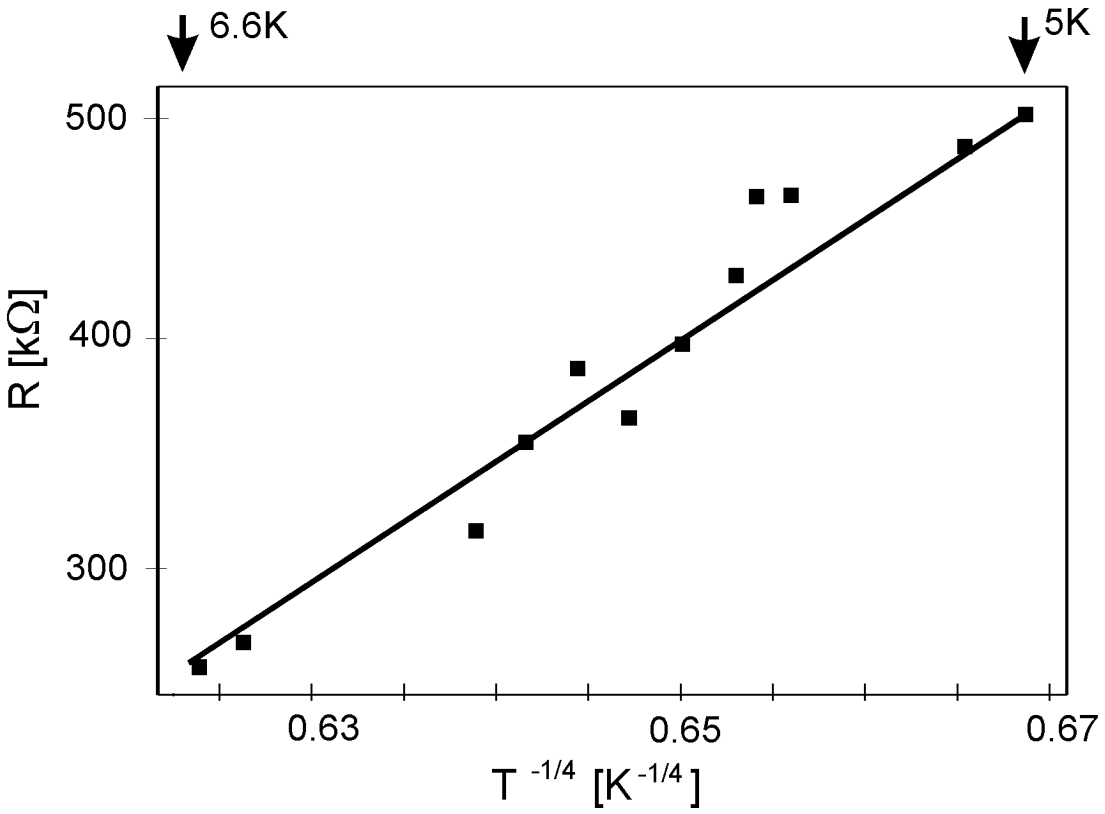

Figure 7.4: Resistivity (in kΩ) of sample E1 as a function of the inverse $T^{-1/4}$ in semilogarithmic scale. The squares show the experimental data, measured at I=40μA and with the electrical field perpendicular to the crystallographic c-axis. The full curve is a fit yielding a temperature dependence as $\rho = \rho_0 e^{(T_0/T)^{1/4}}$, with $T_0 = (5.4)^4$ K and $\rho_0 = 40.5k\Omega$.

directions. The distance between two neighbouring sites in hexagonal SiC depends on the crystallographic direction: parallel or perpendicular to the c-axis. Therefore, the difference in the average hopping distance leads to a difference in the activation energy. The authors found no evidence of hopping conductivity for N_D-N_A < 10^{18}cm^{-3}. Unlike them, we observed in sample E1 the variable range hopping regime besides the nearest neighbour hopping regime.

In our experiments the direction of the electrical current was always perpendicular to the crystallographic c-axis, as in the resistivity studies of Evwaraye et al. [Evwaraye 96, Smith 97]. We studied sample B1 also with dc resistivity measurements in a temperature range between 6K and 23K. The contacts did not show ohmic behaviour for temperatures below 8K. Therefore, only the results for the tem-

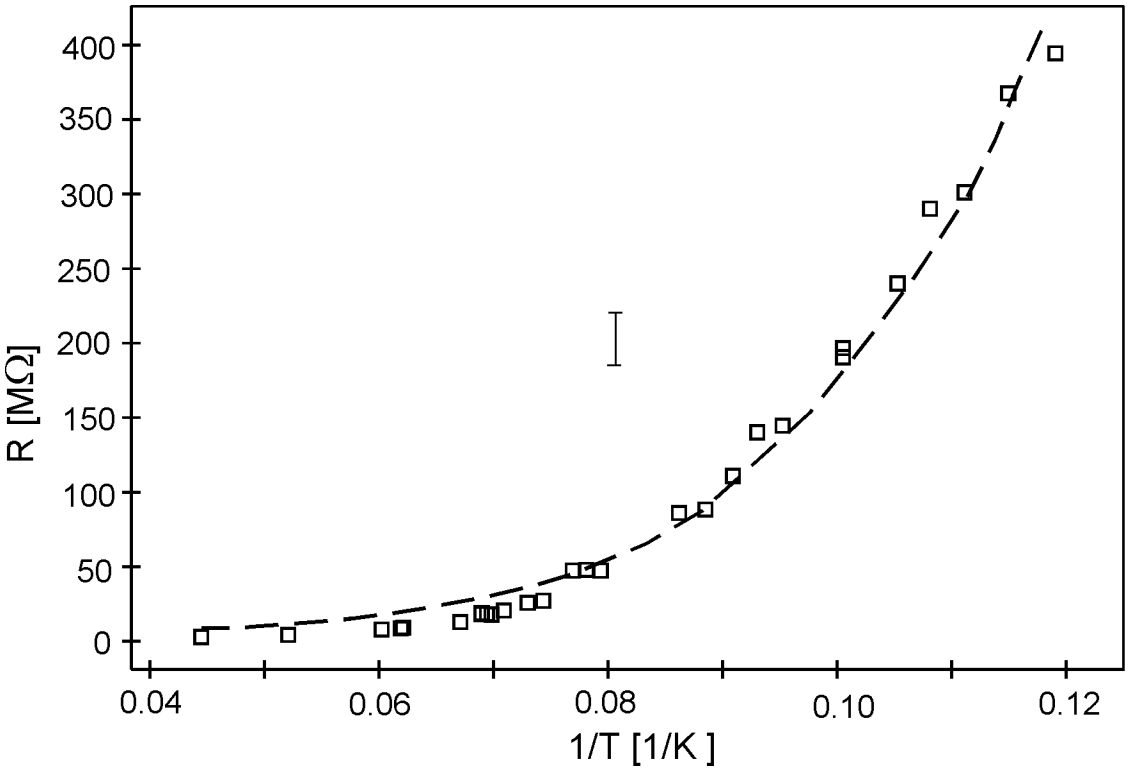

Figure 7.5: Resistivity (in MΩ) of sample B1 as a function of the inverse of the temperature. The squares show the experimental data measured at U=2V and with the electrical field perpendicular to the crystallographic c-axis. The dashed line is a fit yielding a temperature dependence as $\rho = \rho_3 e^{\epsilon_3/kT}$, with $\epsilon_3 = 4.3 \pm 0.2$ meV.

perature range between 8K and 23K were taken into consideration. The resistivity was found to increase by two orders of magnitude when the temperature decreased from 23K to 8K: $\rho(8K)/\rho(23K) = 144$. The resistivity followed an exponential dependence on the inverse of the temperature. Fig. 7.5 shows a fit of the experimental data yielding a behaviour as $\rho \propto exp(\epsilon_3/kT)$, with $\epsilon_3 = (4.3 \pm 0.18)$meV. The activation energy found lies in the typical range for hopping conductivity, as in the case of sample E1. Therefore, hopping conductivity is the dominating charge transport process at low temperatures in these samples.

7.3 Magnetoresistance

Magnetoresistance studies are a further tool for the characterization of semiconductors. In such investigations the increase of the resistance due to the deflection of the conduction electrons by a magnetic field is detected. We measured the magnetoresistance of samples E1, B1 and B2 at room temperature in the interval B= 0...1000 mT. It exhibited the typical behaviour for band-type conduction $(\Delta\rho/\rho) \propto B^2$. At low temperatures, where hopping conduction occurs, we have a different situation. In this case the charge carriers are not electrons in the conduction band, but donor electrons hopping from one localized state to another. As a result, the magnetic field dependence differs from the magnetoresistance at high temperatures or under illumination, where conduction electrons are generated and an anomalous magnetoresistance is expected (see chapter 3).

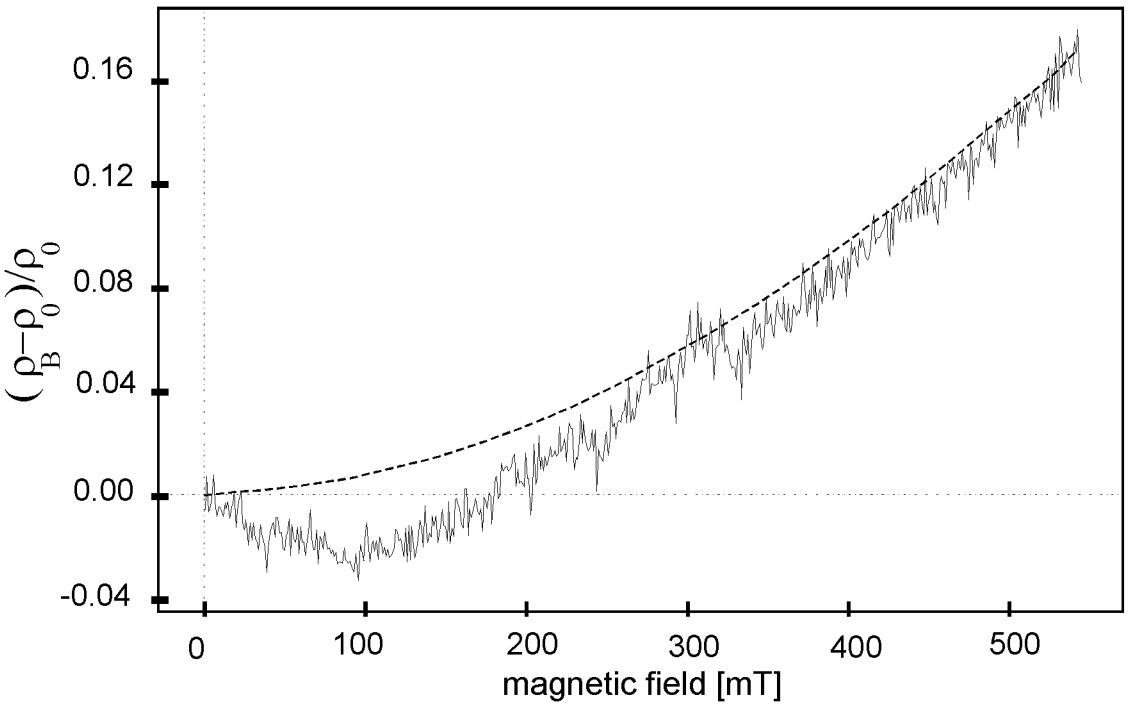

Figure 7.6: Magnetoresistance: $(\rho_B - \rho_0)/\rho_0$ of sample E1 measured at I= 10μA and T=6K (without illumination with light or microwaves). The dashed line is a simulation yielding a dependence $(\rho_B - \rho_0)/\rho_0 \propto exp(B^2)$.

Figure 7.6 shows the magnetoresistance of sample E1 measured in the dark and at

a temperature of 6K. We found an anomalously large magnetoresistance, negative below 180mT and positive for higher magnetic fields. The magnitude of the effect was very sensitive to the temperature. For temperatures above 10K it could not be detected, since it was smaller than the noise. All experiments were conducted at *low field* conditions, i.e. the magnetic length λ was always much larger than the Bohr radius of the donor (see chapter 3, section3): the largest magnetic field was 1T, the corresponding magnetic length $\lambda = 256\mathring{A} \gg a_B = 20\mathring{A}$.

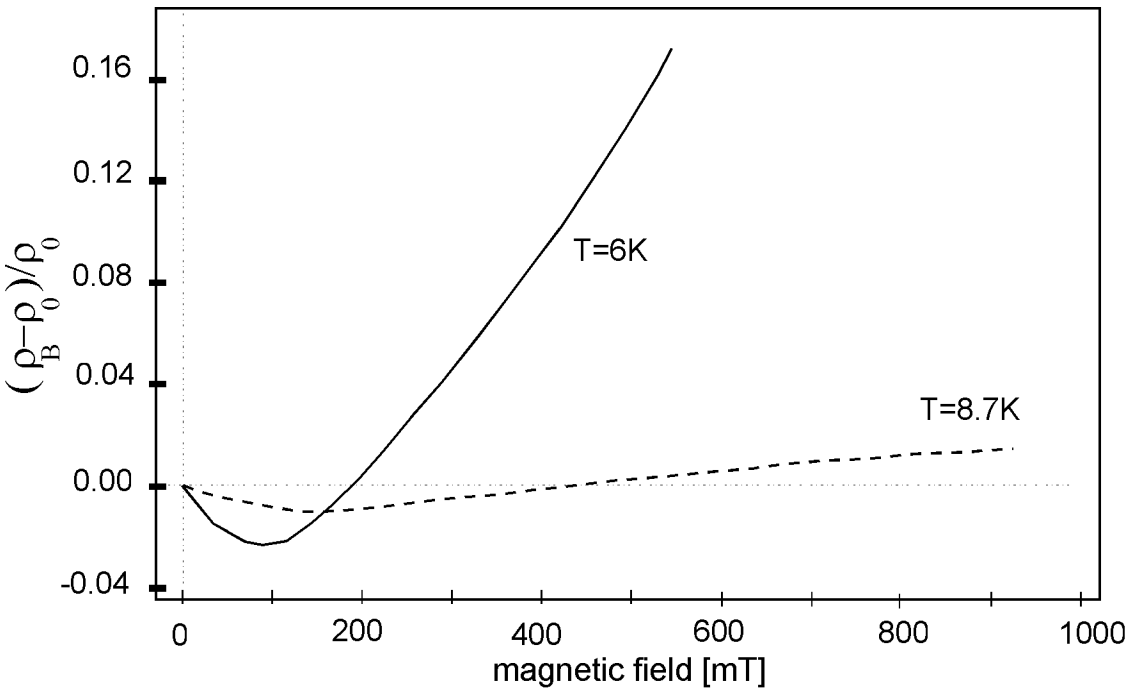

Figure 7.7: Magnetoresistance of sample E1 measured at two different temperatures: 6K and 8.7K. The shown curves result from smoothing the experimental curves.

Two aspects of the magnetoresistance observed at low temperatures differ from the behaviour at high temperatures:

1. the size of the positive contribution. The magnetoresistance of a material is called anomalous when it satisfies the following condition:

$$\Delta\rho_B/\rho \gg (\mu_B B/kT) \;, \tag{7.5}$$

where $\Delta\rho_B = \rho(B) - \rho(0)$. For a magnetic field of 500 mT and a temperature of 6K we obtain $(\mu_B B/kT) \approx 10^{-5}$, which is four orders of magnitude smaller than the experimental value $(\rho(500mT) - \rho(0))/\rho(0) = 0.16$.

2. the existence of a negative contribution, which dominates at low magnetic fields.

Regarding the size of the positive magnetoresistance effect, a similar finding has been measured in different hopping systems. A giant magnetoresistance [Sladek 58] is characteristic for the hopping conduction mechanism. This is due to a decrease of the wavefunctions overlap in the presence of a magnetic field. The positive contribution to the magnetoresistance, which dominates for B $\geq$ 180mT, can be attributed to the typical hopping magnetoresistance: $(\rho_B - \rho_0)/\rho_0 \propto exp(B^2)$ [Shklovskii 79]. In fact, the theoretical expression for the hopping magnetoresistance (eq. (3.16)) is able to describe the experimental results for high magnetic field values, as illustrated by the dashed line in fig. 7.6, which is a simulation yielding a dependence $(\rho_B - \rho_0)/\rho_0 \propto exp(B^2)$.

Fig. 7.7 shows the magnetoresistance of sample E1 measured at two different temperatures: 6K and 8.7K. We observe that the size of the magnetoresistance effect diminishes with increasing temperature. The magnetic field for which the positive contribution beginns to dominate over the negative contribution shiftes to higher values with increasing temperature.

Both the qualitative and the quantitative behaviour shown in fig. 7.6 are very similar to the experimental results obtained by Benzaquen et al. [Benzaquen 88] in highly compensated crystalline gallium arsenide (see fig. 7.8). The authors found also an anomalous magnetoresistance with a positive and a negative contribution dominating at high and low magnetic fields, respectively. Nevertheless, in their investigations the magnetoresistance minimum was found to shift to smaller magnetic field values with increasing temperature. To explain the negative contribution to the magnetoresistance the authors applied Fukuyama and Yoshida's theory [Fukuyama 79]. This theory assumes the existence of localized and delocalized states in the gap, separated by a mobility edge. The Fermi level lies in the region of localized states. The negative magnetoresistance would correspond to a situation where most charge carriers are situated in the upper Zeeman level, which offers a better overlap of the wavefunctions. The experimental findings of Benzaquen et al. as well as our results show qualitative but not quantitative agreement with Fukuyama and Yoshida's theory.

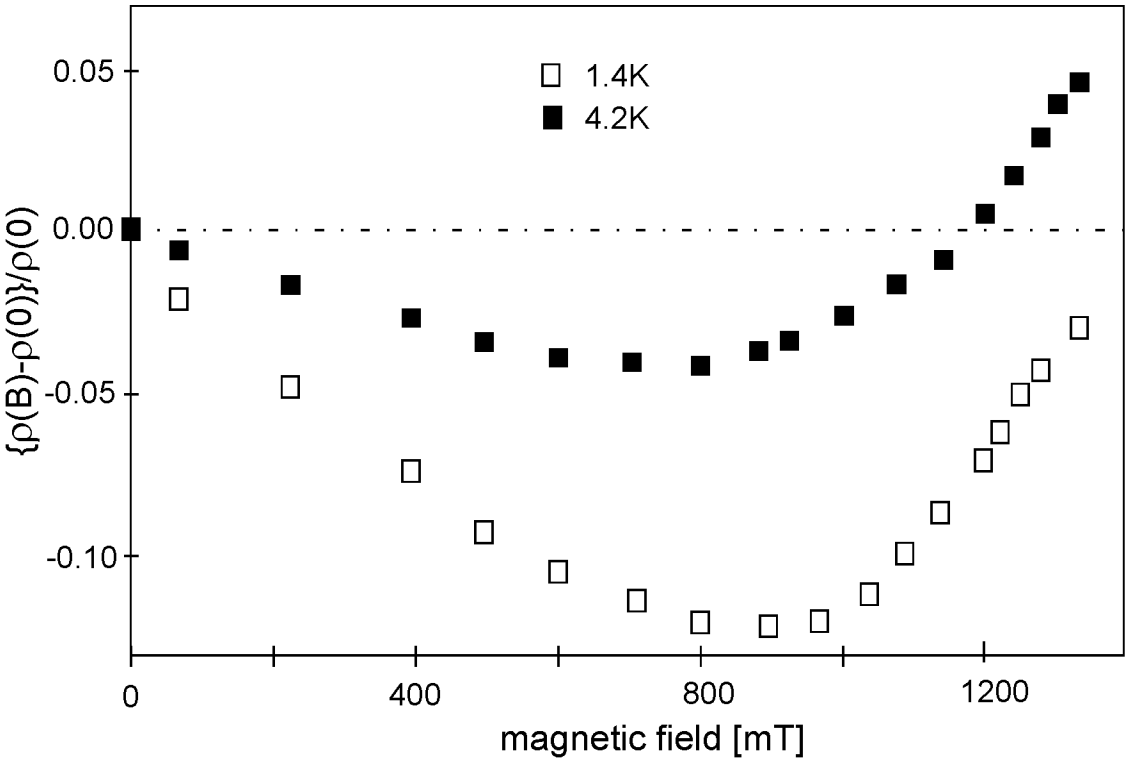

Figure 7.8: Magnetoresistance of an epitaxial n-type GaAs sample as a function of the magnetic field for two values of the temperature [Benzaquen 88].

However, if the charge transport occurs in the nitrogen band, the states will then be either unoccupied or singly occupied. As regards the singly occupied states, in thermal equilibrium the number of donor electrons in the lower Zeeman level will exceed the number of those in the upper Zeeman level. In Fukuyama and Yoshida's picture, this would not lead to a negative, but to a positive magnetoresistance.

A negative magnetoresistance has also been found in amorphous silicon and germanium and is attributed to hopping betwen dangling bond-type states, which can be empty, singly or doubly occupied [Movaghar 78]. In this picture, the hopping probability is much larger than the spin relaxation rate ($\nu_{hop} \gg T_1^{-1}$). Therefore, the fast hopping electrons see an essentially frozen spin system. An electron hopping to a singly occupied state must have the correct spin orientation as the hop is forbidden otherwise. The authors suggested that spin-flip hopping processses would make observable contributions to the conductivity. Subsequently the anomalous magnetoresistance is the result of the modification of the spin-flip relaxation time by the external magnetic field. The resistivity is found to grow first with increasing

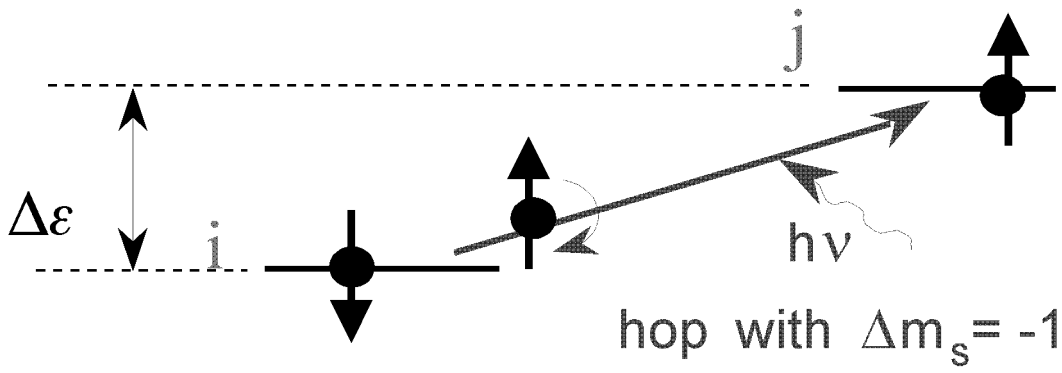

Figure 7.9: Schematic representation of Movaghar and Schweitzer's model for the anomalous magnetoresistance found in amorphous silicon and germanium.

magnetic field and then decrease for higher magnetic field values, in contrast to the behaviour found in silicon carbide samples in this work.

7.4 Microwave induced resistivity decrease

In an EDEPR experiment a static magnetic field and a microwave field are applied to the sample. In the former sections we dealt with the influence of the magnetic field on the resistivity, now we will turn our attention to the effect of a microwave field. We found that the sample resistivity decreases by microwave irradiation. Figure 7.10 shows the behaviour of the resistivity of sample E1 under irradiation with microwaves at a frequency ν_{mw} = 10GHz as a function of the microwave power incident into the cavity at T=9.5K and T=9.15K. The resistivity was found to decrease with increasing microwave power up to a certain power level. The magnitude of the effect depends on the temperature, decreasing with increasing temperature, and on the defect concentration. The microwave power level for which the resistivity stops falling (P_C) decreases as well with increasing temperature. For sample E1 and T=6.5K, I=10μA, P_{mw} = 200mW and B=0 the relative change in the resistivity was found to be $\frac{\rho_{mw}-\rho}{\rho} = -0.8$.

At first sight, the experimentally found resistivity decrease induced by microwave

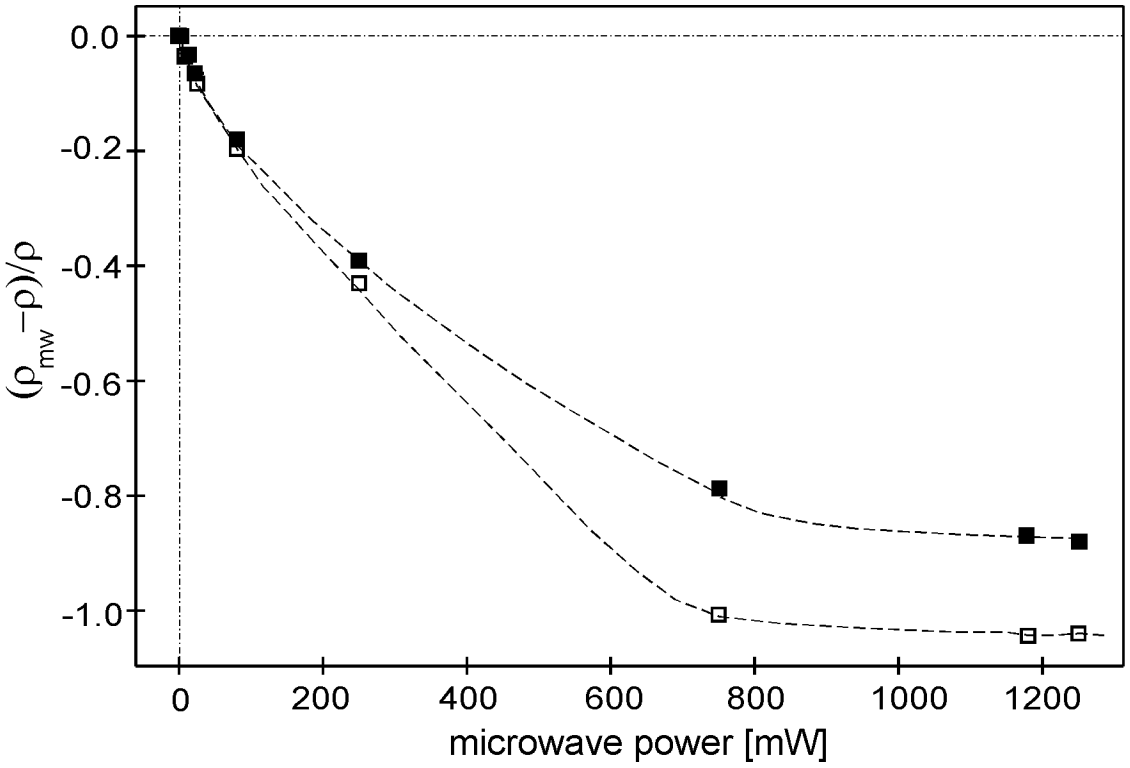

Figure 7.10: Experimentally determined microwave- induced resistivity decrease of sample E1 measured as a function of the microwave power incident onto the cavity. The full and open squares show the experimental data obtained at T=9.5K and T=9.15K, respectively.

irradiation appears to be due to a microwave-induced heating effect, since the resistivity decreases with increasing temperature. An experiment was carried out with the purpose to see the magnitude of the effect. Figure 7.11(a) shows the time evolution of the resistivity of sample E1 after switching on the microwaves. At t=0 the microwaves were off and a stationary state in temperature had been reached. The thermistor at the bottom of the cavity delivered a temperature value of T=9.75K. A voltage-current measurement delivered R=82kΩ for the sample resistance (U=1.64V at I=20μA). At t=t_0 the microwaves were switched on, and a decrease in the voltage across the sample, i.e. a resistivity decrease was observed. The voltage was found to fall in two steps: an immediate response with a steep slope ($\Delta R_1/\Delta t_1 \approx$85K$\Omega$/s) and a slower response ($\Delta R_2/\Delta t_2 \approx$0.073K$\Omega$/s). We can attribute the former to the response of the sample resistivity to the switching on of the microwaves, since the sample mass is just some mgram. The latter would reflect the slower response of the whole system (cavity), which will depend on the cooling power (helium flow

through the cryostate). In the time interval Δt_1 the sample resistance falls from 82kΩ to 64kΩ (the voltage grows from 1.64V to 1.28V at constant current conditions, I=20μA) Δt_1 being 210ms. As regards the slower response, the resistance falls from 64kΩ to 57kΩ in a time interval Δt_2 of 96s, varies slightly and finally reaches a stationary value of 58kΩ for t≥300s. From the different reaction times ($\Delta t_1 \ll \Delta t_2$), we can conclude that the effect of the microwaves on the sample resistivity has two contributions: a direct influence of the microwaves upon the resistivity and an indirect influence due to the heating of the cavity.

A further experiment was performed to separate the behaviour of the sample and the cavity. The time evolution of the signal from the thermistor situated at the bottom of the microwave cavity was recorded for the unloaded cavity, as shown in fig. 7.11(b). This measurement illustrates the response of the cavity temperature to the switching on of microwaves. As in the experiment shown in fig. 7.11(a), at t=0 the system was in thermal equilibrium and at t=t_0 the microwaves were switched on. This lead to a temperature increase of about 0.1K in a time interval Δt approximately equal to the $\Delta t_2 = 96s$ found in the experiment from fig. 7.11(a). The microwave power incident onto the cavity was the same as in the experiment above. Therefore, the slower response found by recording the voltage across the sample comes from the heating of the cavity by the microwaves and subsequent transfer of heat to the sample and the fast response comes from the sample. Since the mass of the sample is very small, we assume that the heating of the sample does not affect appreciably the temperature of the cavity.

Let us now look at the magnitude of the effect. When switching on the microwaves, the sample resistance was found to fall from R_{mw}=82kΩ to R=64kΩ in a time interval $\Delta t_1 = 210ms$. If the only effect of the microwave irradiation were a heating of the sample, the temperature increase ΔT_1 corresponding to this resistivity decrease $\Delta R_1 = -18$kΩ could be estimated from the temperature dependence of the resistivity

$$\rho = \rho_3 exp\left(\frac{\epsilon_3}{kT}\right) \ , \epsilon_3 \approx 4meV,$$

and with an initial temperature T=9.75K we obtain T_{mw} ≈9.2K after switching on. Thus, the effect of the microwaves in the conductivity is equivalent to a temperature increase of ΔT_1 ≈0.6K. If we consider as well the response of the whole system, i.e. the total resistivity change $\Delta R_1 + \Delta R_2$ we obtain ΔT ≈0.7K. Therefore, ΔT_2 ≈0.1K,

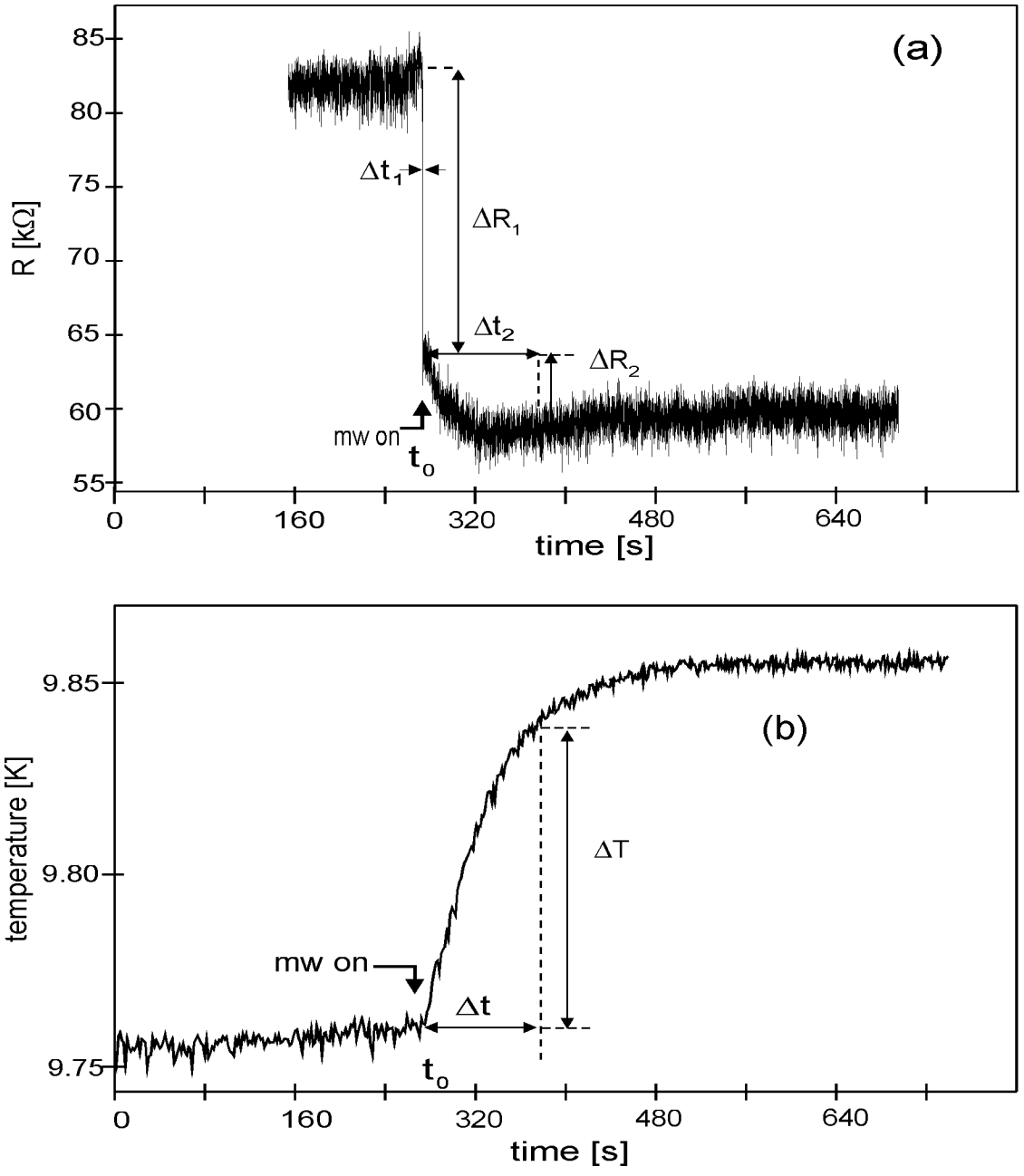

Figure 7.11: (a) Response of the resistance of sample E1 measured as a voltage change under constant current (I=20μA) to the switching on of the microwaves at t=t_0 The temperature measured by the thermistor at the bottom of the cavity at stationary conditions was 9.75K without microwaves (at t=0) and 9.85K (at t=300s) with microwaves. (b) Similar experiment as shown in (a), but in this case the temperature of the unloaded cavity was studied by recording the resistance of the thermistor situated at the bottom of the microwave cavity.

which agrees with the temperature difference delivered by the temperature controller and with the experiment for the unloaded cavity shown in fig. 7.11(b).

From the experiments described above, we see that the microwave irradiation affects the sample resistivity in two different ways. On the one hand, it produces a temperature increase in the cavity, which induces a heating of the sample. On the other hand, it influences directly the sample resistivity. The question is, whether this direct influence is a heating effect or not.

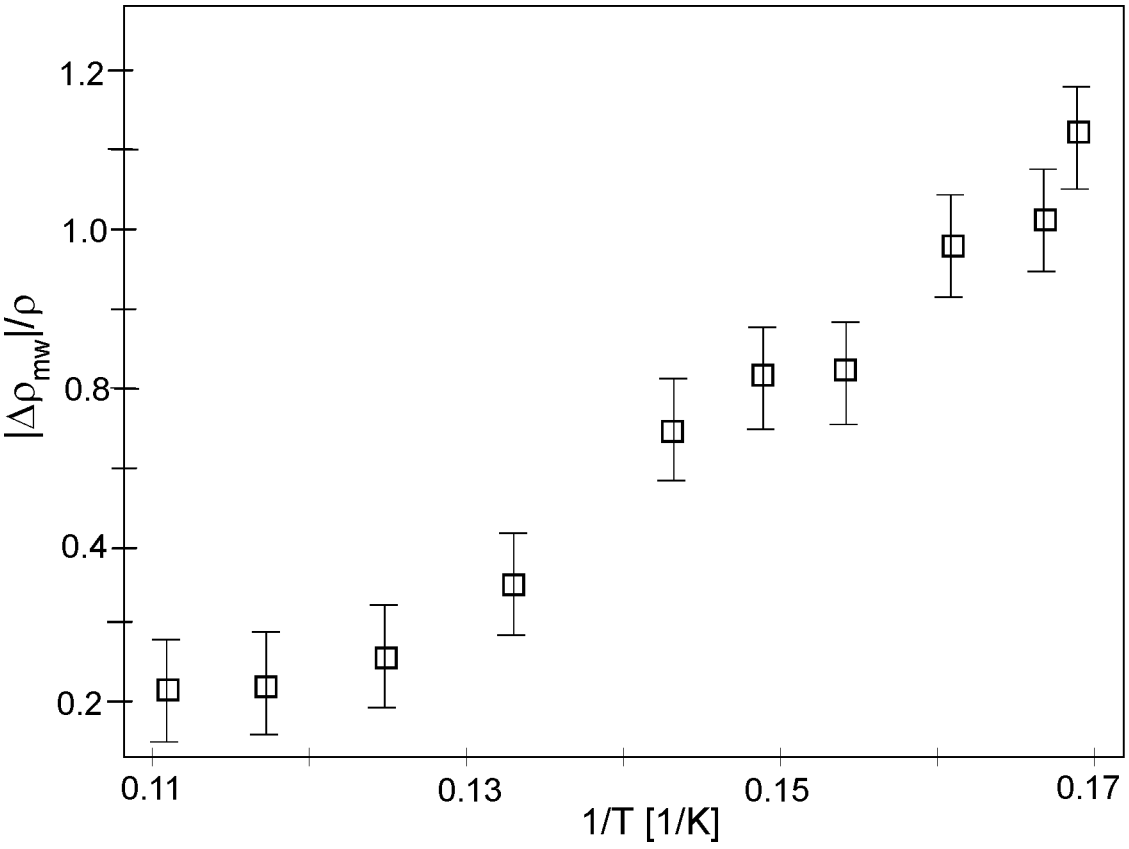

Figure 7.12: Temperature dependence of the relative microwave-induced resistivity decrease $|\Delta\rho_{mw}|/\rho = -(\rho_{mw} - \rho)/\rho$. The squares show the experimental data.

In order to find out whether the microwave-induced resistivity decrease results from a temperature increase, we measured the resistivity without and with microwaves at different temperatures. Figure 7.12 shows the relative resistivity decrease $|\Delta\rho_{mw}|/\rho = -(\rho_{mw} - \rho)/\rho$ of sample E1 at $P_{mw} = 0.2$W as a function of the reciprocal temperature. As noticed above, the effect grows with decreasing temperature.

The behaviour of the two degenerated samples (B3 and B4) differed from that of the lighter doped samples: the resistivity was found to increase under microwave irradiation. This can be qualitatively explained as follows: the nitrogen concentration of both samples exceeds the critical concentration 10^{19}cm^{-3}, therefore the donor states are delocalized, and charge transport is band-like. By microwave irradiation the mobility of the conduction electrons decreases, leading to a resistivity enhancement.

7.4.1 Magnetic field dependence of the microwave absorption

Now let us have a look at the behaviour of the resistivity when both a microwave field and a static magnetic field are present. Figure 7.13 shows the microwave absorption J of sample B1 as a function of the static magnetic field. We see that it decreases first with increasing magnetic field, goes through a minimum at about 100mT and finally grows with increasing magnetic field. The minimum position varies lightly for different samples. The magnitude of the relative effect $\frac{|J(B)-J(0)|}{J(0)}$ diminishes under illumination with light of the sample. It decreases with increasing temperature and increases with increasing microwave power. The behaviour shown in fig. 7.13 was measured prior to the fabrication of electrical contacts on the sample. Therefore the observed magnetic field dependence of the microwave absorption cannot be an effect of the electrical contacts or the wires.

Figure 7.14 shows the microwave-power dependence of the magnetoresistance effect under microwave irradiation for a constant magnetic field value (B=120mT). We see that the effect grows with increasing microwave power up to a certain level ($\approx$1000mW) and keeps constant for higher power levels.

When repeating the experiment, but detecting now the voltage across the sample for a fixed current value, the same qualitative behaviour as before (though inverted, $(\rho(B) - \rho(0)) > 0$ when $(J(B) - J(0)) < 0$ and vice versa) is obtained. There are two possible explanations for the magnetic field dependence of the microwave absorption-signal: a cavity loss effect and a hopping-related microwave absorption.

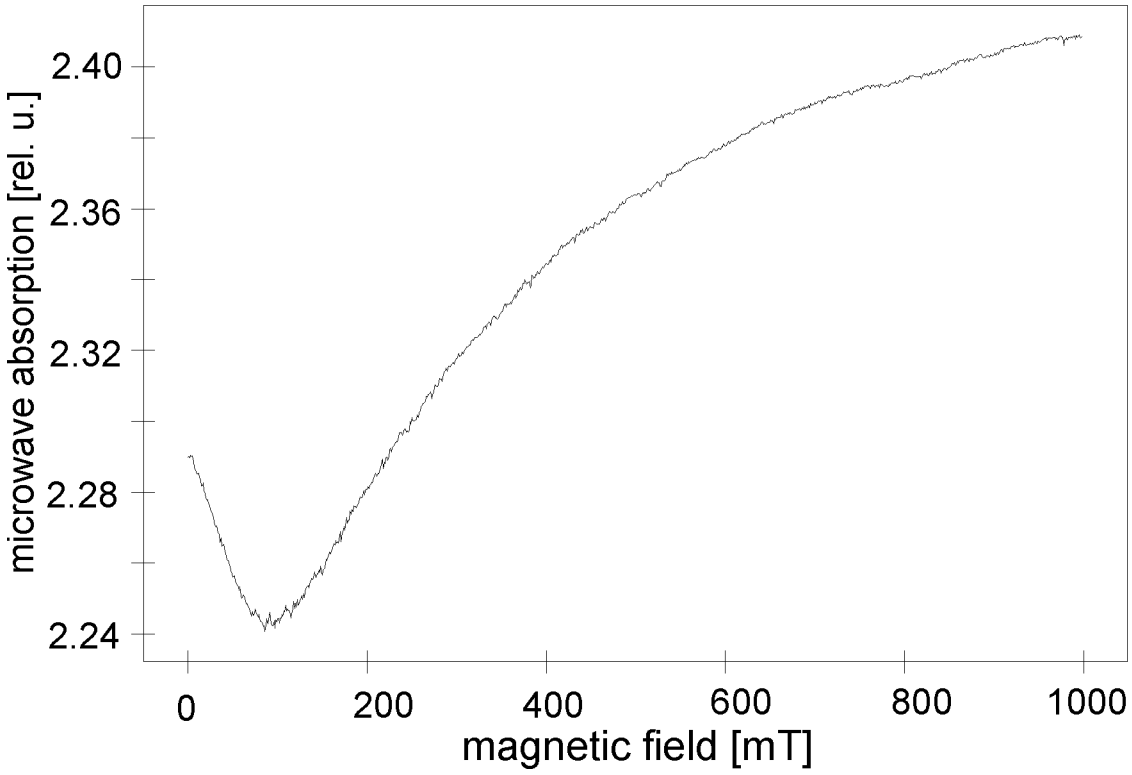

Figure 7.13: Magnetic field dependence of the microwave absorption at T=7.5K and P_{mw}=500mW, sample B1. The sample had no electrical contacts

The former can be explained as follows: as shown in chapter 4, the voltage change at the microwave detector induced by a conductivity change of the sample is given by $\Delta V_{det} \propto -\Delta\sigma\sqrt{P}_{mw} \propto \frac{\Delta\rho}{\rho^2}\sqrt{P}_{mw}$ (see eq. (4.8)). Thus, the magnetoresistance effect presented in section 3 can lead to a significant magnetic field dependence of the quality factor of the microwave cavity, and thus to a magnetic field dependence of the microwave "absorption" signal. The latter explanation would be the relation between hopping-related microwave absorption and hopping conductivity. As mentioned in chapter 3, section 4, the microwave absorption coefficient J is related to the hopping conductivity σ: $J = 4\pi\sigma/c\kappa^{1/2}$.

$$\frac{\Delta J}{J} = \frac{\Delta\sigma}{\sigma} = -\frac{\Delta\rho}{\rho} \tag{7.6}$$

Therefore, a change in the microwave absorption can be indirectly detected as a change in the resistivity.

Figure 7.15 shows the magnetic field dependence of the microwave absorption of sample E1, indirectly detected through a current-voltage measurement. We see that

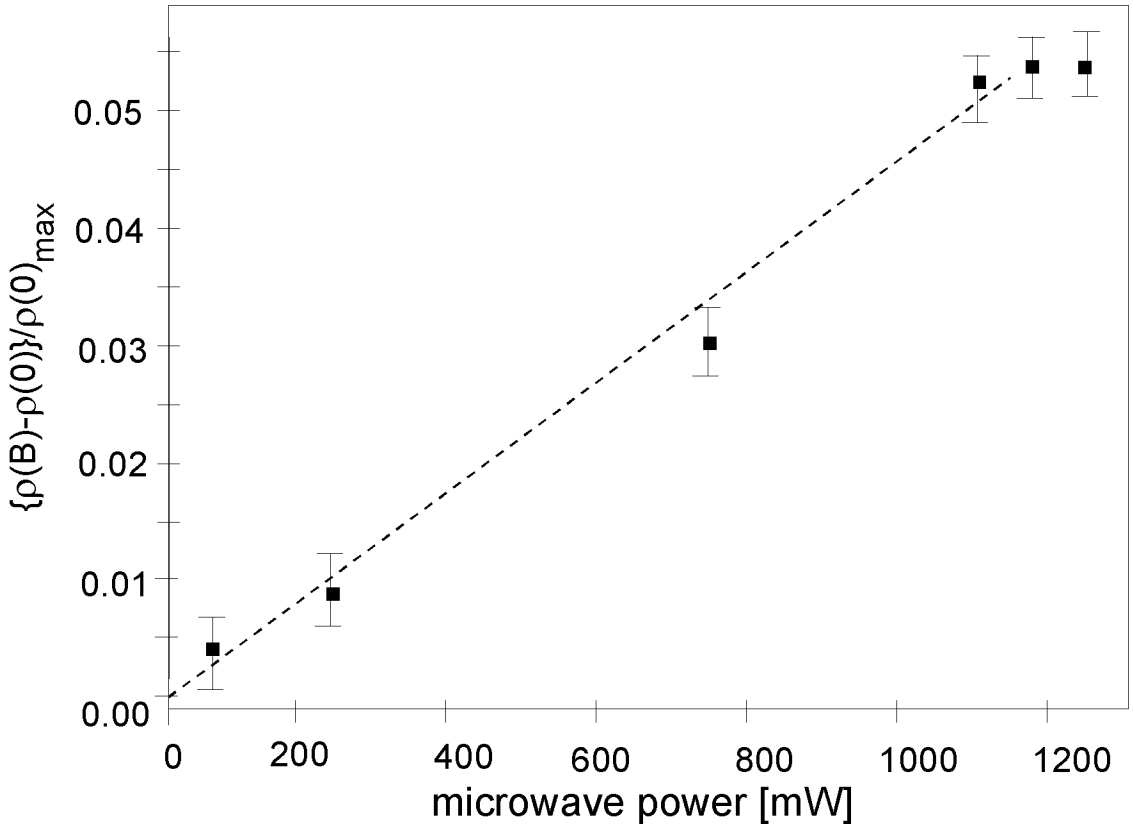

Figure 7.14: Microwave power dependence of the maximum value of the magnetoresistance under microwave irradiation (B(max)≈ 120mT). Sample E2, T=10.5K, I-U measurement, U=4V, I varied from 1.5 to 5μA for the different microwave power levels.

the resistivity increases first with the magnetic field and then decreases below the zero-field value. When the microwave absorption signal was recorded a qualitatively similar (but inverted) behaviour was obtained, as expected from the relation between microwave absorption and resistivity.

If we argue that the magnetic field dependence of the microwave absorption signal arises from the B-field dependence of the resistivity, which affects the quality factor of the cavity, fig. 7.15 and fig. 7.13 would correspond to a direct and an indirect measurement of the magnetoresistance, respectively. But from the comparison of the B-field dependence results in absence and presence of microwaves (section 7.3 and 7.4.1, respectively) we find that in the first case the negative contribution dominates over the positive contribution at low magnetic field values, whereas in the second case the opposite behaviour is observed. Moreover, the magnetoresistance

effect depends more strongly on temperature, whereas the effect under microwave irradiation decreases only lightly with growing temperature and could be detected even at T=50K. As a consequence, the behaviour shown in fig. 7.15 and 7.13 points to a magnetic field dependence of the microwave absorption, which is larger than the magnetoresistance effect at the temperatures used for our studies.

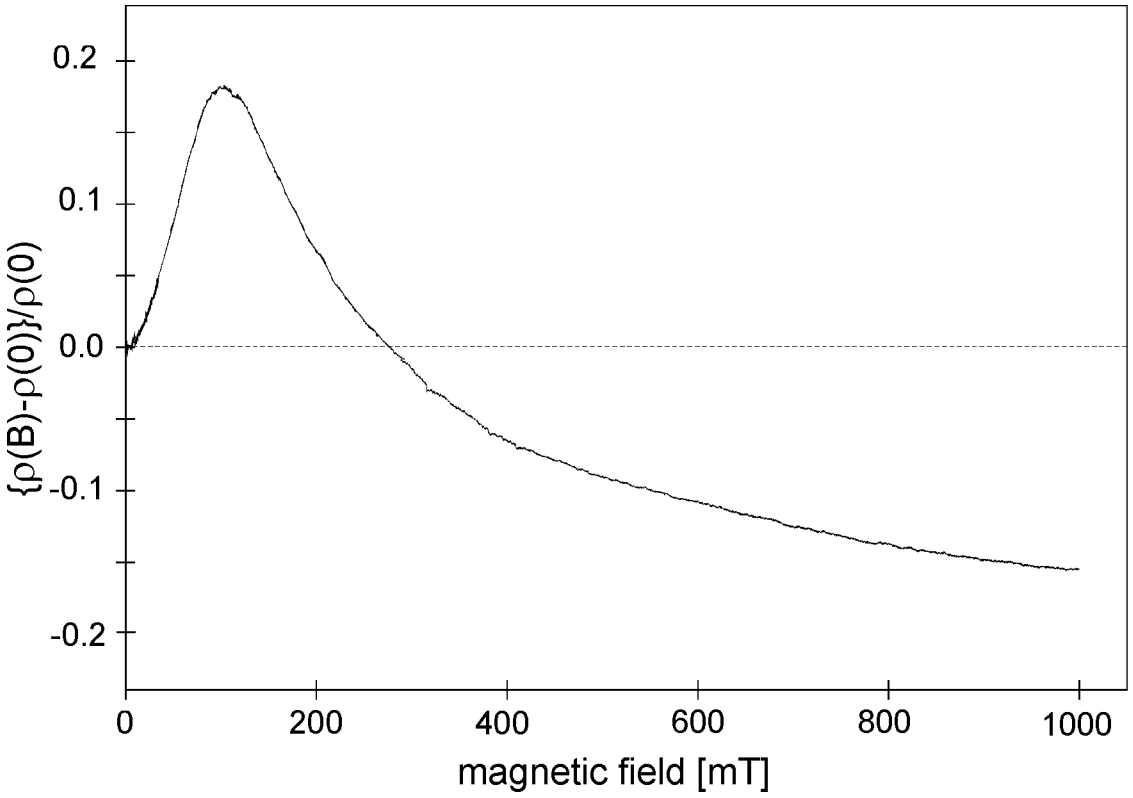

Figure 7.15: Magnetoresistance under microwave irradiation of sample E1 at I=10μA, T=8K and P_{mw}= 750mW

Figure 7.16 shows the resistance of sample E1 as a function of the magnetic field at different conditions: without irradiation with microwaves (a) and with a microwave power of 80mW (b) and 1.2W (c) incident onto the cavity. The cooling power (helium flow through the cavity) was set constant for all measurements. The measurements were performed with the sample in thermal equilibrium with the cavity. The temperature delivered by the thermistor situated at the bottom of the cavity was 8.7K, 10.5K and 11K for curves (a), (b) and (c), respectively. We see that at zero field the irradiation with microwaves induces a resistivity decrease $\Delta R(1)_{mw}$ and $\Delta R(2)_{mw}$ at 80mW and 1250mW, respectively, these resistivity decreases correspond by $\approx$ 80% to the temperature increases measured with the

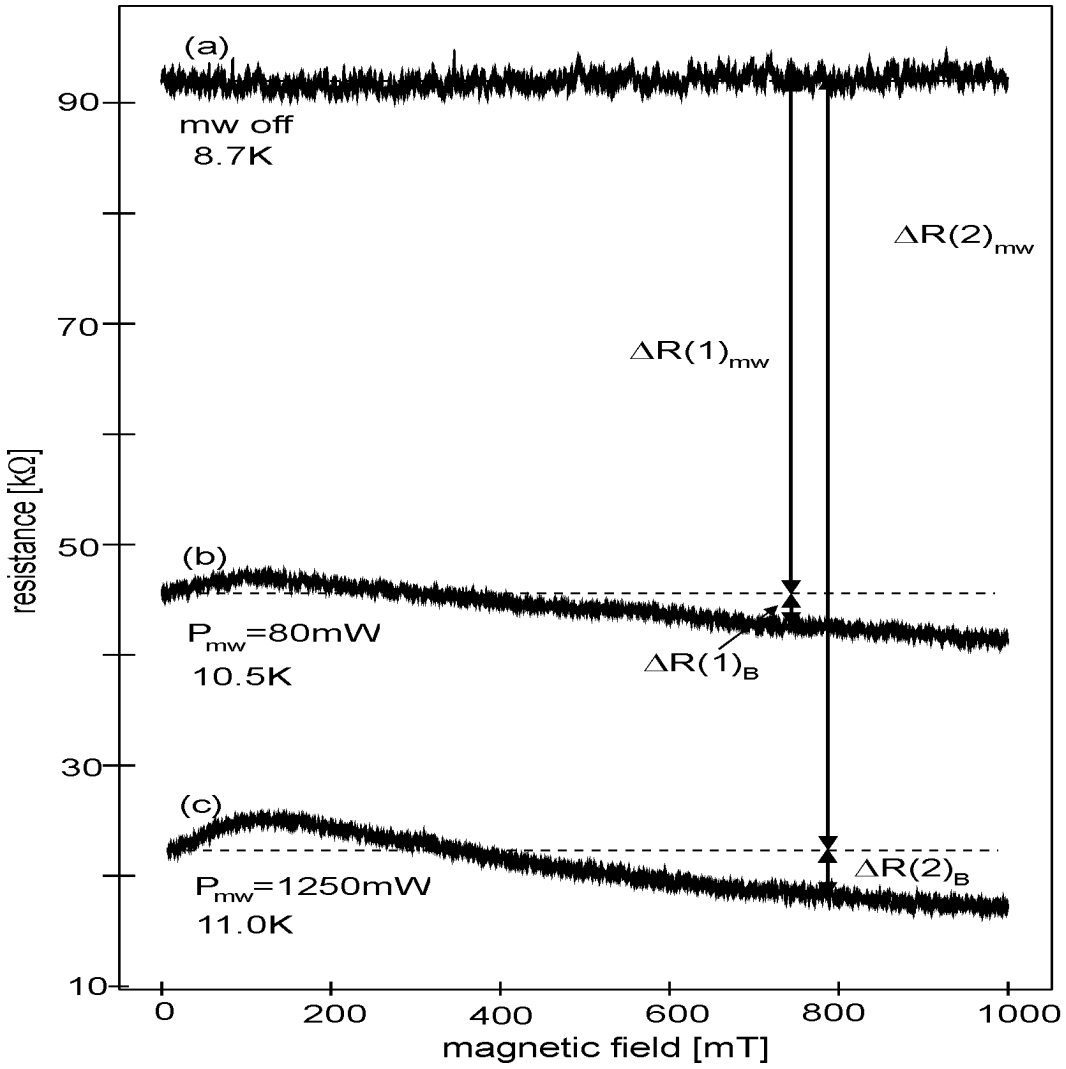

Figure 7.16: Resistance of sample E1 as a function of static magnetic field measured in the absence of microwaves (a) and with a microwave power of 0.080W (b) and 1.2W (c) incident onto the cavity, respectively.

thermistor. Thus the origin of the remaining $\approx 20\%$ is different from a temperature increase. At nonzero magnetic field, an additional resistivity change ($\Delta R(1)_B$, $\Delta R(1)_B$) originates, which is positive for low magnetic field values and negative in other case. We observe that the field-dependent contribution is much smaller than the zero-field contribution: $\Delta R(2)_{mw} = 70K\Omega \gg \Delta R(2)_{B=1T} = 4.6K\Omega$, $\Delta R(1)_{mw} = 48K\Omega \gg \Delta R(1)_{B=1T} = 4.0K\Omega$. Both contributions (as relative effects) were found to increase linearly with microwave power up to a certain level, as illustrated in fig. 7.10 and 7.14. In contrast to ΔR_{mw}, ΔR_B cannot be attributed to a

heating effect.

We performed further studies to see whether the observed behaviour is related to the frequency of the field. For this purpose, we compared the behaviour of the conductivity under irradiation of the sample with a microwave field (10 GHz) and a radiofrequency field (different frequencies were used: ν =1, 2, 10, 50, 100 and 400 MHz, with a maximum power of 6watt). The experiment was performed at T=10K, at this temperature the magnetoresistance effect was negligible. When the sample was subjected to microwave irradiation the resistivity was found to vary with the magnetic field (e.g. R(B=0)=34.9±0.5 kΩ, R(B=500)=31.0±0.5 kΩ R(B=1000)=25.8±0.5 kΩ). Nevertheless, by irradiation with radiofrequencies the resistivity was somewhat higher than that with microwaves and no magnetic field dependence of the resistivity in the range $0 < B < 1T$ could be detected (R(0,500mT,1000mT) = 46.3±0.5 kΩ). In all cases the irradiation induced a temperature increase, but only in the case of irradiation with microwaves did the resistivity depend on the magnetic field. These results suggest that the observed behaviour (fig. 7.13) depends on the frequency of the field, and therefore cannot be fully attributed to a heating effect.

7.5 Discussion

The previous sections have focussed on the electrical investigations conducted with the aim of determining the charge transport mechanism at low temperatures. The fact that the samples exhibit a low resistivity at low temperatures and without light illumination, together with donor concentrations lying in the intermediate concentration range and the presence of compensating impurities, point to hopping as the mechanism responsible for charge transport. The experimentally found behaviour of the resistivity with temperature supports this supposition and delivers the characteristic activation energy.

Hopping conductivity is expected to occur in the concentration range of about $10^{18}cm^{-3}$, for lower concentrations the average distance between donor sites is too large, the wavefunctions overlap is negligible. On the other hand, for higher concentrations ($> 10^{19}cm^{-3}$) the overlap is too large, leading to a delocalization of the

impurity states. The Bohr radius a_B of N_h is $20\mathring{A}$ (see chapter 3), this is 6.5 times the lattice constant in the direction perpendicular to the axial axis, and twice the lattice constant in the axial direction. The typical hopping distance R_ω in the activated hopping regime is $R_\omega \approx 6a_B - 10a_B$, i.e 120-200 $\mathring{A}$ for the hexagonal site nitrogen. The average distance between N_h donors for a nitrogen concentration of $10^{18}cm^{-3}$ is given by $R_m = \{\frac{4\pi}{3}N_D(h)\}^{-1/3} = 125\mathring{A}$, with $N_D(h) = N_D/2$ for the 4H polytype, which has one cubic and one hexagonal position. R_m is about 25 times the lattice constant and 6.25 times the Bohr radius, it lies in the typical range for activated hopping. The nitrogen concentrations of samples E1, B1 and B2 were found to lie in the hopping concentration range $10^{18}cm^{-3} < N_D < 10^{19}cm^{-3}$. It was in these samples were hopping-related effects were found experimentally.

In the case of hexagonal SiC, we have to consider the defects at the quasicubic and hexagonal lattice sites as separate centres, since their energy difference (ϵ (N_c)-ϵ (N_h)) is about 50meV in 4HSiC, about 80meV in 6H-SiC (see table 5.2), one order of magnitude larger than the characteristic hopping energy. If the Fermi level lies near the energy level of nitrogen in the hexagonal lattice site, as for sample E1, hopping will take place only between hexagonal site donors. Therefore the donor concentration to consider is just $N_D(h) = N_D/2$ for 4H-SiC, $N_D(h) = N_D/3$ for 6H-SiC. Analogous statement can be made if the Fermi level lies near the energy level of nitrogen in a quasicubic lattice site, as for sample B1. Hopping will then take place only between quasicubic site donors.

With regard to the anomalous magnetoresistance, this could be explained either as an effect from hopping (due to either spin-flip hops between triplet states or the existence of a mobility edge), or as a Subnikov-de Haas effect. The latter arises from the quantization of the electronic energy states in the presence of a magnetic field, and it occurs only in very strongly doped semiconductors where the Fermi level lies in the conduction or valence band. Therefore, the behaviour illustrated in fig. 7.6 and fig. 7.15 cannot be attributed to the Subnikov-de Haas effect, since the electrical measurements showed that the samples which exhibited a behaviour as shown in fig. 7.6 and fig. 7.15 were not degenerated.

In section 7.4 we have discussed the observed microwave-induced resistivity decrease in terms of a heating of the sample by the microwaves. We have shown that

the sample absorbs microwaves at "off resonance" conditions (i.e. $h\nu_{mw} \neq \epsilon_{EPR}$), leading to a resistivity decrease, and that this effect depends on the static magnetic field. A resistivity decrease under microwave irradiation can be attributed to a heating of the sample by the microwaves. However, the observed magnetic field dependence cannot be explained with a heating of the sample as sole effect of the irradiation with microwaves. Thus, we have a further (smaller) contribution besides the microwave-induced temperature increase.

As noticed in chapter 3, section 4, there are two contributions to the microwave absorption in a hopping system: the resonant absorption and the relaxational absorption. Both contributions are influenced by a static magnetic field. However, both mechanisms should lead to a positive magnetoresistance, in contrast to our results. In chapter 10, we will further discuss the magnetoresistance and the effect of microwave irradiation on the resistivity and relate them to the EDEPR results.

Chapter 8

EDEPR Investigations of SiC

The electrical detection of magnetic resonance is a promising technique for the study of electrically active defects in semiconductors. Up to now it has been successfully used for the investigation of amorphous (e.g. [Lips 96, Graeff 96]) and porous semiconductors (e.g. [Stutzmann 95]), irradiated crystalline semiconductors (e.g. [Stich 96, Laiho 98]), as well as lowly doped and compensated semiconductors. In many cases EDEPR signals arising from surface defects (e.g. [Laiho 95]) or a single isotropic line (e.g. [Carlos 97]) have been detected. For non-irradiated crystalline semiconductors the donor-acceptor recombination was found to be the microscopic mechanism behind EDEPR [Stich 96]. Nevertheless, it was not clear which concentrations of donors and acceptors were needed for the observation of an EDEPR signal. The objective of this work is to deepen our knowledge of the EDEPR technique, in particular for the case of highly doped crystalline semiconductors, in order to be able to predict the optimal conditions for its use as a tool for the investigation of defect centres .

We have focused our work on low resistivity crystalline silicon carbide (bulk and epitaxial material), in particular on samples with a nitrogen concentration varying in the intermediate concentration range, i.e. highly doped but still showing semiconducting behaviour. In chapter 7 we have reported on electrical investigations conducted on the samples, aimed at characterizing the material and determining the charge transport mechanism. In this chapter, the relevant experimental results concerning different aspects of the electrically detected EPR on n-type SiC are presented. The purpose of these studies together with the investigations presented in chapters 9 and 10, was to find conclusive arguments to answer the following

questions:

1. which structural information can be obtained from EDEPR studies?
2. which experimental conditions (temperature, microwave power level, etc.) are most favourable?
3. which systems can be studied with this technique (concentration and compensation of the samples)?
4. which microscopical processes is EDEPR on highly doped semiconductors based on?

8.1 EDEPR signal

Most EDEPR investigations on crystalline semiconducting material have been performed on silicon and germanium. Silicon carbide has scarcely been an object of study by means of this technique. Stich [Stich 96] studied a 6H-SiC silicon carbide mesostructure by means of EDEPR and found a spectrum corresponding to the nitrogen donor. Reinacher et al. [Reinacher 95] detected an EDEPR signal in a light emitting 6H-SiC diode. They concluded that only the recombination current was observed with EDEPR, but could not assign the EDEPR spectrum to a specific defect.

EDEPR investigations on crystalline semiconductors have mostly been performed on lightly doped samples by illuminating the sample with above-bandgap light. Photo-EDEPR as well as ODEPR is based on the spin-dependence of the donor-acceptor recombination or the triplet recombination [Stich 96]. In the case of lightly doped semiconductors, the sample must be illuminated in order to generate charge carriers in the conduction and valence bands and to obtain a non-negligible conductivity at low temperatures. Highly doped semiconductors, however, exhibit a non-negligible dark conductivity even at low temperatures. As reported in chapter 7, this was the case for our samples. The relatively high dark conductivity enables the conduction of EDEPR investigations without illumination of the sample. The microscopical processes involved are expected to differ from those responsible for

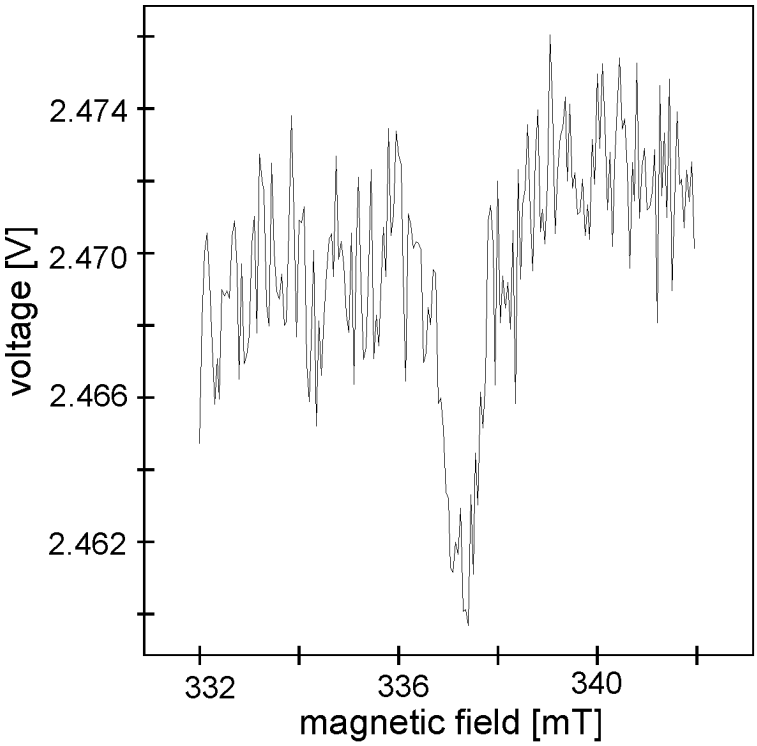

Figure 8.1: EDEPR spectrum of sample E1 measured as a resonant voltage change $\Delta U_{EPR} = -8.23 \cdot 10^{-3}$Volt at constant current conditions I= 10μA. It was measured in the dark at a temperature of T=6.3K, a microwave frequency of $\nu_{mw} = 9.46GHz$ and without modulation of the magnetic field or the microwaves. The sample was orientated with its crystallographic c-axis perpendicular to the magnetic field.

photo-EDEPR.

We performed EDEPR measurements at low temperatures and without illumination of the sample and found a Gaussian EDEPR line at g≈2 with a linewidth of $\Delta H_{pp} =$ 0.4mT when the c-axis of the sample was perpendicular to the static magnetic field. Figure 8.1 shows the EDEPR spectrum of sample E1 measured as a voltage change at constant current conditions (I=10μA). The EDEPR signal was observed in the dark at a microwave power of 200mW, a temperature of 6.3K and a microwave frequency of 9.46 GHz. This measurement was performed without modulation of either the magnetic field or the microwaves. We thus obtain the change in the voltage at resonance conditions in sign and absolute value. Figure 8.1 shows the result of the average of 32 scans, with a total integration time of 6 hours. We

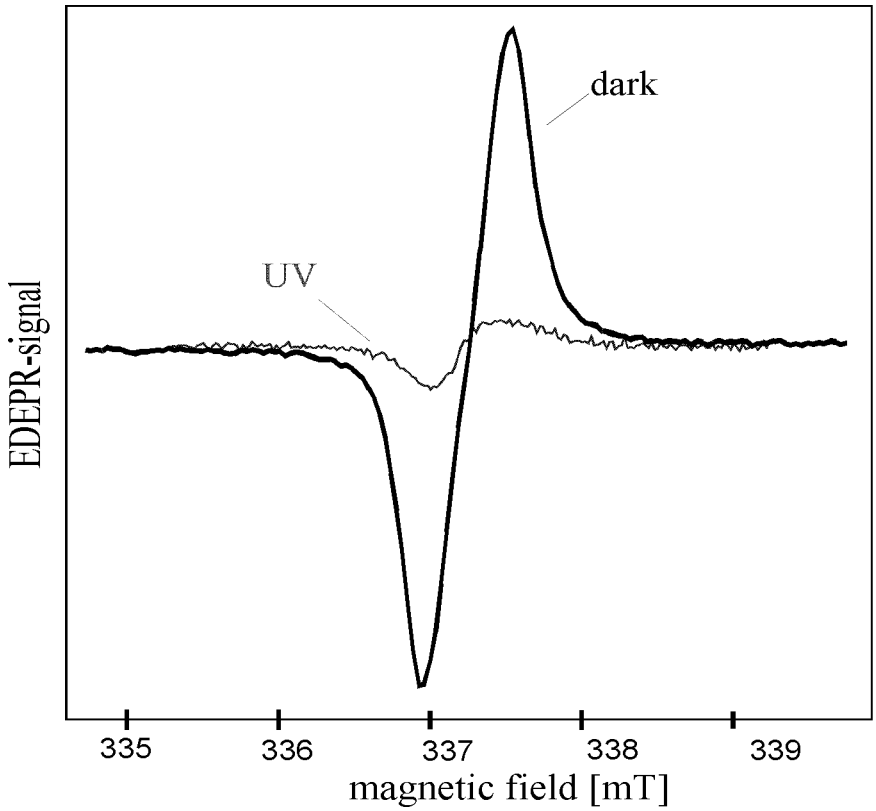

Figure 8.2: EDEPR spectrum of sample E1 measured as a voltage change at I=20μA, T=9K and ν_{mw}=9.46GHz. The thick line shows the spectrum measured in the dark, the thin line shows the spectrum recorded under illumination of the sample with UV light. The static magnetic field was perpendicular to the c-axis of the sample and was modulated with a frequency of 5kHz.

see that the voltage decreases at resonance conditions, and the absolute value is $\Delta U_{EPR} = -8.23 \cdot 10^{-3}$Volt. The relative resistivity decrease is then:

$$\frac{\Delta\rho_{EPR}}{\rho} = \frac{(\Delta U)_{EPR}}{U} = \frac{-8.23 \cdot 10^{-3}}{2.47} = -3.33 \cdot 10^{-3} \tag{8.1}$$

Further measurements at different temperature and microwave power conditions showed in all cases a resistivity *decrease* at spin resonance conditions. A d.c. EDEPR measurement at T=9K, P_{mw} =200mW and I=20μA, for instance, delivered $\frac{\Delta\rho_{EPR}}{\rho} = \frac{\Delta U_{EPR}}{U} \approx -10^{-3}$. These results contrast with the EDEPR signal arising from the spin-dependent recombination, where a resistivity *enhancement* $\frac{\Delta\rho_{EPR}}{\rho} \approx +10^{4}$ [Stich 96] is observed.

Further measurements under illumination of the sample (with UV and halogen light)

showed that the EDEPR signal intensity decreases with increasing light intensity: $|\Delta U_{EPR}(dark)| \approx 10 \cdot |\Delta U_{EPR}(UV)| \approx 2 \cdot |\Delta U_{EPR}(halogen)|$, where $|\Delta U|$ is the EPR-induced voltage decrease at dark, by illumination of the sample with UV light (Hg-lamp) (see fig. 8.2) and halogen light (which contains a small UV part), respectively. The relative effect $\frac{|\Delta U_{EPR}|}{U}$ decreased as well under illumination: $|\Delta U_{EPR}(dark)| \approx 6.5 \cdot |\Delta U_{EPR}(UV)|$.

The spectra shown in fig. 8.1 and fig. 8.2 were recorded for a sample orientation with the crystallographic c-axis perpendicular to the static magnetic field. When the sample was rotated with respect to the magnetic field, the EDEPR line position was found to vary. The obtained EPR parameters correspond to the nitrogen donor, which is present in the substrate and the layer in a concentration of $N \approx 10^{18}\text{cm}^{-3}$ and $N \approx 6 \cdot 10^{15}\text{cm}^{-3}$, respectively. The amplitude of the two outer lines of the hyperfine triplet spectrum was found to be two orders of magnitude smaller than that of the central line shown in fig. 8.1 and fig. 8.2. Such a behaviour of the EPR spectrum of the nitrogen donor has been reported before for samples with a nitrogen concentration $N \geq 10^{18}\text{cm}^{-3}$ and attributed to a delocalization of the unpaired electrons resulting from exchange interaction [Veinger 67]. Therefore, the EDEPR spectrum shown in fig. 8.1 and fig. 8.2 originates from the substrate, since the nitrogen concentrations in the 7μ-layer and the substrate are $N \approx 10^{16}\text{cm}^{-3}$ $N \approx 10^{18}\text{cm}^{-3}$, respectively [Dalibor 96].

Figure 8.3 shows the EDEPR spectrum of sample B1 measured as a voltage change at constant current conditions (I=100) at a temperature of 22K and a microwave frequency of 10.02GHz. The microwave power incident onto the cavity was 1.05W. The magnetic field was modulated with a frequency of 5kHz and the signal detected by making use of lock-in technique. Unlike the EDEPR spectrum of sample E1, shown in fig. 8.2, the EDEPR spectrum of sample B1 shows besides the central line the two outer lines of the hyperfine triplet of the nitrogen donor (^{14}N, 100% abundance, nuclear spin I=1) in 6H-SiC. The observed hyperfine splitting corresponds to the nitrogen donor at the quasicubic sites (a/h$\approx$33 MHz, b/h$\approx$0, see table 5.3). The hyperfine splitting of the donor at the hexagonal site is much smaller (a/h$\approx$2.5MHz, b/h$\approx$0.1, see table 5.3) and is not resolved in the spectrum. In fig. 8.3 we observe that the central line is strongly broadened and its intensity much larger than that of the two outer lines. The lineform is partly Gaussian due to inhomogeneous

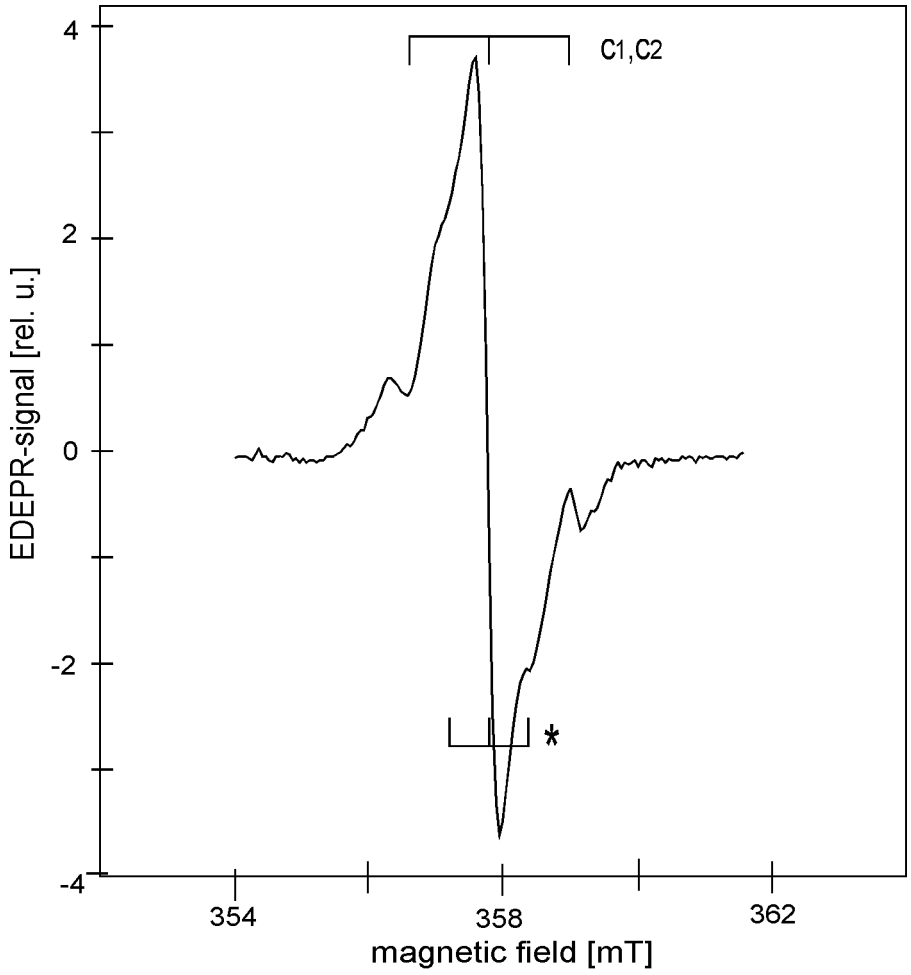

Figure 8.3: EDEPR spectrum of sample B1 measured as a voltage change at I=100μA, T=22K, ν_{mw}=10.02GHz and P_{mw} =1.05W. The magnetic field was modulated with a frequency of 5kHz. The sample was oriented with its crystallographic c-axis perpendicular to the static magnetic field. The EDEPR spectrum corresponds to the nitrogen donor, the central line is broadened and its intensity much larger than that of the outer hyperfine lines. Moreover, two additional lines (*) in the middle of the hyperfine triplet lines are observed.

broadening, partly Lorentzian due to homogeneous contributions from the exchange interaction. Furthermore, two lines (denoted with * in fig. 8.3) appear between the hyperfine lines. Their origin, as well as the broadening of the central line, will be discussed in chapter 9.

8.2 EDEPR-signal dependences

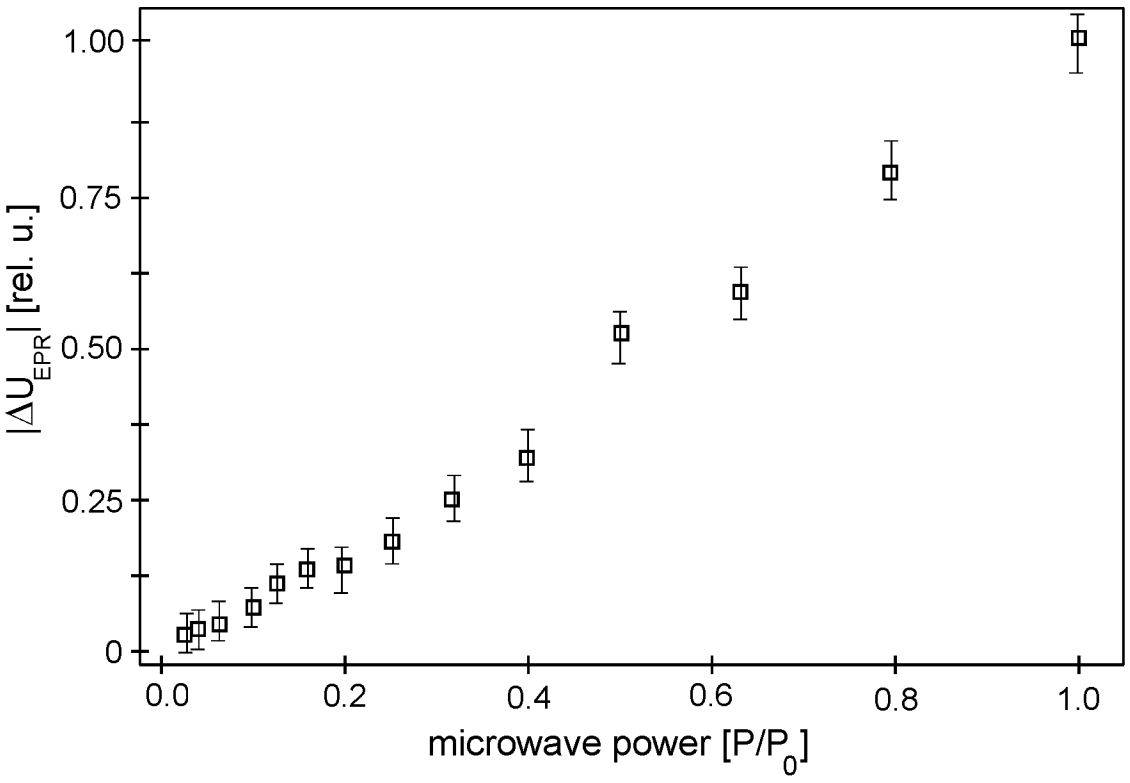

Figure 8.4: Microwave power dependence of the EDEPR signal intensity $|\Delta U_{EPR}|$ (in relative units) measured at T=6.6K and I=90μA. The maximum microwave power incident into the cavity was $P_0 = 200$mW. The corresponding signal intensity was $|\Delta U_{EPR}| \approx 10^{-2}$V. The data shown in the figure is normalized to this maximal value.

In this section the experimental results of the EDEPR signal behaviour with parameters such as microwave power, temperature, modulation frequency and electrical current are presented. The EDEPR signal was measured as a resonant voltage change at constant current conditions. The data were obtained from measurements on sample E1. Sample B1 showed as well an EDEPR signal, it was however much weaker than that of sample E1. The electrical contacts of sample B2 did not work properly at low temperatures, making the detection of an EDEPR signal difficult. The effect of defect concentration (different samples) is reported in chapter 9.

8.2.1 Microwave power dependence

Figure 8.4 shows the microwave power dependence of the EDEPR signal measured at a temperature of 6.6K and a current of 90μA . The signal intensity $|\Delta U_{EPR}|$ exhibits a linear dependence on microwave power up to the maximum power coupled to the cavity: P_0 =200mW. The measurements were subsequently conducted at different temperatures. Figure 8.5 shows the temperature dependence of the slope of the EDEPR signal-microwave power curve $\delta|\Delta U_{EPR}|/\delta P_{mw}$. We found that the slope $\delta|\Delta U_{EPR}|/\delta P_{mw}$ grows with reciprocal temperature.

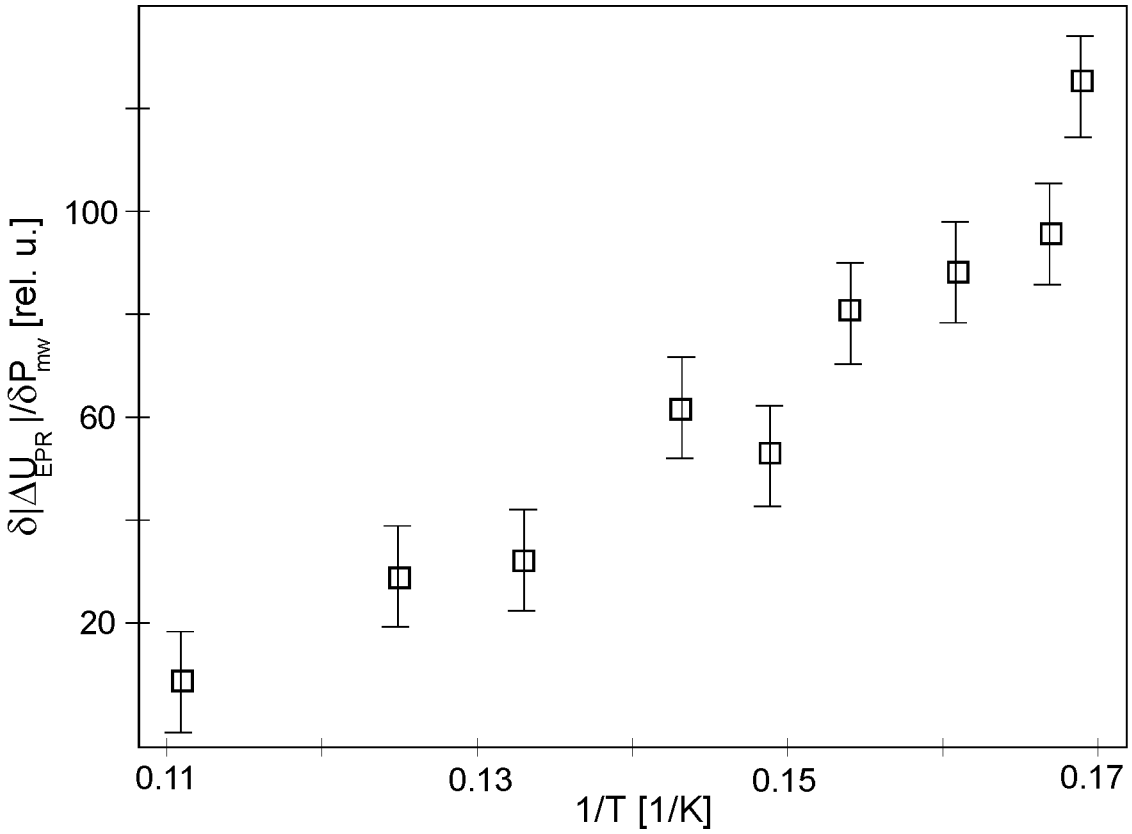

Figure 8.5: Slope of the amplitude of the EDEPR signal relative to the microwave power, $\delta|\Delta U_{EPR}|/\delta P_{mw}$, as a function of the reciprocal temperature in the microwave power range where $\Delta U_{EPR} \propto P_{mw}$. The squares show the slope obtained from experimental microwave power dependences.

Measurements conducted with a new microwave source with a higher output power

(YIG oscillator together with a microwave power amplifier) showed that the signal grows first linearly up to a certain (quite high) microwave power and then keeps constant or diminishes lightly. This is shown in fig. 8.6, where the amplitude of the EDEPR signal, $|\Delta U_{EPR}|$ is shown as a function of microwave power incident into the cavity up to $P_{mw} = 1.2$W. The experimental data are normalized to the maximal signal of about $\Delta U_{EPR} = -|\Delta U_{EPR}| \approx -10^{-2}$.

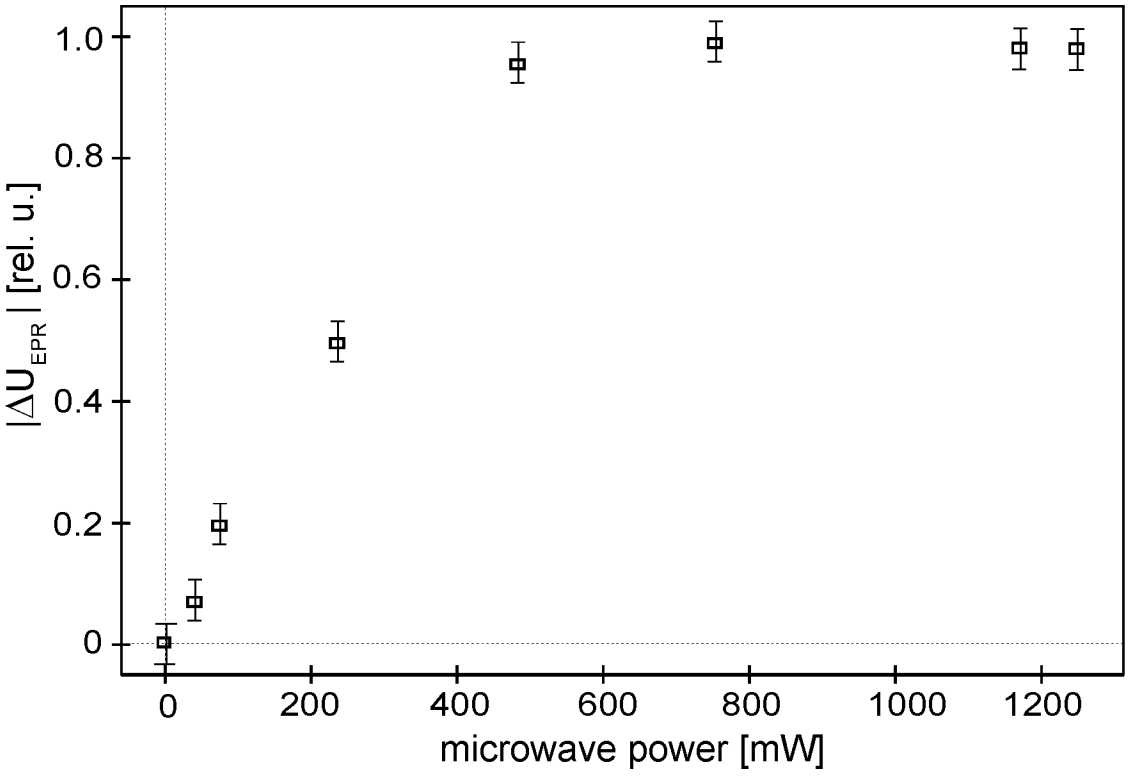

Figure 8.6: EDEPR signal intensity $|\Delta U_{EPR}|$ (in relative units) measured at T=6K and I=90μA as a function of the microwave power incident into the cavity. The circles show the experimental data, which are normalized to the maximal value.

8.2.2 Temperature dependence

We performed EDEPR measurements in a range of temperatures from 4.9 to 20K. We found that $|\Delta U_{EPR}|$ and thus $|\Delta \rho_{EPR}|$ grows with the reciprocal temperature, as shown in fig. 10.9. It shows the temperature dependence of the EDEPR signal measured at a microwave power of 200 mW. We see that it decreases by one order of magnitude in the temperature range 6-10K.

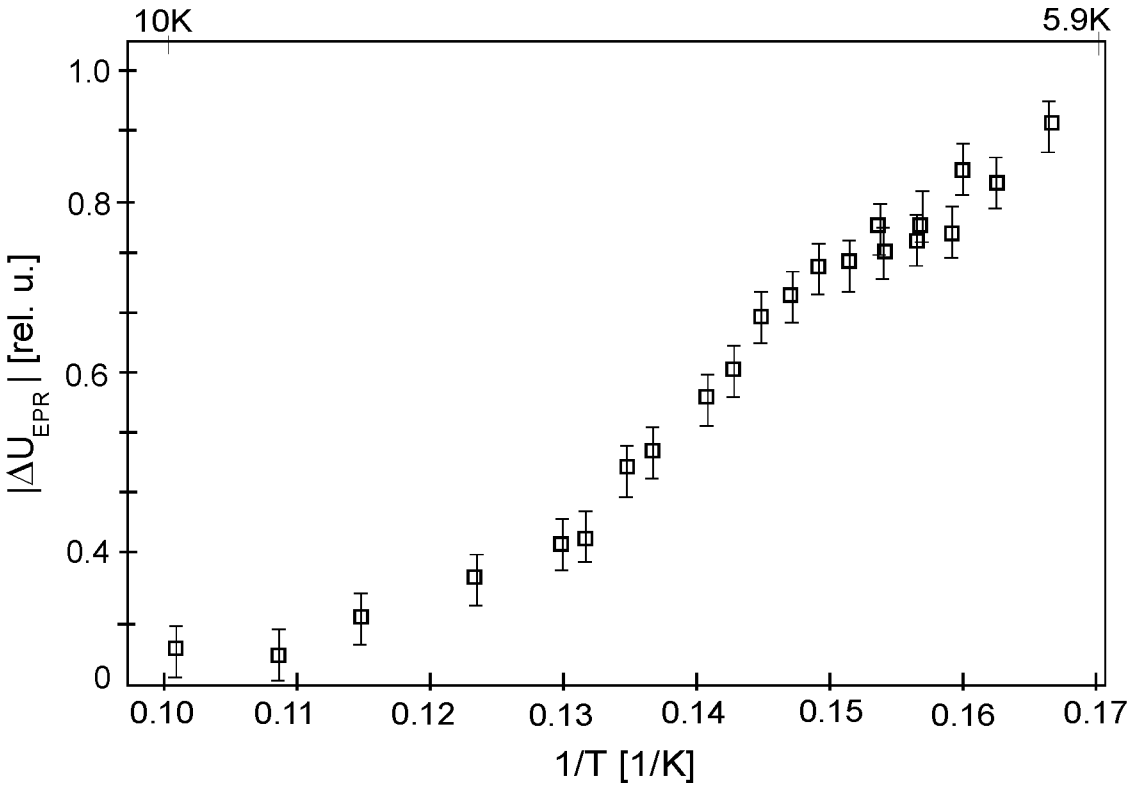

Figure 8.7: EDEPR signal intensity $|\Delta U_{EPR}|$ (in relative units) as a function of the inverse of the temperature. The squares show the experimental data measured at $P_{mw} = 0.2$W and I= 10μA. The EDEPR signal was detected as a voltage decrease at constant current conditions, the maximal value shown in the picture corresponds to a voltage change $\Delta U_{EPR} \approx -10^{-2}$V, and thus a resistance change ΔR_{EPR} of -10kΩ.

8.2.3 Modulation frequency dependence

The influence of the modulation frequency ω on the EDEPR signal is shown in fig. 8.8. The measurements were conducted at 7K and 200mW. The amplitude of the microwaves was modulated and the signal detected by using the lock-in technique. The modulation frequency was varied in the range of 100Hz to 50kHz. As can be seen in fig. 8.8, EDEPR works best for modulation frequencies in the range of 1 to 5kHz, in contrast to the conventional detection of EPR (optimum at about 100kHz). This behaviour has also been observed in the case of photo-EDEPR [Stich 96].

The experimental data for $\omega > 1kHz$ fit best to the following function:

$$|\Delta\rho| = \frac{|\Delta\rho_0|}{\sqrt{1 + w^2\tau^2}} \tag{8.2}$$

with $\tau = (1.6 \pm 0.2)$ms. A similar behaviour has been found for photo-EDEPR on amorphous and crystalline semiconductors [Brandt 92, Stich 96], and the obtained value for τ was interpreted as the carrier lifetime. In our case τ^{-1} would be expected to be related to the EPR-induced additional hopping.

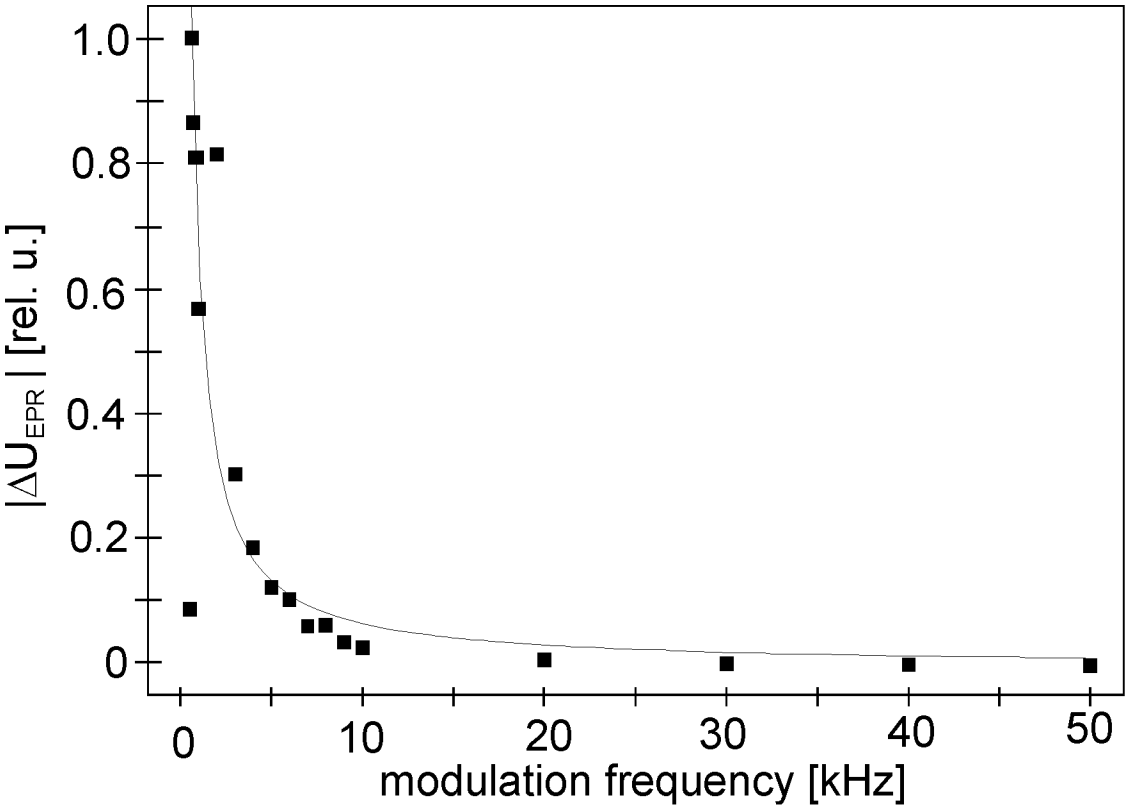

Figure 8.8: EDEPR signal intensity $|\Delta U_{EPR}|$ (in relative units) as a function of the modulation frequency. The microwaves amplitude was modulated with frequencies varying in the range 100Hz to 50kHz. The squares show the experimental data measured at P_{mw} = 0.2W, T=6K and I= 10μA. The EDEPR signal was detected as a voltage decrease at constant current conditions, the maximal value shown in the picture corresponds to a voltage change $\Delta U_{EPR} \approx -10^{-2}$V, and thus a resistance change ΔR_{EPR} of -10kΩ.

From the experimental data and with eq. (8.2) we obtain τ=1.6ms, $W_0 \equiv \tau^{-1} = (0.62 \pm 0.09)$kHz, which is too low for a hopping rate. Moreover, as noticed above,

the same dependence of the EDEPR signal on the modulation frequency with a similar characteristic time τ has been observed for different EDEPR-mechanisms, such as photo-EDEPR on lowly doped crystalline semiconductors and amorphous semiconductors. This fact indicates that the origin of the modulation frequency dependence may have a technical origin, since almost the same characteristic time has always been found for very different materials (crystalline and amorphous semiconductors; silicon, germanium and silicon carbide) and microscopical mechanisms (donor-acceptor recombination, EPR-induced hopping). As a matter of fact, we attribute the observed dependence of the EDEPR signal on the modulation frequency to the constraints of the current-voltage source. The experimental investigations quoted above [Brandt 92, Stich 96] as well as those presented in this work and shown in fig. were performed with a *Keythley* 237 d.c. current-voltage source. The time constant of this device does not allow to change the voltage faster than about 1kHz. As a result, the maximal EDEPR signal is always observed with a modulation frequency around 1kHz, even when the microscopical processes are much faster.

8.2.4 Current dependence

Figure 8.10 shows the experimentally found dependence of the EDEPR signal (measured as a voltage change at constant current conditions) on the electrical current. The resonant voltage decrease $|\Delta U_{EPR}|$ was found to increase linearly with increasing current, but the noise increased as well. As a result, the optimum lies around 50μA. The relative voltage change $|\Delta U_{EDEPR}/U|$, and thus the relative resistivity change $|\Delta\rho_{EPR}/\rho|$ increased as well with increasing current, growing from $\Delta\rho_{EPR}/\rho \approx -3.3 \cdot 10^{-3}$ for I=10μA to $\Delta\rho_{EPR}/\rho \approx -9.34 \cdot 10^{-3}$ for I=200μA. Nevertheless, we must be careful with the interpretation of the experimental data, since the behaviour of the signal with the applied current strongly depends on the sample preparation (quality of the contacts). As a consequence, the optimum current at a given temperature value must be searched for each sample separately.

One important point to be considered for the selection of the current value for EDEPR measurements was, however, always taken into account during the experiments: a current value was chosen, for which the contacts at a given temperature exhibited an ohmic behaviour. This was possible *in situ* in the EDEPR spectro-

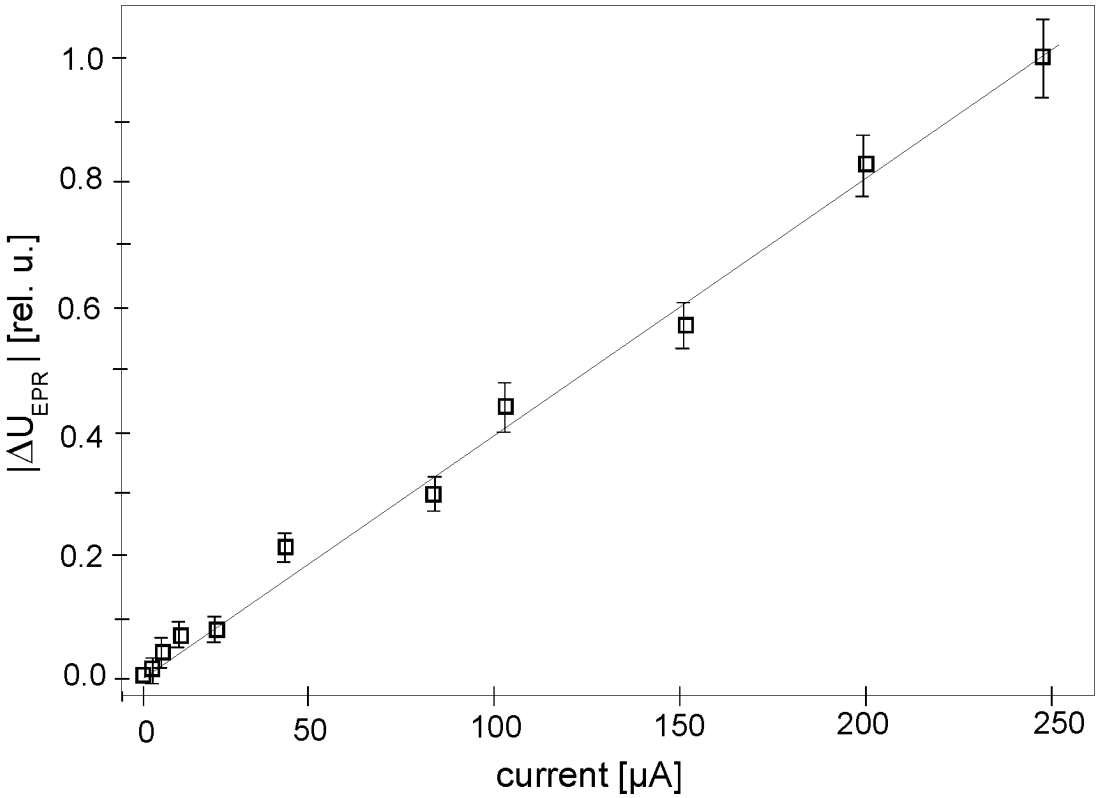

Figure 8.9: EDEPR signal intensity $|\Delta U_{EPR}|$ (in relative units) as a function of the applied current. The squares show the experimental data measured at $P_{mw} = 0.2$W and T=6K. The EDEPR signal was detected as a voltage decrease at constant current conditions, the maximal value shown in the picture corresponds to a voltage change $\Delta U_{EPR} = -0.26$V, with $U = 27.5$V.

meter.

8.2.5 EDEPR-Magnetoresistance

Figure 8.11 shows an EDEPR measurement conducted over a broad magnetic field range, measured at T=7K and I=4μA. The microwave amplitude was modulated with a frequency of 10kHz. The magnetic field was scanned from 0 to 500mT with a step of $\Delta B = 0.05$mT, and the voltage was recorded by making use of lock-in technique. In this spectrum we see both the indirectly detected magnetic field dependence of the microwave absorption ("non-resonant part"), as shown in chapter 7, subsection 4.1, and the EDEPR signal ("resonant part") shown in fig. 8.1.

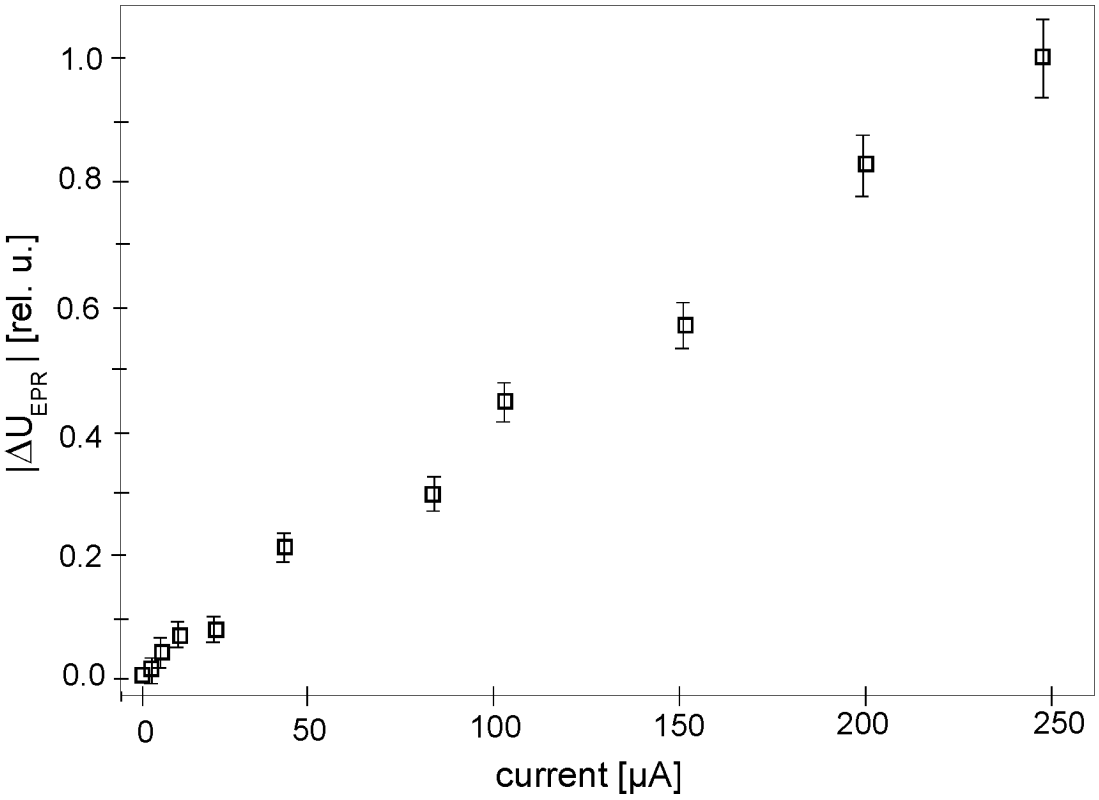

Figure 8.10: EDEPR signal intensity $|\Delta U_{EPR}|$ (in relative units) as a function of the applied current. The squares show the experimental data measured at $P_{mw} = 0.2$W and T=6K. The EDEPR signal was detected as a voltage decrease at constant current conditions, the maximal value shown in the picture corresponds to a voltage change $\Delta U_{EPR} = -0.26$V, with $U = 27.5$V.

In chapter 7 we had already shown the non-resonant part. The reason why the resonant signal (EDEPR signal) was not observed in such experiments is the fact that they were performed without lock-in technique. From the EDEPR d.c. experiment (section 8.1) and the magnetoresistance d.c. measurements under microwave irradiation (section 7.4.1), we see that the EDEPR effect is much smaller than the magnetic field dependence of the microwave absorption ($|\Delta\rho_{EPR}/\rho| \approx 10^{-3} \ll |\Delta\rho_B/\rho| \approx 10^{-1}$). For this reason we need either very long measurement times or the lock-in technique to see the EDEPR signal.

From fig.8.11 we see that the EDEPR signal corresponds to an additional resistivity decrease in a magnetic field region where the resistivity decreases with increasing magnetic field.

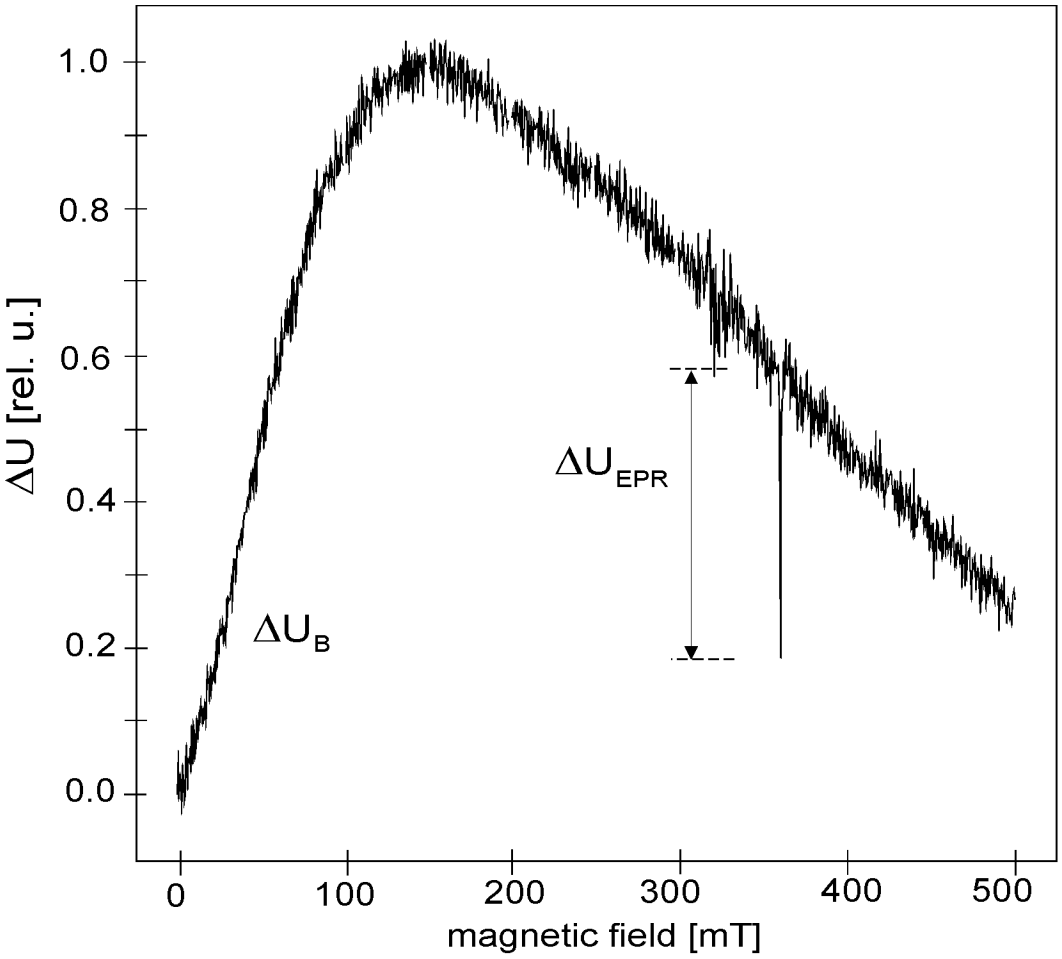

Figure 8.11: EDEPR experiment conducted on sample E1 over a broad magnetic field range, measured at T=7K, and I=4μA. The microwaves amplitude was modulated with a frequency of 10kHz. In this spectrum we see both the magnetic field dependence of the microwave absorption ("non-resonant part"), as shown in chapter 7, subsection 4.1, and the EDEPR signal ("resonant part") shown in fig. 8.1. The sample was orientated with its crystallographic c-axis perpendicular to the magnetic field.

8.3 EDEPR on compensated silicon samples

EDEPR on lightly doped semiconductors, specially silicon, has been extensively investigated. The concentration of possible D^0-A^0 pairs needed for the observation of an EDEPR signal was found to be in the range $10^{11} - 10^{14}\text{cm}^{-3}$ [Stich 96].

sample	N(B)/10^{15}cm^{-3}	N(P)/10^{15}cm^{-3}	annealing	source
s87db	5.5	1.0	no	P.I. Stuttgart
s87dd	5.5	1.0	yes	P.I. Stuttgart
s125e	24.0	1.0	yes	P.I. Stuttgart
s125f	24.0	1.0	no	P.I. Stuttgart

Table 8.1: List of investigated silicon samples.

We investigated compensated silicon bulk samples with concentrations of impurities which were higher than 10^{14}cm^{-3} and still lower than the concentrations for which hopping conductivity appears. None of the samples showed an EDEPR signal.

Chapter 9

Defect concentration effects

The concentration dependence of the EPR spectrum of nitrogen in the silicon carbide polytypes 4H and 6H has been studied by Veinger and Kalabukhova [Veinger 67, Kalabukhova 87] and Greulich-Weber [Greulich-Weber 97], respectively. Both polytypes were found to follow the same behaviour: with increasing nitrogen concentration the hyperfine splitting in the EPR spectra vanished and a new line with increasing linewidth and without hyperfine structure was generated. It has been discussed whether this behaviour can be attributed to the exchange interaction or to hopping between donor sites. In the first case, the disappearance of the hyperfine splitting and the line broadening would be caused by a delocalization of the unpaired electrons resulting from exchange interaction [Veinger 67]. In the second case, it would be the consequence of an averaging of the hyperfine interaction due to a fast hopping of the donor electrons between donor sites in different nuclear spin states [Kalabukhova 87]. EPR investigations using high microwave frequencies (142 GHz) [Kalabukhova 87] showed that at high nitrogen concentration one (4H-SiC) or two (6H-SiC) additional lines appear at fields between those of the hyperfine splitting lines of the quasicubic site donors. The authors pointed to hopping between hexagonal and quasicubic sites as the origin of the additional lines, but could not prove it.

In this work, the behaviour of the EDEPR signal for nitrogen concentrations varying in the intermediate range (the material is still non-degenerated, but the hyperfine splitting in the EPR signal begins to disappear) was studied and compared to the EPR signal behaviour of the same samples. Samples B3 and B4, which had a nitrogen concentration ($> 10^{19}\mathrm{cm}^{-3}$), i.e. beyond the critical concentration for metallic behaviour, showed no EDEPR signal.

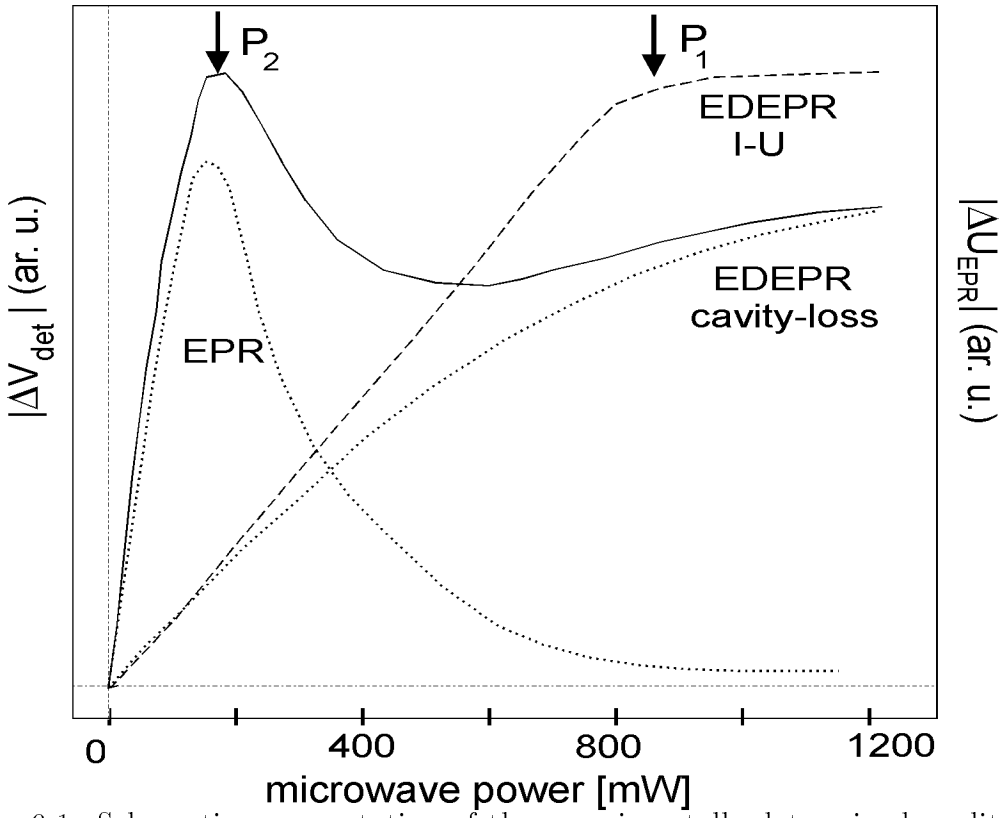

Figure 9.1: Schematic representation of the experimentally determined qualitative behaviour of the signal amplitudes of both the EDEPR-spectrum shown in fig. 8.1 and the corresponding EPR spectrum with microwave power. The dashed line shows the behaviour of the EDEPR signal measured as a resonant voltage decrease $|\Delta U_{EPR}|$ at constant current conditions. The full line shows the behaviour of the absorption signal of the microwave bridge ΔV_{det}. It is striking that it doesn't show the typical saturation behaviour. This can be explained as follows: the "absorption" signal is composed of two contributions: the pure microwave absorption signal (EPR, dotted line) and the signal arising from the cavity losses (cavity-loss detected EDEPR, dotted line). The absorption signal from the microwave bridge ΔV_{det} as well as the EDEPR signal obtained by I-U measurements ΔU_{EPR} (dashed line) are determined experimentally. The saturation behaviour of the EPR signal can be deduced from the microwave power dependence of the other two. P_1 and P_2 denote the microwave power levels for which the EDEPR signal and the EPR signal reach a maximum, respectively. The behaviour outlined in this figure is observed only for low temperatures, at higher temperatures the contribution of the EDEPR signal to the "absorption" signal becomes negligible and the typical saturation behaviour is observed.

9.1 Dependence of the EPR/EDEPR signal on microwave power

The microwave power dependence of both EDEPR and conventionally detected EPR was studied for different samples and different temperatures. The EDEPR signal could be recorded as a change in the sample voltage at constant current conditions for samples E1 and B1, the electrical contacts of which were ohmic. The EPR signal cannot be directly obtained by detecting the "absorption" signal of the microwave bridge, since there are further contributions to the latter signal. As stated in chapter 4, EDEPR can be detected by recording the current-voltage characteristics as well as detecting the signal from the microwave bridge ("cavity detected-EDEPR"). The reason is that a resistivity change of the sample causes a change in the quality factor of the cavity, affecting the microwave bridge-signal. As shown in chapter 4, the voltage change at the microwave detector induced by a resistivity change of the sample is given by $\Delta U_{det} \propto \Delta\sigma\sqrt{P_{mw}} \propto -\Delta\rho\sqrt{P_{mw}}$ (see eq. (4.8)). Therefore, there are two contributions to the microwave-bridge signal: one arising from EPR, the other from EDEPR.

Thus, we expect to find a non negligible contribution from EDEPR to the "absorption" signal of the microwave bridge for highly doped samples exhibiting a large EDEPR effect. As a matter of fact, we found that the "absorption" signal ΔU_{det} did not exhibit the saturation behaviour typical for EPR. We found that the "absorption" signal is still rather large for very high microwave power levels (see fig. 9.1). The experimental behaviour varied with temperature and nitrogen concentration. A behaviour of the microwave "absorption" signal as shown in fig. 9.1 was found at low temperatures for high nitrogen concentrations.

The EDEPR signal was measured as a resonant voltage decrease ΔU_{EPR} at constant current conditions. Therefore, it cannot be compared quantitatively to the microwave "absorption" signal. The fact that the latter signal does not show the typical saturation behaviour at temperatures and donor concentrations for which the EDEPR signal is particularly large, however, points to the interpretation illustrated in fig. 9.1, namely a nonnegligible contribution from the EDEPR-induced cavity loss to the microwave-absorption signal.

As shown in chapter 4, section 4, the signal amplitude at the microwave detector is composed of two terms, the first arises from the magnetic losses (EPR), the second comes from the dielectric losses (quality-factor detected EDEPR):

$$\Delta V_{det} = -Q\chi''\eta\sqrt{P_{mw}} - Q\frac{\Delta\sigma\alpha}{\varepsilon_0 2\pi\nu_{mw}}\sqrt{P_{mw}} \tag{9.1}$$

As to the EPR component, when the derivative of the EPR signal voltage is measured, one obtains for the maximal EPR signal amplitude as a function of the microwave power P_{mw}:

$$\Delta V_{det}(EPR) = c\left(\frac{1}{1+c'P_{mw}}\right)^{3/2}\sqrt{P_{mw}} \tag{9.2}$$

Thus, for low microwave power levels ΔV_{det} grows strongly with $\sqrt{P_{mw}}$, reaches a maximum and decreases hyperbolically as $1/P_{mw}$ for high values of the microwave power, as illustrated in fig. 9.1 (EPR, dotted line). At high microwave power the occupation of the states involved in the EPR transitions becomes equalized, and therefore the net microwave absorption approaches zero.

The EDEPR signal amplitude, i.e. the resistivity decrease at resonance $|\Delta\rho_{EPR}|$ grows linearly with microwave power up to a certain power P_1 and keeps then constant, as illustrated in fig. 9.1. As shown in chapter 8, section 2, it can be written as:

$$\Delta\rho_{EPR} \propto -\frac{c_1 P_{mw}}{1+c_1 P_{mw}} \tag{9.3}$$

As to the contribution from EDEPR to the signal at the microwave detector, from equations (9.3) and (9.1) we obtain:

$$\Delta V_{det}(\text{EDEPR}) \propto -\Delta\sigma_{EPR}\sqrt{P_{mw}} = \frac{\Delta\rho_{EPR}}{\rho^2}\sqrt{P_{mw}} \propto -\frac{c_1 P_{mw}}{1+c_1 P_{mw}}\sqrt{P_{mw}} \tag{9.4}$$

Therefore, whereas the EDEPR signal measured as a voltage change at constant current conditions grows linearly with microwave power for $P_{mw} \leq P_1$, the quality-factor detected EDEPR $\Delta V_{det}(\text{EDEPR})$ grows as $P_{mw}^{3/2}$, as illustrated in fig. 9.1.

Figure 9.2 shows the experimental EDEPR signal intensity (a) and the EPR signal intensity (b) of sample E1 as a function of the microwave power incident on the cavity. The measurements were conducted at different temperatures. The size of the EDEPR signal decreases with growing temperature $\Delta\rho_{EPR}(7K) > \Delta\rho_{EPR}(9K) >$

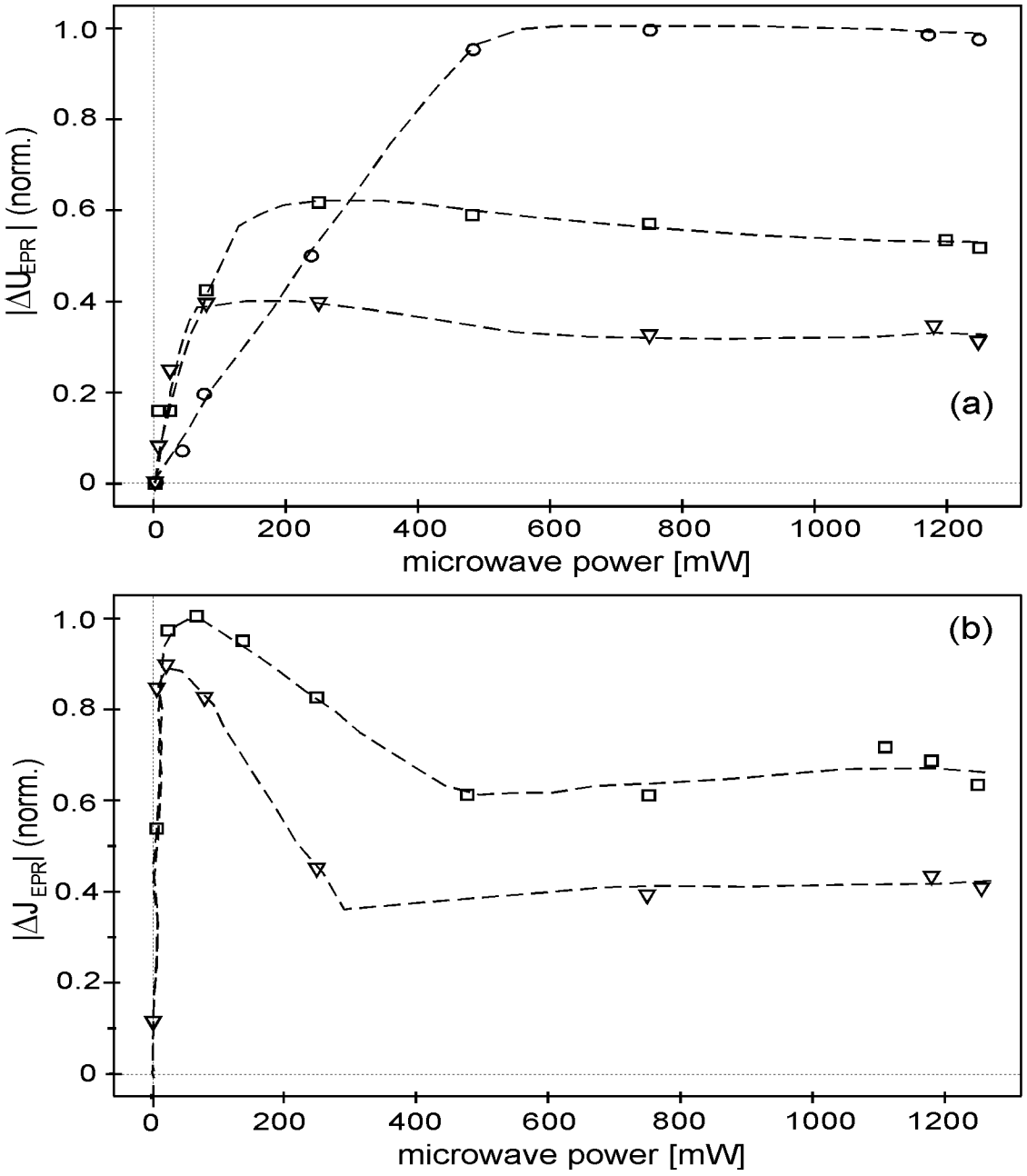

Figure 9.2: (a): Microwave power dependence of the EDEPR signal of sample E1 measured as a voltage decrease $|\Delta U_{EPR}|$ at constant current conditions. (b): Microwave power dependence of the microwave "absorption" signal $|\Delta J_{EPR}|$ of sample E1. The experimental data were obtained at T=6K ($\circ$) T=9K ($\sqcap$) and T=13K ($\bigtriangledown$).

$\Delta\rho_{EPR}(13K)$ As shown in fig. 9.2(a), the intensity of the EDEPR signal reaches its maximum value for a microwave power P_1 = 80mW, 250mW and 750mW at a temperature of 13K, 9K and 6K, respectively. These microwave power levels are two or three orders of magnitude higher than those usually required for conventional detection of EPR. For higher microwave power levels, $P_{mw} > 800$mW, the EDEPR signal decreases slightly. For such high powers, however, non-linear effects may play a role. As shown in fig. 9.2(b), the intensity of the EPR signal reaches a maximum at low microwave power levels, decreases, grows again and finally keeps constant with increasing microwave power.

In the case of sample B1, which has a lower nitrogen concentration than sample E1, the EDEPR signal is very small and does not affect appreciably the absorption signal. As a result, the microwave-bridge signal exhibits the saturation behaviour typical for EPR, as shown in fig. 9.3.

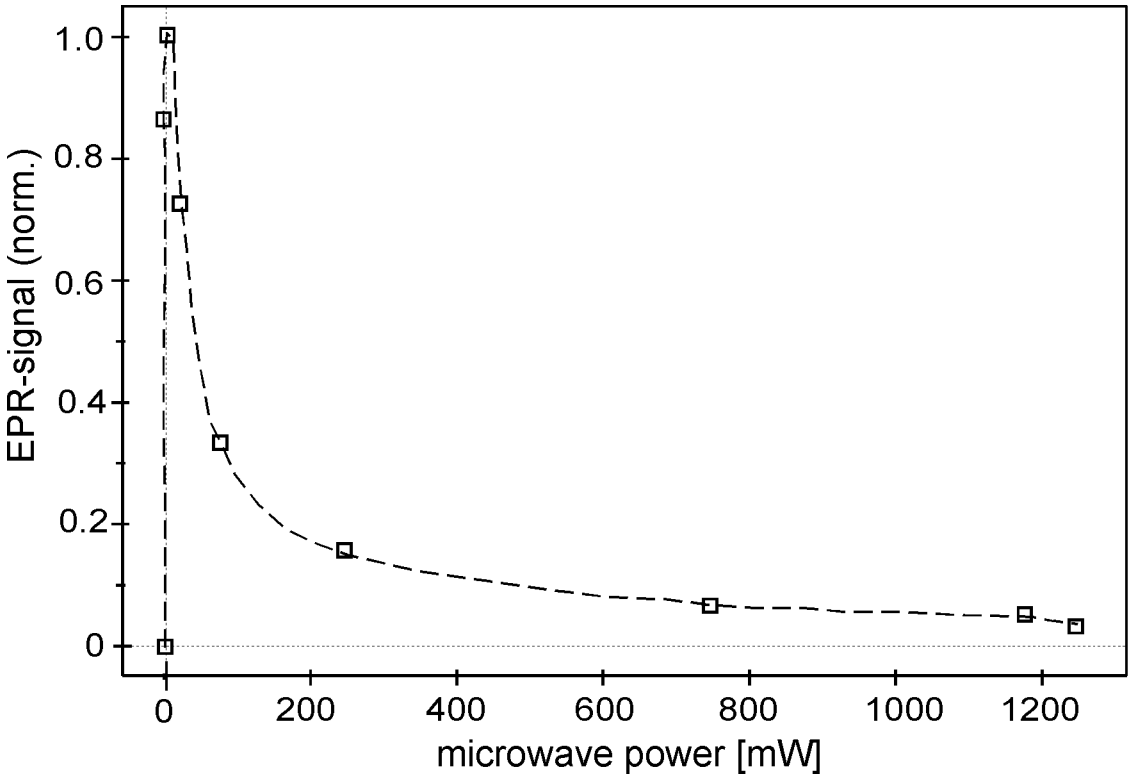

Figure 9.3: Saturation behaviour of the EPR signal of sample B1 at T=15K.

The "cavity-detected" EDEPR is advantageous when the sample lacks good oh-

mic contacts. As reported in chapter 5, the technique of producing good electrical contacts for silicon carbide must still be developped further. In our case, the contacts on the more lightly doped samples (B1 and B2) were not completely ohmic or exhibited a considerable noise at low temperatures, making the direct detection of EDEPR difficult.

9.2 Additional EPR lines

Figure 9.4 shows the nitrogen EPR spectrum (conventionally detected) of sample B1 (bulk 6H-SiC with a nitrogen concentration of $2.5{\cdot}10^{18}\mathrm{cm}^{-3}$ and a concentration of compensating centres of $0.9{\cdot}10^{18}\mathrm{cm}^{-3}$, thus at low temperatures all hexagonal site donors and some of the quasicubic site donors will be ionized, whereas the rest of quasicubic site donors will be occupied) measured in the dark, T=20K and P_{mw} = 2.5mW. It shows the hyperfine splitting of the two quasicubic sites, which cannot be distinguished from each other. Furthermore, we see two additional lines, situated exactly in the middle between the nitrogen hyperfine lines of the quasicubic sites. Such additional lines have been reported before. There has been controversy about their origin. There were two attempts for their explanation. Some authors (e.g. [Maier 91]) attributed the additional lines to quasi-forbidden transitions with $\Delta m_s = \pm 1$, $\Delta m_I = \pm 1$. A second possible explanation was that the resonance lines are caused by nitrogen pair defects [Veinger 67]. However, there were so far no further indications from other experiments that would point to the existence of such nitrogen pairs.

Figure 9.5 shows the angular dependence of the EPR signal of sample B1 measured in the dark at a temperature of 9K and a microwave frequency of 10.02GHz. The dotted-dashed lines show the angular dependence of the EPR spectrum of nitrogen at the quasicubic sites. Between the three hyperfine lines arising from the nuclear spin I=1 of ^{14}N two further lines appear. The EPR spectrum of the nitrogen donor at the hexagonal lattice site is not observed, since the Fermi level lies near the energy level of nitrogen at the quasicubic sites, as shown in chapter 7, section 1. Besides the lines arising from the nitrogen donors, another line is observed (dashed line), exhibiting a larger anisotropy and with $g_{||}$ = 2.006. The signal amplitude diminishes when the c-axis of the sample is rotated away from the magnetic field

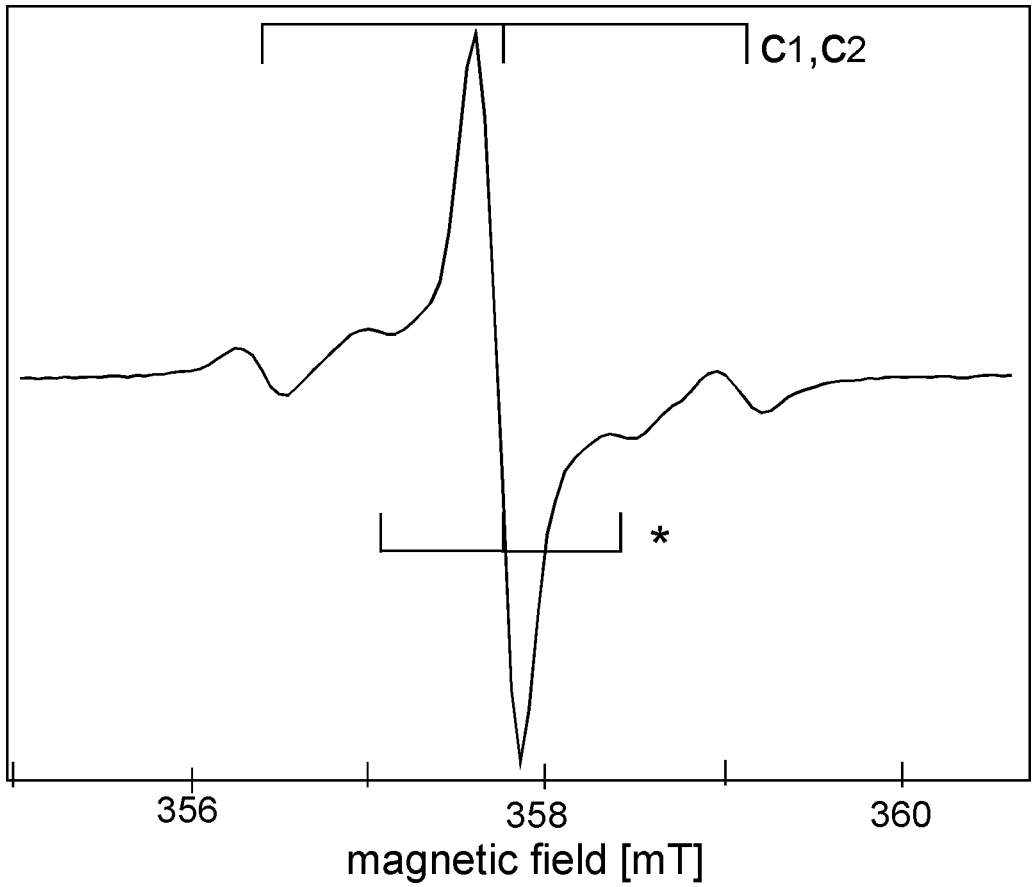

Figure 9.4: EPR spectrum of nitrogen in 6H-SiC (sample B1) showing additional lines (*) measured in the dark at ν_{mw} = 10.02GHz, T=20K, P_{mw} = 2.5mW.

direction. We observe that the two additional lines denoted in fig. 9.4 with (*) follow exactly the same angular dependence as the hyperfine lines of the nitrogen donor at the quasicubic sites. This fact strengthens the argument that these lines arise from the quasicubic site nitrogen donor.

In chapter 7 we have shown that the conductivity of sample B1 at low temperatures is dominated by hopping of electrons among nitrogen donors. Therefore, the appearance of additional EPR lines could be attributed to hopping between nitrogen donors. In this picture, an electron can be localized at one donor or hop between two or more donors to and fro. For the derivation of the resulting EPR spectrum, we can make an analogy to the case of tumbling complexes in low viscosity liquids or gases, where either a powder spectrum or an average of the orientation-dependent terms of the spin-Hamiltonian is obtained (*motional averaging*), depending on the

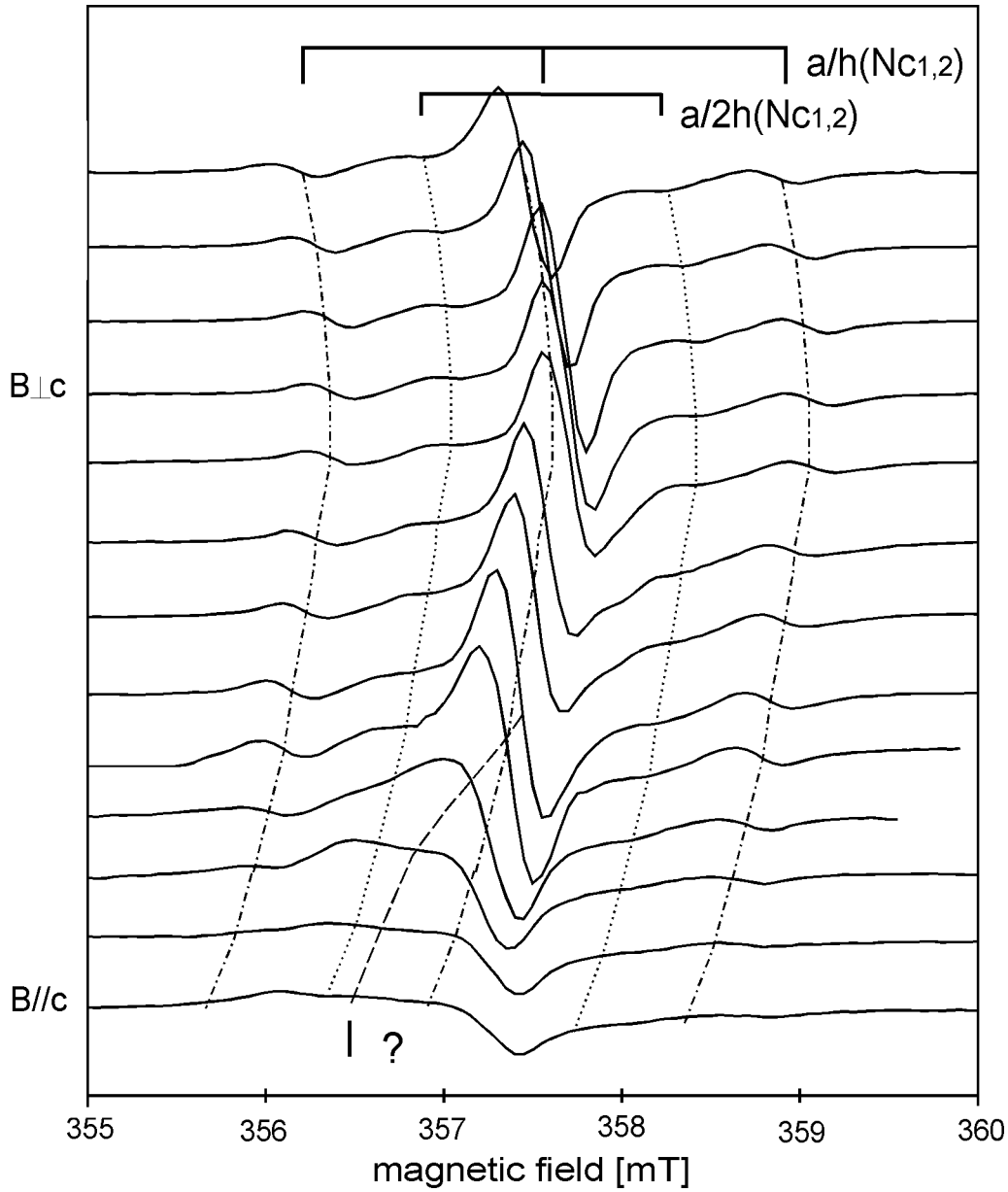

Figure 9.5: EPR angular dependence of sample B1 measured in the dark at 9K and 10.02 GHz. We observe the EPR spectrum of the nitrogen donor with a hyperfine splitting of 1.18mT characteristic for the quasicubic sites in 6H-SiC (dotted-dashed lines) together with an EPR line showing a higher anisotropy (dashed line). In addition to the nitrogen lines, two further EPR lines where found situated exactly in the middle of the nitrogen hyperfine lines.

tumbling rate (see e.g. [Pake 73]). In our picture we expect to obtain different EPR spectra depending on the hopping rate ν_h as compared to the hyperfine in-

teraction constant in frequency units. The hyperfine interaction for the nitrogen donor at the quasicubic lattice sites is $a/h \approx$33MHz for 6H-SiC, $a/h \approx$51MHz for 4H-SiC, the anisotropic contribution being negligible (see table 5.3). The hyperfine interaction for the hexagonal sites is much smaller, and is usually not resolved in the EPR spectra. Therefore, if there are electrons hopping between nitrogen donors at quasicubic lattice sites, the obtained EPR spectra will differ from the static EPR spectrum, depending on ν_h as compared to 50MHz.

In the case of slow hopping ($\nu_h \ll$ 50MHz), the EPR spectrum observed will be that associated with the instantaneous state at the moment of observation. For an electron hopping between donors i and j this means that the hyperfine interaction observed will be that with either nuclear spin I_i or nuclear spin I_j. As a result, no additional EPR lines should arise from a slow hopping. In the case of fast hopping ($\nu_h \gg$ 50MHz), however, a spectrum will be obtained in which the hyperfine term has its average value. In this picture, additional EPR lines as shown in fig. 9.4 are expected. Since the electron can hop between a donor i with a nuclear spin state $m_I(i) = \pm 1$ and a donor j with a nuclear spin state $m_I(j) = 0$, the average of the hyperfine interaction term leads to EPR lines corresponding to a half of the hyperfine interaction, provided the time spent by the electron at site i is equal to the time spent at site j. Nevertheless, this picture is only valid for a hopping which is fast compared to the hyperfine interaction but slow compared to the EPR transition rate: 50MHz$\ll \nu_h \ll \nu_{EPR}$. If the hopping rate is comparable to or larger than the EPR rate only the central line of the triplet will be observed.

When assuming that the hopping rate satisfies 50MHz$\ll \nu_h \ll \nu_{EPR}$ and that all nitrogen donors at hexagonal lattice sites and a part of the donors at quasicubic lattice sites are ionized, the resulting EPR spectrum will be given by a superposition of that shown in fig. 9.6b, c, or d (for electrons hopping between 2, 3 or 4 donors to and fro, respectively) and the "normal" EPR spectrum of the nitrogen donor at a quasicubic lattice site (fig. 9.6a). As noticed in chapter 2, the isotropic part of the hyperfine interaction a is proportional to the spin density at the nucleus $|\phi(0)|^2$. In a simplified picture, we can say that if the electron hops between a donor i and a donor j, it will remain a certain time t_i at donor i, leading to a spin density $|\phi(0)|^2(i)$ at nucleus i and a certain time t_j at donor j, leading to a spin density $|\phi(0)|^2(j)$ at nucleus j. The hyperfine interaction will be given by $\vec{\mathbf{S}} \cdot \underline{\underline{A}} \cdot \vec{\mathbf{I}}(i)$ during a time t_i and

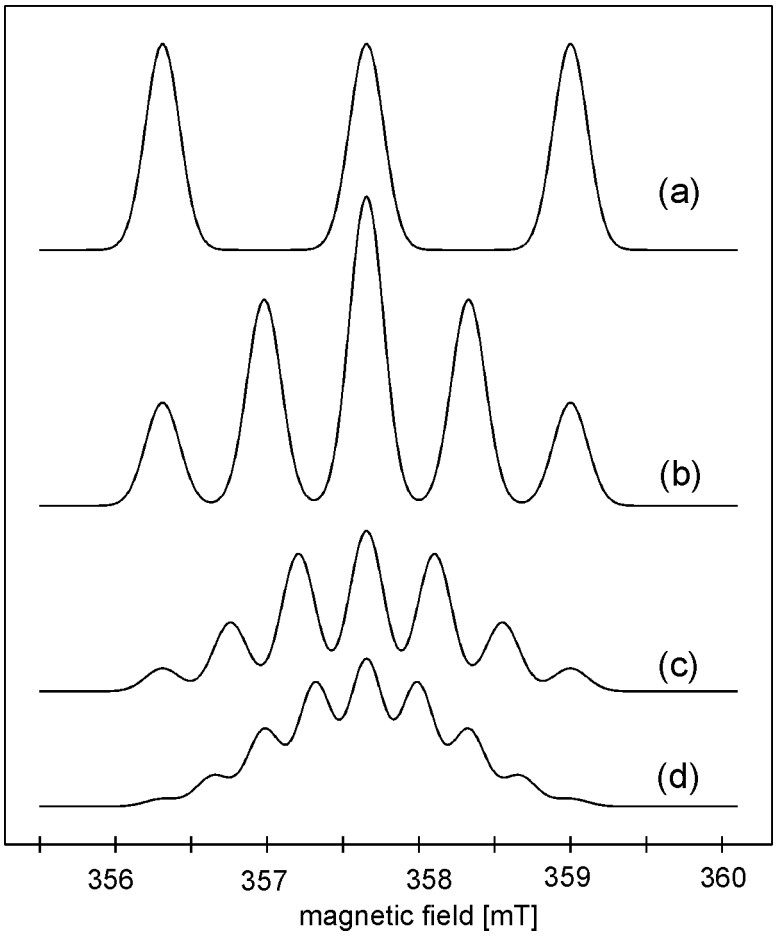

Figure 9.6: Simulated X-band EPR spectra of the nitrogen donor at a quasicubic lattice site in 6H-SiC for the static case (a), and for donor electrons hopping between two (b), three (c) or four (d) donors with a frequency 50MHz$\ll \nu_h \ll \nu_{EPR}$ (see text).

by $\vec{\mathbf{S}} \cdot \underline{\underline{A}} \cdot \vec{\mathbf{I}}(j)$ during a time t_j. Generally, $t_i \neq t_j$, because the electron will spend a longer time in the energetically most favourable state. But the states between which hopping at low temperatures takes place are almost equal in energy, therefore $t_i \approx t_j$.

In first degree of approximation we obtain for the hyperfine interaction term of the spin Hamiltonian $am_s m_I(i)$ during a half of the time and $am_s m_I(j)$ during the other half. Since the nuclear spin of ^{14}N (99.4%) is I=1, there are different possible configurations for the nuclear spin states of i and j, $(m_I(i), m_I(j))$, namely (-1,-1), (-1,0), (-1,1), (0,-1), (0,0), (0,1), (1,-1), (1,0) and (1,1). For the configuration (1,0), for in-

stance, the motional averaging leads to an hyperfine term $am_s\frac{m_I(i)+m_I(j)}{2} = \frac{1}{2}am_s$ and thus to such an additional EPR line as observed in sample B1 (see fig. 9.4). We can illustrate the effect of motional averaging by saying that the electron feels an "averaged nuclear spin", which is given by $m_{Iav} = (m_I(i) + m_I(j))/2$, i.e. $m_{Iav} = \pm 1, \pm 1/2, 0$ with a relative weight of 1, 2 and 3, respectively. This leads to two additional EPR lines showing half of the hyperfine structure, as e.g. in the spectrum shown in fig. 9.4. Analogous arguments can be given for an electron hopping between three or more donors. Figure 9.6 shows the simulated EPR spectra of nitrogen at a quasicubic site in 6H-SiC together with simulated EPR spectra for the case of an electron hopping between 2, 3 and 4 donors, respectively. As we can see in the picture, all configurations contribute to the central EPR line corresponding to $m_I = 0$. This would contribute to the larger amplitude of the central line as compared to the $m_I = \pm 1$ hyperfine lines. A futher contribution to the central line would be due to the faster hopping electrons, with hopping frequencies comparable to the EPR transition rate. The simulations shown in fig. 9.6 are based on the assumption that hopping takes place between nitrogen donors at quasicubic sites (N(c)), i.e. for a situation where the Fermi level lies near the energy level of the nitrogen donor at a quasicubic lattice site, as is the case of sample B1.

If hopping takes place between donors at hexagonal sites (N(h)), as for sample E1, new EPR lines will also appear at fields between those of the hyperfine splitting of the hexagonal site nitrogen donor. However, since the hyperfine interaction of the N(h) donor is much smaller, we will not be able to distinguish these additional lines.

Thus, we can interpret the EPR spectrum of sample B1 shown in fig. 9.4 as the result of the addition of the spectrum of donor electrons hopping between two quasicubic sites (let us denote the corresponding concentration with N_{2c}) and the spectrum of the singly occupied nitrogen donors at quasicubic lattice sites (with a concentration given by N_c), with relative intensities N_{2c}/N_c. Moreover, the electrons hopping with a rate ν_h which is not much smaller than the EPR transition rate (let us denote the corresponding concentration with N_f) will only contribute to the central line of the triplet. There is also a contribution to the linewidth arising from exchange interaction. From the intensities of the additional lines relative to the $m_I = \pm 1, 0$ hyperfine lines the quotients N_{2c}/N_c and N_c/N_fcan be determined. As we can see in fig. 9.6(a) and 9.6(b), the singly occupied donors contribute to the central line

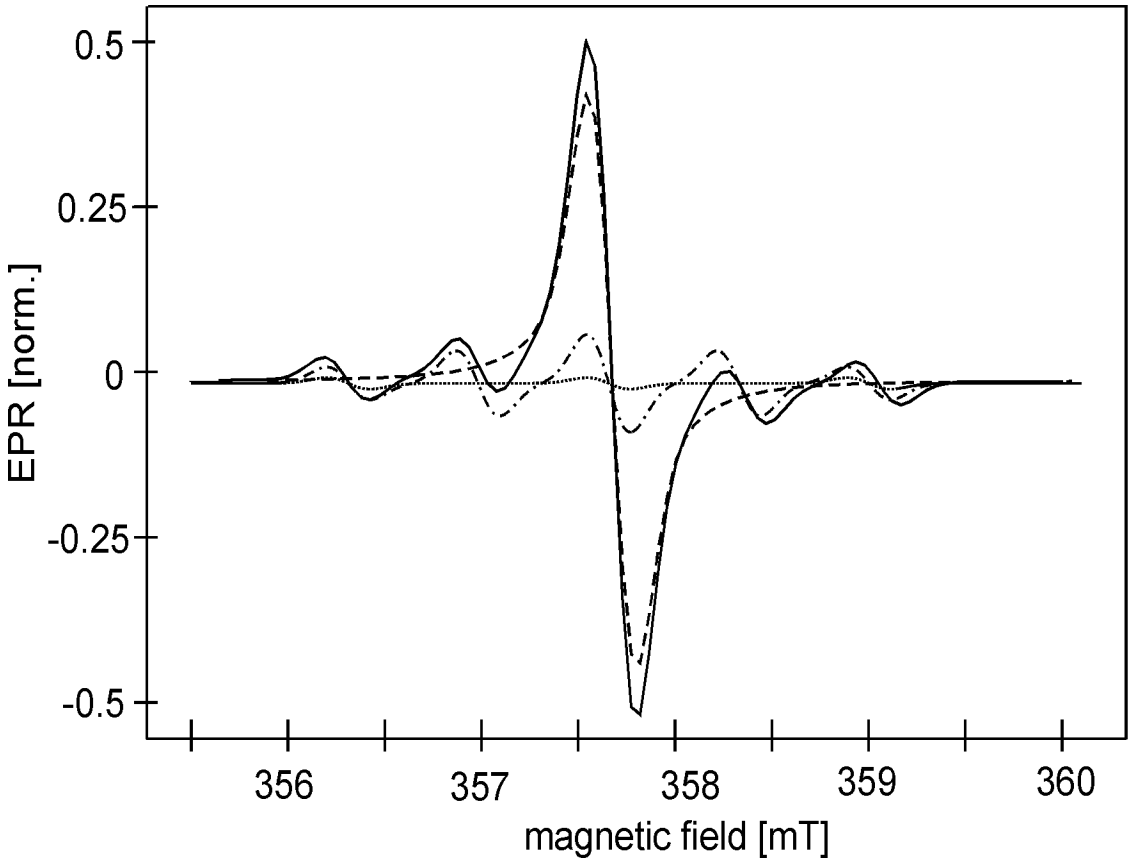

Figure 9.7: Simulated EPR spectrum of nitrogen in 4H-SiC (full line) showing additional lines. The dotted line, the dotted-dased line and the dashed line correspond to the simultaed EPR spectra for the single donors (N_c), donor pairs (N_{2c}) and fast hopping donor electrons (N_f), with relative concentrations N_{2c}/N_c=3.8 and N_f/Nc=66.

and the ± 1 lines with a ratio 1:1, whereas the donor electrons hopping between two donors contribute to the central line, the $\pm 1/2$ lines and the ± 1 lines with a ratio 3:2:1 and the fast hopping electros contribute only to the central line. By analysing the relative intensities of the different lines of the experimental spectrum we obtain: $N_{2c}/N_c = 3.8$ and N_f/N_c=66. Figure 9.7 shows an EPR spectrum simulated with these relative concentrations. For the spectrum arising from the fast hopping electrons an EPR line with 50% Gaussian and 50% Lorentzian character was simulated, for the other cases Gaussian lines were used.

The EPR spectrum of sample B2 (4H-SiC bulk material with a lightly higher nitro-

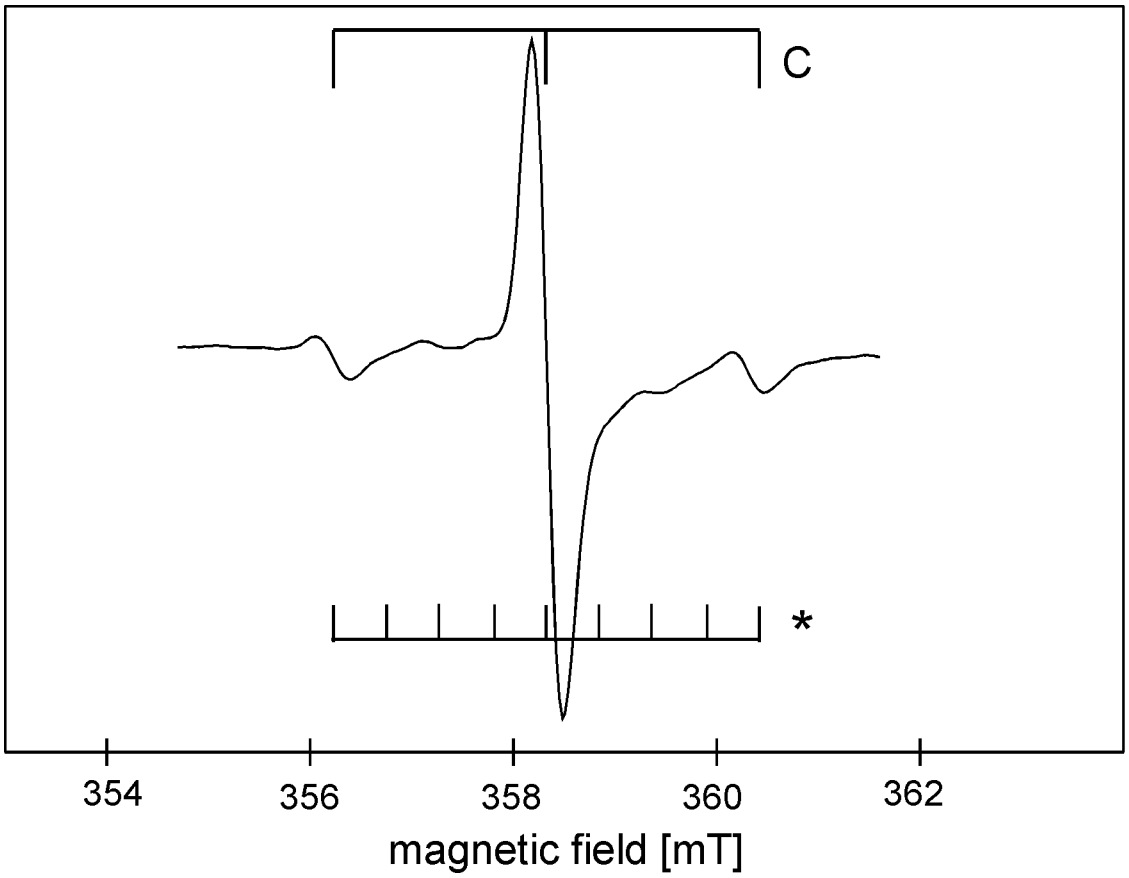

Figure 9.8: EPR spectrum of nitrogen in 4H-SiC (sample B2) showing additional lines (*) corresponding to 1/4, 1/2 and 3/4 of the hyperfine interaction, measured in the dark at ν_{mw} = 10.02GHz, T=6K, P_{mw} = 8mW.

gen concentration) showed not two, but six additional lines (see fig. 9.8) corresponding to a fourth, a half and three fourths of the hyperfine interaction, respectively. This corresponds to a situation where a donor electron hopps between four N(c) donors. In this case, the averaged nuclear spin felt by the electron will be given by $m_{Iav} = \pm 1, \pm 3/4, \pm 1/2, \pm 1/4$ and 0 with a relative weight of 1, 4, 10, 16 and 19, respectively. This leads to an EPR spectrum as shown in fig. 9.6d, which will add to the "normal" EPR spectrum of the nitrogen donor (fig. 9.6a). Sample B2 could not be studied by means of temperature dependent Hall or resistivity measurements, due to the bad behaviour of the electrical contacts at low temperatures. As a result, we could'nt determine the concentration of compensating impurities or the average activation energy for hopping. Nevertheless, from the EPR spectrum shown in fig. 9.8 we can say that at low temperatures hopping occurs among quasicubic site donor states. Thus, at low temperatures all hexagonal site donors and some qua-

sicubic site donors are ionized. Therefore, the concentration of acceptors is larger than the concentration of nitrogen at the hexagonal sites, as for sample B1. From the experimentally determined intensities of the additional hyperfine lines relative to the $m_I = \pm 1, 0$ lines the concentration of electrons shared by four donors can be calculated. If N_{4c} denotes the concentration of electrons hopping between four donors and N_c the concentration of singly occupied donors in quasicubic sites, then we obtain N_{4c}/N_c=0.45. Moreover, there are further donors hopping fast, therefore contributing only to the central line with a relative concentration N_f, N_f/N_c=16.

As reported above, the existence of two additional EPR lines between the N(c) hyperfine lines led to the discussion about their origin. These two lines could be attributed to quasiforbidden EPR transitions with $\Delta m_s = \pm 1$, $\Delta m_I = \pm 1$ as well as to donor pairs. The measured spectrum shown in fig. 9.8, however, cannot be explained with quasiforbidden EPR transitions. Quasiforbidden EPR transitions with $\Delta m_s = \pm 1$, $\Delta m_I = \pm 1$ would lead to two additional lines situated in the middle of the hyperfine lines, quasiforbidden transitions with $\Delta m_s = \pm 1$, $\Delta m_I = \pm 2$ would just make a contribution to the central line of the triplet. Thus, the only possible explanation for the appearance of the six additional lines is that some of the donor electrons are shared by four nitrogen donors. This leads to an EPR spectrum as shown in fig. 9.6d superimposed on the single-nitrogen spectrum.

To date the origin of the additional lines has been discussed without performing an electrical characterization of the studied samples. As presented in chapter 7, we have determined the concentration of nitrogen and compensating centres and identified hopping conductivity as the dominating charge transport mechanism at low temperatures. Sample B1 as well as sample B2 were studied with electrical methods. Their nitrogen concentration was found to lie in the concentration range where hopping conduction is expected to occur. Both samples are partially compensated. From the experimentally determined temperature dependence of the resistivity of sample B1 we showed that hopping dominates indeed the conductivity at low temperatures. The EDEPR spectrum of sample B1 (see fig. 8.3) shows, despite broadening, the hyperfine triplet and the two additional lines. Thus, from the electrical investigations together with the appearance of additional lines corresponding to 1/4, 1/2 and 3/4 of the hyperfine interaction, we can conclude that the additional EPR lines arise from a donor-electron hopping among two or more nitrogens.

Chapter 10

EDEPR Mechanism

As shown in chapter 8, the EDEPR effect studied in highly doped (but still showing semiconduting behaviour) crystalline n-type silicon carbide corresponds to a resonant resistivity decrease and is a large effect: a relative effect up to $\Delta\rho/\rho \approx -10^{-2}$ has been measured. In this section the relevant experimental results presented in the previous sections are discussed in terms of the microscopical processes reponsible for the EDEPR signal. In chapter 4, section 4.2, we described different EDEPR mechanisms reported in the literature: spin-dependent scattering, spin-dependent donor-acceptor recombination, triplet recombination, anomalous hopping and EPR-energy transfer. We propose a further mechanism, namely a heating of the electrons at resonance conditions. Now we will discuss the ability of the different models to describe the experimental findings.

As shown in chapter 7, samples E1, B1 and B2 were highly doped but still showed semiconducting behaviour. The EDEPR measurements were performed in the dark, and the signal diminished when the sample was illuminated. In addition to it, the EPR transitions induce a resistivity *decrease*. These facts exclude the donor-acceptor recombination, the triplet recombination and the spin-dependent scattering as possible mechanisms for EDEPR on highly doped crystalline SiC, since these processes occur under illumination and lead to a resistivity *increase* at resonance conditions, as noticed in chapter 4.

Electrical investigations showed that hopping is the dominant charge transport mechanism at the low temperatures where an EDEPR signal is observed. Two EDEPR mechanisms have been reported before, which were able to explain the resonant

resistivity decrease found in the hopping regime in amorphous silicon and germanium and crystalline silicon and germanium, respectively. These mechanisms are, as mentioned in chapter 4, the anomalous hopping model and the EPR-energy transfer. The former was proposed for the explanation of EDEPR results in amorphous silicon and germanium and corresponds to a situation where singly and doubly occupied states are present. In this picture a hop to an occupied state is only possible if the electron spins are antiparallel to each other. EPR transitions transfer electron pairs with parallel spins to an antiparallel state, inducing an increase of the hopping rate and therefore a resistivity decrease [Movaghar 78a]. In the samples studied in this work hopping takes place among nitrogen states, which can be either unoccupied or singly occupied. As a consequence, this mechanism is out of the question for the explanation of the EDEPR effect investigated in this work.

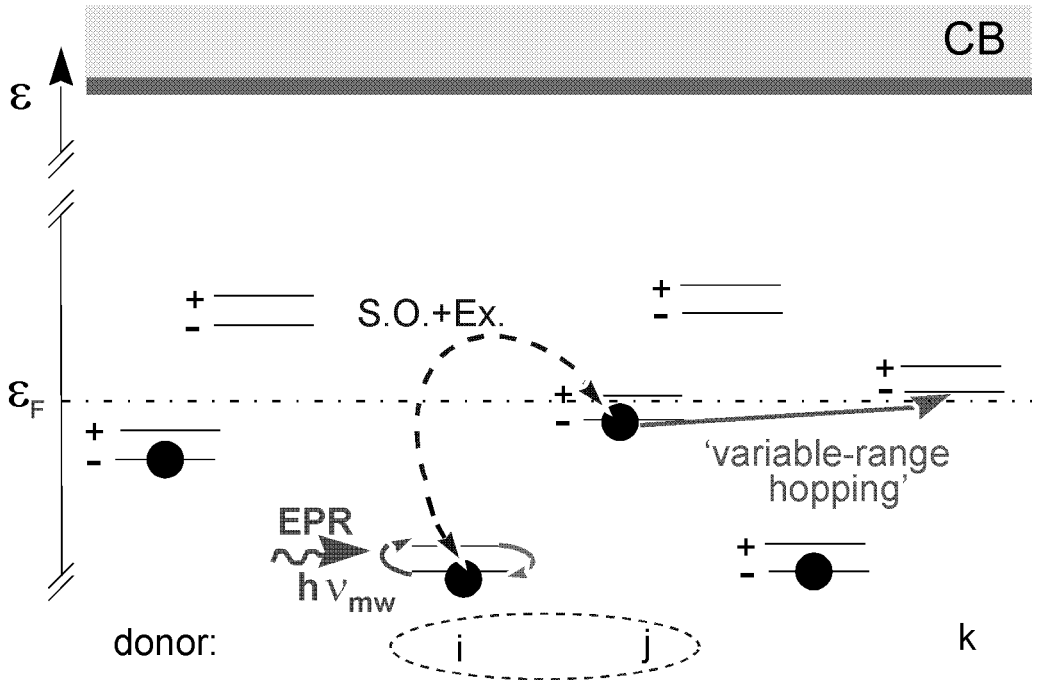

Figure 10.1: Scheme of the EPR-energy transfer. The donor electron at site i absorbs a microwave photon and is excited to the upper Zeeman level. Then, it returns to its lower Zeeman level while the electron at site j near the Fermi level ϵ_F hops to site k.

In chapter 7 we showed that the sample resistivity decreases with increasing temperature as well as under microwave irradiation. Therefore, the observed resistivity

decrease at spin resonance conditions may be due to a heating of the sample due to the microwave power absorbed at resonance or to the transfer of the microwave energy to the hopping electrons (e.g. energy-transfer model). As regards the EPR energy transfer model, illustrated in fig. 10.1, it was proposed by Kamimura and Mott [Kamimura 76]. The authors explained the resistivity decrease at donor spin resonance conditions observed in n-type silicon and germanium with donor concentrations belonging to the intermediate range [Morigaki 72] as a transfer of the EPR energy to the hopping electrons. The energy transfer would occur by the combined action of the exchange interaction and the spin-orbit interaction (denoted with $Ex.$ and $S.O.$ in fig. 10.1). This mechanism would consist of two processes. First a localized electron at a site denoted by i is subjected to the microwave field, and is excited to the upper Zeeman level by absorbing the microwave energy $h\nu_{mw} = g\mu_B B$. Then a localized electron at ϵ_F hops from a site j to site k by the exchange interaction with the localized electron at site i. The hop becomes possible through the absorption of the EPR energy by the electron at site j. The exchange interaction conserves the total spin of two electrons. But the authors suggested that if we take into account the spin-orbit interaction which mixes the different spin states, the localized electron at E_F can hop without changing its spin state, although the excited spin at site j reverses its direction to return to its lower Zeeman level. The states were assumed to be s-like, but if the distortion of the s-like wavefunction due to the overlap of neighbouring donor wave functions and/or due to the ellipsoidal energy surface of conduction band minima in Si and Ge are taken into consideration, the spin-orbit interaction does not vanish.

The EDEPR signal investigated in this work has several properties in common with that found by Morigaki and Onda [Morigaki 72] in silicon and germanium and discussed by Kamimura and Mott [Kamimura 76]: the donor concentration is high, but below the semiconductor-metal transition, the resistivity decreases by microwave irradiation at off resonance conditions and the EDEPR signal corresponds to a resonant resistivity decrease. Nevertheless, the temperatures at which our measurements were performed were higher ($T \geq 5K$ as compared to $4.2K \geq T \geq 1.5K$) and the donor states lie deeper in the band gap (50-100 meV as compared to 10meV), and thus the Bohr radii are smaller (therefore, the overlap of the defect wavefunctions for a given concentration will be smaller), than by Morigaki and Onda's investigations.

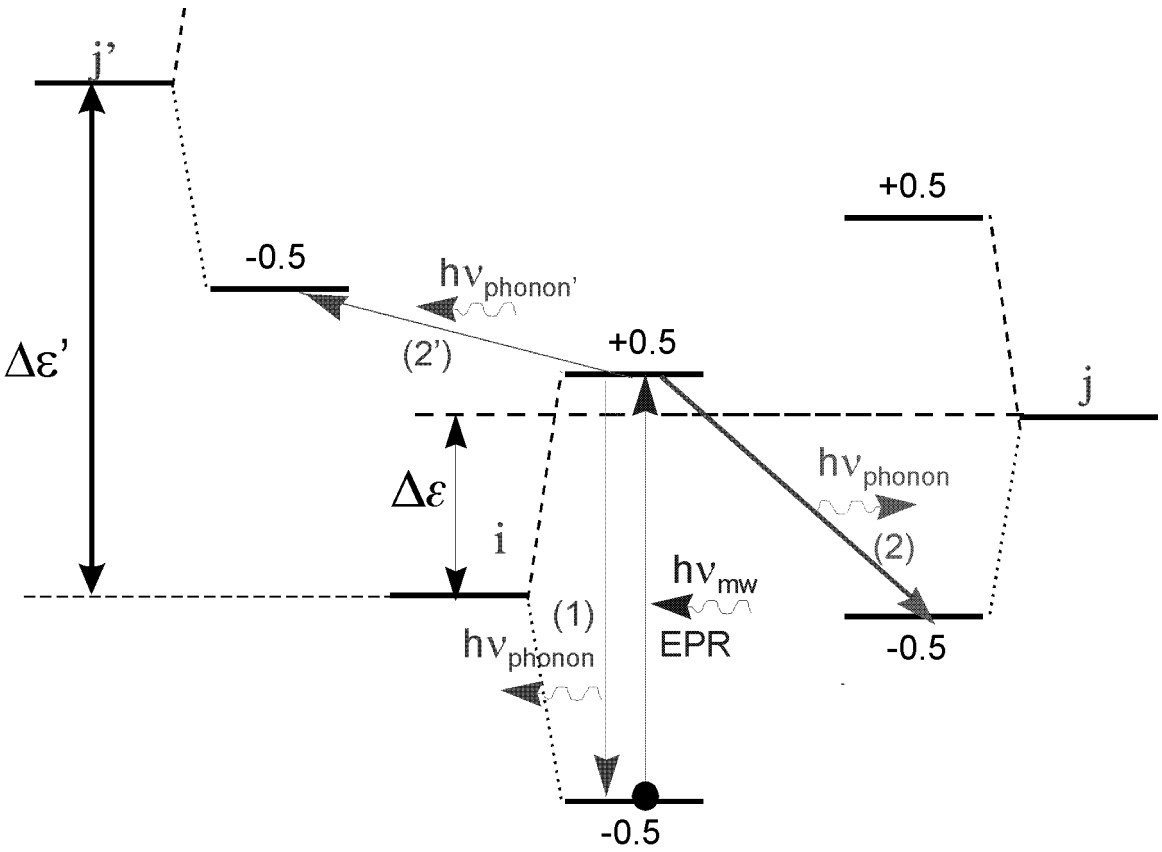

Figure 10.2: Hopping process accompanied by a spin-flip as relaxation process. First the electron at site i is excited to the upper Zeeman level by absorbing a microwave photon, then three different relaxation processes are possible. Process (1) corresponds to the "normal" spin-lattice relaxation, the electron returns to the lower Zeeman level emitting a phonon of energy $h\nu_{phonon} = h\nu_{mw}$. In process (2) the electron hops to a neighbouring ionized donor j reversing its spin and emitting a phonon of energy $h\nu_{mw} - \Delta\epsilon$, $\Delta\epsilon$ being the difference in the potential energy of the donors i and j. This phonon can induce additional hopping. Process (2') is like process (2), except that the potential energy difference between the donors $\Delta\epsilon'$ is larger and the electron must absorb a phonon of energy $\Delta\epsilon' - h\nu_{mw}$.

Let us discuss further possible mechanisms that could explain our experimental results. Morigaki and Onda [Morigaki 72] described a further mechanism that would lead to a resistivity decrease at EPR conditions, but concluded that this mechanism was not able to explain the order of magnitude of the observed effect. Figure 10.2 shows a schematic illustration of this mechanism. They proposed that there are two processes contributing to the spin-lattice relaxation: the direct process (T_1

process, denoted with (1)) and a hopping related one (2). In the former the electron returns to the lower Zeeman level, emitting a phonon whose energy coincides with the Zeeman energy. In the latter the electron hops to a neighbouring vacant donor site, simultaneously reversing its spin orientation. Thus the energy of the emitted phonon in (2) is given by the addition or subtraction of the Zeeman energy and the potential energy difference of the donor sites (see fig. 10.2). These phonons can induce additional hopping of donor electrons.

A further mechanism could be the process denoted with (2') in fig. 10.2: the electron at site i is excited to the upper Zeeman level and then the hop to site j' accompanied by a spin-flip becomes more probable than the hop without spin-flip since the energy needed has diminished. This could occur with a nonnegligible probability if the difference in the potential energy of i and j' $\Delta\epsilon'$ were comparable to the EPR energy $h\nu_{mw}$.

The processes denoted with (2) and (2') in fig. 10.2 as well as the energy-transfer model illustrated in fig. 10.1 can make nonneglible contributions to the conductivity, provided the average energy difference between donor sites is not much larger than the microwave energy. An analogous statement can be made for the "non resonant" case: we showed in chapter 7 that the resistivity decreases under microwave irradiation. This effect could be attributed to the hopping-related microwave absorption described in chapter 3, section 4. As mentioned in 3.4, photon-induced hopping is a further mechanism besides phonon-activated hopping, and it is influenced by applying a static magnetic field. An electron at site i can hop to an unoccupied site j by absorbing a microwave photon, provided the energy separation between both sites is equal to the photon energy: $\epsilon_{ij} = h\nu_{mw}$. The microwave energy corresponding to a frequency of 10GHz is $h\nu_{mw} \approx 4 \cdot 10^{-5}$eV. For this definite energy, there will be a certain number of donor pairs composed of one neutral (i) and one ionized donor (j) having an energy difference approximately equal to the microwave energy. An electron can thus hop from site i to site j by absorbing a microwave photon. The corresponding hopping distance R_{ij} can be calculated by using eq. (3.8). With a density of states at the Fermi level $N(\epsilon_F) = 5 \cdot 10^{21} eV^{-1} cm^{-3}$ (obtained from the experimental value of ϵ_3 with $\epsilon_3 \approx \frac{1}{N(\epsilon_F)a^3}$ as well as from the experimental value of

T_0 with $T_0 \approx \frac{24}{\pi}\frac{\alpha^3}{kN(\epsilon_F)}$) one obtains:

$$R_{ij} = \left(\frac{4\pi}{3}N(\epsilon_F)\epsilon_{ij}\right)^{-3} = \left(\frac{4\pi}{3}N(\epsilon_F)h\nu_{mw}\right)^{-3} \approx 300\mathring{A} \ . \qquad (10.1)$$

This distance is about 15 times the Bohr radius of the nitrogen donor in the hexagonal position, larger than the typical hopping distance $6a_B - 12a_B$. We see that the microwave energy is much smaller than the average energy difference ϵ_3 characteristic for the activated hopping regime, and therefore the corresponding hopping distance is much larger than the average distance between donors. Thus, a resonant microwave absorption leading to additional hopping, as described in section 3.4, could at best play a role at very low temperatures, in the variable range hopping regime.

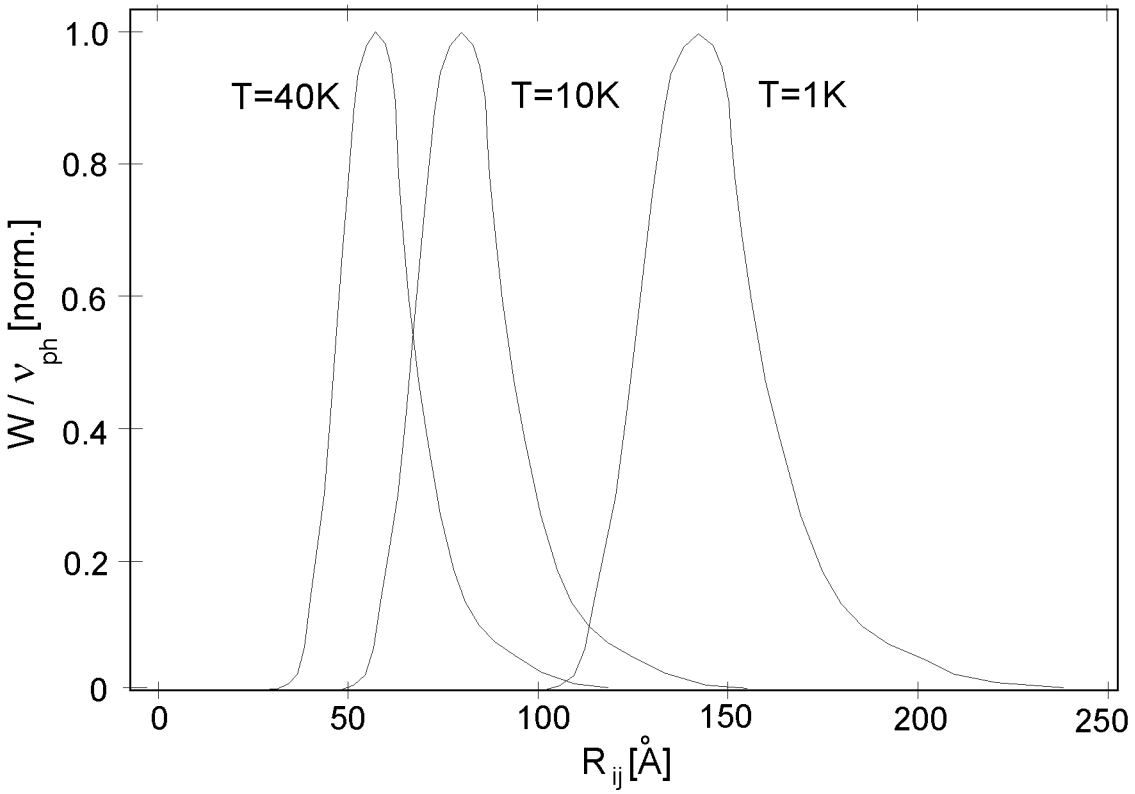

Figure 10.3: Simulation of the hopping probability as a function of the distance between donors R_{ij} for different temperatures using eq. (3.4): $W_{ij} = \nu_{ph}exp(-2\alpha R_{ij} - \frac{\epsilon_{ij}}{kT})$ and eq. (3.8): $\epsilon_{ij} = \left((4\pi/3)R_{ij}^3 N(\epsilon_F)\right)^{-1}$. The curves are normalized to the respective maximum value.

Figure 10.3 shows a simulation of the hopping probability in units of ν_{ph} (W_{ij}/ν_{ph}) as a function of the distance between donors R_{ij} for different temperatures using eq.

(3.4): $W_{ij} = \nu_{ph} exp(-2\alpha R_{ij} - \frac{\epsilon_{ij}}{kT})$ and eq. (3.8): $\epsilon_{ij} = \left((4\pi/3)R_{ij}^3 N(\epsilon_F)\right)^{-1}$. The curves are normalized to the respective maximum value, which varies strongly with temperature, as can be deduced from eq. (3.4): $W_{ij}(40K) \gg W_{ij}(10K) \gg W_{ij}(1K)$. As illustrated in fig. 10.3, the lower the temperature, the larger the distance between two donors for which the hopping probability is largest. The temperature for which the hopping probability W_{ij} has a maximum at $R_{ij} = 300\mathring{A}$ is smaller than 1K.

Mechanisms 2 and 2' in fig. 10.2 could be a possible explanation of the anomalous magnetoresistance observed at low temperatures (fig. 7.6). Since these hopping processes involve a spin-flip, the corresponding hopping probability will depend on the magnetic field. The magnetoresistance would then result from the magnetic field dependence of the spin-lattice relaxation time.

Now let us discuss the hopping-related microwave absorption, which was briefly outlined in chapter 3, section 4. Figure 10.4 shows the temperature dependence of the hopping microwave conductivity arising from the resonant contribution. In the figure the only temperature-dependent factor $\sigma_0^{res} \propto tanh(h\nu_{mw}/2k_BT)$ (from eq. (3.20)) is depicted. This factor has a transparent physical meaning: it is the equilibrium population difference between the lower and upper levels of the resonant pair. Since for a microwave frequency of 10GHz $h\nu_{mw}/2k_BT \ll 1$ for T$\geq$ 1K, the conductivity grows linearly with the reciprocal temperature.

Now we will estimate the maximum value of the conductivity that would arise from the microwave absorption by "resonant" pairs with an energy difference approximately equal to the microwave energy at X-band. This can be written as (see chapter 3, section 4)

$$\sigma_0^{res}(\nu_{mw}) = \frac{2\pi^3}{3} a_B N(\epsilon)^2 \frac{e^4}{\kappa} \nu_{mw} r_\nu^3 \tanh\left(\frac{\hbar\omega}{2kT}\right), \qquad (10.2)$$

where r_ν is the minimum "arm" of the pair with interlevel spacing $h\nu$. This approximation is valid for the case where the Coulomb repulsive energy $e^2/\kappa R$ is much larger than both the microwave energy and k_BT. We can use this expression, since

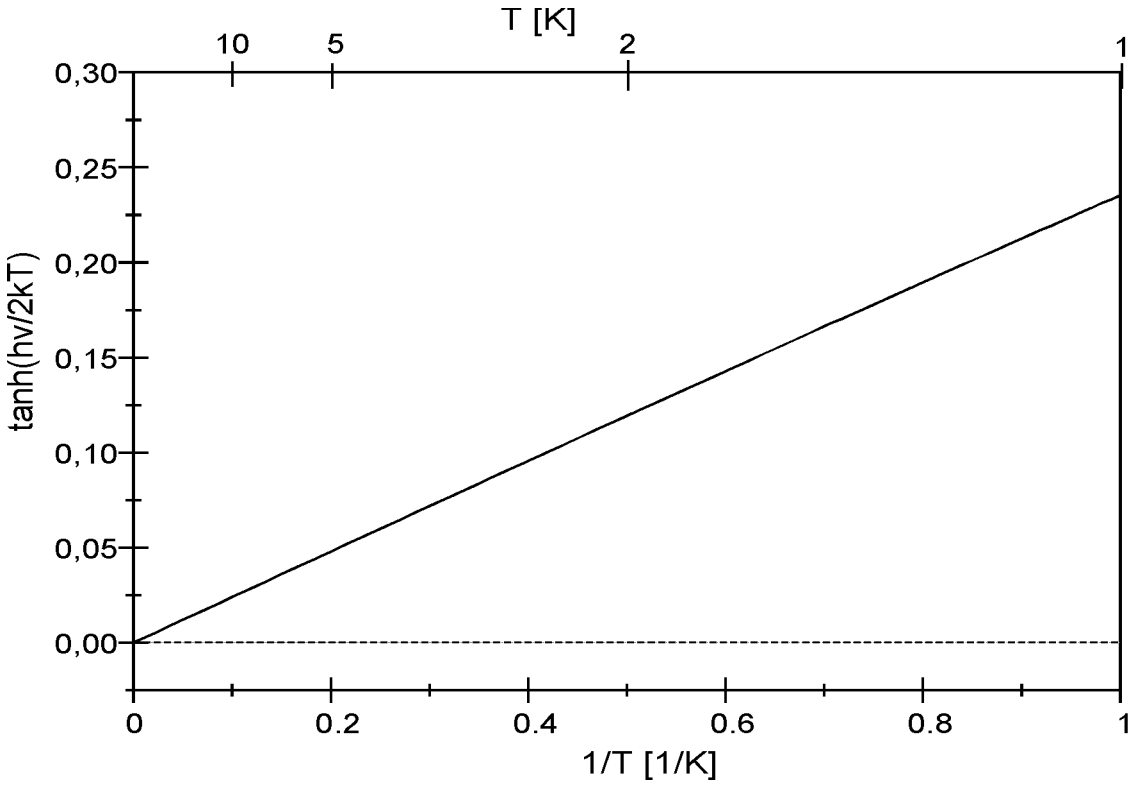

Figure 10.4: Temperature dependence of the hopping microwave conductivity arising from the resonant pairs. In the figure the only temperature-dependent term $\sigma_0^{res} \propto tanh(h\nu_{mw}/2k_BT)$ (from eq. (3.20)) is depicted. Since $h\nu_{mw}/2k_BT \ll 1$ in this temperature range T> 1, we observe a linear dependence ($tanh(x) \approx x$ when $x << 1$).

in our case

$$e^2/\kappa R \approx 0.2eV(R = 100\mathring{A}) \gg k_BT \approx 0.9 \cdot 10^{-3}eV(T = 10K) \gg h\nu_{mw} \approx 4 \cdot 10^{-5}eV \tag{10.3}$$

With $r_\nu = 10^{-9}$cm, $N(\epsilon) = 5 \cdot 10^{21}\text{eV}^{-1}\text{cm}^{-3}$, $a_B = 2 \cdot 10^{-7}$cm, $\nu = 10^{10}\text{s}^{-1}$ and $\kappa \approx 10 \cdot \kappa_0$ we obtain:

$$\sigma_0^{res} \approx 4 \cdot 10^{-5}\Omega^{-1}cm^{-1} \tanh\left(\frac{h\nu_{mw}}{2kT}\right) . \tag{10.4}$$

As can be seen in fig. 10.4, for the temperatures of study, T$\geq$ 5K, the factor $\tanh\left(\frac{\hbar\omega}{2kT}\right)$ is smaller than 0.05. Therefore, we can write for the microwave conductivity in the temperature range of study: $\sigma_0^{res} \leq 2 \cdot 10^{-6}\Omega^{-1}cm^{-1}$. As a result, the

conductivity arising from the resonant absorption of microwaves will make a considerable contribution at a temperature of 5K, at which the conductivity in the absence of microwaves was found to be $\sigma \approx 7 \cdot 10^{-6} \Omega^{-1} cm^{-1}$: $\sigma_0^{res}/\sigma = 0.25$. With increasing temperature the conductivity increases and the microwave conductivity decreases, as a result the relative effect of the "resonant" microwave absorption decreases strongly with temperature. Thus, this mechanism contributes to the resistivity decrease observed under microwave irradiation, specially at low temperatures, but cannot explain the order of magnitude of the microwave-induced resistivity decrease found experimentally.

Moreover, as reported in chapter 4, there is a further contribution to the microwave absorption in a hopping system, namely the relaxational absorption. It is due to the oscillating microwave electrical field, which generates an oscillation in the energy difference of two donor states. The microwave power used in our investigations was quite large (up to 1200mW incident into the cavity), therefore the corresponding electrical field could generate a nonnegligible oscillating component in the energy separation of a given pair of states, leading to a relaxational absorption. For the case $e^2/\kappa R \gg k_B T$, $h\nu_{mw}$ the relaxational absorption can be written:

$$\sigma_0^{rel}(\nu_{mw}) = 2\pi a_B N(\epsilon)^2 \frac{e^4}{\kappa} \nu_{mw} r_c^3 \ . \tag{10.5}$$

Thus, we obtain $\sigma_0^{rel} \leq 7.5 \cdot 10^{-6} \Omega^{-1} cm^{-1}$. The relaxational contribution depends only very lightly on temperature. As mentioned in chapter 3, it results from the modulation caused by the alternating microwave electric field in the energy difference of the states. Therefore, a considerable contribution to the conductivity is expected for high values of the electric field, i.e. for high microwave power levels. The sample was situated in the middle of an EPR cavity, ideally the microwave electrical field at the sample position should be zero and the magnetic field should be maximal. But in practice this is not the case, as a matter of fact we were able to measure EDEPR by detecting the dielectric losses (quality factor-detected EDEPR). As a result, we may have a nonnegligible contribution to the conductivity arising from the relaxational absorption, even at 10K. This could explain the observed behaviour even at the higher temperatures, e.g. the fact that the microwave absorption depends on the static magnetic field.

Thus, the resonant microwave absorption (photon-induced hopping) could explain the microwave-induced resistivity decrease as well as the resistivity decrease at spin resonance conditions (EDEPR) for very low temperatures, but not for the temperature range T> 5K studied in this work. In contrast to our investigations, in the experimental work of Morigaki and Onda the measurements were conduted at helium temperatures, the corresponding average hopping distance $R_w \approx 500\mathring{A}$ is comparable to the hopping distance corresponding to an energy difference $\Delta\epsilon = h\nu_{mw} \approx 4 \cdot 10^{-5}$eV.

We propose a further mechanism for EDEPR in the hopping regime, namely a heating of the donor electrons at spin resonance conditions. At spin resonance conditions the spin system absorbes microwave energy P_{EPR}, which is subsequently transferred to the surroundings through the spin-lattice relaxation. The temperature of the crystal thus increases at resonance conditions. This could explain the observed EPR-induced resistivity decrease $\Delta\rho_{EPR}$.

All enumerated EDEPR mechanisms are possible explanations for a resistivity decrease at spin resonance conditions in a hopping system. Now, we will discuss the mechanisms in terms of the experimental results presented in the former sections.

1. *Temperature dependence:* The EDEPR signal amplitude $|\Delta\rho_{EPR}|$ was found to decrease with increasing temperature. This behaviour may arise from the temperature dependence of the resistivity ($\rho \propto exp(\epsilon_3/kT)$, $\rho \propto exp\{(T_0/T)^{1/4}\}$ for the nearest neighbour hopping and variable range hopping regimes, respectively) and from the temperature dependence of the spin-lattice relaxation time T_1. The spin-lattice relaxation time T_1 decreases with increasing temperature and can be obtained from MCDA measurements [Spaeth 92] or from the saturation behaviour of the EPR signal (given by the saturation constant s) with the assumption that the spin-lattice relaxation time T_1 and the spin-spin relaxation time T_2 are almost equal:

$$T_1 \approx T_2 \Rightarrow s \propto T_1 \cdot T_2 \approx T_1^2 \quad .$$

   Nevertheless, in this case none of these methods can be applied, since a MCDA signal from nitrogen in SiC is not known, and the EPR signal shows no saturation (see chapter 10). On the other hand, if the EDEPR effect were due to

a heating effect, then we would have to consider the temperature dependence of the specific heat, which is expected to follow a T^3 behaviour.

2. *microwave power dependence:* The EDEPR signal amplitude $|\Delta\rho_{EPR}|$ was found to grow linearly with microwave power up to a certain value and remain constant for higher power levels. This behaviour agrees with a heating effect as well as with an energy-transfer mechanism.

3. *order of magnitude:* The EPR-induced resistivity decrease was found to be a large effect (up to $\Delta\rho_{EPR}/\rho \approx -10^{-2}$). As regards the energy-transfer or the hopping-related relaxation mechanisms described above, these mechanisms cannot explain the order of magnitude of the observed effect, since the EPR energy is much smaller than the average energy difference between donor states. In the investigations of Morigaki and co workers the observed relative resistivity decrease was $|\Delta\rho_{EPR}/\rho| \leq 10^{-2}$. In our case the states lie deeper in the energy gap and they are consequently stronger localized. As a result, both the probability for photon-induced hopping for a microwave frequency of 10GHz and the exchange interaction for a given defect concentration are smaller. As a consequence, the maximal relative effect that would arise from an EPR *energy transfer mechanism* as described by Kamimura and Mott would be of the order $|\Delta\rho_{EPR}|/\rho \leq -10^{-4}$, much smaller than the observed effect. In the next section we will make an estimation of the EPR-induced heating effect and see whether this mechanism can explain the experimental values of $\Delta\rho_{EPR}/\rho$.

10.1 Temperature change at resonance conditions

As reported in chapter 8, we have observed a resistivity decrease at spin resonance conditions in highly doped n-type SiC and conducted a series of investigations aimed at finding out the underlying microscopical processes. In this chapter, we have discussed different microscopical mechanims for the EDEPR effect in highly doped SiC and proposed a possible simple explanation for the EDEPR effect, namely a heating of the sample at resonance conditions responsible for the resonance decrease. At resonance the spin system absorbes microwave energy, which is transferred to the surroundings by relaxation processes. As a result, the crystal is heated at

resonance conditions. This section deals with the order of magnitude and temperature behaviour of this EPR-induced heating effect and its ability to explain the EDEPR effect in low resistivity samples.

When microwave energy is absorbed in a crystal, it is converted to heat, and the crystal temperature rises. In the absence of a mechanism for heat removal the temperature increase ΔT induced by the absorption of microwave power P_{mw} during a time interval t is given by:

$$\Delta T = \frac{\int_0^t P_{mw} dt}{MC_v} \tag{10.6}$$

where the microwave power P_{mw} is given in watt, the specific heat C_v in joules per gram degree and the mass of the sample M in grams. At spin resonance conditions the spin system absorbes microwave energy P_{EPR}, which is subsequently transferred to the lattice surroundings through the spin-lattice relaxation. The temperature of the crystal thus increases at resonance conditions. This could explain the observed EPR-induced resistivity decrease ρ_{EPR}:

$$P_{EPR} \Longrightarrow \Delta T_{EPR} \Longrightarrow \Delta\rho_{EPR}$$

Let us estimate the order of magnitude of the heating effect, that is, the magnitude of the temperature change induced by the absorption of microwaves at magnetic resonance conditions. We assume that there is no mechanism of heat removal and compare the obtained ΔT_{EPR} with the temperature increase corresponding to the experimentally observed resistivity decrease $\Delta\rho_{EPR}$. To begin with, we calculate the microwave power absorbed at resonance at the temperature and microwave attenuation conditions (9K, 0.2W) of the d.c. EDEPR experiment for sample E1. As shown in chapter 2, the microwave power absorbed by the spin system at resonance is given for a Gaussian line by:

$$P_{EPR} = \frac{1}{4}\gamma^2 B_1^2 h\nu n_0 g(\nu) \cdot \frac{1}{1 + \frac{1}{2}\gamma^2 B_1^2 T_1 g(\nu)} \tag{10.7}$$

We restrict ourselves to the case of non-saturation, in case of which the second factor can be neglected:

$$P_{EPR} \approx \frac{1}{4}\gamma^2 B_1^2 h\nu n_0 g(\nu) \tag{10.8}$$

In order to calculate P_{EPR}, we need to know the value of the microwave magnetic field at the sample position in the cavity. The average magnetic field in the cavity is given by [Poole 83]

$$\left\langle B_1^2 \right\rangle_c = \frac{2}{\pi}\, Q_L\, \frac{V_w}{V_c} \left\langle B_1^2 \right\rangle_w \tag{10.9}$$

Here, Q_L is the loaded quality factor, V_c the volume of the cavity, V_w the volume of the section of waveguide which is one wavelength long and $\langle B_1^2 \rangle_w$ the average value of the magnetic field in the waveguide. The last quantity can be calculated from the microwave power P_w incident on the waveguide, for a TE_{10} rectangular X band waveguide [Poole 83]:

$$\left\langle B_1^2 \right\rangle_w = \frac{1}{4} B_w^2 \approx 1.3\ 10^{-3} P_w \tag{10.10}$$

Here, B_w is the maximal value of the $\vec{\mathbf{B}}$ vector propagating along the cavity and is given in Gauss, P_w in watt. In our experiment $V_c = 66 \cdot 10^{-6} m^3$, $V_w = 6.9 \cdot 10^{-6} m^3$, $Q_L \approx 2000$. This corresponds to an average microwave magnetic field $\langle B_1 \rangle$ of 1.78 Gauss for 0.2 watt microwave power incident on the cavity.

We now calculate the absorbed microwave power at $P_{mw} = 0.2 watt, T = 9K$, where we first have to find out the lineshape function $g(\nu)$ This can be obtained from the experimental data (linewidth and magnetic field position of the resonance line and microwave frequency) below saturation by means of the expression [Poole 83]:

$$g(\nu) = \frac{2\sqrt{\pi}}{\delta} exp\left(\frac{-(\gamma B_0 - 2\pi\nu)^2}{\delta^2}\right) \tag{10.11}$$

we obtain for the lineshape function at the absorption maximum $g(\nu) = 3.3 \cdot 10^{-13}$. By substituting these values in eq. (10.8) we obtain $P_{EPR} = 2.6 \cdot 10^5 Js^{-1} g(\nu)$, $P_{EPR} = 8.5 \cdot 10^{-8} Js^{-1}$ for the maximum absorbed power.

We can now use eq. (10.6) to estimate the temperature increase induced by the absorption of this power. By substituting $C_v(9K) = 5.73 \cdot 10^{-4}$ joule gram$^{-1}K^{-1}$ (extrapolated from the smoothed experimental data obtained by Koshchenko et al.

for hexagonal SiC with a donor concentration of 10^{18} [Koshchenko 79]), $M = 5 \cdot 10^{-3}$ gram and $P_{EPR} = 8.5 \cdot 10^{-7} Js^{-1}$ we obtain

$$\Delta T_{EPR} = \frac{\int_0^t 8.5 \cdot 10^{-8} Js^{-1} dt}{2.9 \cdot 10^{-6} JK^{-1}} \ , \tag{10.12}$$

leading to a $\Delta T_{EPR} = 0.035$ K s^{-1} Δt at the microwave absorption maximum. For an integration time of 1s, we obtain for the EPR-induced temperature increase at T=9K, P$_{mw} = 0.2W$: $\Delta T_{EPR} = 0.035$ K s^{-1}·1s =35 mK. This is the maximal temperature change that can be induced at resonance conditions during a time interval Δt =1s, since we have not considered any losses for this estimation.

We may now compare this estimated temperature change through the resonant microwave absorption with the temperature difference that would lead to the experimentally found resistivity decrease. As reported in chapter 8, we performed d.c. EDEPR experiments and at a temperature of 9K and a microwave power of 0.2W we found a relative resistivity change of $\Delta\rho/\rho = -10^{-3}$. By using the expression for the temperature dependence of the nearest neighbour hopping ($\rho = \rho_3 exp(\epsilon_3/kT)$, with $\epsilon_3 \approx 4meV$), we find that this resistivity change corresponds to a temperature change of about ΔT$\approx$ 2.3mK, a tenth of the maximal possible EPR-induced temperature increase ΔT_{EPR} estimated by using eq. (10.6). Therefore, the resistivity decrease observed at EPR conditions can be due to a heating effect. As already noticed, the estimated EPR-induced temperature increase of 35mK is the maximal possible temperature enhancement, since the estimation was made without considering any mechanism of heat removal. In the experiment, however, the sample was constantly cooled down with helium. As a result, most of the heat will be removed by the helium flow and the actual temperature change at resonance conditions is expected to depend on the cooling power and be smaller than the maximal temperature change of 35mK.

10.2 Temperature measurement

We have seen that the order of magnitude of the EPR-induced temperature change could be able to explain the EDEPR effect provided there is no further mechanism of heat removal. This section deals with an experiment carried out on purpose to see

whether the sample temperature increases at resonance. A simple method for the detection of a temperature change is the use of a Weastone bridge with two variable resistors and two further resistors having a high temperature sensitivity. From the latter, one is in thermal contact with the sample and the other acts as a reference. We used (see fig. 10.5) two diodes for this purpose, as their resistivity for a given voltage value is strongly temperature dependent. Both diodes were situated in the cavity and surrounded by helium gas, one of them was stuck to the sample with a conductivity glue. At off-resonance conditions both diodes are at the same temperature. If a constant voltage U is applied to the bridge with the diodes forward biased, a current $I_D = U/2R_D$ will flow through them. The variable resistances can be equalized to the resistances of the diodes at the given voltage and temperature $R_R = R_D(U/2, T)$, the bridge voltage then becomes equal to zero.

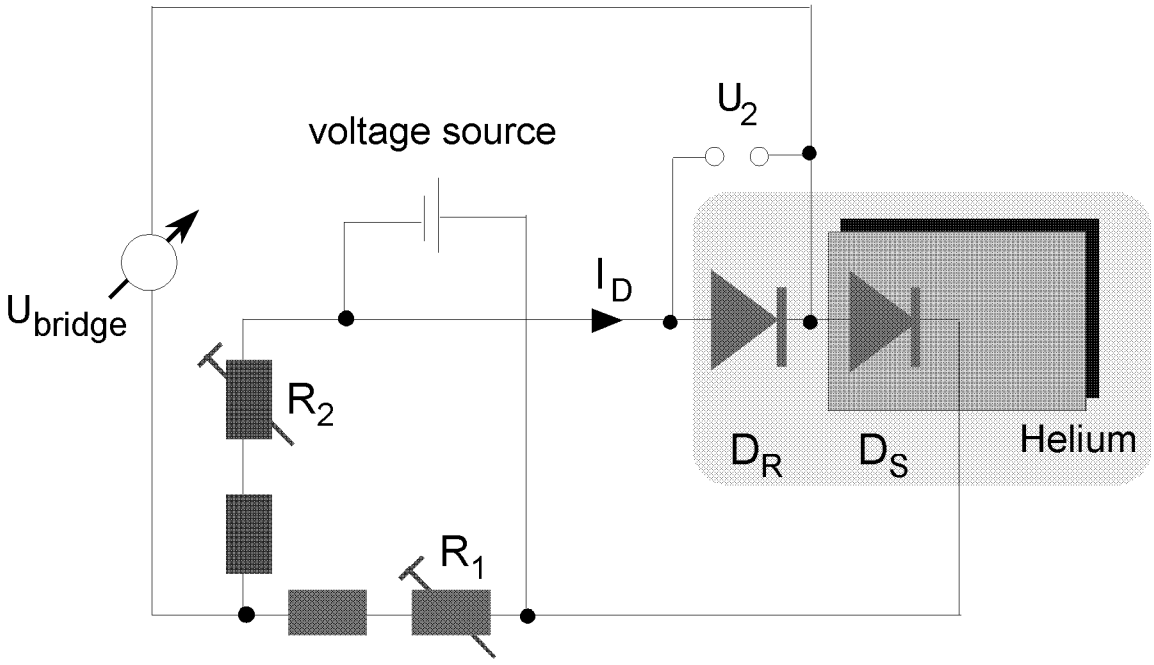

Figure 10.5: Schema of the experimental construction for the measurement of the EPR thermal effect

At magnetic resonance conditions, the temperature of the sample increases, and heat is subsequently transferred to the diode D_S (see fig. 10.5). Thus, diode D_S feels a higher temperature than D_R and, as a consequence, the diodes have different current-voltage characteristica. As a result, the bridge voltage differs from zero at spin resonance conditions. This enables us to detect the resonance by recording the

bridge voltage while scanning the magnetic field at a fixed microwave frequency.

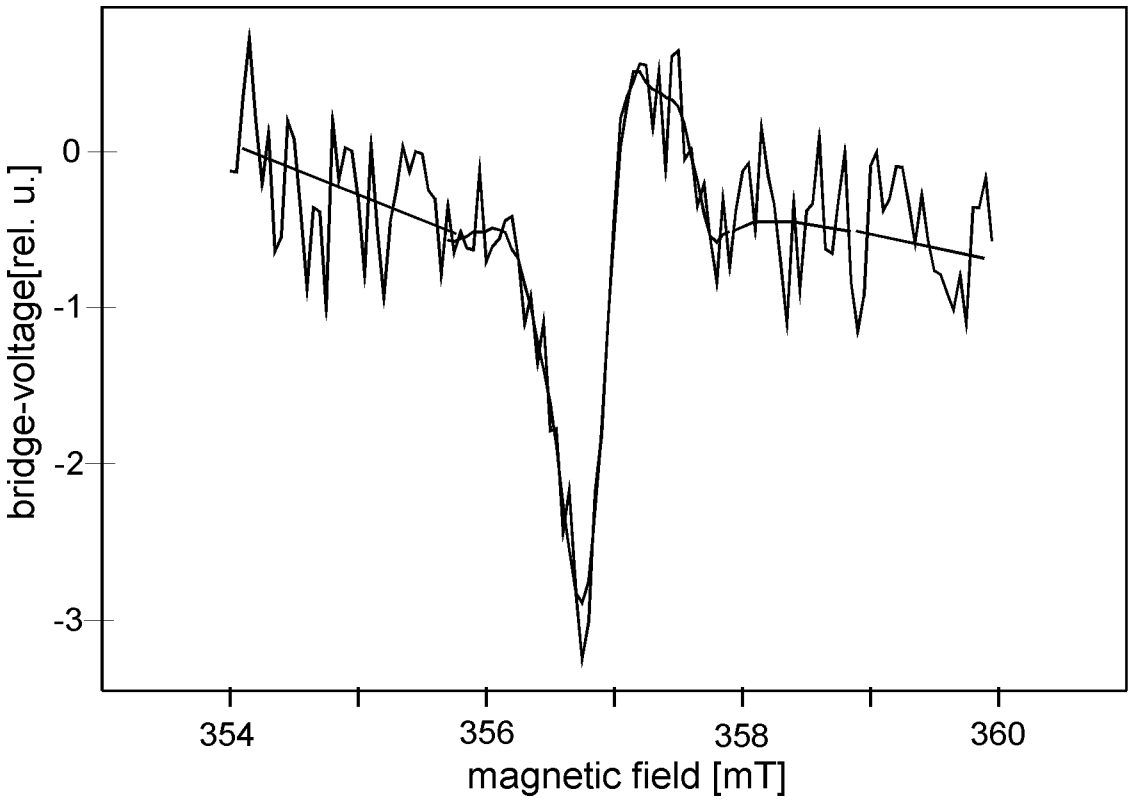

Figure 10.6: Indirect temperature measurement, carried out at T=6.7K, $P_{mw} = 250mW$. The bridge voltage was recorded while scanning the magnetic field. The magnetic field was modulated with 40kHz. The shown spectrum resulted from the addition of 49 scans.

The diodes have to fulfil three conditions to become appropriate for this experiment: small mass, proper operation at low temperatures and strong temperature dependence of their electrical behaviour. The first condition led us to the choice of SMD diodes for high frequency applications. A series of these diodes was tested and the SMD pin diode BAR 64-03W turned out to show the best temperature behaviour. This diode type was consequently used for the measurement of the EPR thermal effect. Prior to sticking the diode to the sample, we conducted EPR measurements on it. No EPR signal in the magnetic field region of interest was found, and therefore this diode type fulfilled all requirements for its use in the experiment.

We conducted a magnetic resonance experiment by irradiating the sample with microwaves and scanning the magnetic field, recording, however, not the microwave

absorption, but the bridge voltage. First of all, the bridge voltage was equalized to zero by varying the resistances R_1 and R_2. This was done at off-resonance at B=354mT$\neq B_{EPR}$. The magnetic field was subsequently scanned and the bridge voltage was detected.

The signal noise due to the temperature noise and other noise sources was much higher than the expected signal, therefore a lock-in technique had to be used. Since we want to measure a heat-flow effect, the magnetic field modulation is selected to be 40kHz, higher than the typical EDEPR modulation frequency of 5kHz.

Figure 10.6 shows the signal resulting from the addition of 49 scans measured at a temperature of 6.7K and a microwave power of 250mW. Although we used lock-in technique for sensitivity enhancement, a single scan did not suffice to see a signal. When a lower modulation frequency was used, no signal could be found, even after adding 50 scans. With a modulation frequency of 40kHz, the experiment was reproducible as long as the magnetic field was scanned fast enough (not more than one second per 0.05mT). This can be explained as follows: the sample as well as the diodes are surrounded by helium gas. If the the magnetic field is scanned too slowly over the resonance, the heat is dissipated before it can be detected.

The spectrum shown in fig. 10.6 shows that there is a change in the bridge voltage, and thus a heat transfer from the sample to the diode D_S, at EPR conditions. We furthermore performed a d.c. detection of the bridge voltage in order to determine the sign of the temperature change. This was however not possible, even after the addition of 78 scans (see fig. 10.7(a)), as could be expected from the weakness of the signal obtained with lock-in technique. Nevertheless, we can take some information from this experiment. As we see in fig. 10.7, the bridge voltage and thus the temperature difference between the two diodes varies with the magnetic field. A voltage decrease corresponds to a higher temperature of the sample diode as compared to the reference diode. Figure 10.7(b) shows that the microwave absorption increases with increasing magnetic field in the region around the resonance ("non-resonant absorption") (see chapter 8, fig. 8.9). Furthermore, there is an additional "resonant" microwave absorption at EPR conditions. Thus, the decrease in the bridge voltage with growing magnetic field can be interpreted as an increase of the temperature of the diode D_S, and thus of the sample itself, arising from the increasing

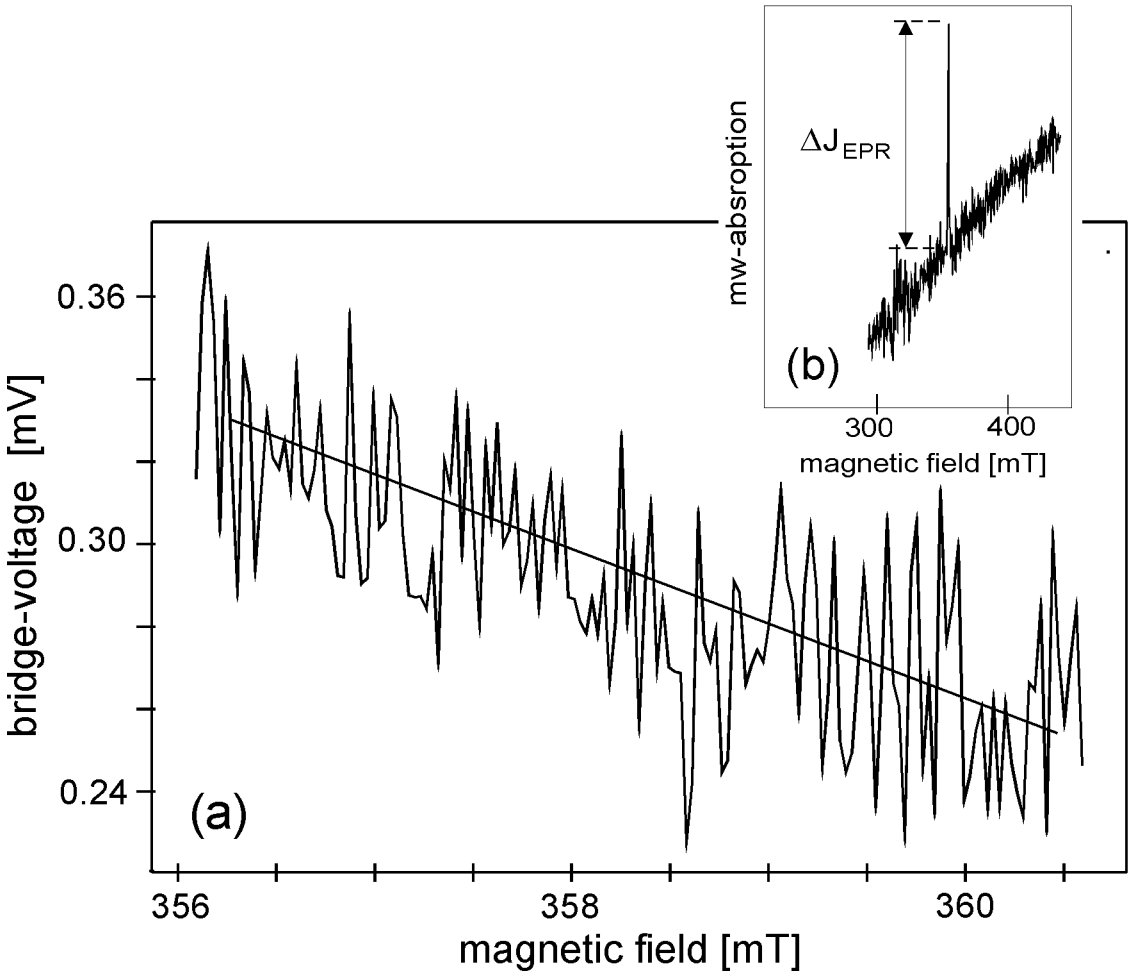

Figure 10.7: (a):Indirect temperature measurement carried out at T=6.5K, $P_{mw} = 750mW$. The bridge voltage was recorded while scanning the magnetic field. The current flow through the diodes was almost equal to the current through the resistances $I_D \approx I_R \approx 70\mu$A. The bridge voltage was about -0.3mV. The shown spectrum resulted from the addition of 78 scans. (b): Microwave absorption of sample E1 (measured at 7K with by modulating the microwaves amplitude) as a function of the static magnetic field. ΔJ_{EPR} denotes the "resonant" absorption at EPR conditions.

microwave absorption by the sample. In fig. 10.6 we can see that, as well as in fig. 8.11, above 200mT both the resonant and non-resonant parts have the same sign. As we know from the d.c. experiment, the non-resonant contribution corresponds to a temperature increase. Therefore, we can say that the resonance signal shown in fig. 10.6 can be attributed to a resonant temperature increase: $\Delta T_{EPR} > 0$.

Thus, we have proved that there is a temperature change at spin resonance conditions (bridge experiment using lock-in technique, fig. 10.6) and that it is indeed a temperature increase (d.c. bridge experiment, fig. 10.7).

10.3 EDEPR-signal dependences

In chapter 8 the experimental results of behaviour if the EDEPR signal of sample E1 with parameters such as microwave power, temperature, modulation frequency and electrical current were presented. The EDEPR signal was measured as a resonant voltage change at constant current conditions. The data were obtained from measurements on sample E1. Now we will discuss them in terms of the EPR-induced temperature increase model.

As shown in section 10.1, the order of magnitude of the observed resonant resistivity decrease can be explained with this model. The experiment presented in section 10.2 showed that there is in fact a temperature increase at EPR conditions. The decrease of the EDEPR signal amplitude by illumination with light, as shown in fig. 8.2, can be explained as follows: under illumination charge carriers are excited to the conduction and valence band, and therefore band-type conductivity competes with hopping conductivity. In the case of band-type conduction the mobility decreases with increasing temperature, in contrast to the case of hopping conduction, and the dependence on temperature is weaker.

10.3.1 Temperature dependence of the EPR-induced heating effect

A further step towards clarifying whether a heating effect can be responsible for the EDEPR signal is to look at the experimental temperature dependence of the EDEPR signal. As stated in chapter 8, it decreases with increasing temperature. Now we will compare the measured behaviour with the one expected from a heating effect.

As can be seen in eq. (10.6), besides the absorbed microwave power we must consider the specific heat C_v. The specific heat depends on the temperature, and varies with polytype and doping [Morelli 93, Parafenova 90]. Experimental investigations on 6H-SiC showed a T^n temperature dependence with $n = 3$ for very pure or highly compensated material and $n = 2$ in other case [Morelli 93]. The T^2 dependence is attributed to the scattering of phonons by electrons in an impurity band [Slack 64].

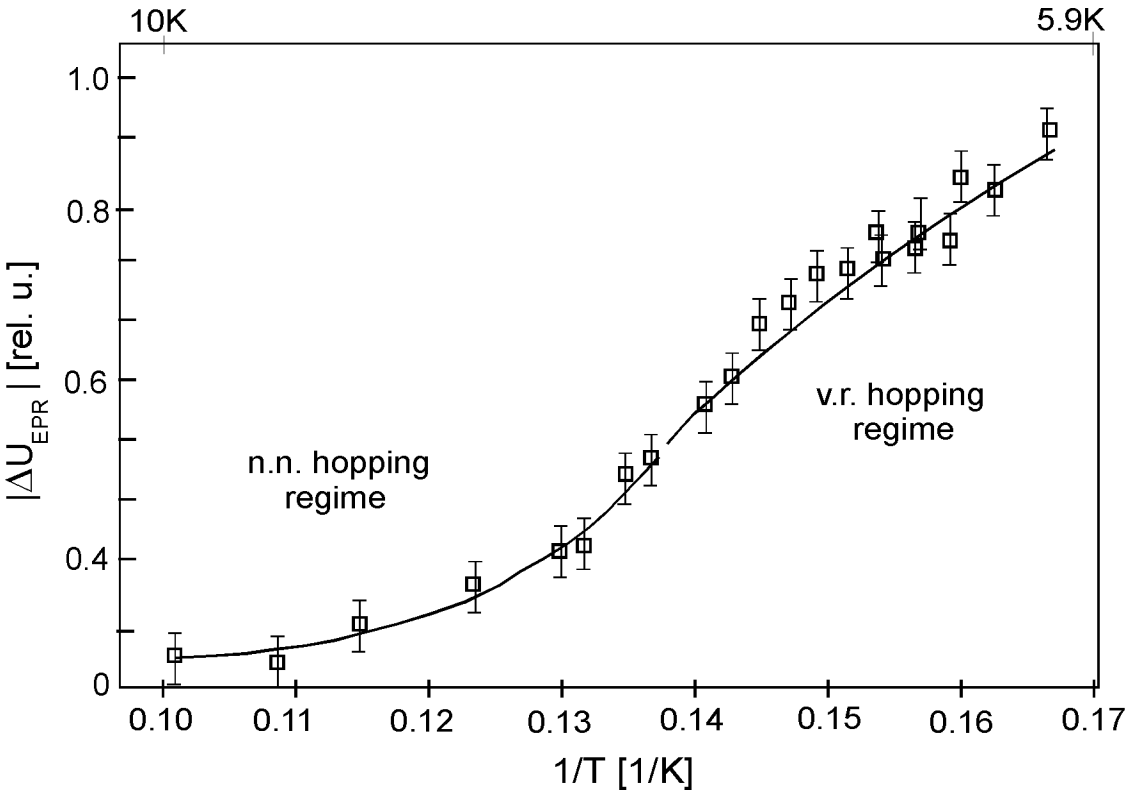

Figure 10.8: EDEPR signal intensity (in relative units) mesured as a resonant voltage decrease at constant current conditions displayed as a function of the inverse temperature. The maximum displayed $|\Delta U_{EPR}|$ corresponds to 10mV. The squares show the experimental data measured at $P_{mw} = 0.2$ watt and I= 10μA, the solid lines are simulations assuming $\Delta U_{EPR} \propto -T^{-5}\exp(\epsilon_3/k_BT)$ and $\Delta U_{EPR} \propto -T^{-17/4}\exp((T_0/T)^{1/4})$ for the nearest neighbour hopping regime and the variable range hopping regime, respectively.

From Hall studies we can say that none of the samples in which an EDEPR signal could be measured was degenerated. Therefore, the specific heat is expected to show a T^3 behaviour.

The microwave power P_{EPR} absorbed by the crystal at resonance depends on the temperature through the spin-lattice relaxation time (see eq.(10.7)):

$$P_{EPR} = \frac{1}{4}\gamma^2 B_1^2 h\nu n_0 g(\nu) \cdot \frac{1}{1+\frac{1}{2}\gamma^2 B_1^2 T_1 g(\nu)} \tag{10.13}$$

$$T_1 \propto T^m, \; m = -1, -5, -7, -9 \tag{10.14}$$

$$\tag{10.15}$$

where $cte = \frac{\gamma^2 B_1^2 T_2}{1+(\gamma B_0-\omega)^2 T_2^2}$. The exponent m is equal to -1 for the direct relaxation process and to -5, -7 or -9 for the indirect one. In practice, several processes may occur simultaneously, and the temperature dependence must be obtained from experimental data. Nevertheless, the dependence of P_{EPR} on temperature is much weaker than that of the specific heat. As a result, the temperature dependence of the EPR-induced temperature increase is expected to be dominated by the temperature dependence of the specific heat , $C_v \propto T^3$:

$$\Delta T = \frac{\int_0^t P_{EPR} dt}{MC_v(T)} \propto \frac{\int_0^t P_{EPR} dt}{T^3} \tag{10.16}$$

Thus, we have seen that the temperature increase induced by the absorption of microwave power by the spin system at spin resonance conditions ΔT_{EPR} follows a T^{-3} behaviour. As regards the corresponding resistivity decrease, it will depend on the dominant charge transport process at the respective temperature. For the nearest neighbour hopping regime, where the resistivity behaves as $\rho = \rho_3 \exp(\epsilon_3/k_B T)$, the resistivity decrease due to the microwave absorption at spin resonance conditions can be written for a small temperature change ΔT:

$$\Delta\rho = \frac{\delta\rho}{\delta T}\Delta T = -\frac{\rho_3\epsilon_3}{k_B}\frac{1}{T^2}\exp(\epsilon_3/k_B T)\Delta T \tag{10.17}$$

As we see from eq. (10.17), the temperature dependence of $\Delta\rho$ arises from the temperature dependence of both the resistivity and the specific heat . For the variable range hopping regime, where the resistivity behaves as $\rho = \rho_0 \exp((T_0/T)^{1/4})$, we can analogously write:

$$\Delta\rho = -\frac{\rho_0 T_0^{1/4}}{4}\frac{1}{T^{5/4}}\exp((T_0/T)^{1/4})\Delta T \tag{10.18}$$

By using equation (10.6) we obtain for the resistivity decrease per integration time Δt:

$$\frac{\Delta\rho}{\Delta t} = -\frac{\rho_3\epsilon_3}{k_B}\frac{P_{EPR}}{MC_v}\frac{1}{T^2}\exp(\epsilon_3/k_B T) \tag{10.19}$$

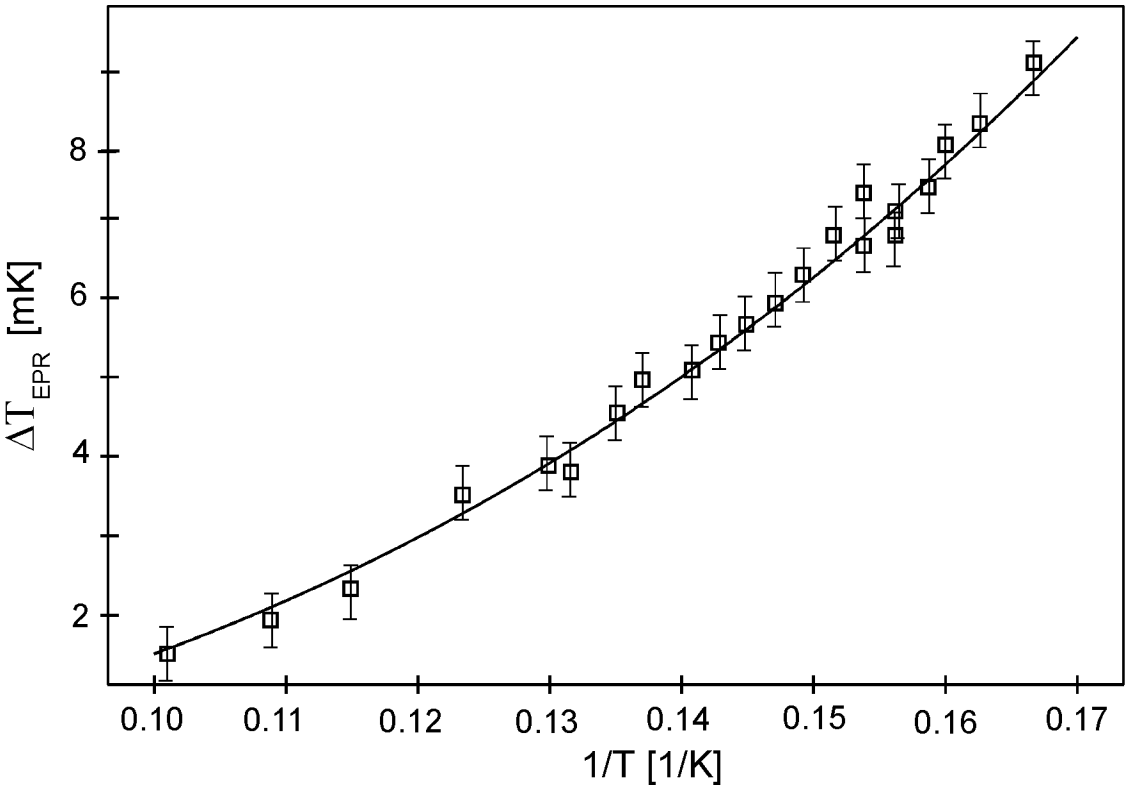

Figure 10.9: Temperature change at spin resonance conditions as a function of the inverse temperature. The squares show the data derived from the experimentally determined voltage changes measured at P_{mw} = 0.2 watt and I= 10μA, the solid line is a simulation assuming a T^{-3} dependence.

for the nearest neighbour regime and:

$$\frac{\Delta\rho}{\Delta t} = -\frac{\rho_0 T_0^{1/4}}{4}\frac{P_{EPR}}{MC_v}\frac{1}{T^{5/4}}\exp((T_0/T)^{1/4}) \tag{10.20}$$

for the variable range hopping regime. Since the specific heat varies with temperature as $C_v \propto T^3$, we obtain from eq.(10.19) for the nearest neighbour hopping regime:

$$\frac{\Delta\rho}{\Delta t} = -c_1\frac{1}{T^5}\exp(\epsilon_3/k_B T)\ , \tag{10.21}$$

where c_1 contains the temperature-independent terms. An analogous equation can be written for the variable-range hopping regime:

$$\frac{\Delta\rho}{\Delta t} = -c_2 \frac{1}{T^{17/4}} \exp((T_0/T)^{1/4}) \ , \tag{10.22}$$

For obtaining eq. (10.21) and (10.22) we have neglected the temperature dependence of the microwave power absorbed at resonance P_{EPR}. In chapter 8 we saw that the EDEPR signal, measured as a voltage decrease at constant current conditions $|\Delta U_{EPR}|$, grows with the reciprocal temperature. Now we can use equations (10.21) and (10.22) and compare the corresponding temperature dependence of the resistivity with the experimental data. Figure 10.8 shows the experimentally determined values for $|\Delta U_{EPR}|$ together with a simulation using equations (10.21) and (10.22). We observe that the simulation fits quite well to the experimental data. Therefore, the experimentally determined temperature dependence of the EDEPR signal points to a EPR-induced heating effect.

For a better illustration, we estimated the temperature increase ΔT_{EPR} corresponding to each experimental ΔU_{EPR} shown in fig. 10.9 by using $\Delta T_{EPR}(9K) = 2.3$mK and equations (10.17) and (10.18). Figure 10.9 shows the temperature dependence of the EPR-induced temperature decrease of sample E1 derived as described above from the experimental EDEPR data obtained at a microwave power of 200mW and a current of 10μA together with a simulation yielding a T^{-3} dependence.

10.3.2 Microwave-induced resistivity decrease

As noticed in chapter 8, the resistivity decreases under microwave irradiation and this effect grows with decreasing temperature. If the resistivity decrease is the result of a heating of the sample, then we can argue as in the case of the EPR-induced temperature increase described in section 7.4, but substituting the microwave power absorbed at resonance P_{EPR} with the microwave power absorbed off resonance P_{off}. Therefore, we obtain for the resistivity change due to a heating effect of the microwaves:

$$\frac{\Delta\rho_{mw}}{\Delta t} = -\frac{\rho_3 \epsilon_3}{k_B} \frac{P_{off}}{MC_v} \frac{1}{T^2} \exp(\epsilon_3/k_B T) \tag{10.23}$$

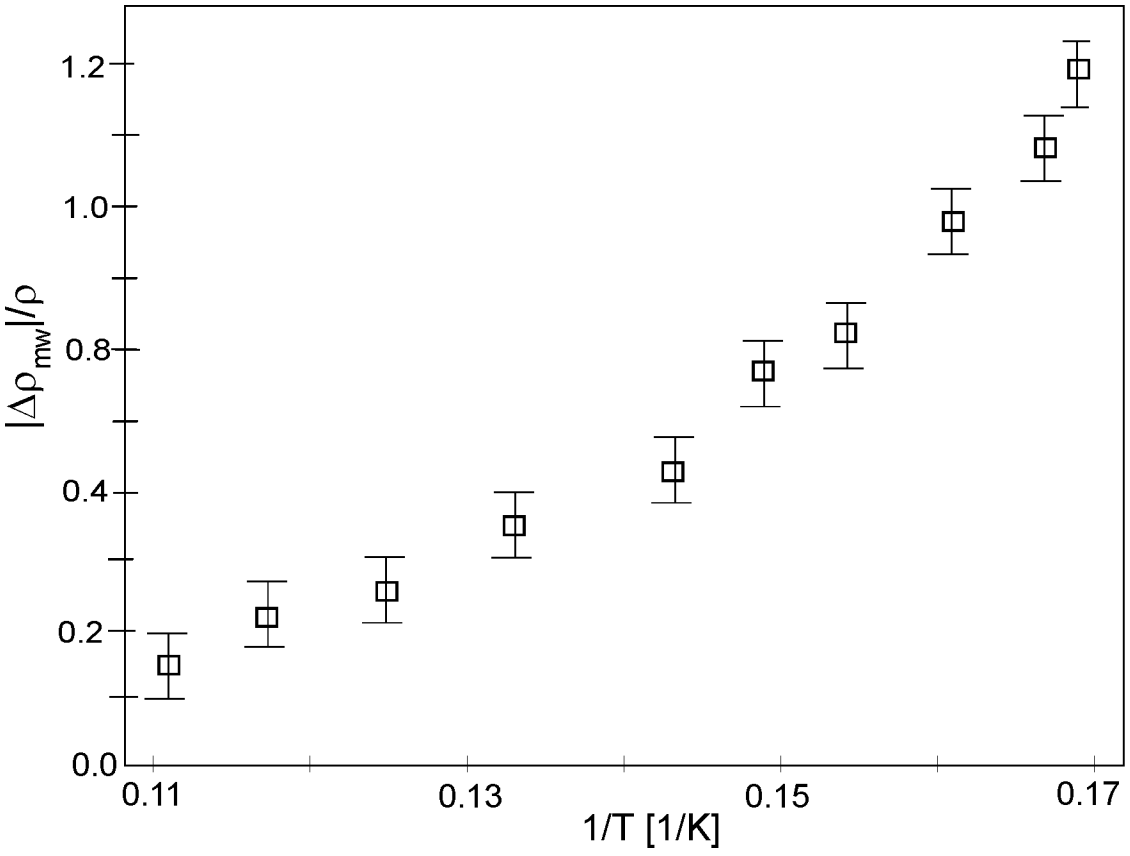

Figure 10.10: Temperature dependence of the microwave-induced resistivity decrease. The squares show the experimental data.

for the nearest neighbour regime and:

$$\frac{\Delta\rho_{mw}}{\Delta t} = -\frac{\rho_0 T_0^{1/4}}{4}\frac{P_{off}}{MC_v}\frac{1}{T^{5/4}}\exp((T_0/T)^{1/4}) \tag{10.24}$$

for the variable range hopping regime. With $C_v \propto T^3$ we obtain for the relative resistivity change:

$$\frac{\Delta\rho_{mw}}{\rho} \propto -\frac{1}{T^n} \tag{10.25}$$

with n=5 and 17/4 for the nearest neighbour hopping and variable range hopping regime, respectively. Figure 10.10 shows the relative resistivity decrease of sample

E1 at $P_{mw} = 0.2$W as a function of the reciprocal temperature. We observe that the relative effect grows somewhat steeper with the reciprocal temperature at low temperatures, as expected from $\frac{\Delta\rho_{mw}}{\rho} \propto -\frac{1}{T^5}$ as compared with $\frac{\Delta\rho_{mw}}{\rho} \propto -\frac{1}{T^{17/4}}$. Nevertheless, the experimental data do not fit completely the theory, since we have to consider the resonant microwave absorption at the lower temperatures, and the relaxational absorption, which varies only very lightly with temperature.

10.3.3 Microwave power dependence

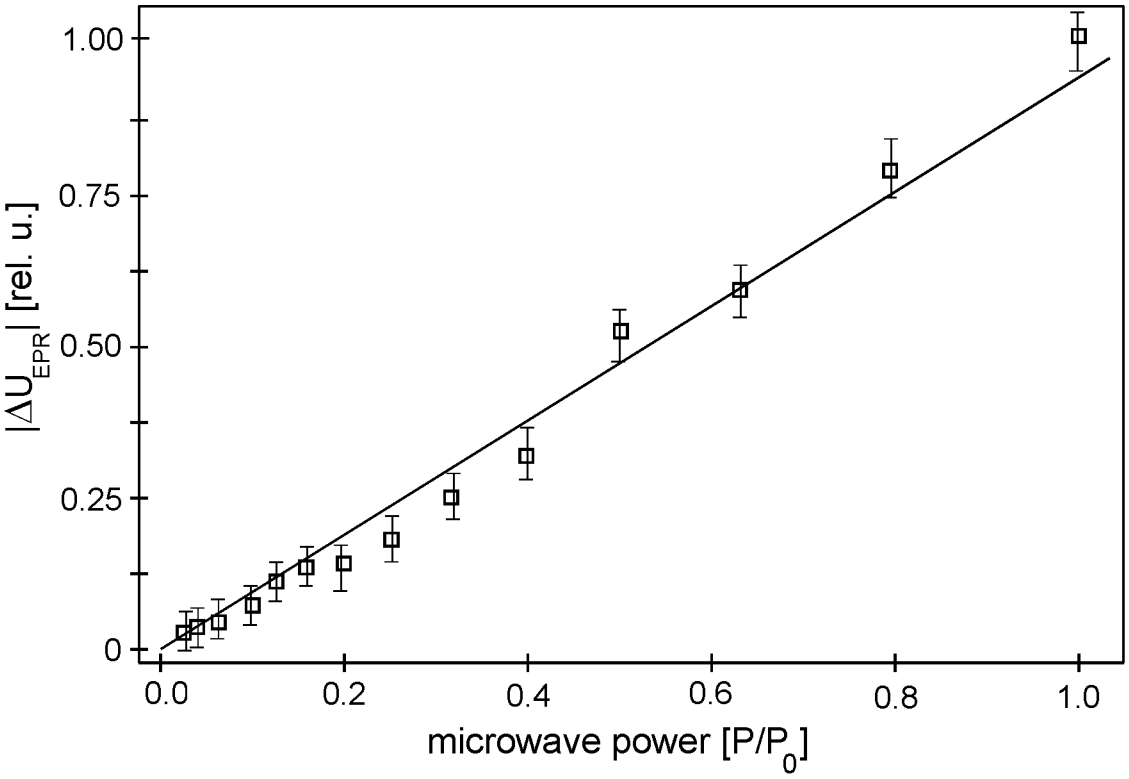

Figure 10.11: Microwave power dependence of the EDEPR signal intensity $|\Delta U_{EPR}|$ (in relative units) measured at T=6.6K and I=90μA. The squares show the experimental data, the full curve is a fit assuming a linear dependence. The maximum microwave power incident into the cavity was $P_0 = 200$mW. The corresponding signal intensity was $|\Delta U_{EPR}| \approx 10^{-2}$V. The data shown in the figure is normalized to this maximal value.

Figure 10.11 shows the microwave power dependence of the EDEPR signal measured at a temperature of 6.6K and a current of 90μA . The signal intensity $|\Delta U_{EPR}|$

exhibits a linear dependence on microwave power up to the maximum power coupled to the cavity: P_0 =200mW. The measurements were subsequently conducted at different temperatures, figure 10.12 shows the temperature dependence of the slope of the EDEPR signal-microwave power curve $\delta|\Delta U_{EPR}|/\delta P_{mw}$. We found that the slope $\delta|\Delta U_{EPR}|/\delta P_{mw}$ grows with reciprocal temperature. As shown before, the EDEPR signal resulting from a heating effect depends on temperature as:

$$|\Delta U_{EPR}| \propto \frac{P_{EPR}}{T^5} exp(\epsilon_3/k_B T)\Delta t \tag{10.26}$$

for the nearest neighbour hopping regime and as:

$$|\Delta U_{EPR}| \propto \frac{P_{EPR}}{T^{17/4}} exp\left((T_0/T)^{1/4}\right)\Delta t \tag{10.27}$$

for the variable range hopping regime, where Δt denotes the integration time. The microwave power absorbed at resonance P_{EPR} is proportional to the power incident onto the cavity P_{mw}. From equations (10.26) and (10.27) and neglecting the dependence of P_{EPR} on temperature we can write for the slope $\delta|\Delta U_{EPR}|/\delta P_{mw}$:

$$\delta|\Delta U_{EPR}|/\delta P_{mw} \propto \frac{1}{T^5} exp(\epsilon_3/k_B T)\Delta t \tag{10.28}$$

for the nearest neighbour hopping regime and

$$\delta|\Delta U_{EPR}|/\delta P_{mw} \propto \frac{1}{T^{17/4}} exp\left((T_0/T)^{1/4}\right)\Delta t \tag{10.29}$$

for the variable range hopping regime. In fig. 10.12 we actually observe two slopes, which can be explained with eq. (10.28) and (10.29). However, in contrast to the results shown in fig. 10.8, the small number of data does not suffice to decide whether the theory describes properly the experimental data.

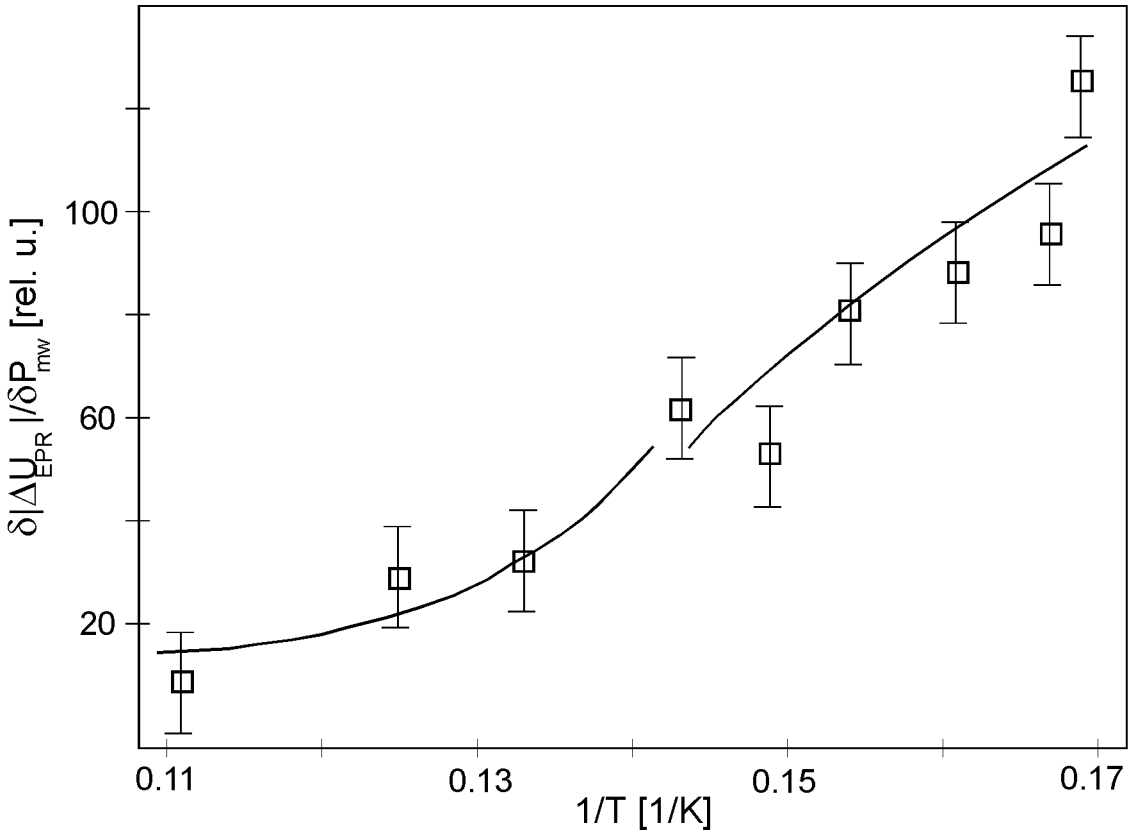

Figure 10.12: Slope of the amplitude of the EDEPR signal relative to the microwave power, $\delta|\Delta U_{EPR}|/\delta P_{mw}$, as a function of the reciprocal temperature in the microwave power range where $\Delta U_{EPR} \propto P_{mw}$. The squares show the slope obtained from experimental microwave power dependences. The lines are simulations with the expressions from eq. (10.28) and (10.29).

Measurements conducted with a new microwave source with a higher output power (YIG oscillator together with a microwave power amplifier) showed that the signal grows first linearly up to a certain (quite high) microwave power and then keeps constant or diminishes lightly. It can thus be written as:

$$|\Delta\rho_{EPR}| \propto \frac{c_1 P_{mw}}{1 + c_1 P_{mw}} \tag{10.30}$$

This is shown in fig. 10.13, where the amplitude of the EDEPR signal, $|\Delta U_{EPR}|$ is shown as a function of microwave power incident into the cavity up to $P_{mw} = 1.2$W. The experimental data are normalized to the maximal signal of about $\Delta U_{EPR} = -|\Delta U_{EPR}| \approx -10^{-2}$.

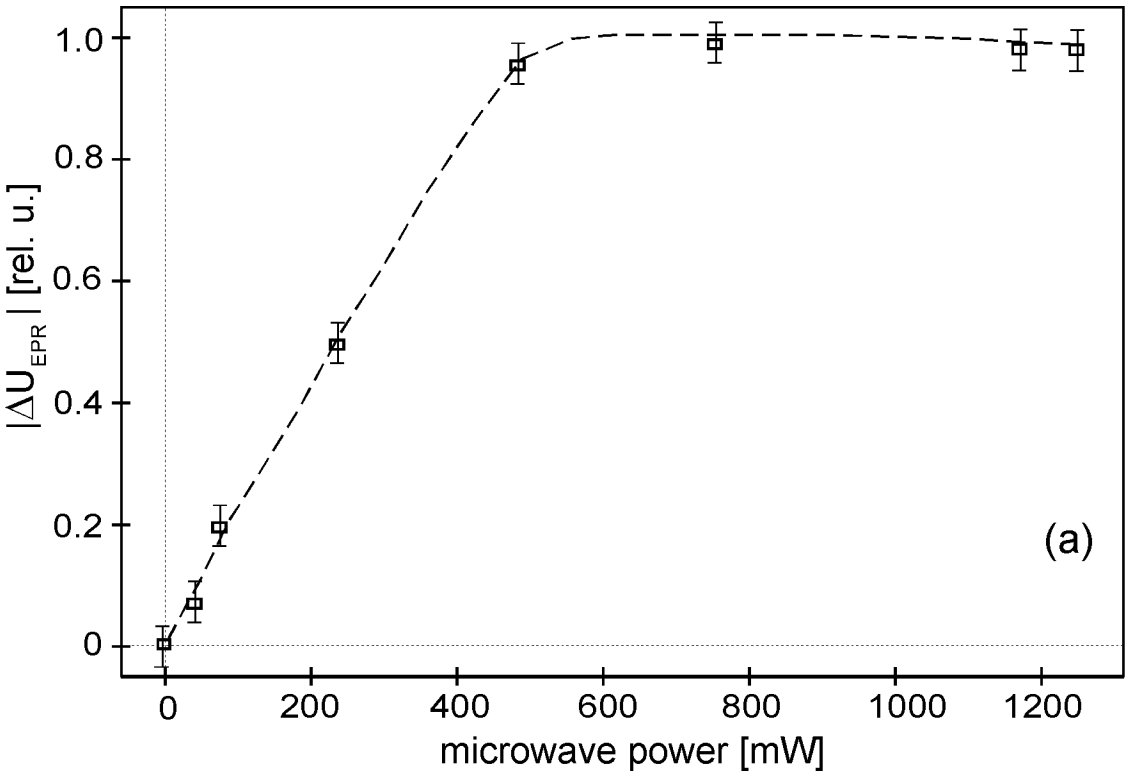

Figure 10.13: EDEPR signal intensity $|\Delta U_{EPR}|$ (in relative units) measured at T=6K and I=90μA as a function of the microwave power incident into the cavity. The circles show the experimental data, which are normalized to the maximal value.

10.3.4 Current dependence

Figure 8.9 shows the experimentally found dependence of the EDEPR signal (measured as a voltage change at constant current conditions) on the electrical current. The resonant voltage decrease $|\Delta U_{EPR}|$ was found to increase linearly with increasing current, but the noise increased as well. As a result, the optimum lies around 50μA. The relative voltage change $|\Delta U_{EDEPR}/U|$, and thus the relative resistivity change $|\Delta\rho_{EPR}/\rho|$ increased as well with increasing current, growing from $\Delta\rho_{EPR}/\rho \approx -3.3 \cdot 10^{-3}$ for I=10μA to $\Delta\rho_{EPR}/\rho \approx -9.34 \cdot 10^{-3}$ for I=200μA. An EDEPR signal arising from an EPR-induced temperature increase should not depend on the static electric field. Nevertheless, we must be careful with the interpretation of the experimental data, since the behaviour of the signal with the applied current strongly depends on the sample preparation (quality of the contacts). As a

consequence, the optimum current at a given temperature value must be searched for each sample separately.

10.4 Conclusions

In this work we have shown from electrical investigations on n-type hexagonal SiC samples with a nitrogen concentration in the range $10^{18} < N < 10^{19}$ and partial compensation that hopping conductivity dominates the charge transport at low temperatures. In one of these samples we were able to observe the variable range hopping regime besides the activated hopping regime. Other authors (e.g. [Smith 97]) had studied SiC samples with similar concentrations and observed the activated hopping regime. The obtained value for ϵ_3 was 4-5meV, in agreement with the 4meV obtained in our investigations. Unfortunately, the contact technology on silicon carbide is not as well developped as for silicon. This makes the conduction of electrical and EDEPR investigations at low temperatures difficult. For this reason we could not study the resistivity of sample B1 in the variable range hopping regime, since for such low temperatures the contacts did not work properly.

Furthermore we observed an anomalously large magnetoresistance at temperatures T< 9K with a negative and a positive contribution dominating at low and high magnetic fields, respectively. An anomalous magnetoresistance has been previosly observed in amorphous silicon and germanium [Movaghar 78] as well as crystalline GaAs [Benzaquen 88], but not in silicon carbide.

The resistivity was found to decrease under irradiation with microwaves. We found that this effect is mostly due to a heating of the sample by the microwave field, but partly due to a hopping-related effect. The magnetoresistance under microwave irradiation exhibited an anomalous behaviour, with a positive and a negative contribution dominating at low and high magnetic fields, respectively. Such a behaviour has not been reported before. The size of the effect decreases with temperature, but with a much weaker dependence than the magnetoresistance in the absence of microwaves.

Two of the samples (B1, B2) showed additional EPR lines in the middle of the hyperfine triplet lines of the nitrogen donor at the quasicubic lattice sites. Such additional lines had been reported before, and their origin had been object of controversy. We performed electrical and EDEPR investigations on sample B1 (it was not possible in the case of sample B2 due to the bad quality of the contacts to the samples at low temperatures). They allowed us to determine the concentration of donors and acceptors, and thus the position of the Fermi level at low temperatures and to identify hopping among donor states as the origin of the additional lines.

In this chapter we have discussed the experimental investigations of EDEPR of highly doped but still semiconducting silicon carbide. We have seen that the experimental results can be explained with the EPR-induced temperature increase mechanism. The microwave power absorbed by the spin system at resonance is transferred to the lattice surroundings through the spin-lattice relaxation, leading to a temperature increase. Since the resistivity in the hopping regime falls strongly with growing temperature, the EPR-induced temperature increase is observed as a resonant resistivity decrease.

Morigaki and co-workers [Morigaki 72] performed EDEPR investigations on highly doped (but still showing semiconducting behaviour) crystalline silicon and germanium doped with phosphorous. In the temperatures used for the EDEPR investigations the samples showed variable range hopping conductivity. The hyperfine structure was not resolved, as for sample E1 in our work. The EDEPR signal of sample B1 in our work, however, shows the hyperfine splitting together with the additional lines arising from hopping. The experimental results of Morigaki and co-workers were explained by Kamimura and Mott [Kamimura 76] in terms of an EPR-energy transfer to the hopping electrons (2 in fig. 10.14) due to the action of the exchange interaction and the spin-orbit interaction. Since, in contrast to our studies, the measurements were conduted at liquid helium temperatures, this mechanism could be able to explain the observed resonant resistivity decrease. Nevertheless, the EPR-induced temperature increase model presented in this work (3 in fig. 10.14) could as well contribute to or be the origin of the observed EDEPR signal.

As stated in chapter 8, the purpose of this work was to understand the mechanisms

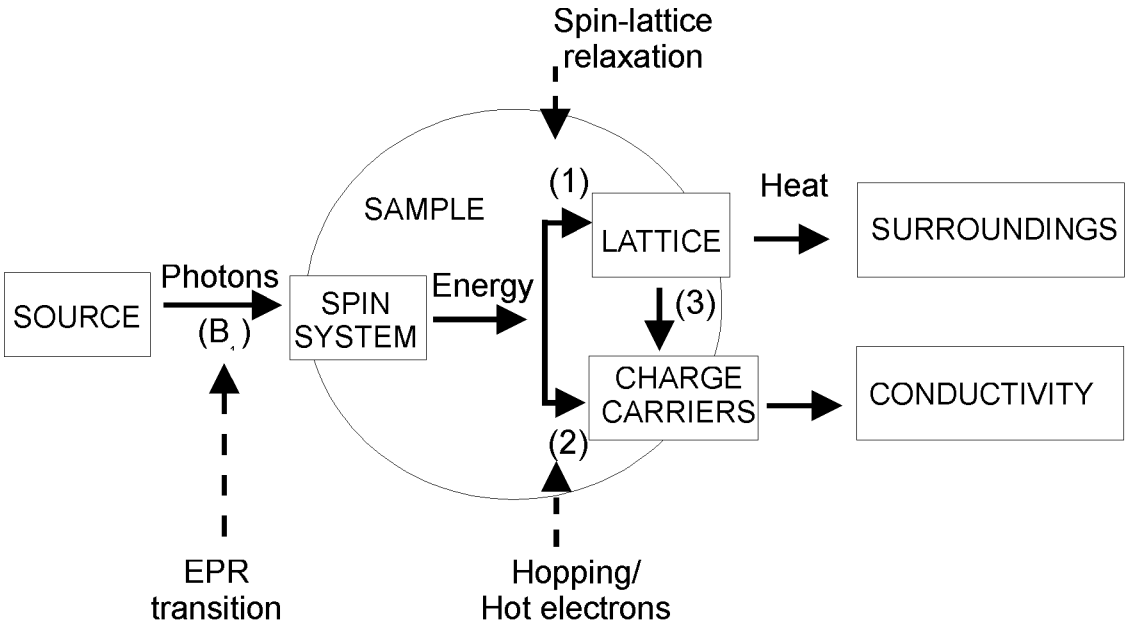

Figure 10.14: Energy flow in a magnetic resonance experiment. The spin system absorbs the photon energy and loses it by energy diffusion to the lattice (1), which allows continuing absorption of photons to occur. Energy passes from the photon source (usually a microwave oscillator) to the sample and from this to the surroundings. In absence of mechanisms for heat removal the sample temperature increases, leading to a conductivity enhancement (3). The spins can as well lose the EPR energy directly to the carriers at the Fermi level (2), inducing an increase of the conductivity.

responsible for the EDEPR of highly doped semiconducting samples. Now we can answer the questions we put in chapter 8:

1. *which structural information can be obtained from* EDEPR *studies?* As seen in the EDEPR studies of sample B1 and E1, the g-tensor values are obtained, and when the defect concentration is not too high, the hyperfine splitting and the additional lines arising from hopping are observed (sample B1). Thus, the same information is obtained as with the conventionally detected EPR for the same defect concentration. The lower signal to noise ratio of the EDEPR spectra arises mainly from the noise in the current-voltage signal due to the bad behaviour of the contacts at low temperatures.

2. *which experimental conditions (temperature, microwave power level, etc.) are*

most favourable? Low temperatures and high microwave powers are favourable. Nevertheless, not too high microwave power levels are recommendable to avoid line broadening. As regards the temperature, the relative effect $\Delta\rho_{EPR}/\rho$ grows with decreasing temperature.

3. *which systems can be studied with this technique (concentration and compensation of the samples)?* Semiconductors with defect concentrations lying in the hopping regime and partial compensation.

4. *which microscopical processes is* EDEPR *on highly doped semiconductors based on?* At resonance the spin system absorbs energy, through spin-lattice this energy is transferred to the lattice surroundings. This leads to a temperature increase at resonance conditions, enabling additional hopping.

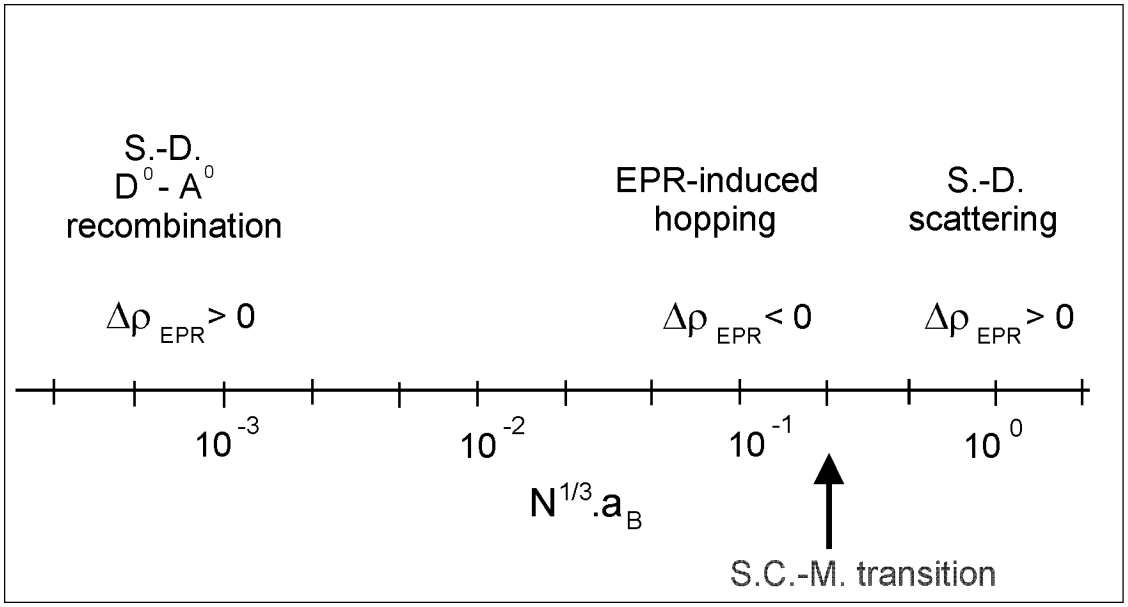

Figure 10.15: EDEPR mechanisms as a function of $N^{1/3} \cdot a_B$, where N denotes the defect concentration and a_B the Bohr radius. The transition from semiconducting to metallic behaviour (S.C.-M. transition) occurs at $N^{1/3} \cdot a_B \approx 0.3$, as noticed in chapter 3.

In this work we have discussed an EDEPR mechanism for highly doped (but still below the semiconductor-metall transition) crystalline semiconductors and proposed an enhancement of the hopping conductivity due to the EPR-induced temperature

increase as responsible for the EDEPR signal. Other authors have studied the EDEPR for very low or very high defect concentrations, and found different microscopical processes responsible for the EPR-induced resistivity change. For low defect concentrations the spin dependent donor-acceptor recombination has been found to be the mechanism underlaying EDEPR (e.g. [Stich 96]). The resistivity increases at spin resonance conditions. The optimum defect concentrations for this mechanism lie in the range $10^{11} - 10^{13}\text{cm}^{-3}$. On the other hand, for very high concentrations above the semiconductor-metal transition the resistivity has been found to increase as well at EPR conditions. In this case the EDEPR effect has been attributed to spin-dependent scattering at neutral impurities (e.g. [Honig 66]). In the concentration range between the spin-dependent recombination range and the hopping range no EDEPR results have been reported to date. We studied silicon samples with concentrations lying in this range (around 10^{15}cm^{-3}) and different compensation degrees, but we could not find any EDEPR signal. It seems that the EDEPR technique is not appropiate for the study of samples with defect concentrations lying in this range. This may be explained as follows: on the one hand, these concentrations are too low for hopping conductivity to occur, since the average distance between the defects is too large. On the other hand, these concentrations are too large for the spin-dependent recombination mechanism, since the recombination rate is too high as compared to the EPR rate. This can be illustrated as shown in fig. 10.15. Since the EDEPR mechanism for a given concentration will vary for different materials and different defect centres, it is depicted as a function of $N^{1/3} \cdot a_B$, with N the defect concentration and a_B the Bohr radius. The semiconductor-metal (S.C-M.) transition separates the region between EPR-induced hopping and spin-dependent hopping. It lies at $N_C^{1/3} \cdot a_B \approx 0.3$, as noticed in chapter 3. For the nitrogen donor at hexagonal lattice sites ($a_B = 20\mathring{A}$) this means $N_C(hex) = 3.4 \cdot 10^{18}\text{cm}^{-3}$, i.e. a total nitrogen concentration of $N_C = 6.8 \cdot 10^{18}\text{cm}^{-3}$. For the quasicubic site nitrogen donor the critical concentration is somewhat larger, since the effective Bohr radius is somewhat smaller: $a_B = 15\mathring{A}$, $N_C(cub) = 8 \cdot 10^{18}\text{cm}^{-3}$, i.e. $N_C = 1.6 \cdot 10^{19}\text{cm}^{-3}$. As to the 6H polytype, the Bohr radii of the nitrogen donors ($a_B = 13\mathring{A}$ and $10\mathring{A}$ for the hexagonal site and the quasicubic sites, respectively) are smaller than in 4H-SiC. As a result, the critical concentration for the hexagonal site donor is $N_C(hex) = 2.7 \cdot 10^{19}\text{cm}^{-3}$ and the total concentration $N_C = 8.1 \cdot 10^{19}\text{cm}^{-3}$. Thus, the critical concentration for the semiconductor-metal transition shiftes somewhat with both the lattice site and the polytype. The concentration range for which e.g. EPR-induced hopping occurs shiftes the same way, since hopping depends on the

overlap of the wavefunctions and thus on the Bohr radius. The values of the Bohr radii given above correspond to $a^{corr}_{B,eff}$, the Bohr radii obtained from the effective mass theory (EMT) $a_{B,eff}$ and corrected with a factor:

$$a^{corr}_{B,eff} = a_{B,eff} \cdot \left(\frac{\epsilon^{corr}_{EMT}}{\epsilon^{exp}} \right) \ , \tag{10.31}$$

where ϵ^{corr}_{EMT} denotes the energy level position obtained from the effective mass theory and ϵ^{exp} the corresponding experimental value [Kohn 57]. Figure 10.16 illustrates the different EDEPR mechanisms as a function of nitrogen concentration for 4H-SiC. The hopping regime lies in the range between $10^{18} - 10^{19}\text{cm}^{-3}$. Finally, it must be said that besides the concentration of the majority imprities, the degree of compensation must be taken into consideration. For the donor-acceptor recombination the concentration of donor-acceptor pairs is the important parameter. In the case of hopping, unoccupied sites and thus compensating impurities are needed.

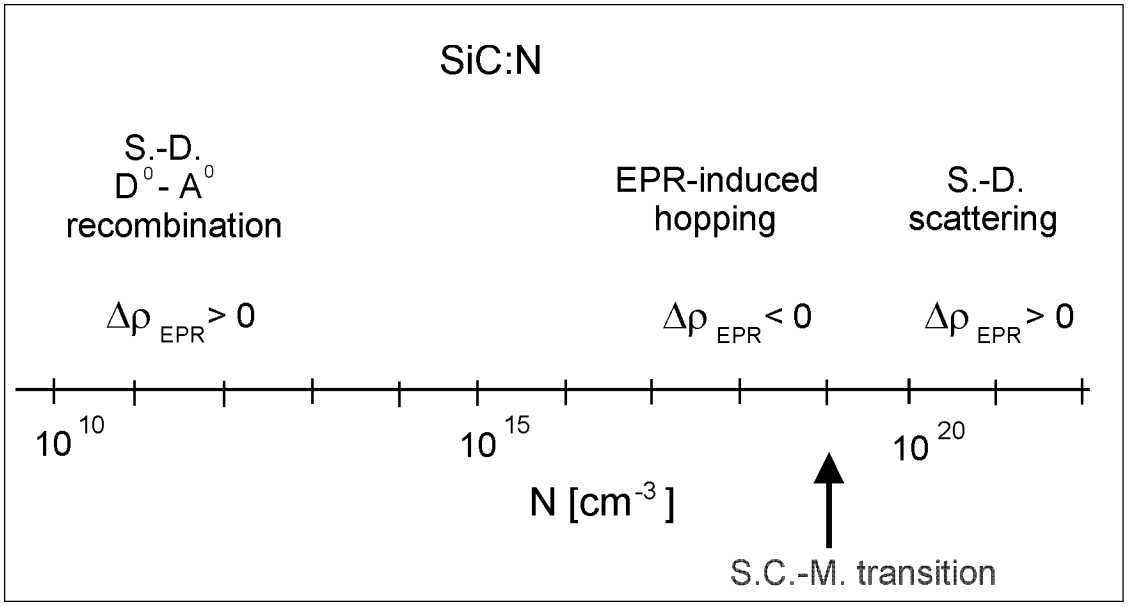

Figure 10.16: EDEPR mechanisms as a function of defect concentration for n-type 4H-SiC:N. The transition from semiconducting to metallic behaviour (S.C.-M. transition) occurs at $N^{1/3} \cdot a_B \approx 0.3$, as noticed in chapter 3.

Chapter 11

Further EDEPR investigations

In the previous chapters we have shown studies of the EDEPR signal of sample E1 measured as a resistivity decrease induced by EPR transitions of the nitrogen donor. Nevertheless, for certain current/voltage conditions further lines besides the EDEPR line arising from nitrogen appear, as shown in fig. 11.1. Figure 11.1 shows the EDEPR signal of sample E1 measured in the dark as a voltage change at constant current conditions at T=9K, ν_{mw} =10.02GHz and for two different current values: I=10μA and 100μA. Sample E1 is an epitaxial layer, the nitrogen concentration of substrate being three orders of magnitude larger than that of the layer. As a result, the conductivity of the substrate is much larger than that of the layer. The electrical contacts were prepared on the layer. This was, however, only 7μm thick. As a consequence, the electrical current flows through both layer and substrate. A voltage gradient arises between layer and substrate due to the fact that the substrate resistivity is much lower than that of the layer, generating a diffusion current and a recombination current between layer and substrate, as illustrated in fig. 11.2. Thus, we have a similar situation as in a diode, and we may obtain an EDEPR signal in the same way as has been observed in diodes. EDEPR has been observed in p-n diodes (e.g. [Solomon 76], [Stich 93]) and in gate controlled diodes [Kaplan 80], where an increase in the recombination rate was seen as an increase in the forward bias diode current. The mechanism underlaying the EDEPR in p-n junctions is based on spin dependent recombination processes, but in contrast to the donor-acceptor spin dependent recombination briefly outlined in chapter 4, in this case charge carriers recombine directly at a paramagnetic deep defect without the need for other effects nearby (for review see e.g. [Rong 91]). When the recombination current is involved in the spin-dependent recombination of the charge carriers

at paramagnetic defects [Solomon 76] an EDEPR signal can be observed. In order to obtain a significant EDEPR signal, the current-voltage characteristic must be given by the recombination current. Therefore, the EDEPR signal depends strongly on the current-voltage conditions, as we observed in our experiments on sample E1. The EDEPR signal of sample B1, which is a bulk crystal, did not show such a behaviour for any current value.

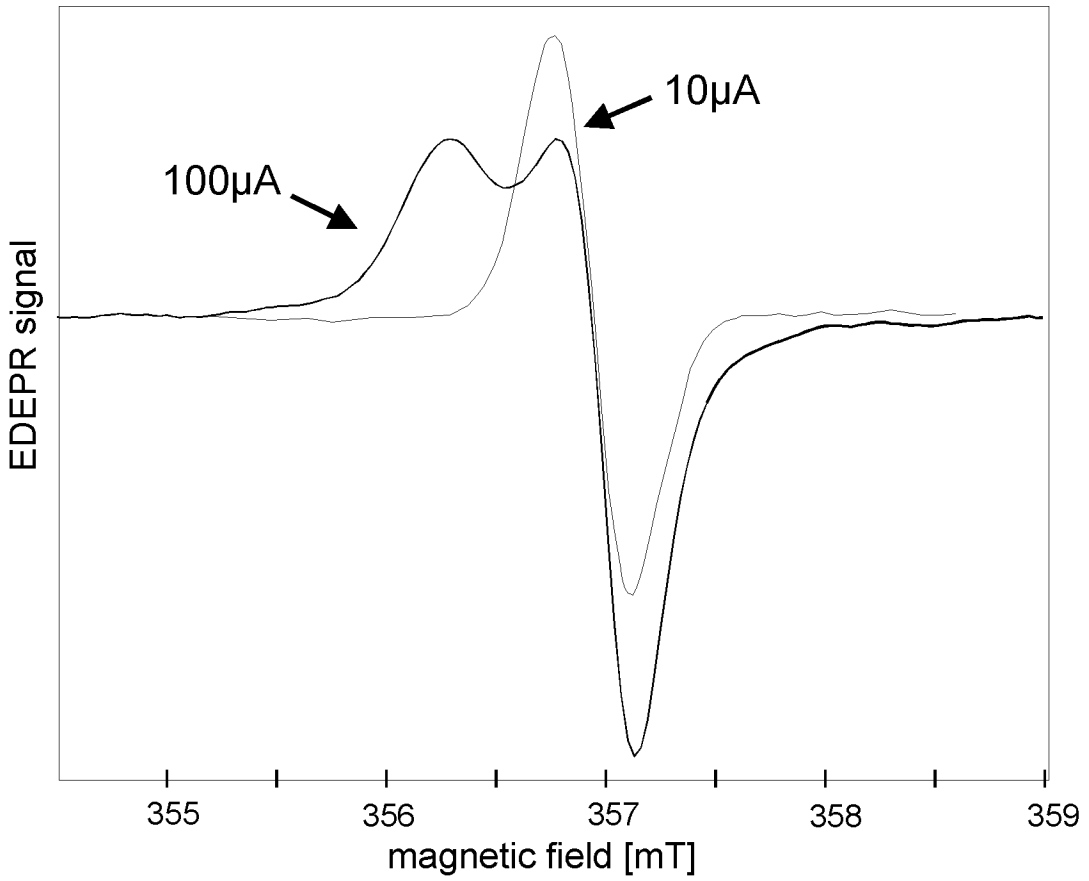

Figure 11.1: EDEPR signal of sample E1 measured in the dark as a voltange change at constant current conditions at T=9K, ν_{mw} =10.02GHz and for two different current values: I=10μA and 100μA. The crystallographic c-axis of the sample formed an angle of -10 deg with the magnetic field.

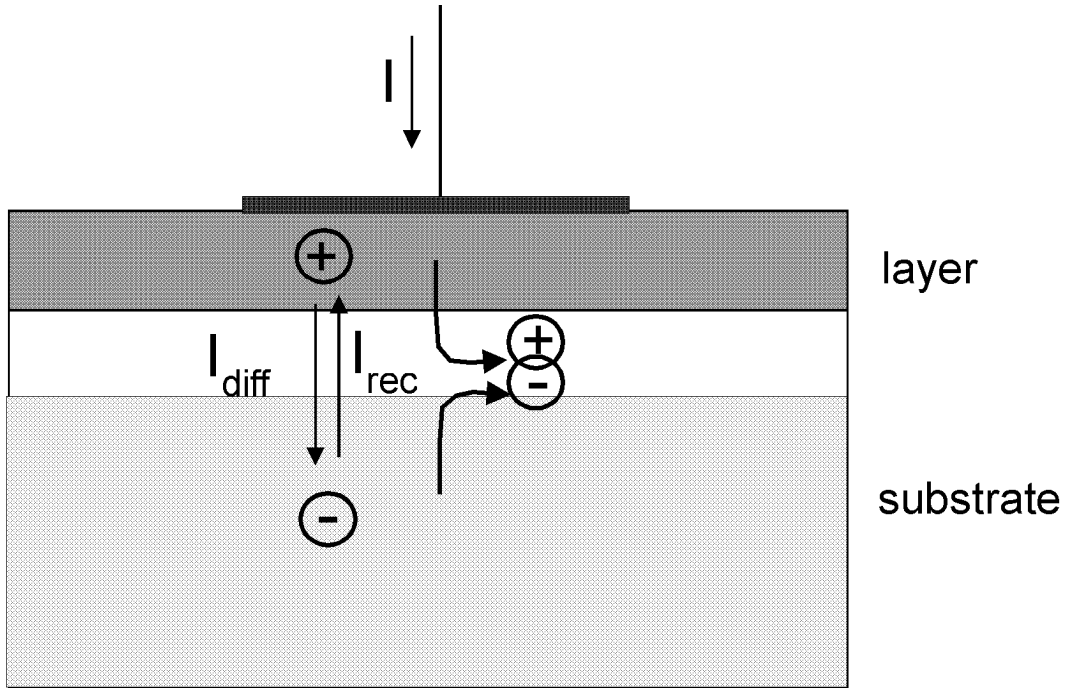

Figure 11.2: Schematic illustration of the potential gradient in the epitaxial layer. Analogous to the case of a p-n junction, the current through layer and substrate is composed of the diffusion current I_{diff} and the recombination current I_{rec}.

11.1 EDEPR angular dependence

Figure 11.3 shows the EDEPR spectrum of sample E1 measured in the dark at a temperature of T=9K, a current of I=100μA, a microwave frequency of ν =10.02GHz and a microwave power of P_{mw} =80mW. The crystallographic c-axis of the sample formed an angle of -10 deg with the magnetic field. The full line corresponds to the measured EDEPR spectrum, the dashed lines are a simulation yielding two Gaussian lines with a linewidth of 0.4mT and are centred at 356.4mT and 356.9mT, respectively.

We recorded the angular dependence of the EDEPR signal of sample E1, measured in the dark at a temperature of 9K, a current of 100μA, a microwave frequency of 10.02GHz and a microwave power of 80mW. The sample was rotated from -80 deg to 180 deg, with Θ =0 corresponding to a position where the crystallographic c-axis is parallel to the magnetic field and Θ =90 corresponding to the c-axis perpendicular to the magnetic field. We found several lines with different intensities in the interval

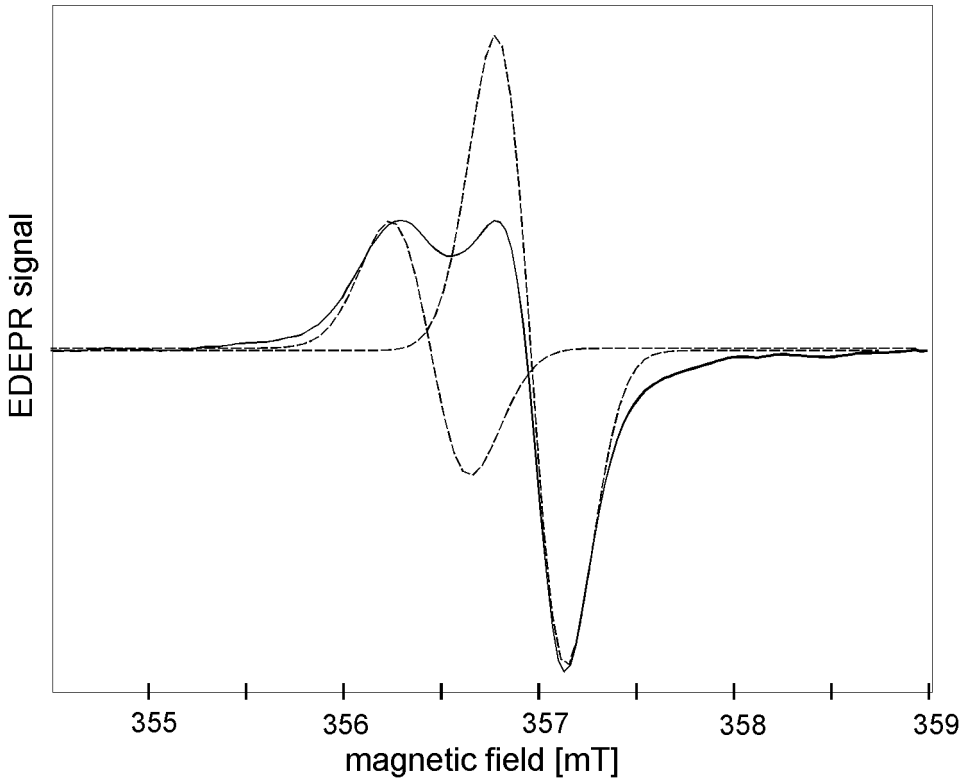

Figure 11.3: EDEPR spectrum of sample E1 measured in the dark at 9K, I=100μA and 10.02 GHz. The crystallographic c-axis of the sample formed an angle of -10 deg with the magnetic field. The full line corresponds to the measured EDEPR spectrum, the dashed lines are a simulation yielding two Gaussian lines centered at 356.4mT and 356.9mT, respectively.

$355\text{mT} \leq B \leq 359\text{mT}$.

Figure 11.4 shows the peak data corresponding to the above mentioned EDEPR angular dependence together with simulations (dashed lines) with the EPR parameters of the most common dopants in SiC besides nitrogen (boron and phosphorous) as well as the silicon- and carbon-dangling bonds. The corresponding parameters, together with their references, are given in table 8.1. The peak data (squares) represent the position of the EDEPR lines. Large and small squares stand for large and small signal amplitudes, respectively. For certain orientations the lines overlapped, in these cases the peak data were obtained by making a fitting with Gaussian lines, as shown in fig. 11.3. The full lines represent fittings to the experimental data. Curve (1), which fits very well to the experimental data, is a simulation with the

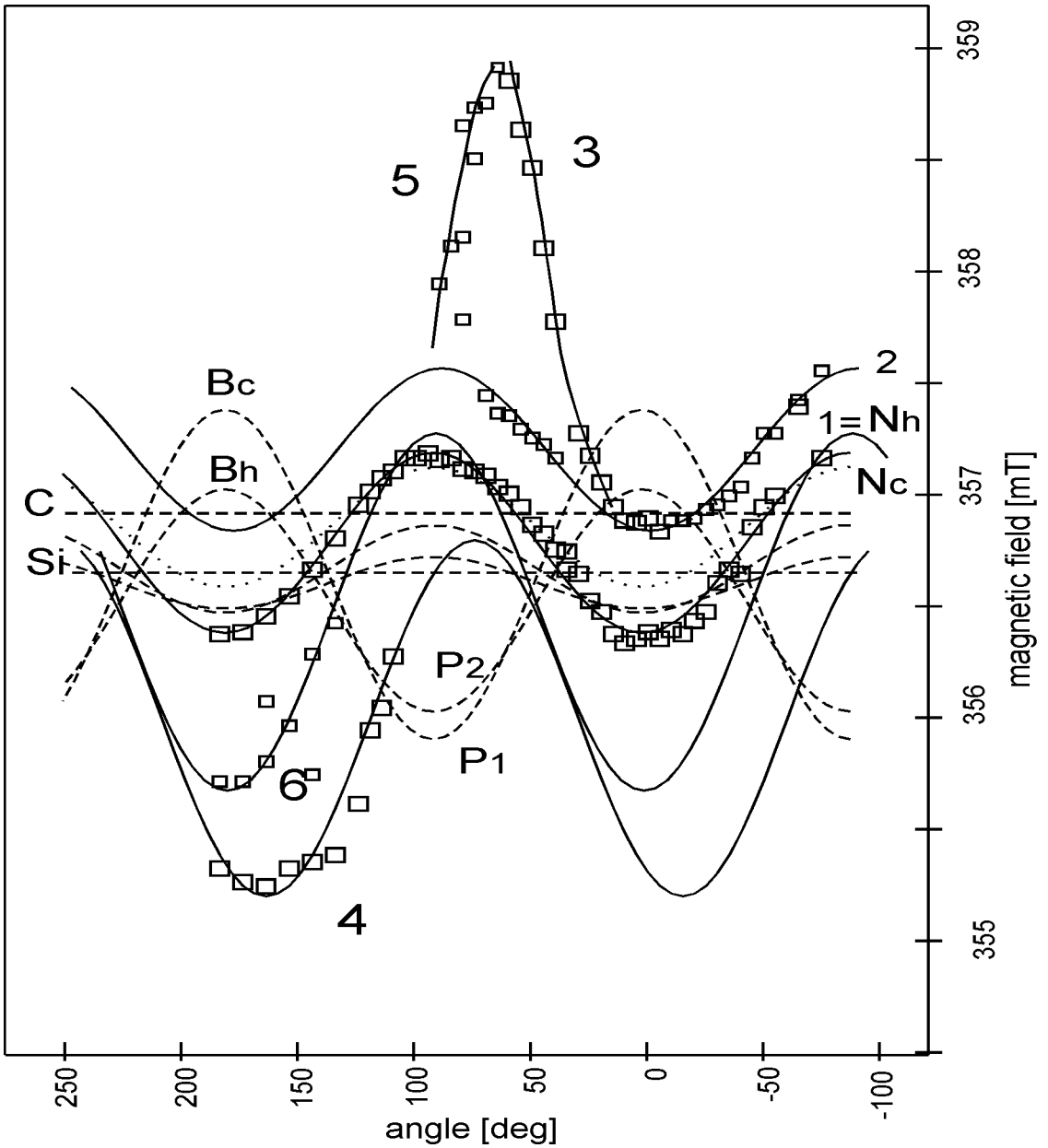

Figure 11.4: Rotation pattern of the EDEPR spectrum measured in the dark at 9K, I=100μA and 10.02 GHz. The full curves (1 to 6) are the result of simulations with the parameters given in the text. The dotted curve is a simulation with the EPR parameters for nitrogen at the cubic lattice site. The dashed curves are simulations with the literature data for the EPR parameters of the typical impurities boron (B_c, B_h) and phosphorus (P_1, P_2) (without hf splitting) and of the silicon- and carbon-dangling bonds (Si and C, respectively). The squares show the position of the EDEPR signals.

literature EPR parameters of the nitrogen donor at the hexagonal site. The dotted line is a simulation with the EPR parameters of the nitrogen donor at the quasicubic site (only the central line of the triplet is drawn). The difference in the g-factors of both nitrogen donors is rather small, and in X-band their respective signals are difficult to separate. We see, however, that the anisotropy of the experimental line fits much better to that of the hexagonal site, rather than to that of the quasicubic site. The hyperfine structure of nitrogen is not resolved. Such a behaviour has been reported before for samples with a high nitrogen concentration. Conventional EPR measurements at a lower microwave power showed the two outer hyperfine lines of the nitrogen donor at the quasicubic site. The signal amplitude of these lines was a hundredth of the amplitude of the central line.

Curves (2) to (6) were obtained from fittings of the experimental peak data. The corresponding EDEPR lines have one thing in common: they are only observed for certain orientations of the sample with respect to the direction of the static magnetic field . Curve (2) exhibits an anisotropy very similar to that of the nitrogen donor at the hexagonal position. This could be attributed to a nitrogen donor in another polytype, i.e. to the presence of crystallites from a polytype different from 4H. The obtained g factor was compared with literature data for the nitrogen donor in other common SiC-polytypes, but no agreement was found.

Curves (3) to (6) show a stronger anisotropy than curves (1) and (2). In the case of (4) and (5), it is striking that the orientations for which the magnetic field position of the resonance is maximum or minimum do not agree with those of the nitrogen donor. Their principal axis systems are shifted about 15 degrees with respect to those of nitrogen.

When considering the fact that the sample is an epitaxial layer, then we can understand why some of the signals are shifted about 15 degrees from the others. This angle would correspond to the so-called "off-angle" from epitaxial growth. In this case, the c-axis of the 7μm layer forms an angle of 15 degrees with the c-axis of the substrate. Since the substrate exhibits a higher conductivity than the layer and the electrical contacts were fabricated on the layer, the electrical current will flow through both the layer and the substrate. As a result, we see the EDEPR signal of paramagnetic centres from both the layer and the substrate, with orientations

shifted by 15 degrees from each other.

Thus, signals (1), (2) and (6) would arise from the substrate and signals (3) to (5) from the layer or viceversa. The EDEPR spectrum of nitrogen, a broad central line with an amplitude much larger than those of the outer hyperfine lines, points to a nitrogen concentration of $N \approx 10^{18}\text{cm}^{-3}$ [Veinger 67]. It thus originates from the substrate, since the nitrogen concentrations in layer and substrate are $N \approx 10^{16}\text{cm}^{-3}$ $N \approx 10^{18}\text{cm}^{-3}$, respectively [Dalibor 96]. Thus signals (1), (2) and (5) would, in fact, arise from centres in the substrate and the others from centres in the layer or the interface between layer and substrate.

The g-values obtained from the fitting to the experimental data (curves (2) to (5) were compared to the literature data for defects in 4H-SiC, but no agreement could be found. As the sample is an epitaxial layer, a high concentration of dangling bonds was expected to be present in the interface between 4H-SiC substrate and 4H-SiC layer. For that reason we made a simulation with the EPR literature values for the carbon- and the silicon-dangling bonds ($g = 2.0025$ and $g = 2.0040$, respectively). Nevertheless, EPR signals arising from dangling bonds are reported to be isotropic broad signals, in contrast to our EDEPR spectra. The EDEPR lines, except the nitrogen line, may correspond to structural defects in the layer-substrate interface. They can only be observed at certain current-voltage conditions.

The conventional EPR angular dependence of sample E1 showed the EPR spectrum of the nitrogen donor, together with a further EPR line exhibiting a higher anisotropy ($g_{||}$=2.0019 ,$g_{\perp} \ll g_{||}$). This line is identical with the EDEPR line measured in the same sample and denoted with (3) in fig. 11.4. The outer hyperfine lines of the nitrogen donor spectrum could be detected. Their amplitude was two orders of magnitude smaller than that of the central line.

11.2 K-band investigations

Further EPR investigations at a higher microwave frequency (K-band, 25GHz) were performed for a better understanding of the EDEPR spectrum measured at X-band.

Centre	$g_{\|\|}$	$g_\perp$	a/h [MHz]	b/h [MHz]	reference
N_h	2.0055(2)	2.0010(2)	2.900(1)	0.080(1)	[Kalabukhova 87]
N_k	2.0043(2)	2.0013(2)	50.970(1)	0.004(1)	[Kalabukhova 87]
B_k	2.0063(2)	2.0046(2)			[Greulich-Weber 97]
B_h	2.0019(2)	2.0070(2)			[Greulich-Weber 97]
P_1	2.0049	2.0031	1.562	0.894	[Feege 95]
P_2	2.0041	2.0028	8.7	4.2	[Feege 95]
(2)	2.003	1.997			this work
(3)	2.0019	$\approx$0			this work
(4)	2.013	2.004			this work
(5)	2.015	1.991			this work
(6)	2.009	2.000			this work

Table 11.1: g values for common impurity centres in 4H-SiC and for the EDEPR lines measured in this work. The values for the phosphorous centres correspond to the 6H-polytype. The values for the 4H-polytype, however, are expected to be similar.

The sample was rotated from -10 to 110 deg., 0deg. being the orientation for which the crystallographic c-axis is parallel to the direction of the static magnetic field. Figure 11.5 shows the corresponding peak data together with simulations using the EPR parameters of the nitrogen donor at the hexagonal site (full lines) and the nitrogen donor at the quasicubic site (dashed lines). The EPR lines corresponding to the nitrogen donor (large squares) had a much larger amplitude than the other EPR lines. The outer hyperfine lines of the spectrum of nitrogen at the quasicubic lattice site were observed when lower microwave power levels were applied. The dotted-dashed lines in fig. 11.5 represent fittings of the experimental data.

As in the EDEPR-angular dependence at 10GHz, we observe lines (2 and 3) exhibiting the same anisotropy as the nitrogen donor. Moreover, a further line with a larger anisotropy is observed, the high symmetry-orientations of which are shifted by about 15 deg from those of nitrogen. The line with $g_{||}$=2.0019 and $g_\perp \ll g_{||}$, which had been observed in X-band EPR and EDEPR, could not be detected. A possible explanation for this could be the different microwave power levels used in X-band and K-band. The maximal microwave power that can be coupled to the K-band cavity is $\leq 0.5mW$, whereas for the X-band measurements the microwave power incident into the cavity was $\geq$ 100mW. The low microwave powers available at the K-band spectrometer could also be the reason why no K-band EDEPR signal could

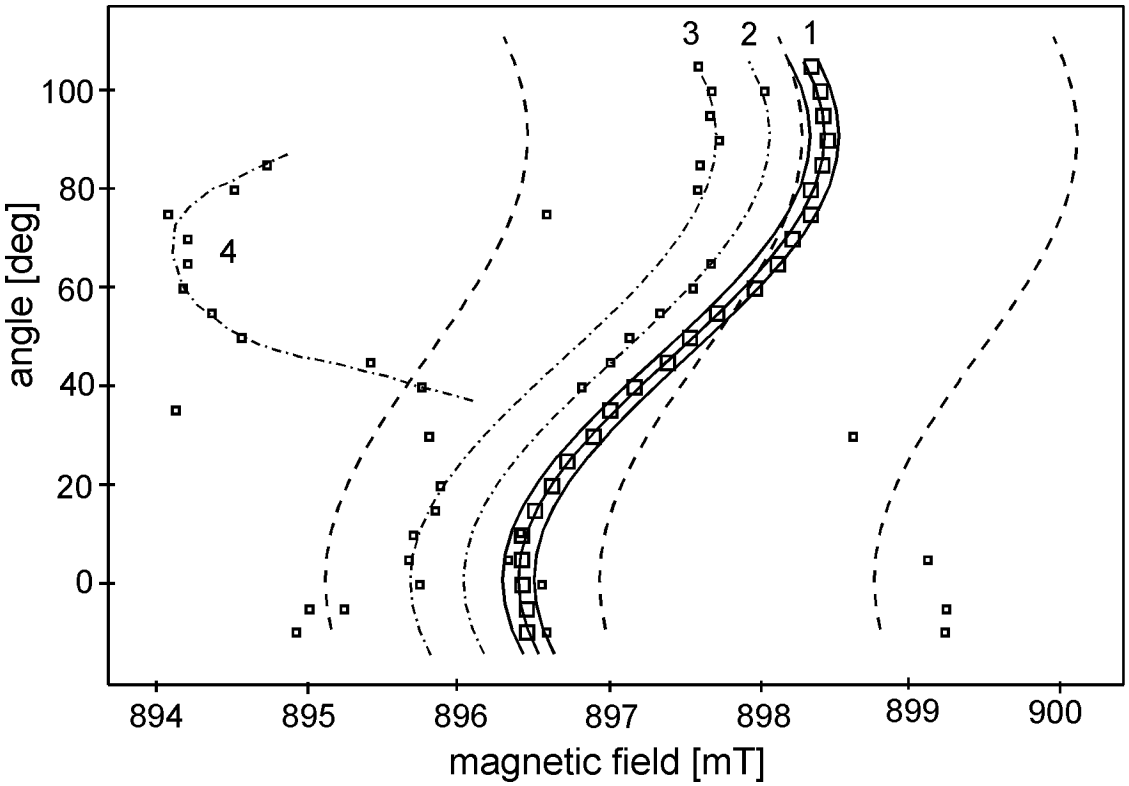

Figure 11.5: Rotation pattern of the EPR spectrum of sample E1 measured in the dark at 7K and 25.11 GHz. The squares represent the experimental data, the full and dotted-dashed curves are the result of simulations with the EPR parameters for the nitrogen donor at the hexagonal and the quasicubic site, respectively. The dotted-dashed lines are fittings of the experimental peak data.

be detected. Moreover, the influence of the nickel contacts on the quality factor of the cavity was much stronger than in X-band, since the K-band cavity is smaller, leading to high noise component in the current-voltage signal.

11.3 Conclusions

In this chapter we have shown that for certain current values new EDEPR lines appear (see fig. 11.4). This, together with the large difference in the conductivity of layer and substrate, points to a situation similar to that found in p-n junctions, where an EDEPR signal has only been observed for certain current values, for which the current-voltage characteristic is given by the recombination current. Therefore,

at a current of e.g. I=100μA, at which the EDEPR angular dependence shown in fig. 11.4 was recorded, the recombination current would dominate and this would lead to the appearance of new EDEPR lines (corresponding to defects at which the charge carriers recombine) added to the EDEPR signal of the nitrogen donor in the substrate.

In the last years EDEPR investigations of devices have been performed by several groups, e.g. EDEPR measurements on single quantum well diodes [Carlos 98, Bayerl 98], but in many cases only a single isotropic broad line has been observed, delivering no structural information of the defects.

In our EDEPR results, the magnetic-field position of the additional lines as well their intensity exhibited a strong angular dependence. Moreover, the high-symmetry orientations of some of these EDEPR lines was shifted about 15 degrees from those of the signal from the nitrogen donor in the substrate. Similar lines could be observed by conventionally-detected K-band EPR investigations (see fig. 11.5), their intensity being much smaller than that of the nitrogen donor-EPR signal. These lines may be attributed to structural defects in the substrate-layer interface.

Chapter 12

Abstract

Electron paramagnetic resonance (EPR) methods are powerful techniques for the determination of defect structures. For the study of small or low resistivity samples (epitaxial layers, diodes, etc.) electrically detected electron paramagnetic resonance (EDEPR) offers several advantages over conventionally detected EPR: it delivers information on microscopic defect structure with an enhanced detection sensitivity and the expensive microwave detection technique becomes superfluous. Up to now it has been successfully used for the investigation of amorphous and porous semiconductors as well as irradiated crystalline semiconductors. However, in the case of non-irradiated crystalline samples it was not clear which concentrations of donors and acceptors were needed for the observation of an EDEPR signal. The aim of this work was to deepen our knowledge of the EDEPR method, in particular for the case of highly doped crystalline semiconductors, in order to be able to predict the optimal conditions for its use. For this purpose, different n-type bulk and epitaxial silicon carbide samples with high nitrogen concentrations were studied by means of electrical characterization techniques, EPR and EDEPR.

To begin with, electrical investigations were conducted which aimed at the determination of the defect concentration and compensation as well as the dominating charge transport mechanism at the low temperatures typical for EDEPR investigations. Furthermore the influence of microwave irradiation was investigated. Studies of the temperature and magnetic field dependence of the resistivity showed that hopping was the dominating conduction process at low temperatures for partly compensated samples with a nitrogen concentration N_D in the range of $10^{18}\mathrm{cm}^{-3} < N < 10^{19}\mathrm{cm}^{-3}$.

The EDEPR signal was measured in the dark and was found to correspond to a resisitivity decrease at spin resonance conditions, in contrast to the case of the donor acceptor recombination. The order of magnitude of the EDEPR effect at optimum conditions was $\Delta\rho_{EPR}/\rho \approx 10^{-3}$. Experimental studies of the EDEPR signal behaviour with parameters such as temperature, microwave power, modulation frequency and defect concentration provided the necessary information to discuss the microscopical processes responsible for the resistivity decrease at spin resonance conditions. We found that the same structural information is obtained from EPR and EDEPR studies.

In contrast to an earlier proposed mechanism, namely the transfer of the EPR energy to the hopping electrons by the combined action of the exchange interaction and the spin-orbit interaction, we discuss a heating of the sample at resonance conditions as responsible for the resonant resistivity decrease. At resonance the spin system absorbs microwave energy, which is transferred to the surroundings by relaxation processes. As a result, the crystal is heated at resonance conditions. An experiment was carried out on purpose to see whether the sample temperature increases at resonance. A direct measurement of the resonant temperature change was performed. In fact a temperature increase at spin resonance conditions was found.

In samples with a nitrogen concentration of about $1 - 3 \cdot 10^{18}\mathrm{cm}^{-3}$ two additional EPR/EDEPR lines were found, as compared to the hyperfine triplet spectra (I=1 for ^{14}N) for low defect concentrations. The additional lines were situated exactly in the middle between two nitrogen hyperfine lines. Such additional lines have been reported before, and their origin has been subject of controversy. Not two but six additional EPR lines, the position of which corresponds to $\pm 1/4$, $1/2$ and $3/4$ of the hyperfine splitting of nitrogen at the quasicubic position, were found in a further sample. From the experimentally determined temperature dependence of the resistivity of these samples we show that hopping dominates the conductivity at low temperatures. Thus, we show that the additional EPR lines arise from a donor-electron hopping between two or four nitrogens, respectively.

For certain current conditions one of the samples, which was an epitaxial layer, behaved as a p-n junction due to the difference in the conductivity of layer and

substrate and new EDEPR lines appeared. We attribute them to defects in the layer-substrate interface, at which the charge carriers recombine in a spin dependent way.

Bibliography

[Achtziger 97] Achtziger N and Witthuhn W, Appl. Phys. Lett. **71** (1), 110 (1985).

[Anderson 53] Anderson P W and Weiss P-R, Rev. Mod. Phys. **25**, 269 (1953).

[Baranov 98] Baranov P G, Il'in I V, and Mokhov E N, Phys. Solid State **40** (1), 31 (1998).

[Bayerl 98] Bayerl M-W, Brandt M-S, Angerer H, Ambacher O and Stutzmann M, Phys. Stat. Sol. (b) **210**, 389 (1998).

[Benzaquen 88] Benzaquen Phys. Rev. B **38**, 10933 (1988).

[Biskupski 80] Biskupski G, Dubois H, Laborde O, and Zotos X, Phil. Mag. **B42**, 19 (1980).

[Bloch 46] Bloch F, Phys. Rev. **70**, 460 (1946).

[Bloembergen 48] Bloembergen N, Purcell E-M and Pound R-V, Phys. Rev. **73**, 679 (1948).

[Boettger 85] Boettger H and Bryksin V V, *Hopping Conduction* Akademie-Verlag Berlin (1985).

[Bourgoin 79] Bourgoin J C, Frossati G, Ravex A, Thoulouze D, Vandorpe M, and Vaksmann B, Phys. Stat. Sol. A **92**, 585, (1979).

[Brandt 92] Brandt M S, Thesis, Max-Planck-Institut für Festkörperforschung, Stuttgart (1992).

[Brandt 98] Brandt M S, Bayerl M W, Stutzmann M, and Graeff C F O, Journal of Non-Crystalline Solids **227-30**, 343-7 (1998).

[Busch 46] Busch G and Labhart H, Helv. Phys. Acta **19**, 463 (1946).

[Burgemeister 79] Burgemeister E A, von Muench W and Pettenpaul E, J. Appl. Phys. **50**, 5790 (1979).

[Carlos 97] Carlos W E and Nakamura S, Appl. Phys. Lett. **70** (15) 2019 (1997).

[Carlos 98] Carlos W E and Nakamura S, Journal of Crystal Growth, **189-190** 794 (1998).

[Castner 59] Castner T G, Phys. Rev. **115**, 1506 (1959).

[Christmann 92] Christmann P, Wetzel C, Meyer B-K, Asenov A and Endrö s, Appl. Phys. Lett. **60** (15), 1857 (1992).

[Chandi 88] Chandi D J and Chang K J, Phys. Rev. Lett. **61**, 873 (1988).

[Chroboczed 66] Chroboczed J A and Sladek R J, Phys. Rev. **151**, 595 (1966).

[Coates 75] Coates R, and Mitchell E W J, Adv. Phys. **24**, 593 (1975).

[Crofton 97] Crofton J, Porter L M, and Williams J R, Phys. Stat. Sol. (b) **202** 581 (1997).

[Dalibor 96] Dalibor T, private communication

[Dean 77] Dean P-J, Choyke W-J and Patrick L, Journal of Luminescence **15**, 299 (1977).

[Dersch 84] Dersch H and Schweitzer L, Phil. Mag. B **50**, 397 (1984).

[Edwards 78] Edwards P-P and Sienko MJ, Phys. Rev. **B17**, 2575 (1978).

[Evwaraye 96] Evwaraye A O, Smith S R, Mitchel W C, and Roth M D, J. Appl. Phys. Lett. **68** 22, 3159 (1996).

[Feege 95] Feege M, Doctoral Thesis, Universität-GH Paderborn (1995).

[Fritzsche 60] Fritzsche H and Cuevas M, Phys. Rev. **119**, 1238 (1960).

[Fukuyama 79] Fukuyama H and Yosida K, J. Phys. Soc. Jpn. **46**, 102 (1979).

[Galperin 86] Galperin Y M and Priev E Y, Sov. Phys. Solid State **28**, 385 (1986).

[Gershenzon 74] Gershenzon G M, Kurilenko I N, Litvak-Gorskaya L B, Sov. Phys. Semicond. **8** 689 (1974).

[Götz 93] Götz W, Schöner A, and Pensl G, J. Appl. Phys. **73** (7), 3332 (1993).

[Graeff 96] Graeff C F O, Kawachi G, Brandt M S, Stutzman M and Powell M J, J. of Non-Crystalline Solids **198-200**, 1117 (1996).

[Greiner 91] Greiner W, *Klassische Elektrodynamik*, Verlag Harri Deutsch (1991).

[Greulich-Weber 93] Greulich-Weber S, Mat. Sci. Forum, ICDS 17, 143-147 (1993).

[Greulich-Weber 95] Greulich-Weber S, Feege M, Spaeth J-M, Kalabukhova E-N, Lukin S-N and Mokhov, Solid State Comm. **93** (5), 393 (1995).

[Greulich-Weber 97] Greulich-Weber S, Phys. Stat. Sol. (a), **162**, 95 (1997).

[Gueron 65] Gueron M and Solomon I, Phys. Rev. Letters **15** 667 (1965).

[Halbo 68] Halbo L and Sladek R J, Phys. Rev. **173**, 794 (1968).

[Harris 95] Harris G L, Kelner G and Shur M, *Properties of Silicon Carbide*, Emis Datareviews Series No. 13, INSPEC, London (1995).

[Hedgcock 70] Hedgcock F T, Raudorf T W, Solid State Commun. **8**, 1819 (1970).

[Hemmingsson 98] Hemmingsson C G, Son N T, Ellisom A, Zhang J and Janzén E, Phys. Rev B **58** 16, R10119 (1998).

[Honig 66] Honig A and Maxwell R, *Proc. Intern. Conf. on Physics of Semiconductors, Kyoto, 1966* j. Phys. Soc. Japan **21** 559 (1966).

[Honig 66a] Honig A, Phys. Rev. Lett. **17** (4), 186 (1966).

[Hung 50] Hung C S and Gleissman J R, Phys. Re. **79** 726, (1950).

[Ionov 83] Ionov A N, Shlimak I S, and Matveev M N, Solid State Commun. **47**, 763 (1983).

[Johnson 74] Johnson J A and Lark-Horovitz K, Phys. Rev. **72**, 531 (1974).

[Käckell 94] Käckell P, Wenzien B., and Bechstedt F, Phys. Rev. B **50** 15, 10761 (1994).

[Kalabukhova 87] Kalabukhova E N, Kabdin N N and Lukin S N, Sov. Phys. Solid State **29** (8), 1461 (1987).

[Kalabukhova 90] Kalabukhova E N, Lukin S N, Shanina B D, Artamonov L V, and Mokhov E N, Sov. Phys. Solid State **32** 3, 482 (1990).

[Kamimura 76] Kamimura H and Mott N, J. Phys. Soc. Japan **40**, 1351 (1976).

[Kamimura 89] Kamimura H and Aoki H *The Physics of Interacting Electrons in Disordered Systems* Oxford Science Publications, New York (1989).

[Kaplan 78] Kaplan D, Solomon I and Mott N-F Le Journal de Physique-Lettres, **39**, L51-L54 (1978).

[Kaplan 80] Kaplan D and Pepper M Solid State Commun., **34**, 803-805 (1980).

[Kawata 80] Kawata A, J. Phys. Soc. Japan. **49**, 628 (1980).

[Kishimoto 77] Kishimoto N and Morigaki K, J. Phys. Soc. Japan. **42** 1, 137 (1977).

[Kishimoto 81] Kishimoto N, Morigaki K, and Murakami K, J. Phys. Soc. Japan **50**, 1970-1977 (1981).

[Kohn 57] Kohn W, Sol. State Phys. **5**, 257 (1957).

[Koshchenko 79] Koschenko V I, Demidenko A F, Prokof'eva N K, Yachmenev V E and Radchenko AF, Inorganic Materials (USSR) **15** 1017-9 (1979).

[Laiho 95] Laiho R, Vlasenko L S and Vlasenko M P, Material Science Forum, **196-201** (1), 517 (1995).

[Laiho 98] Laiho R, Afanasjev M M, Vlasenko M P and Vlasenko L S, Phys. Rev. Lett. **80** (7) 1489 (1998).

[Landolt-Börnstein 82] von Münch in Landolt-Börnstein III/17a, *Halbleiter*, p. 132 Springer Verlag, Berlin, Heidelberg, New York (1982).

[Lannoo 81] Lannoo M and Bourgoin J *Point Defects in Semiconductors* (Springer Series in Solid State Sciences 43), Springer Verlag Berlin Heidelberg (1981).

[Lanoo 94] Lanoo M, Stievenard D, Deresmes D, and Vuillaume D, Mat. Sci. Forum **143-147**, pt. 3, 1359-63 (1994).

[Lee 67] Lee W W and Sladek R J, Phys. Rev **158**, 788 (1967).

[Lee 67a] Lee W W and Sladek R J, Phys. Rev **158**, 794 (1967).

[Lépine 72] Lepine D, Phys. Rev. **B6**, 436 (1972).

[Limpijumnong 99] Limpijumnong S, Lambrecht W R L, Rashkeev S N, and Segall B, Phys. Rev. B **59** (20), 12890-99 (1999).

[Lips 96] Lips K, Lerner C and Fuhs W, J. of Non-Crystalline Solids **198-200**, 267 (1996).

[Longo 59] Longo T A, Ray R K, and Lark-Horovitz K, J. Phys. Chem. Solids **8**, 259 (1959)

[März 99] März M, Doctoral Thesis, Universität-GH Paderborn (1999)

[Mansfield 91] Mansfield R *Hopping Transport in Solids* (eds M Pollak and B I Shklovskii), p. 469. North-Holland, Amsterdam.

[Massarani 77] Massarani B, Caillot M, and Bourgoin J C, Phys. Rev. B **15**, 2224 (1977).

[Maxwell 66] Maxwell R and Honig A, Phys. Rev. Lett. **17** (4), 188 (1966).

[Maier 91] Maier K, Doctoral Thesis, Freiburg (1991).

[Mell 80] Mell H, Schweitzer L, and Voget-Grote U, J. noncrystall. Solids **35-36**, 639 (1980).

[Mendz 80] Mendz G and Haneman D *A new model of spin dependent resonance at Si surfaces* J. Phys. C: Solid St. Phys., **13**, 6737-59 (1980).

[Mendz 79] Mendz G, Miller D-J and Haneman D *Photoconductive resonance in silicon: theory and experiment* Phys. Rev. B, **20** (12), 5246-51 (1979).

[Miller 60] Miller A and Abrahams S, Phys. Rev. **120** 745 (1960).

[Moore 95] Moore W J, Freitas J A, Jr and Lin-Chung P J, Solid State Comm. **93** (5), 389-392 (1995).

[Morelli 93] Morelli D, Hermans J, Beetz C, Woo W S, Harris G L and Taylor C, Inst. Phys. Conf. Ser. (UK) **137** 313-6 (1993).

[Morigaki 72] Morigaki K and Onda M, J. Phys. Soc. Japan **33** 1031 (1972).

[Mott 61] Mott N F and Twose W-D, Adv. Phys. **10**, 107 (1961).

[Mott 68] Mott N F, J. non-crystall. Solids **1**, 1 (1968).

[Mott 79] Mott N F and Davis E A *Electronic Processes in Noncrystalline Materials*, 2nd edition. Clarendon Press, Oxford.

[Mott 90] Mott N F, *Metal-insulator transitions, 2nd ed* Taylor and Francis (1990).

[Mott 93] Mott N F, *Conduction in non crystalline materials, 2nd ed.* Oxford University Press (1993).

[Movaghar 77] Movaghar B and Schweitzer L, Phys. Stat. Sol. (b) **80**, 491 (1977).

[Movaghar 78] Movaghar B and Schweitzer L, J. Phys. C: Solid State Phys. **11**, 125 (1978).

[Movaghar 78a] Movaghar B, Schweitzer L and Overhof H, Phil. Mag. B **37** (6), 683 (1978).

[Movaghar 80] Movaghar B, Ries B and Schweitzer L, Phil. Mag. B **41** (2), 159 (1980).

[Movaghar 80a] Movaghar B, Ries B, and Schweitzer L, Phil. Mag. B **41**, 141 (1980).

[Nishino 83] Nishino S, Powel J A and Will H A, Appl. Phys. Lett. **42**, 460 (1983).

[Overhof 76] Overhof H, Festkörperprobleme **16**, 239 (1976).

[Osaka 79] Osaka Y, J. Phys. Soc. Japan **47**, 729 (1979).

[Parafenova 90] Parafenova I I, Tairov Y M and Tsvetkov V F, Sov. Phys. Semicond. (USA) **24** 158-61 (1990).

[Pake 73] Pake G E and Estle T L, *The Physical Principles of Electron Paramagnetic Resonance* 2nd. edition, W. A. Benjamin Inc., Reading, Massachusetts (1973)

[Patel 81] Patel J L, Nicholls J E, and Davies J J, J. Phys. C: Solid State Phys. **14**, 1339 (1981).

[Patrick 72] Patrick L, Phys. Rev. B **5**, 2198 (1972).

[Pensl 93] Pensl G and Choyke W J, Physica B **185** 264 (1993).

[Persson 97] Persson C and Lindefelt U, J. Appl. Phys., **82** (11) 5496 (1997).

[Pollak 91] Pollak M and Shklovskii B *Hopping Transport in Solids*, North Holland (1991).

[Poole 83] Poole C P, *Electron Spin Resonance*, Wiley, New York (1983).

[Reinacher 95] Reinacher N M, Brandt M S and Stutzmann M, Mat. Sci, Forum **196-201**, 4, 1915 (1995)

[Rheinke 98] Rheinke J, Thesis, Universität-GH Paderborn, (1998).

[Rhoderik 88] Rhoderik E H and Williams R H, *Metal Semiconductor Contacts*, 2nd ed., Clarendon Press, Oxford (1988).

[Rong 90] Rong F-C, Poindexter E-H, Harmatz M, Buchwald W-R and Gerardi G-J, Solid State Communications **76** (8) 1083 (1990).

[Rong 91] Rong F-C, Poindexter E-H, Warren W-L and Keeble D-J, Solid State Elect. **34** (8) 835 (1991).

[Schadt 94] Schadt M, Pensl G, Devaty R P, Choyke W J, Stein R and Stephani D, Appl. Phys. Lett. **65** (24), 3120 (1994).

[Schaffer 94] Schaffer W J, Negley G H, Irvin K G, and Palmour, *Diamond, Silicon Carbide and Nitride Wide Bandgap Semiconductors*, **339** 595 (1994).

[Schmidt 66] Schmidt J and Solomon I, C. R. Acad. Sci. (France) **263B** 169 (1966).

[Schoepe 88] Schoepe W, Z. Phys. B-Condensed Matter **71**, 455 (1988).

[Shklovskii 71] Shklovskii B I, Efros A L, and Yanehel IY, JETP Lett. **14**, 233 (1971). English translation: Springer, 1984.

[Shklovskii 79] Shklovskii B I and Efros A L *Electronic Properties of Doped Semiconductors* Nauka, Moscow (1976) English translation: Springer, 1984.

[Shklovskii 81] Shklovskii B I and Efros A L, Zh. Eksp. Teor. Fiz. **81**, 406(1981) [Sov. Phys. JETP **66**, 1215].

[Shklovskii 84] Shklovskii B I and Efros A L, *Electronic Properties of Doped Semiconductors*, Springer Verlag (1984).

[Shlimak 83] Shlimak I S, Ionov A N, and Shklovskii B I, Sov. Phys.-Semicond. **17**, 314 (1983).

[Slack 64] Slack G A, J. Appl. Phys. **35** 3460 (1964).

[Sladek 58] Sladek R J, J. Phys. Chem. Solids **5**, 157 (1958).

[Smith 97] Smith S R, Evwaraye A O, and Mitchel W C, Phys. Stat. Sol. (a) **162** 227 (1997).

[Solomon 76] Solomon I, Solid State Communications, **20** 215 (1976).

[Spaeth 92] Spaeth J-M, Niklas J R and Bartram R H *Structural Analysis of Point Defects in Solids: An Introduction to Multiple Magnetic Resonance Spectroscopy* (Springer Series in Solid State Sciences 43), Springer Verlag, Heidelberg, (1992).

[Sridhara 98] Sridhara S G, Devaty R P, adn Choyke W J, Journal of Applied Physics **84** (5), 2963 (1998).

[Stich 93] Stich B, Greulich-Weber S, Spaeth J-M and Overhof H, Semicond. Sci. Technol., **8**, 1385-1392 (1993).

[Stich 95] Stich B, Greulich-Weber S and Spaeth J-M J. Appl. Phys. **77** (4), 1-8 (1995).

[Stich 96] Stich B, Thesis, Universität-GH Paderborn, (1996).

[Stutzmann 95] Stutzmann M and Brandt M S, Phys. Stat. Sol. (b) **190**, 97 (1995).

[Suttrop 90] Suttrop W, Pensl G, and Lanig P, Appl. Phys. A **51**, 231 (1990).

[Suttrop 92] Suttrop W, Pensl G, and Choyke W J, J. Appl. Phys. **72** (8), 3708 (1992).

[Tairov 78] Tairov Y M and Tsvetkov V F, J. Cryst. Growth **43**, 209 (1978).

[Tokumoto 82] Tokumoto H, Mansfield R, and Lea M J, Phil. Mag. **46**, 93 (1982).

[Veinger 67] Veinger A I, Soviet Phys. -Semicond. **1**, 14 (1967).

[Vlasenko 86] Vlasenko L S, Vlasenko M P, Lomasov V N, and Khramtsov, Sov. Phys. JETP **64** (3), 612 (1986).

[Vlasenko 90] Vlasenko L S *Proceedings of the 20th International Conference on Physics of semiconductors*, Thesaloniki, Greece, **1** 714 (1990).

[Voget-Grote 76] Voget-Grote U, Stuke J and Wagner H, *Structure and Excitation of Amorphous Solids* (New York: American Institute of Physics), 85 (1976).

[Woodbury 61] Woodbury H-H and Ludwig G-W, Phys. Rev. **124**, 1083 (1961).

[Xiong 93] Xiong Z and Miller D-J, Appl. Phys. Lett., **63** (3), 352 (1993).

[Zavoisky 45] Zavoisky E, J. Phys. UdSSR **9**, 211& 245 (1945).

[Zhang 89] Zhang H, Pensl G, Dörnen A, and Leibenzeder S, Extended Abstracts 89-2 699 (1989).

List of Figures

List of Tables

AKNOWLEGMENTS

I would like to express my sincerest thanks to the following persons:

Prof. J.-M. Spaeth for admitting me into his group and for his constant readiness for discussion.

Prof. H. Overhof for valuable tips and discussions.

Priv.-Doz. Dr. S. Greulich-Weber for his constant support and many valuable discussions.

Mrs. Anna Merle for her constant help and her frienship.

B. Langhanki, Dr. M. März, I. Tkach, Dr. B. Stich and Dr. T. Pawlik for the skillfull help and the nice collaboration.

J. Portoles, Dr. M. Pinheiro, Dr. M. Linde for being good friends as well as colleagues.

All the Spaeth-Arbeitsgruppe for the nice collaboration.

The people from Hall-Labor, Heliumkeller and Mechanische Werkstatt.

Dr. Katharina Kalabukhova, Dr. Anu Agarwal for the nice discussions, which did not always deal with physics.

My friends, specially Cristina, Margot, Michaela and José Luis for their support during all phases of this work.

My friends in Huesca, specially Anabel, Susana, Jorge and Ignacio, who left us too soon, as well as my Latin and Moroccan friends in Paderborn for so much warmth.

My family for their loving support. *Gracias* papá, mamá, Patricia, Juan Luis, Ruth, yaya and the others. Thanks as well to the Mazili family, *shukran djiddan*.

And last but not least, to my husband Hassan for his neverending patience and support during the most difficult times, *shukran habibi*.

Since I have probably forgotten somebody, this is for you: thank you.

gracias gracias gracias gracias gracias gracias gracias gracias gracias gracias